KINETIC STUDIES OF SINGLET MOLECULAR OXYGEN USING A DISCHARGE FLOW/SHOCK TUBE

by

K.R. GRANT, M.Sc.

A thesis submitted to the University of Keele in partial fulfilment of the requirements for the Degree of Doctor of Philosophy.

Department of Chemistry
University of Keele

March 1981

TO MY PARENTS

The work reported in this thesis was carried out by the author, Dr. M.D. Pedley and Dr. P.M. Borrell under the supervision of Dr. Peter Borrell. In the tables the shocks with run numbers beginning with C were performed and analysed by the author.

ACKNOWLEDGEMENTS

In presenting this thesis I would like to thank the following people for their assistance.

Dr. Peter Borrell for his supervision and advice during the course of this work.

Professor I.T. Millar for provision of laboratory facilities.

Dr. Mike Pedley and Dr. Patricia Borrell my co-workers.

The technical staff of the Department particularly Peter Holbrook, Bob Dix, Ralph Pattison and Chris Cork.

Mrs. Iris Jones, Mrs. Margaret Furnival and Mrs. Christine Owen for their excellent typing of the thesis.

The University of Keele for financial support for the years 1977-1980.

UNITS AND ABBREVIATIONS

As far as possible this thesis is written in S.I. units, however some non-S.I. units are retained where they are more familiar or suitable. For example pressures may be quoted in torr, wavenumbers in cm^{-1} and second order rate constants in $\ell\ mol^{-1}\ s^{-1}$.

For ease of reading and typing the full spectroscopic notation for the electronic states of oxygen is abbreviated; $O_2(^1\Delta_g)$ is referrred to as delta, $O_2(^1\Sigma_g^+)$ as sigma, collectively the states are referred to as singlet molecular oxygen or singlet oxygen.

ABSTRACT

A discharge flow/shock tube has been used to investigate some reactions of singlet molecular oxygen. Results have been obtained at high temperatures and also at room temperature using the apparatus as a conventional discharge flow system.

A high temperature study of the emissions from $O_2(^1\Delta_g)$ at 634 nm, 703 nm and 579 nm confirms their bimolecular nature. The relative emissivities of these three dimol emissions have been obtained, enabling radiative rate constants relative to that for the 634 nm emission at 295 K to be estimated.

Monitoring of the dimol emission at 579 nm enabled the vibrational relaxation of oxygen to be followed. A linear Landau-Teller plot for results up to 1650 K was obtained. The relaxation is more rapid than that expected for ground state oxygen, this is interpreted as evidence for vibration-vibration exchange between the ground state and $O_2(^1\Delta_g)$.

Also by using the 579 nm emission a rate constant for collisional quenching of $O_2(^1\Delta_g)$ v=1 at room temperature has been obtained. This process is slow compared to reactions involving $O_2(^1\Delta_g)$ v=0.

The energy pooling reaction and the collisional quenching of $O_2(^1\Sigma_g^+)$ by O_2, N_2, Ar, CO_2 and N_2O have been followed using the emission at 762 nm. Quenching rate constants at 295 K have been measured for CO_2 and N_2O. Rate constants for collisional quenching and for the energy pooling reaction have been measured at high temperatures. Positive temperature dependences are obtained for the quenching by O_2, N_2 and for the energy pooling reaction, negative dependences for the quenching by CO_2 and N_2O. Arrhenius plots are non-linear, the different temperature dependences are interpreted on

the basis of long or short range interactions. The quenching by Ar proved too slow to be measured by this technique. The rate constant for the energy pooling reaction up to 1850 K showed no composition dependence, confirming the nature of the reaction.

CONTENTS

Chapter 1

INTRODUCTION

1.1. Preface

Kinetics is a source of much information in the study of chemical structure and reactivity, a combination of kinetic and thermodynamic data allows chemical processes to be understood and so predictions about the course and rate of novel reactions to be made.

The singlet states of oxygen are of special interest because they are the low lying excited states of a common, biologically important molecule. They could therefore be involved in many processes of physical and biological interest. While the extreme metastability of the singlet states makes oxygen almost unique it allows the fundamental nature and interactions of excited states to be probed. Because of these considerations the number of papers published on singlet oxygen has increased dramatically in recent years, necessitating regular reviews.[1,2]

The biological aspects of singlet oxygen chemistry are beyond the scope of this thesis and suffice it to say that delta has been implicated in the formation of cancer, in blood disease and in ageing processes in Man[3].

Though singlet oxygen is now known to be of less importance in atmospheric pollution than was once thought[4] to the researcher interested in the more physical aspects of chemistry it is still a fruitful field of study. Vibrational relaxation, luminescence, energy transfer and quenching have all been investigated.[1,2] In such work the temperature dependence of the process is particularly informative and in the specific case of the quenching of sigma Thrush[5] has suggested that it is essential to the clarification of the quenching mechanism.

So an apparatus in which singlet oxygen could be produced and heated would be most useful; there have been basically two approaches to this problem.

One is to modify an established room temperature technique, in this case time resolved laser induced fluorescence, to other temperatures.[6,7] This is accomplished by flowing a thermostatted liquid, usually water or methanol, around the reaction cell. This method has the advantages of photon counting techniques, that is the repetition of laser shots enabling the precision to be increased without prohibitively increasing the experiment time, but has the drawback that only a small temperature range may be studied, 200-400 K. While this temperature range is adequate for most purposes the reactions of singlet oxygen, particularly the quenching of sigma, display little temperature dependence and so a wide range is desirable.

A different approach is to combine two separate techniques, one low temperature and one high temperature, to yield a technique with the advantages of both. Such an apparatus is the discharge flow/shock tube.

It is the use of a discharge flow/shock tube to study singlet molecular oxygen that this thesis describes. This first chapter serves both to introduce the technique and the area of study and concludes with an indication of the results it was hoped to obtain.

1.2. Gas Phase Kinetics.

The discharge flow/shock tube is a combination of two well established techniques and in this section a brief survey of each is given. As well as a description of the technique and apparatus the area of study and limitations of each are discussed.

The section ends with a review of the previous work carried out using discharge flow/shock tubes and an appreciation of their use in physical chemistry.

1.2.1. Use of Flow Tubes in Gas Kinetics.

Flow tubes were among the first techniques devised to follow fast reactions[8], initially in the liquid state but later in the gas phase as well. A schematic flow tube is shown in figure 1.1.

Essentially the reaction of two species A and B is studied as a function of distance as they are carried down the tube in the carrier gas M. By moving the inlet pipe, which runs axially down the tube, it is possible to vary the contact time between the reactants and thus sample the mixture at intervals during the reaction. With the assumptions that mixing is homogenous and there are no concentration gradients it is possible to obtain rate constants for a variety of gaseous processes. The preferred method of generating atoms or radicals is a microwave discharge, this has the advantage over thermal methods of versatility - a discharge will fragment virtually any molecule. This can however be a problem in that a variety of fragments may be produced leading to secondary reactions.

An immense variety of detectors can be used to monitor the progress of the reaction. During the flow at any point along the tube the concentration of products is constant so slow detectors may be used. Mass spectrometry, chemiluminescence, electron spin resonance and

Figure 1.1 Schematic Flow Tube

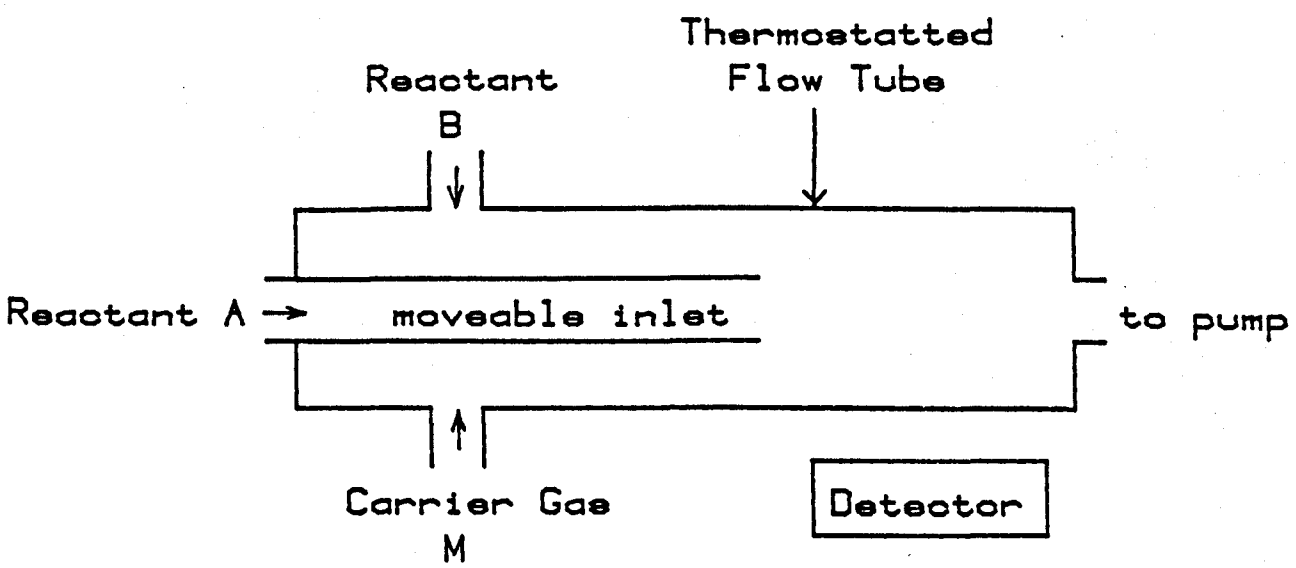

absorption have all been used successfully to follow flow tube reactions[8].

Thus a discharge flow system is an excellent method for studying many fast reactions ($k = 10^4 - 10^{10}$ ℓ mol^{-1} s^{-1}) at low pressures (< 10 torr, 1.3 k Pa) and within the temperature range 200-600 K. This final constraint is severe because the measurement of rate constants across a wide temperature range is important, particularly for reactions with a non-Arrhenius temperature dependence.

1.2.2. The Effect of Temperature on Chemical Reaction Rates.

If a chemical reaction were dependent solely on the collision of two molecules then the temperature dependence of the rate constant would be governed simply by that of the collision rate, thus

$$k \propto T^{\frac{1}{2}}$$

Consideration of the observation that chemical reactions were not instantaneous led Arrhenius to the concept of activation being an essential pre-requisite to reaction. He derived an equation relating the observed rate constant to a theoretical quantity, the activation energy, thus

$$k = A \exp\left(\frac{-E}{RT}\right) \qquad (1.1)$$

For a reaction displaying Arrhenius behaviour the increase in rate constant with temperature can be rapid. Use of (1.2) shows that for an activation energy of 50 kJ mol^{-1} the rate constant doubles between 290 and 300 K.

$$\ln \frac{k_2}{k_1} = -\frac{E}{R}\left\{\frac{1}{T_2} - \frac{1}{T_1}\right\} \qquad (1.2)$$

If however the activation energy is small then the temperature dependence of the pre-exponential factor A can become important. This can be shown to be related to the number of collisions occurring and so varies with the square root of the temperature.

Other temperature dependencies are known. For example the Landau-Teller theory of vibrational energy transfer predicts that the probability of energy transfer per collision P, will be related to the temperature by

$$\log_{10} P \propto T^{1/3}$$

Experiments on vibrational relaxation usually measure a relaxation time τ which is related to the probability by

$$P^{-1} = Z\tau(1 - (\exp - h\nu/kT)) \qquad (1.3)$$

where Z is the collision rate. Hence

$$\log_{10} \tau \propto T^{-1/3}$$

The classical theory of Landau and Teller has been superceded by the quantum approach of Schwartz, Slawsky and Herzfeld[9]. They found several temperature dependent terms, one of which was a $T^{-1/3}$ term. This is usually dominant, leading to a linear Landau-Teller plot but in some cases other temperature dependencies are known. For example polar molecules may show an inverse dependence where attractive forces dominate the interaction[9] e.g. HCl. The vibrational relaxation of oxygen is one of the reactions discussed in this thesis and provides a good example of Landau-Teller behaviour in the temperature range studied.

Apart from observing the temperature dependence of known reactions high temperatures can be used to investigate the behaviour of novel systems. Radicals and unstable intermediates can be produced in measurable concentrations, the relative contributions of different energy levels, particularly vibrational to an overall reaction can be assessed and high temperature processes e.g. pyrolysis and combustion can be studied under controlled conditions.

The pre-requisite for all these studies is the same; it is necessary to heat the reaction mixture homogenously over a sufficient time to allow measurements to be made. Shock tubes are the main method for such studies above 600 K.[10,11]

1.2.3. Use of Shock Tubes in Gas Kinetics.

Figure 1.2 shows a diagram of a simple pressure driven shock tube and a schematic of the propagation of a shock wave in such an apparatus.

The shock tube operates as follows. A driver gas is let into a section of the shock tube separated from the test section by a thin diaphragm. At a certain pressure in the driver section the diaphragm bursts and the driver gas expands into the test section. The formation of the shock wave can be understood if the expanding driver gas is seen as a piston accelerating to a constant velocity v, greater than the speed of sound in the cool gas a.

The first increment of velocity, dv, causes a compression wave to be propagated into the test gas with velocity a. With a second increment dv another wave is despatched but it is travelling into slightly heated gas and has a greater velocity a + da. After a sequence of such events the piston reaches its final velocity v and the compression waves, of gradually increasing velocity, have coalesced

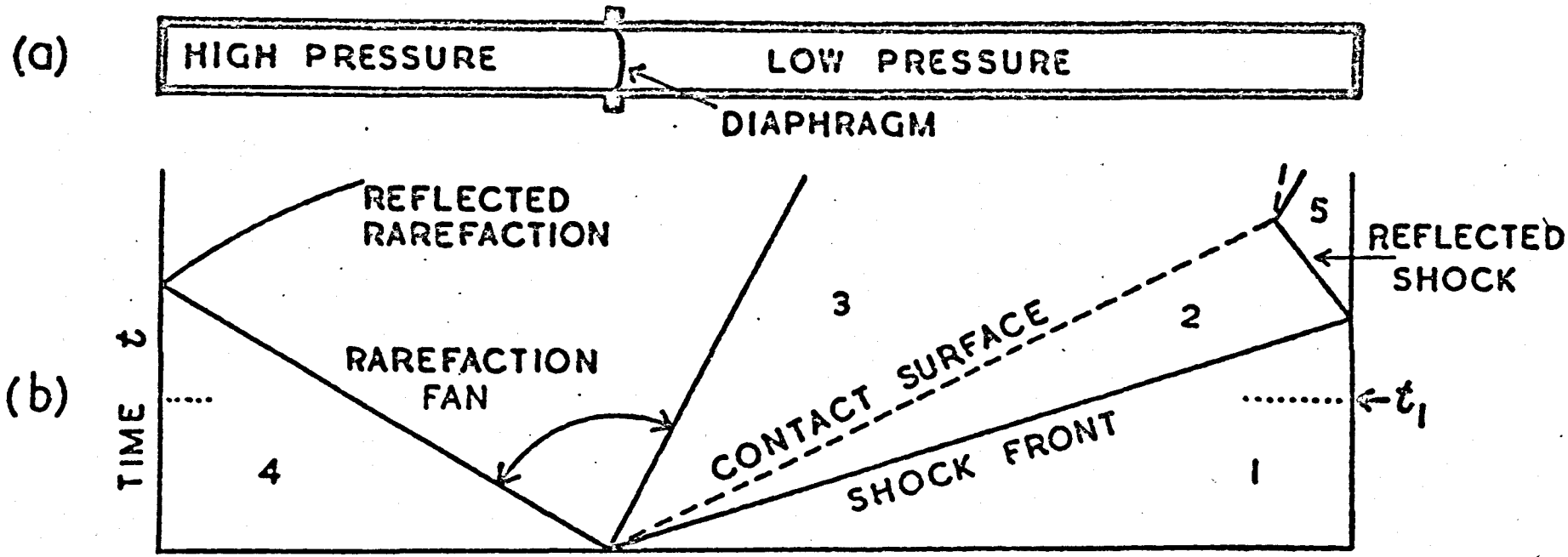

Figure 1.2 a) Shock Tube

b) Propagation of Shock

into a shock wave. This wave separates the cool from the shocked gas, is normal to the tube walls and is narrow, the shock temperature being achieved in $<10^{-9}$ s. A reverse process operates behind the piston. A series of weak expansion waves are propagated through the gas which travel with decreasing speed through the cooling gas without coalescing - this is called the rarefaction fan.

Observations of the heated test gas may be made during the hot-flow time, that is the time between the arrival of the shock front and the contact surface - the leading edge of the expanding driver gas.

Consideration of mass, momentum and energy conservation across the shock front lead to equations which relate the final pressure (P_A), density (ρ_A) and temperature (T_A) of the gas to a measurable quantity, the shock velocity[12]. For a monatomic or frozen gas, that is one where the vibrations are inactive

$$\frac{P_A}{P_1} = \frac{2\gamma M^2 - (\gamma - 1)}{\gamma + 1} \tag{1.4}$$

$$\frac{\rho_A}{\rho_1} = \frac{(\gamma + 1)M^2}{(\gamma - 1)M^2 + 2} \tag{1.5}$$

$$\frac{T_A}{T_1} = \frac{P_A}{P_1} \Big/ \frac{\rho_A}{\rho_1} \tag{1.6}$$

where M = mach number of shock = v/a

γ = specific heat ratio

Thus a shock tube can be used to produce a high temperature, rapidly and uniformly, in a gas. It's limitations are mainly those of non-reproducibility[11]. Variations in diaphragm thickness, test gas pressure and other factors mean that no two shocks produce

identical conditions. Furthermore, flow irregularities and imprecisely determined shock conditions lessen the accuracy. Nevertheless the technique has found many applications in chemistry and physics. Combustion phenomena, pyrolysis, dissociation and ionisation of gases, vibrational and rotational relaxation, supersonic flow and high temperature spectroscopy are a few of the many areas in which shock tubes have been successfully applied[10].

The adaptation of the shock tube to a specific chemical problem, that is the study of metastables and the measurement of rate constants will now be discussed.

1.2.4. The Discharge Flow/Shock Tube.

This thesis is concerned with the study of singlet oxygen in a discharge flow shock tube and in this section a brief history of the development of the technique is given.

Hartunian, Thompson and Hewitt[13] constructed the first discharge flow/shock tube in 1966. In their apparatus the radio frequency discharge was applied around the shock tube and the shock and gas flow were in the same direction (c.f. the present apparatus figure 2.1). They studied the temprature dependence of the chemiluminescent recombination reactions

$$CO + O \rightarrow CO_2 + h\nu(\lambda = 500\ nm)\ T = 400 - 1000\ K \quad (1.7)$$

$$NO + O \rightarrow NO_2 + h\nu(\lambda = 630\ nm)\ T = 400 - 1000\ K \quad (1.8)$$

They also speculated as to the suitability of such an apparatus to the study of surface catalysis.

Gross[14,15,16] and Cohen[15,16], working in the same laboratory, then used the technique to study a variety of chemiluminescent reactions.

$$N + N \rightarrow N_2 + h\nu(\lambda = 580\text{-}700\ nm) \quad T = 300\text{-}2400\ K \quad (1.9)$$

$$N + O \rightarrow NO + h\nu(3\ bands) \quad T = 300\text{-}2400\ K \quad (1.10)$$

$$SO + O \rightarrow SO_2 + h\nu(\lambda = 320\ nm) \quad T = 300\text{-}1500\ K \quad (1.11)$$

Breen, Quy and Glass[17] produced a paper on the vibrational relaxation of oxygen and hydrogen using a discharge flow/shock tube and showed that shock propagation into a discharged, flowing gas was normal. Only recently have these authors reported any further work[18], on the radical abstraction reaction.

$$H + N_2O \rightarrow N_2 + OH + h\nu(\lambda = 4717\ nm) \quad T = 1473\text{-}2710\ K \quad (1.12)$$

They suggest that this reaction can be used as a source of hydroxyl radicals to study the reactions of this atmospherically important species.

Meanwhile Borrell, Borrell and Brittain[19] had also been developing a discharge flow/shock tube. Initial studies were of an atomic nitrogen discharge, later the apparatus was used to study singlet oxygen. Singlet oxygen lends itself to a discharge flow/shock tube study. The features that makes it particularly suitable are the mechanism of formation of the excited states and the stability of delta.

As will be shown in a later section delta is formed in the microwave discharge and is quenched only slowly. This means that the discharge can be remote from the shock tube and still produce a measurable concentration of delta at the observation station. Having the discharge separate allows any unwanted by-products to be deactivated before entering the test section and removes any possibility of flow irregularities caused by the discharge or adding reactants mid-way down the shock tube. Sigma is continually formed from

delta in the energy pooling reaction[20]. As delta is present throughout the length of the shock tube the proportion of sigma is always significant, despite it being deactivated several orders of magnitude faster than delta.

Finally there is the fact that the emissions from singlet oxygen, using which the excited states are monitored, occur in a part of the spectrum where it is practical for measurements to be made. Pyrex does not transmit below 300 nm, measurements above 900 nm are complicated by the need to use infra-red detectors.

Studying singlet oxygen this apparatus has been used both as a conventional discharge flow system, Borrell, Borrell and Pedley observing the deactivation of delta by oxygen[21]; and also at high temperatures in the study of the quenching of sigma by oxygen and nitrogen[22].

This brief survey indicates the usefulness of the discharge flow/shock tube, it combines the versatility of the discharge flow system with the temperature range of a shock tube. In the next section the subject of this discharge flow/shock tube study, singlet oxygen, is described.

1.3. Singlet Molecular Oxygen

This section describes the structure, spectroscopy and reactions of singlet molecular oxygen, the system to which the discharge flow/shock tube technique is applied in this laboratory. It is not a comprehensive literature survey; while the discovery and early work on singlet oxygen is described the emphasis is on the most recent work.

1.3.1. Structure and Spectroscopy.

The electronic structure of molecular oxygen is $KK(\sigma_g 2_s)^2 (\sigma_u 2_s)^2 (\pi_u 2_p)^4 (\pi_g 2_p)^2$, and is shown schematically in figure 1.3. It is necessary to consider the two outer electrons to generate the spectroscopic states of ground electronic state oxygen.

In a diatomic molecule the electrons move in an electrostatic field of axial symmetry. The orbital angular momentum vector of the electrons precesses about the internuclear axis[23] and has component along it of M_L, where

$$M_L = L, L-1, L-2 \ldots -L \tag{1.13}$$

and

$$L = \sum^{n} \ell_1 + \ell_2 + .. \ell_n \tag{1.14}$$

In such a field M_L is degenerate with $-M_L$ and so different states can be classified according to $|M_L|$ thus

$$\Lambda = |M_L| \tag{1.15}$$

Integer values of Λ from zero are designated Σ, π, Δ etc. and all, except Σ, are doubly degenerate.

In the molecule the individual electron spins can be said to form a resultant $\underline{S}$, which precesses about the internuclear axis under

Figure 1.3 Electronic Structure of Oxygen

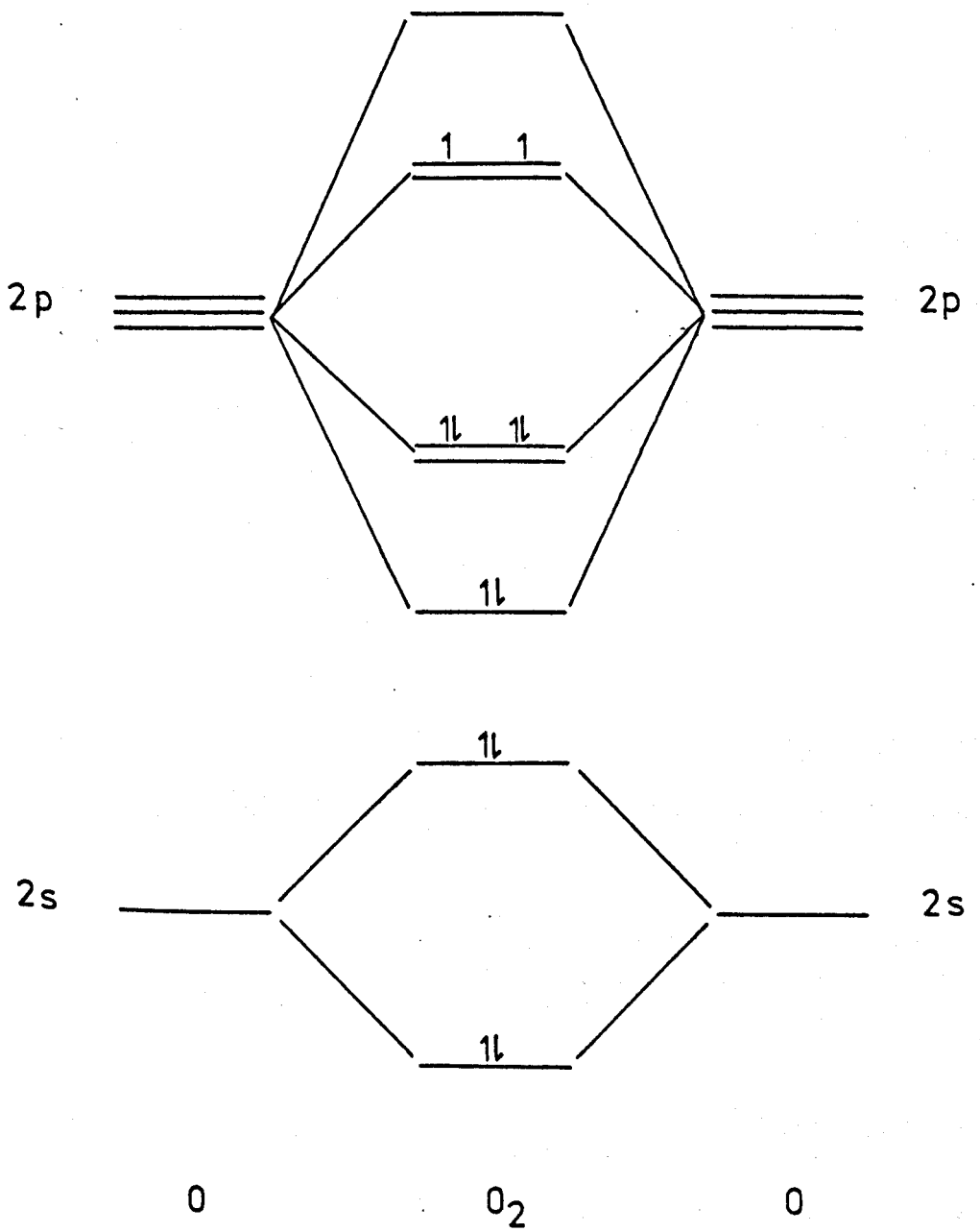

the influence of the magnetic field of the orbital electrons with constant component M_s. Values of M_s are designated Σ

$$\Sigma = S, S-1, S-2 \ldots -S \tag{1.16}$$

As already explained for Σ states there is no internal magnetic field and so no splitting occurs provided the molecule does not rotate and is not in an external magnetic field.

To apply these rules to oxygen assume first the electrons are in different orbitals, i.e. a Σ state as $L = 0$. The four possible spin orientations are shown below; α and β refer to spin direction, 1 and 2 to the electrons, also shown is the symmetry with respect to electron exchange.

$\alpha(1)$	$\alpha(2)$	symmetric
$\beta(1)$	$\beta(2)$	symmetric
$\alpha(1)$	$\beta(2)$	anti-symmetric
$\alpha(2)$	$\beta(1)$	anti-symmetric

Of these four configurations the first two, the spin parallel combinations, are acceptable; the last two are not acceptable as they suggest a distinguishibility of electrons. Linear combinations may be taken

$$\frac{1}{\sqrt{2}} (\alpha(1)\,\beta(2) + \alpha(2)\,\beta(1)) \quad \text{symmetric}$$

$$\frac{1}{\sqrt{2}} (\alpha(1)\,\beta(2) - \alpha(2)\,\beta(1)) \quad \text{anti-symmetric}$$

These are acceptable as representations of the wavefunction; there are now three symmetric and one anti-symmetric spin wavefunctions. The total wavefunction, the product of space and spin parts must be anti-symmetric with respect to electron exchange so the

triplet must combine with an anti-symmetric space wavefunction. Symmetry of the wavefunction with respect to reflection through a plane joining the nuclei is denoted by + or −, thus the triplet must combine with the anti-symmetric space wavefunction, Σ^-; and the singlet with Σ^+.

If both electrons are in the same $p\pi^*$ orbitals, (it is immaterial which) a $^1\Delta$ state is generated.

Symmetry of the wavefunction with respect to inversion through the centre of symmetry of the molecule is denoted by g or u to indicate whether there is a change of sign (g = gerade; even). Both the $p\pi^*$ orbitals of oxygen are g so the terms are $^3\Sigma_g^-$, $^1\Sigma_g^+$ and $^1\Delta_g$.

In the isolated non-rotating molecule there are three degenerate $^3\Sigma_g^-$ states, two degenerate $^1\Delta_g$ states and a single $^1\Sigma_g^+$ state.

Hund's rules state that the term of maximum multiplicity lies lowest in energy, for terms of equal multiplicity that of greatest orbital angular momentum lies lowest. Hence the order of states for molecular oxygen is $^3\Sigma_g^-$, $^1\Delta_g$, $^1\Sigma_g^+$.

Because they are generally produced together the two lowest excited singlet states are often collectively referred to as singlet molecular oxygen or singlet oxygen. Figure 1.4 shows some of the lower states of molecular oxygen[24].

Electric dipole transitions from the ground state to the singlet states are spin, symmetry (g; u) and, in the case of delta, orbitally forbidden. However their presence as atmospheric emission bands is well known[23], where they occur as magnetic dipole transitions, but their intensities are low as they are still not fully allowed.

$$O_2(^1\Delta_g) \rightarrow O_2(^3\Sigma_g^-) + h\nu(\lambda = 1270\ nm) \qquad (1.17)$$

Figure 1.4 Electronic States of Oxygen

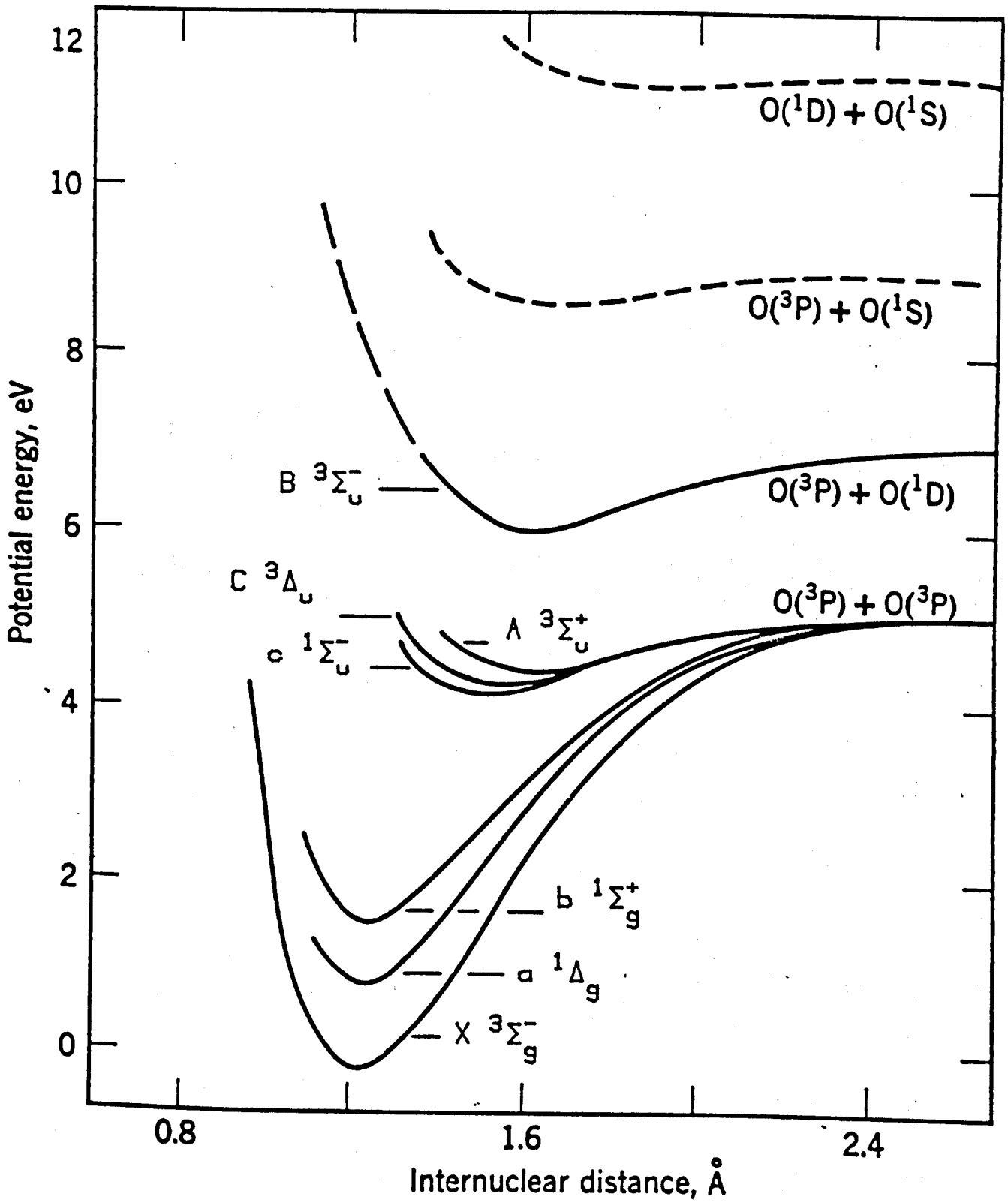

Table 1.1

Observed Dimol Transitions

States of Dimol Pair	Transition Wavelength /nm	Vib. States v'	v''
$(^1\Delta_g)$ $(^1\Delta_g)$	703.8*	0	1
	634.3*	0	0
	579.8*	1	0
$(^1\Delta_g)$ $(^1\Sigma_g^+)$	514.2*	0	1
	476.1*	0	0
	444.7	1	0
$(^1\Sigma_g^+)$ $(^1\Sigma_g^+)$	405.1*	0	1
	381.1*	0	0
	361.7	1	0
	344.2	2	0
	328.3	3	0

Figure 1.5 Singlet Oxygen Emissions Studied

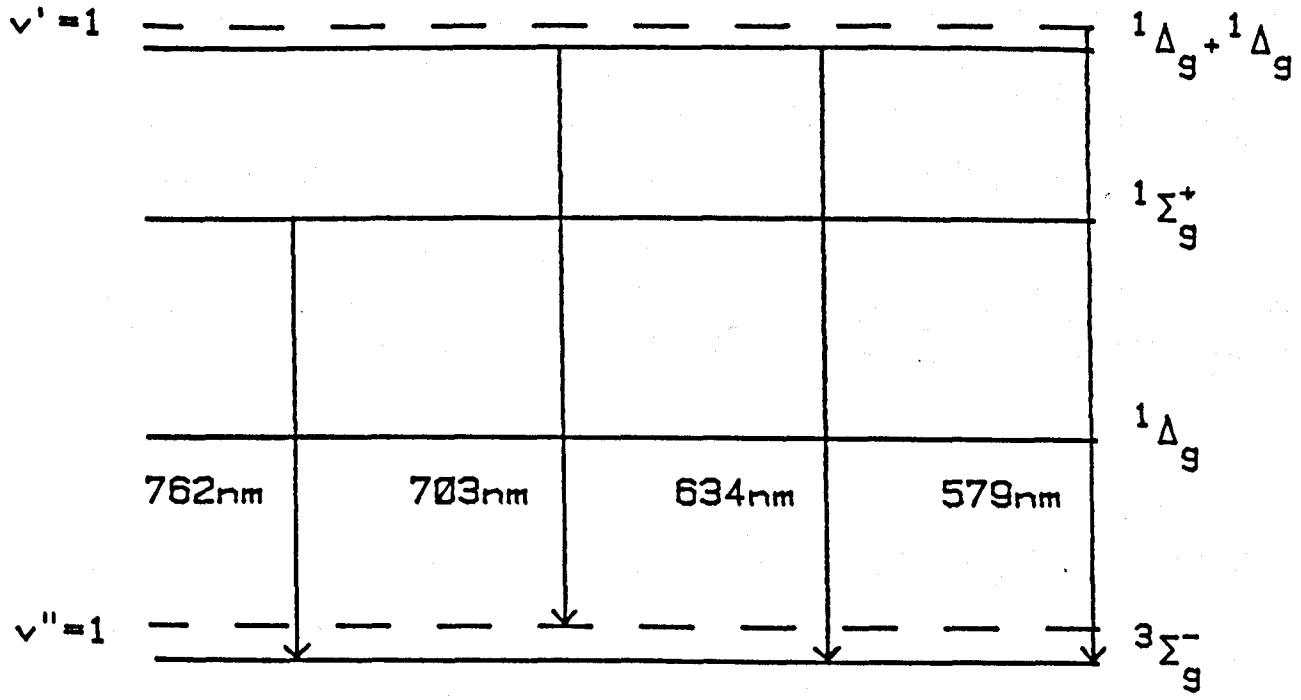

Delta lies 0.977 eV above the ground state, it has a radiative lifetime of 64.6 min ($A = 2.58 \times 10^{-4}\ s^{-1}$) at zero pressure[25].

$$O_2(^1\Sigma_g^+) \rightarrow O_2(^3\Sigma_g^-) + h\nu(\lambda = 762\ nm) \qquad (1.18)$$

Sigma lies 1.626 ev above the ground state, the average of the most recent values of its lifetime is 13 s ($A = 0.075\ s^{-1}$)[26].

Kasha[27] has suggested that the key to the understanding of the spectroscopic and photochemical behaviour of singlet oxygen lies in the simultaneous transitions that are possible for colliding singlet oxygen pairs. For example the simultaneous transition of two colliding delta molecules gives rise to an emission (a dimol emission) at 634 nm, twice the energy of the single molecule transition.

$$O_2(^1\Delta_g) + O_2(^1\Delta_g) \rightarrow O_2(^3\Sigma_g^-) + O_2(^3\Sigma_g^-) + h\nu(\lambda = 634\ nm) \qquad (1.19)$$

The Wigner Spin Conservation Law states that during an intermolecular collision the total spin must not change. The spin of two reactants A and B on collision can only have one of the following values

$$(S_A + S_B),\ (S_A + S_B - 1) \ldots .\ \ |S_A - S_B|$$

A similar series can be written for the products X and Y. For the reaction to be spin allowed the two series must have a number in common.

The dimol emission process (1.19) is therefore spin allowed, the resultant ground state pair having singlet, triplet and quintet components.

A list of observed dimol transitions is given in Table 1.1, those that have been seen in emission from discharged oxygen are marked with

an asterisk[28]. The singlet states are sufficiently long lived to enable dimol emissions to be obvious at pressures below one atmosphere. In absorption however pressures in excess of 100 atmospheres are necessary[27].

In figure 1.5 the emissions from singlet oxygen that are studied in this work are illustrated.

1.3.2. Preparation of Singlet Molecular Oxygen.

There are five main methods for the preparation of singlet molecular oxygen in the gas phase, each will now be briefly outlined.

1. Electric Discharges through Oxygen.

Microwave discharges are a readily controlled method of producing singlet oxygen at useful concentrations over a wide pressure range, estimates put the delta concentration at up to 20% of the total flow and sigma at < 0.2% of this[29]. The mechanism of formation of singlet molecular oxygen by this method appears to be by atom recombination to form $O_2(^1\Delta_g)$. This is suggested by the fact that the maximum delta concentration is seen several centimeters downstream of the discharge. Sigma is then formed from delta in the energy pooling reaction[20].

$$O_2(^1\Delta_g) + O_2(^1\Delta_g) \rightarrow O_2(^1\Sigma_g^+) + O_2(^3\Sigma_g^-) \qquad (1.20)$$

It was mentioned earlier that a microwave discharge will fragment virtually any molecule and while this is useful it might also lead to the formation of unwanted by-products. The by-product of the preparation of singlet oxygen is atomic oxygen.

Ogryzlo and Bader[30] have shown that one of the most effective methods of removing atomic oxygen from the discharge products is by flowing the gas over a mercury surface upstream of the discharge. This causes a surface of mercuric oxide to be deposited after the discharge.

2. Photolysis of Ozone.

This process has been intensively studied in recent years not only as a source for singlet oxygen but also because it is a major mechanism of ozone loss in the atmosphere[4].

Below 310 nm there is sufficient energy for ozone to be photodissociated to form delta and an oxygen (^1D) atom.

$$O_3 + h\nu(210 - 310\ nm) \rightarrow O_2(^1\Delta_g) + O(^1D) \qquad (1.21)$$

This reaction proceeds with a quantum yield of $O(^1D)$ formation of one and is the major photodissociation mechanism for atmospheric ozone above 25 km[4].

At wavelengths greater than 310 nm there is insufficient energy for (1.21) to occur. Castellano and Schumacher[31] have shown that irradiation of ozone in the region 310 - 330 nm results in the formation of singlet oxygen and $O(^3P)$.

$$O_3 + h\nu(310 - 330\ nm) \rightarrow O_2(^1\Delta_g \text{ or } ^1\Sigma_g^+) + O(^3P)$$

This process is thought to be of importance in the lower atmosphere where the shorter wavelengths are unable to penetrate[4].

3. Chemical Methods.

Since the initial work on the red chemiluminescence observed on mixing sodium hypochlorite and hydrogen peroxide this area has been neglected, at least in the gas phase. However Murray and Kaplan[32,33] have devised a method for producing delta by heating a solid ozone-triphenyl phosphite complex

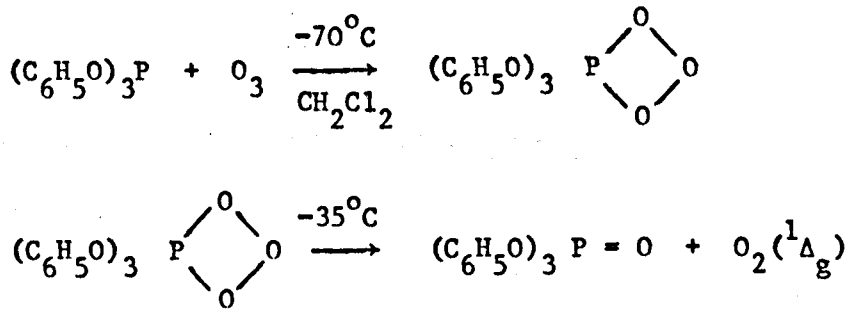

4. Photosensitization.

In solution this is a well tried method for producing excited molecules. While in solution the use of dyes and ketones as photosensitizers is routine in the gas phase unusual systems have been developed. Abrahamson et al[34,35,36] have used SO_2 to produce sigma, Frankiewicz and Berry[37] to produce delta. Steer, Sprung and Pitts[38] have used benzene in their studies of the role of singlet oxygen in air pollution.

5. Laser Excitation.

Most of the methods mentioned so far have suffered from one major drawback - they lead to the formation of both excited states. The production of one state in isolation is obviously of importance when attempting to specify which state is involved in a particular reaction. It is here that laser excitation is of use. The intensity of laser sources means that singlet oxygen can be produced by direct excitation and furthermore the narrow bandwidth enables particular vibrational levels to be populated.

Matheson et al[39] and Parker and Ritke[40] have produced $O_2(^1\Delta_g)v=1$ by direct excitation from the ground state using 1070 nm light from a Nd-glass laser. Tunable dye lasers have been used to produce sigma in both it's ground[41] and first[42] vibrational levels. Recently Kohse-Hoinghaus and Stuhl[7,43] have used a VUV hydrogen laser to

dissociate oxygen, singlet oxygen then being formed by energy transfer from $O(^1D)$.

1.3.3. Reactions of Singlet Molecular Oxygen.

1. Chemical Reaction.

Delta is the suspected reactive species in the following reactions, both of which have been seen in the gas phase[4].

ENE Reaction

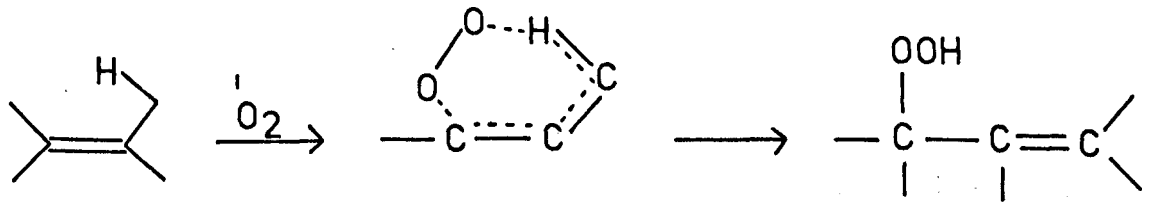

Cycloaddition

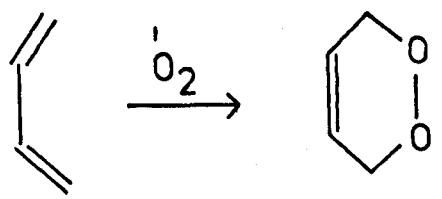

2. Energy Transfer

(a) The Energy Pooling Reaction

$$O_2(^1\Delta_g) + O_2(^1\Delta_g) \rightarrow O_2(^1\Sigma_g^+) + O_2(^3\Sigma_g^-) \qquad (1.20)$$

This reaction was first postulated by Young and Black[20] to account for the observed interdependence of the excited state concentrations; $[O_2(^1\Sigma_g^+)] \alpha [O_2(^1\Delta_g)]^2$. After many attempts that were affected by impurities the room temperature rate constant for this reaction was measured accurately by Derwent and Thrush[44] to be $1.22 \pm 0.3 \times 10^4$ ℓ mol^{-1} s^{-1}.

Schurath[45] has studied this reaction by observing the emission from sigma. He found the (2,0) transition to be much stronger at

room temperature than one would expect for a Boltzmann distribution. The energy pooling reaction is exothermic and up to two vibrational quanta may be distributed amongst the products. Schurath found that the relative probabilities of populating $O_2(^1\Sigma_g^+)v=2$, 1, 0 are in the ratio 1:0.06:0.5 respectively.

As will be shown in Chapter 6 the discharge flow/shock tube may be used to study the temperature dependence of the energy pooling reaction. Studies in mixtures enable the nature of the reaction to be confirmed.

(b) Miscellaneous Processes.

There are few molecules with excited states lying low enough for energy transfer to be feasible, however one such is SO. Indeed their similar electronic structure means that they have similar spectroscopic states and emissions from both $SO(^1\Delta)$[46] and $(^1\Sigma^+)$[47] are known.

Recently Ishiwata and Tanaka[48] have studied the system $O/COS/O_2(^1\Delta_g)$, producing O and $O_2(^1\Delta_g)$ in a microwave discharge. They observed emissions from $O_2(^1\Sigma_g^+)$, $O_2(^1\Delta_g)$, $SO(^1\Sigma^+)$ and SO_2. As well as being formed in the oxygen energy pooling reaction they found that $O_2(^1\Sigma_g^+)$ was formed by

$$SO(^3\Sigma^-) + O_2(^1\Delta_g) \rightarrow SO(^1\Delta) + O_2(^3\Sigma_g^-) \qquad (1.22)$$

$$SO(^1\Delta) + O_2(^1\Delta_g) \rightarrow SO(^3\Sigma^-) + O_2(^1\Sigma_g^+) \qquad (1.23)$$

Furthermore SO itself could undergo an energy pooling reaction analagous to that of oxygen

$$SO(^1\Delta) + SO(^1\Delta) \rightarrow SO(^1\Sigma^+) + SO(^3\Sigma^-) \qquad (1.24)$$

It is the extreme metastability of the lowest excited singlet states of both O_2 and SO, caused by their low energy and spin configuration, that enables them to undergo such reactions.

On mixing singlet oxygen with iodine a spectacular yellow chemiluminescence is seen from $I_2(^3\pi_{ou}^+)$, due to consecutive energy transfer from sigma and delta[49].

$$I_2(^1\Sigma_g^+) + O_2(^1\Sigma_g^+) \rightarrow I_2(^3\pi_u) + O_2(^3\Sigma_g^-) \qquad (1.25)$$

$$I_2(^3\pi_u) + O_2(^1\Delta_g) \rightarrow I_2(^3\pi_{cu}^+) + O_2(^3\Sigma_g^-) \qquad (1.26)$$

3. Quenching of Singlet Molecular Oxygen.

In figure 1.6 (reproduced from Ogryzlo[2]) the rate constants for the gas phase quenching of sigma and delta are displayed. The data are arranged across the figures according to molecular type. The area around each molecule represents the spread of experimental measurements and the line the 'best value'. The figures do not contain all measurements but several general trends are apparent.

(a) Quenching of sigma generally has a larger rate constant than that of delta. This can be attributed to the fact the the process

$$O_2(^1\Sigma_g^+) + M \rightarrow O_2(^1\Delta_g) + M \qquad (1.27)$$

is spin allowed for singlet quenchers while the corresponding process for delta (1.28) is forbidden

$$O_2(^1\Delta_g) + M \rightarrow O_2(^3\Sigma_g^-) + M \qquad (1.28)$$

That sigma is quenched to delta now seems certain, two pieces of evidence can be cited in favour of this. First the observation that when sigma is prepared free of delta directly by irradiation from the ground state and then quenched, emission from delta is seen[50].

Figure 1.6 Quenching Rate Constants

a) Quenching of Sigma

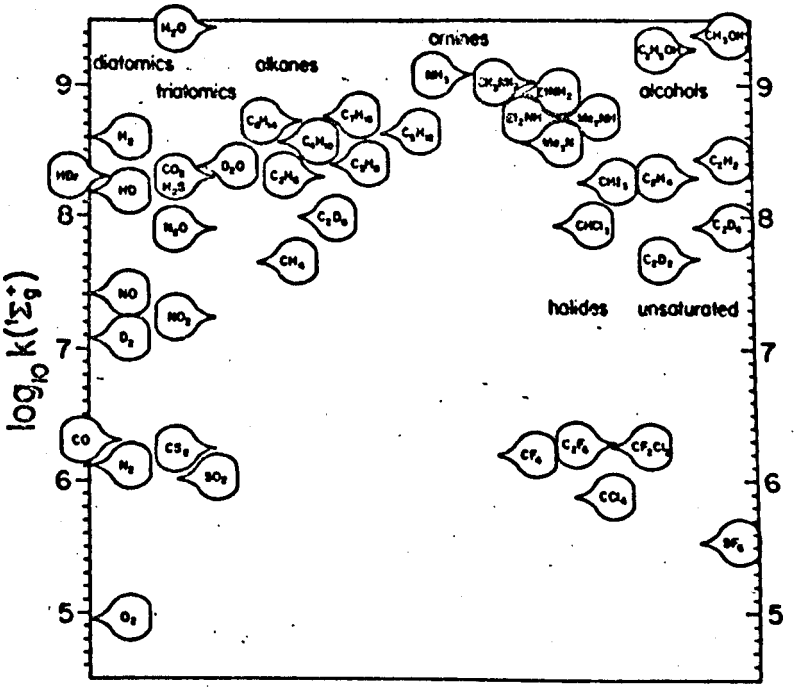

b) Quenching of Delta

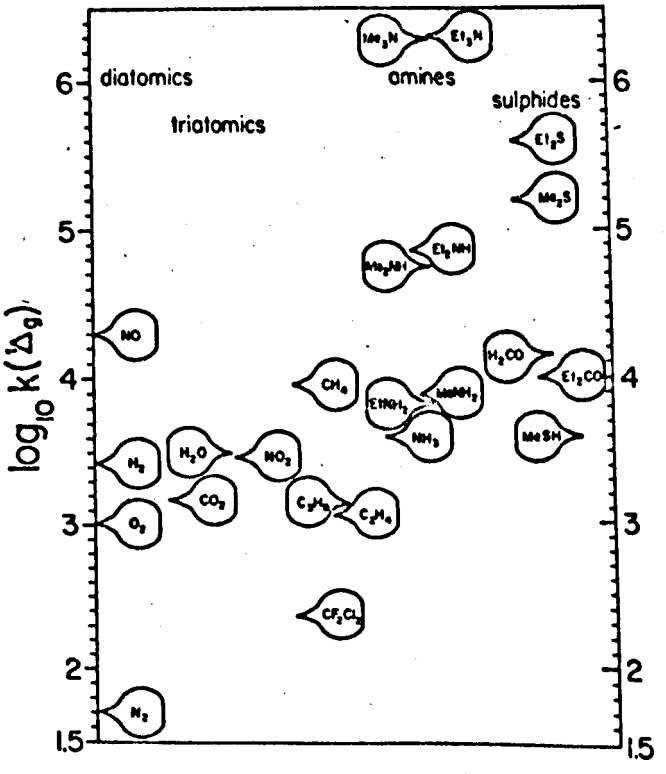

Secondly Thomas and Thrush[51] have studied the vibrational levels of the quencher excited in the quenching of sigma. For the quenching with HCl the highest vibration level of the quencher excited was found to be v=2, which is 5.1 kJ mol^{-1} (427 cm^{-1}) endothermic if $O_2(^1\Sigma_g^+)v=o$ is quenched to $O_2(^1\Delta_g)v=o$. They found no evidence for the precence of $O_2(^1\Sigma_g^+)v=1$ nor populated vibrational levels of HCl above v=2, which would be probable if $O_2(^1\Sigma_g^+)$ were quenched to the gound state. This indicates that quenching occurs to singlet delta. Indeed no indication of quenching to the ground state was seen even with the paramagnetic NO.

(b) Hydrogen containing compounds quench both sigma and delta efficiently. This effect can be traced to the large vibrational frequency of hydrogen. On quenching some of the energy of the excited state is taken up as vibration of the quencher. The nearer to resonance are the energy released and the quencher's vibrational spacing the faster is quenching (this effect is discussed more fully in relation to the observed isotope effects in Chapter 7).

(c) Amines and sulphides quench both states rapidly, the rate constant for delta showing a marked increase with substitution.

Ogryzlo and Tang[52] have discovered a correlation between the logarithm of the quenching rate constant of delta and the ionization potential of the amine, which decreases with increasing substitution. This suggests a charge transfer complex is formed with the amine as donor. Moreover new bands are seen in the amine spectrum in the precence of singlet oxygen[53], again good evidence for the formation of a charge transfer complex. No such correlation exists for the quenching of sigma.

In this section some of the general features of the gas phase quenching of singlet oxygen have been noted. This literature survey cannot be complete without mention of the theoretical work done on

the quenching of sigma. This work is mentioned briefly here, it is discussed more fully in relation to the discharge flow/shock tube results in Chapter 7.

Two theoretical approaches to the quenching of sigma have been developed, they differ as to the distance at which the quenching reaction is seen to take place. The first model was developed by Kear and Abrahamson[50]. It envisages a short range mechanism, quenching occurs on the repulsive part of the intermolecular potential. The alternative theory, due to Braithwaite, Davidson and Ogryzlo[54] sees quenching as a long range process. Both theories assume that the energy lost by the excited state is gained by the quencher in vibration. For a quenching reaction that is nearly resonant the two theories predict markedly different temperature dependencies, the long range process showing a negative temperature dependence and the short range a positive. It is because of this that a study of the temperature dependence of the quenching reaction is important.

Ogryzlo and co-workers produced the first temperature dependent studies of the quenching of sigma, using hydrogen[6] and hydrogen bromide[55] as quenchers. Neither study was conclusive. In the case of hydrogen both the long and short range theories predicted a rise in quenching rate constant with temperature. In the case of hydrogen bromide there was little change in measured rate constant across the temperature range (190 - 380 K). A study of the quenching across a wider temperature range and with a variety of quenchers would hopefully clarify the picture. This is one of the areas in which the present apparatus can make a contribution.

1.4. The Aim of the Present Work.

The purpose of this project was to extend the work previously done on singlet oxygen using a discharge flow/shock tube[56].

In particular it was hoped that the suitability of the apparatus to the study of the temperature dependence of reaction rates would allow the contributions of the long and short range interactions in the quenching of sigma to be explored. The range of rate constants that can be measured[56] (10^5 - 5 x 10^8 ℓ mol^{-1} s^{-1}) means that a variety of quenchers may be used. Use of polyatomic molecules would be interesting in that their greater number of vibrational modes allows them to come closer to resonance and so provide a more discriminating test. Furthermore it was hoped to study any resulting vibrational excitation by using their infra-red emission. This might also allow the importance of resonance in the quenching reaction to be assessed.

While the quenching of delta is generally too slow to be studied it was hoped to observe the dimol emissions in more detail. Three dimol emissions of delta are visible in the present apparatus, at 634 nm, 579 nm and 703 nm (see Table 1.1). It would be interesting to compare the behaviour of these emissions, all previous studies have tended to just note the existence of the dimol emissions without any further investigation.

The energy pooling reaction can also be studied, an investigation of the temperature and composition dependence of the reaction was undertaken.

Finally, this work can be seen as part of a continuing assessment and adaptation of the discharge flow/shock tube technique to chemical kinetics.

Chapter 2

EXPERIMENTAL

The discharge flow/shock tube apparatus, figure 2.1 and plates 1 and 2 had been constructed by previous workers in this laboratory and will be described only in outline.

2.1. The Apparatus.

2.1.1. The Shock Tube.

It was mentioned in Chapter 1 that the high temperature gas can only be studied in the time between the arrival of the shock front and the contact surface. However this hot flow time may also be limited by two other events, namely, the arrival of the reflected rarefaction fan and the reflected shock. The time of these events is determined by tube dimensions and gas properties, in the present apparatus it is the arrival of the contact surface that limits hot flow time.

The shock tube used in these studies is of 5 m overall length, external diameter 51 mm. The driver section is stainless steel 1.25 m long; the test section is a single length of pyrex tubing (Corning Ltd.). Joints to it are made using QVF couplings with PTFE gaskets (Corning Ltd.). The tube is mounted on a frame of Handy Angle, using rubber tube supports to absorb the stress of shock firing.

With the photomultipliers in their usual position, 4 m from the diaphragm, the theoretical hot flow times are 1400 μs for a Mach 3 shock and 600 μs for a Mach 5 shock. Measured hot-flow times for these speeds are 400 μs and 250 μs respectively.

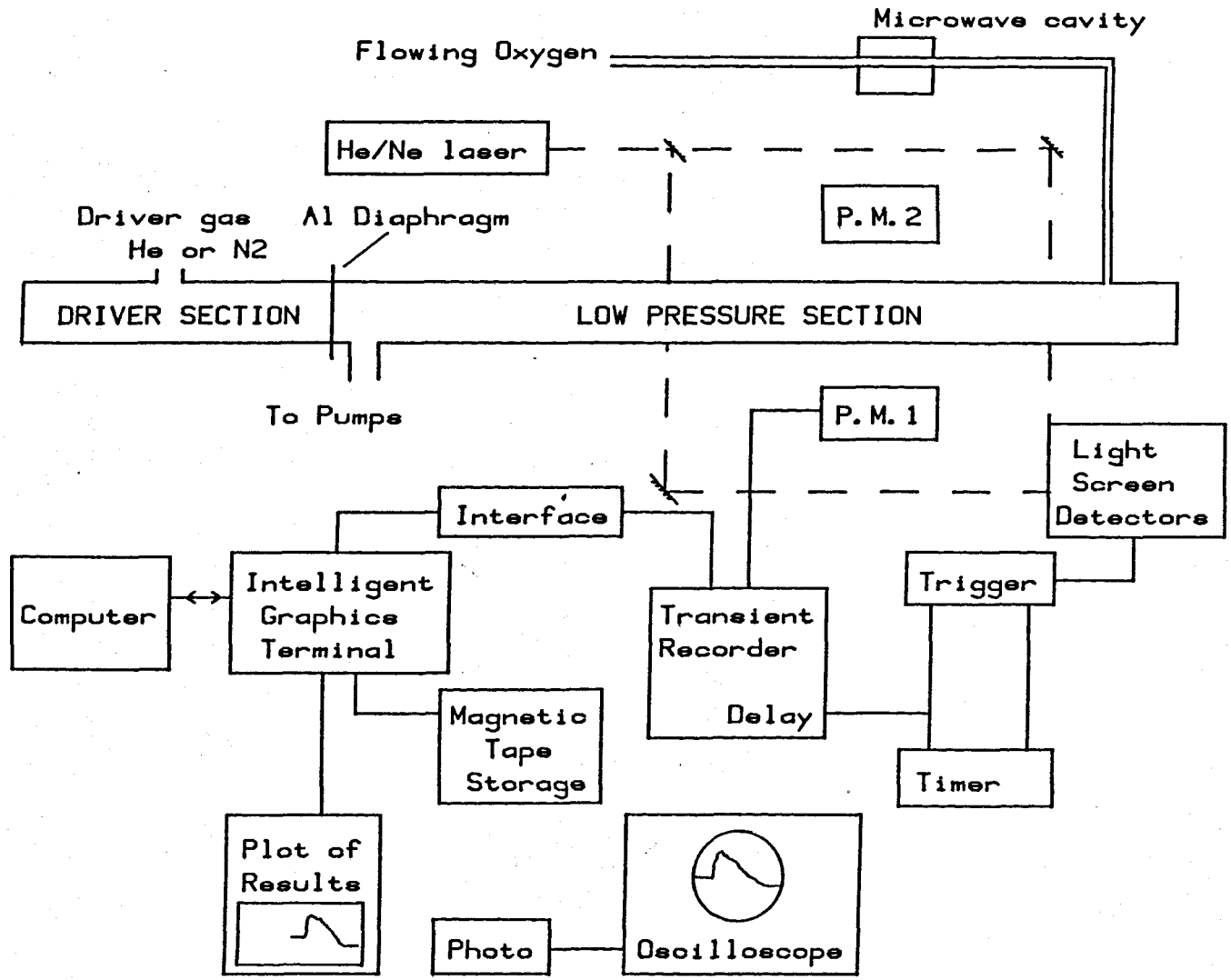

Figure 2.1 The Discharge Flow/Shock Tube

Plate 1

The Discharge Flow/Shock Tube, looking towards the driver section. At the far left the driver gas handling equipment is visible. The shock tube, covered in black cloth, can be seen behind the test gas entry system.

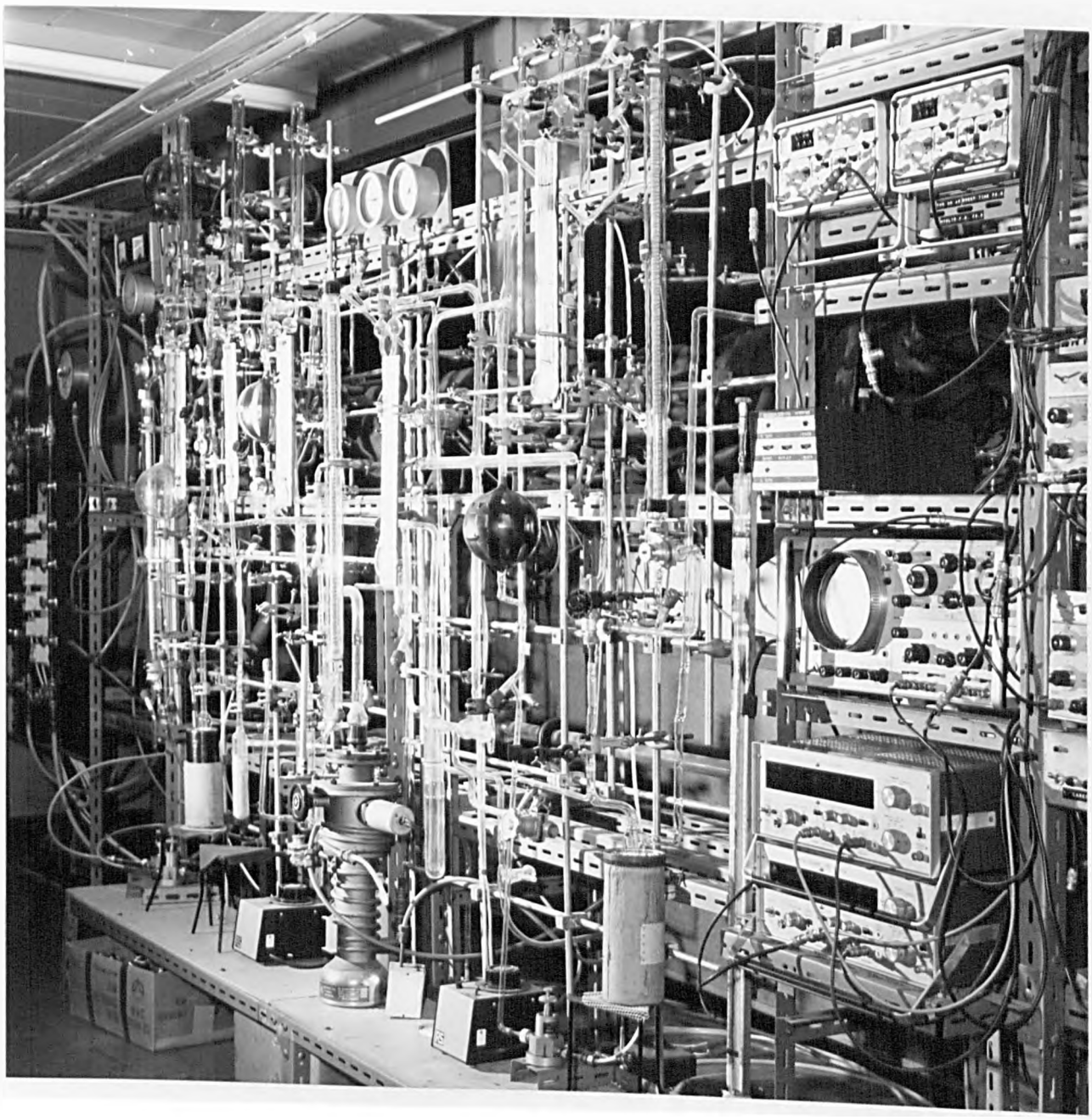

Plate 2

The Discharge Flow/Shock Tube, looking towards the discharge. The transient recorders, oscilloscopes and timers can be seen. The console on the right houses the light screen photomultipliers.

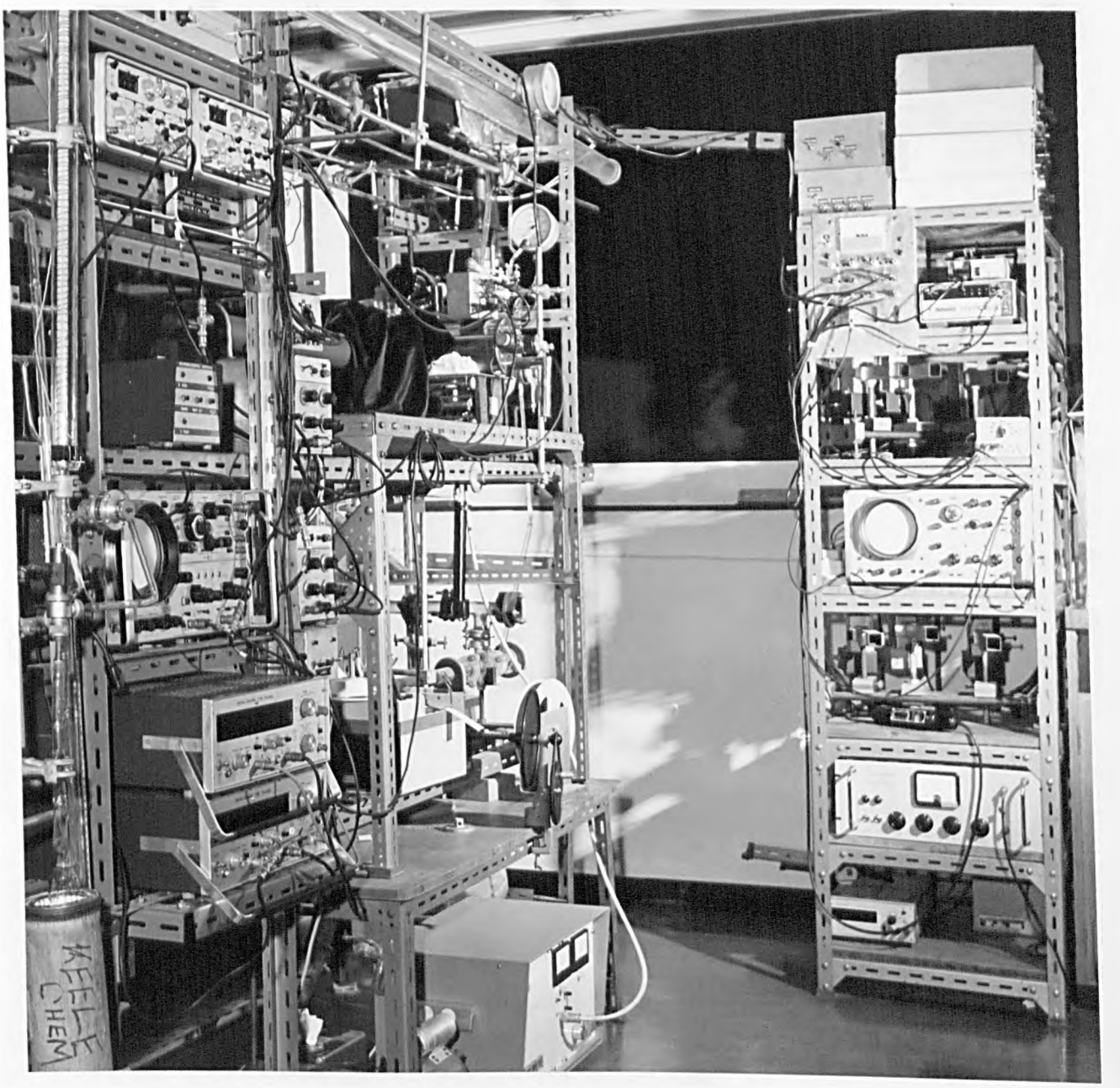

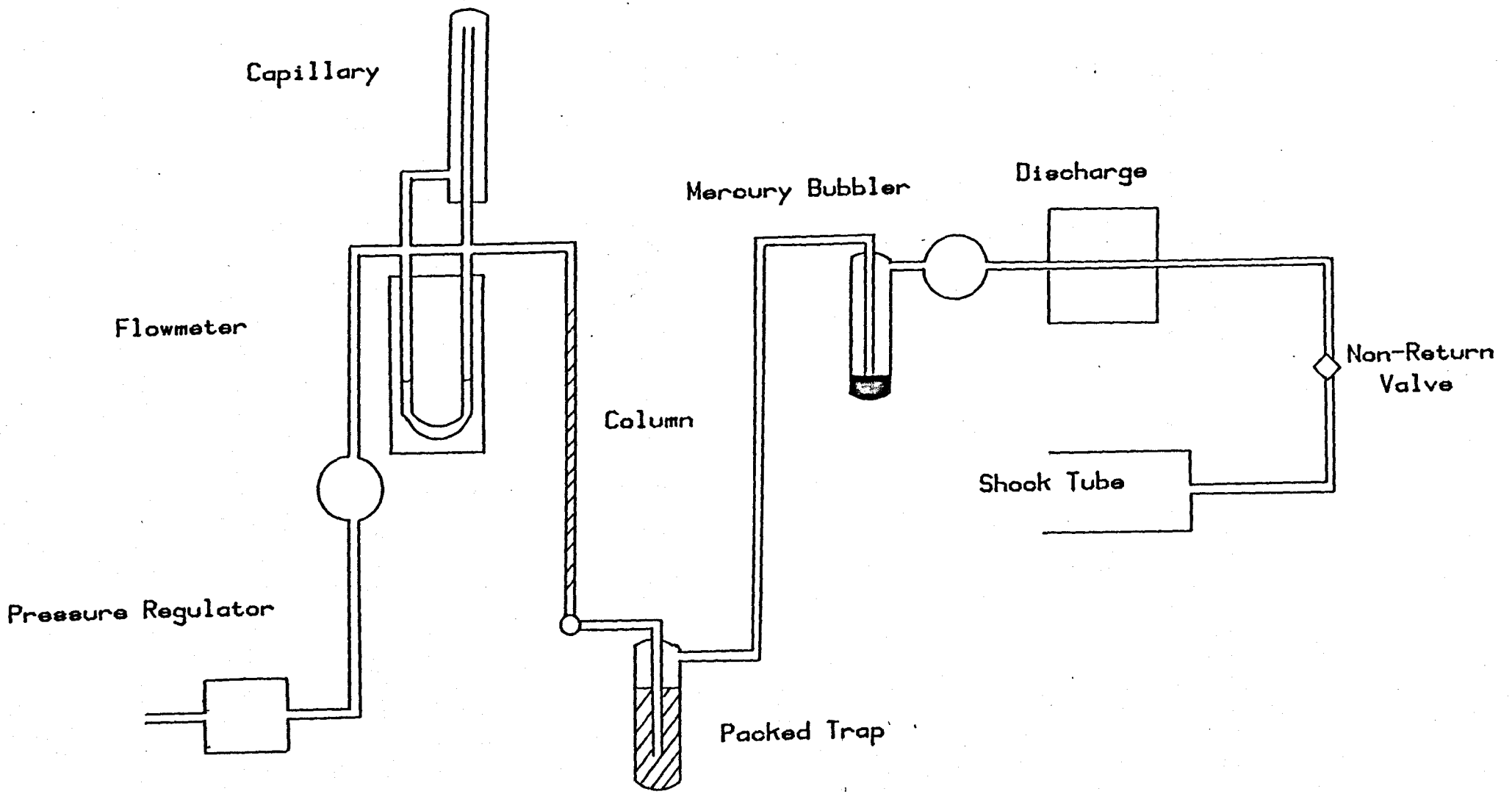

Figure 2.2 Diagram of Gas Entry and Discharge Sections
(shown for oxygen, other gases by-pass discharge)

2.1.2. The Driver Section.

Shock equations show the fastest speeds are obtained using hydrogen as a driver gas. However, because of the explosion hazard, hydrogen was not used; the next best alternative, helium, and nitrogen (BOC Ltd. commercial grade) were chosen.

The gases pass from the cylinders through a trap (1 m long, 50 mm diameter) packed with molecular sieves 4A and 13X into the driver section. Both the driver and test sections were regularly cleaned by pulling through a tight fitting wad of cotton wool soaked in ether, followed by thorough pumping.

The driver section is separated from the test section by an aluminium diaphragm clamped in position between two rubber o rings. Two thicknesses of aluminium, 0.002" and 0.004", bursting at 2.67 atm (2.7×10^2 kPa) and 6.35 atm (6.4×10^2 kPa) respectively were used in these experiments. By adjustment of driver gas composition shock speeds from 0.8 km s^{-1} to 1.6 km s^{-1} could be obtained.

2.1.3. The Gas Handling Equipment.

Figure 2.2 shows the gas entry and discharge sections.

The test gases (BOC Ltd.) oxygen (99.5%), nitrogen (99.5%), argon (99.996%), carbon dioxide (99.95%) and nitrous oxide (99.5%) were all treated in a similar manner. From the cylinder the gas passes via 6 mm and 10 mm nylon tubing to pressure regulators (Edwards VPC1), the pressure on the outlet side is reduced to about 60 torr below atmospheric pressure as measured on a mercury manometer. The gas then passes through a flowmeter, the amount of gas passing being controlled by a needle valve (Edwards Ltd.) and switched on and off by an adjacent tap (Rotaflo or Springham).

Flow in the test section is maintained by an Edwards 1SC 3000

pump. Using a flow control valve (Corning Ltd.) the pressure in the test section is adjusted to approximately 6.5 torr (0.87 kPa) on a Brandenburg dial gauge for all experiments, the pressure being accurately measured using a diethyl phthalate manometer.

Total flow into the test section is kept at 28 ml s^{-1} at 1 atmosphere, corresponding to a linear flow velocity at the test pressure of about 1.5 m s^{-1}.

Gas flow and shock are in opposite directions, this arrangement provides a greater concentration of excited state molecules at the observation station.

Flow rates of gases are measured using capillary flowmeters; the pressure difference caused by laminar viscous flow through the capillary being measured on a diethyl phthalate manometer. In order to allow variable amounts of gases to be mixed several capillaries were constructed; each was calibrated with oxygen to relate the volume of gas delivered to the manometer height in the following way.

For any height on the flowmeter the initial pressure was measured using a diethyl phthalate manometer; the main pump was isolated and the gas allowed to flow for a measured time. The gas flow was stopped and the final pressure in the tube measured. By shutting of the gas flow and main pump simultaneously a pressure rise due to the gas already in the system could be determined, thus a pressure rise due to a gas flow over a known time could be calculated. The volume of the apparatus was obtained by measuring the pressure rise attendant on allowing a 1 litre bulb of air at atmospheric pressure to expand into the evacuated system. The volume determined in this way was 15.2 litres. In this way a flow of oxygen per second at atmospheric pressure could be determined, and related to the height of the flowmeter.

To relate this value for oxygen to other gases their viscosities

Table 2.1

Viscosities of Gases at 295K

Gas	Viscosity/ kg s^{-1} m^{-1} 10^{-5}
Oxygen	2.04
Nitrogen	1.76
Argon	2.20
Carbon Dioxide	1.51
Nitrous Oxide	1.46

had to be estimated. This was done by plotting out the literature values of viscosity[57] against temperature and interpolating a value at 295 K. Values obtained in this way are listed in Table 2.1.

After passing through the flowmeter the gases travel through a column (60 cm long x 1 cm i.d.) and a trap packed with molecular sieve 4A. When flowing oxygen, nitrogen and argon the traps were cooled to 77 K. The columns are wound with nichrome wire and, by passing a current, can be heated and so regenerated. All three columns were regularly treated in this way. The additives argon, carbon dioxide and nitrous oxide all passed through the same entry system. When changing gases the columns and trap were thoroughly pumped out and then the new additive was allowed to flow through for some time before experiments were started.

At this point the three gas entry systems differ, oxygen flowing over a mercury surface and into the discharge, all other gases joining after the discharge.

2.1.4. The Discharge Section.

The discharge is produced in a 10 mm quartz tube by a 2450 MHz microwave generator (E.M.S. Microtron 200) operated, unless otherwise specified, at 100 W. The cavity is a $\frac{1}{4}$ wave radial type (E.M.S. 214L). Tuning of the cavity is facilitated with the aid of a reflected power meter, the cavity being adjusted to minimize this reading. A stream of compressed air is used to cool the discharge area.

Prior to entering the discharge the oxygen flows over a mercury surface. Atomic oxygen is removed and a film of mercuric oxide is deposited after the discharge. This mercuric oxide film is periodically removed to prevent excessive accumulation by washing with nitric acid.

That the atomic oxygen has been reduced to negligible levels has been confirmed by adding nitrogen dioxide to the flow[56]. Any atomic

oxygen present will react to produce nitric oxide via the rapid reaction (2.1)

$$O + NO_2 \rightarrow NO + O_2 \qquad (2.1)$$

The nitric oxide will then react with more atomic oxygen in the chemiluminescent reaction (2.2), giving rise to a readily visible white glow

$$NO + O \rightarrow NO_2 + h\nu \qquad (2.2)$$

Thus the presence of atomic oxygen in the discharged gas is signalled by the appearance of the white glow[30]. No such glow was seen and it is deduced that no atomic oxygen is present.

The discharge section is surrounded by a Faraday cage to reduce microwave leakage into the laboratory[58].

A blackened Rayleigh horn reduced transmission of light from the glowing discharge to the photomultipliers.

2.1.5. Determination of Shock Speed.

The final gas conditions; temperature, pressure and density are determined by the shock speed and gas composition and can be calculated from the shock velocity using standard shock equations. It is therefore of the utmost importance that the shock velocity be determined as accurately as possible. In these experiments helium/neon lasers are used as tripwires, both to determine the shock velocity and to fire the recording apparatus. A block diagram of the recording and velocity determination system is shown in figure 2.3.

Light from the lasers (Ferranti GP2, 1 mW; Rofin 7906, 1.5 mw) passes via a system of mirrors through the tube to three photomultipliers (E.M.I. 9660B), the beam of laser 1 being split by a half silvered mirror. These moveable photomultipliers are set so that the arrival of the

Figure 2.3 The Recording and Velocity Measuring Apparatus

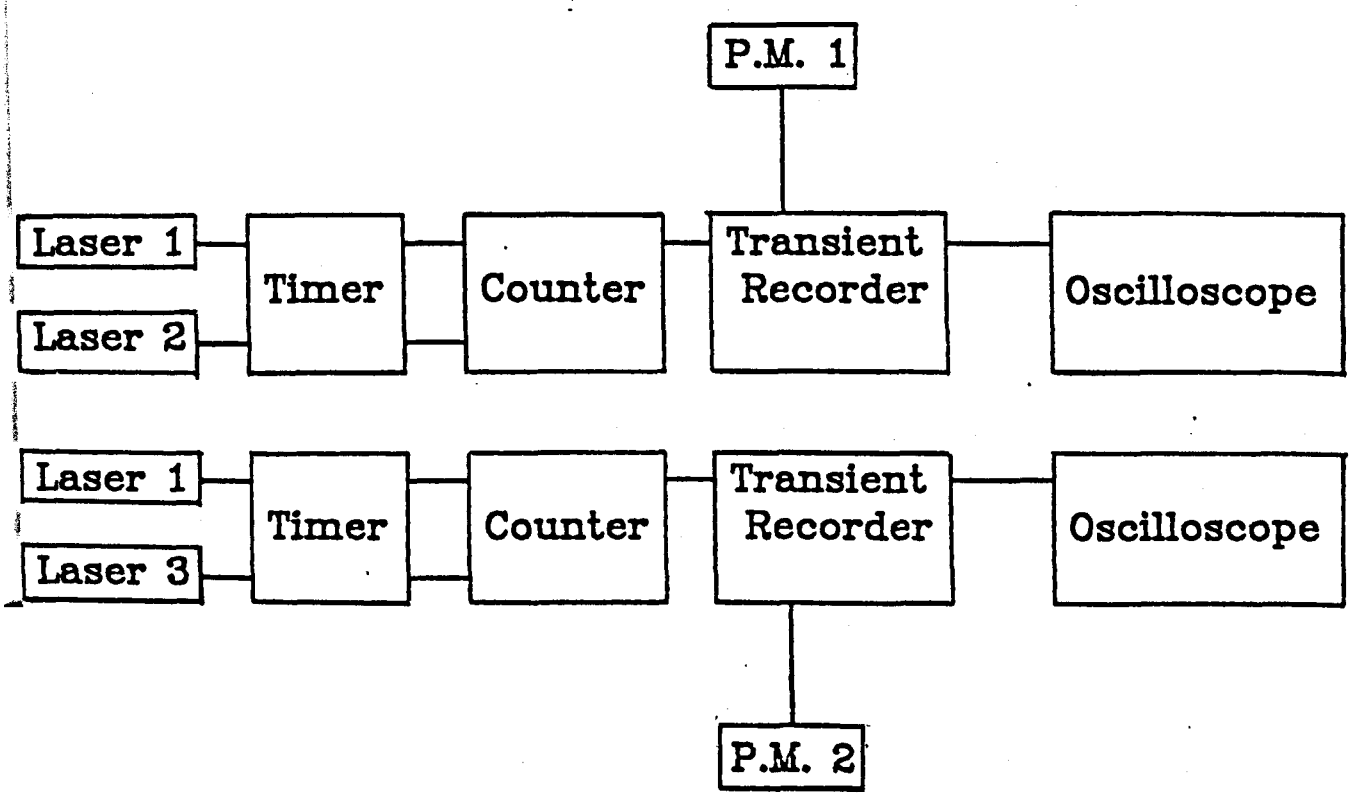

shock front can cause a pulse which is used to trigger the timers. A long path length, in this case 5 m, and a stable base are essential for the correct functioning of such a system. Pedley[56] has shown that refraction of the beam in the dense gas at the shock front is insufficient to cause firing, he suggests that both refraction and reflection are operative.

Arrival of the shock front at laser beam 1 starts two time interval meters (Hewlett Packard 5263A); it's subsequent arrival at beams 2 and 3 stops then. The time intervals thus produced are measured with counters (Venner TSA 5536, resolution 1 μs; Hewlett Packard 5304A, resolution 0.5 μs), knowing the distance between the beams allows the shock speed to be calculated. In all experiments the two measurements of shock speed differ by less than 0.5%.

2.1.5.1. Calculation of Shock Conditions.

If the shock encompasses a temperature in which vibrations become active the density and temperature in the shock will change with time. The initial, vibrationally frozen temperature given by (1.6) will decrease to the relaxed value as energy is taken up in vibrations. In order to calculate the condition of the shocked gas a computer programme, based on one written by Millikan[59], is used.

The initial temperature, pressure and composition of the gas are known, hence the specific heat ratio and so the speed of sound at room temperature, a, can be calculated.

$$a = \left(\frac{\gamma RT}{M}\right)^{\frac{1}{2}}$$

where γ = mean specific heat ratio

M = mean molar mass

For any shock velocity u, the frozen shock condition can be calculated using (1.4), (1.5) and (1.6). With these values an enthalpy difference across the shock front can be calculated using (2.5).

$$\Delta H = \frac{u}{2}\left\{1 - \left(\frac{\rho_1}{\rho_A}\right)^2\right\} \qquad (2.3)$$

By polynomial fitting of the tabulated values of enthalpy against temperature[60] another enthalpy difference, $\Delta H'$, can be determined. The difference between these values yields an error which is used to correct the frozen temperature. New values of the density and pressure ratios at the new temperature T' are calculated using

$$\left(\frac{\rho_2}{\rho_1}\right)' = \left(\frac{P_A}{P_1}\right)\Big/\left(\frac{T_2}{T_1}\right)'$$

and

$$\left(\frac{P_2}{P_1}\right)' = 1 + \frac{u^2 M}{RT_1}\left\{1 - \left(\frac{\rho_2}{\rho_1}\right)'\right\}$$

This completes one round of the iteration and another is begun using the new values of temperature, density and pressure. The cycle stops when the error falls below a predetermined limit.

An essentially similar programme calculates the post-shock conditions of a polyatomic gas. Dissociation is ignored, this is reasonable given the temperatures achieved in this shock tube[10]. The effect of dissociation in the case of nitrous oxide is discussed in Chapter 6.

2.1.6. The Monitoring and Recording Apparatus.

Four emissions from singlet oxygen were studied in this work; from sigma at 762 nm and from the delta dimol at 634 nm, 579 nm and 703 nm.

Interference filters (Balzer Ltd.) were used to isolate the emissions. The transmission curves of all filters were obtained prior to use on a Pye Unicam SP800 ultra-violet/visible spectrophotometer. All were found to have approximately the same transmittance at their maxima (about 40%) and the same half-width (14 nm); however the maximum was not always at the requested wavelength. The filters used in this work had peak transmittances at 630 nm (for the 634 nm emission), 579 nm, 706 nm (for the 703 nm emission) and 761 nm (for the 762 nm emission). The limitations imposed by such considerations are discussed in Chapter 4.

One type of photomultiplier (E.M.I. 9658B) was used to monitor all emissions; the quantum efficiency at each wavelength is given in Table 2.2, obtained from the manufacturer's published data[61].

Two photomultipliers were used, one mounted in a moveable housing (Products for Research Inc.) the other stationary (Oxford Instruments). Both housings had filter holders constructed 8 cm in front of the cathode, with variable slits to control the intensity of the various emissions(figure 2.4). Lenses were not used in the work reported here. Previous experience has shown that if the lens is placed between the tube and the photomultiplier any increase in intensity is outweighed by the decrease due to the greater distance between the tube and the photomultiplier and also by transmission losses. Recent experiments with a short focal length lens behind the slit have however shown an increase in intensity, by approximately 20%.

Using the moveable photomultiplier the change in concentration

Table 2.2

Quantum Efficiency of E.M.I. 9658B Photomultiplier

Wavelength/nm	Quantum Efficiency/%
579	14.6
634	11.2
703	7.8
762	5.0

Figure 2.4 Photomultiplier and Housing

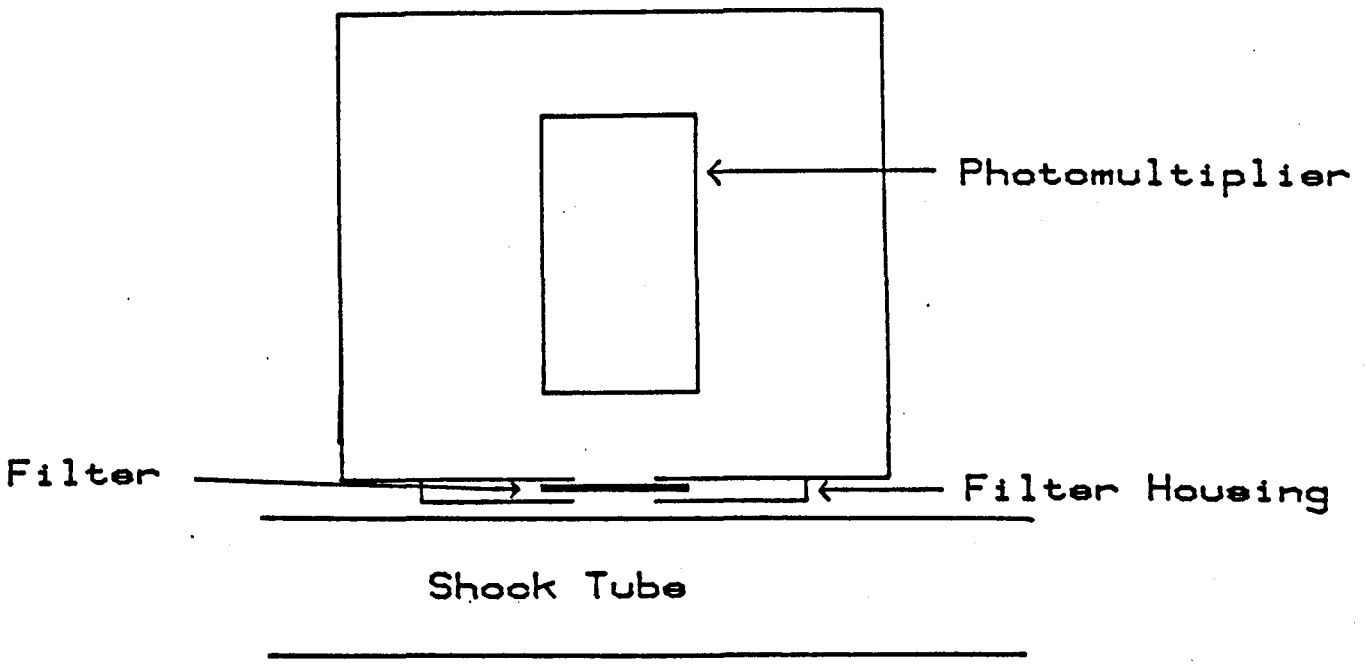

Figure 2.5 Photomultipliers and Shock Tube

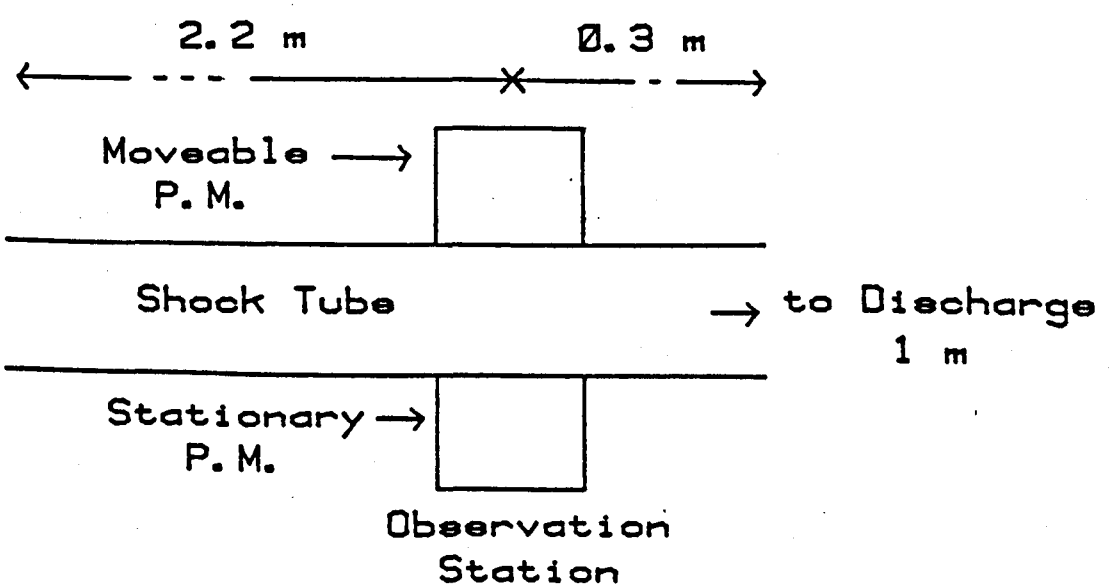

of excited state molecules down the tube may be measured (see Chapter 3 and figure 2.5).

Each photomultiplier was operated at the maximum voltage specified by the supplier, using a Brandenburg 472 R E.H.T. supply. The rise times of the photomultipliers are determined by their anode load resistors, in this case 51 kΩ and the slew rate of the voltage followers. Using a square wave pulsed L.E.D. and minimum slit width the rise times were found to be 5 μs. The voltage followers were connected to digital voltmeters (Solartron 7040, sensitivity 0.01 mV; 4440, sensitivity 0.1 mV; Hewlett Packard 3438A, sensitivity 0.1 mV) or to the transient recorders (Datalab DL905).

The arrival of the shock front at light screen 1 also triggers the two transient recorders (see figure 2.3). These have variable sweep speed and delay so that the entire shock event, from pre-shock glow to the end of hot flow time, could be recorded. Depending on the sweep speed chosen the time resoltuion of the output trace was either 0.5 μs or 1 μs.

The transient recorders trigger two oscilloscopes (Hewlett Packard series 140) allowing the shock trace to be displayed. These traces were then photographed so that a visual record of each shock was kept.

In these experiments the emission from singlet oxygen is monitored as a function of time during shock heating. When a shock is run into undischarged pure oxygen no emission is seen at any of the wavelengths monitored.

The quality of results from these experiments depends on the accuracy of recording of voltage against time. Consequently the voltage and time scales of the crystal controlled transient recorders and oscilloscopes were periodically checked against the ouput of a

signal generator (Marconi TF2010). The accuracy of the two timers was checked during routine servicing.

Up to shock number C152 the digitised data passed from the transient recorders via an interface to a tape punch (Data Dynamics 1133) and thence to a disc file on the University's ICL 4130 machine for analysis by interactive computer graphics. In February 1979 a Hewlett Packard 2647A intelligent graphics terminal and 9872A plotter were acquired at the same time as the University obtained a GEC 4082 mainframe. This caused a change in the method of data acquisition and analysis.

The 2647 can operate as a passive VDU and can also be programmed in BASIC and it's graphics extension AGL. Facility is also provided for recording on two magnetic tape cassettes (capacity 110 K bytes) and for the control of a plotter. Consequently the digitised outputs of the transient recorders were recorded on cassette immediately after each shock. A number of these can be stored before they are transferred to the 4082 together with their run parameters for later analysis. During the analysis of the shock trace the results are displayed on the 2647 which is run in conjunction with the 4082. The detailed operation of the new graphics programme is described in Chapter 3, after the introduction and development of the equations involved.

2.2. Standard Operating Procedure.

This section describes the usual mode of operation of the apparatus, any modifications to this general scheme are described in the relevant chapter.

(i) The tube, gas handling sections and driver sections are evacuated for about half an hour. Dewars of liquid nitrogen are placed around the traps on the oxygen and nitrogen lines.

(ii) The gas cylinders are turned on, the flows are adjusted to the correct level using the needle valves. The downstream pressure is adjusted to about 6 torr on the Brandenburg pressure gauge, an accurate reading of the pressure is taken with the diethyl phthalate manometer. The room temperature is noted. The discharge is lit with a tesla coil, the power is adjusted to 100 W, the cooling air is switched on. The overhead lights are extinguished, the photomultipliers switched on and the apparatus is left to come to a steady state, generally for about 30 minutes.

(iii) If required a glow down the tube is measured, the photomultipliers are then positioned opposite one another. As the voltage followers saturate at 8V a rough estimate of the maximum shock glow is made and the slits adjusted accordingly. The pre-shock glows are now noted, after which the photomultiplier outputs are connected to the transient recorders, which are adjusted, depending on shock speed and emission being studied, to give optimum use of sensitivity and recording time.

(iv) The laser light screens are adjusted, the timers and transient recorders are primed.

(v) The driver section is isolated from it's pump and the driver gas or gases are let in. When sufficient pressure has been achieved the diaphragm bursts and the shock is propagated down the tube.

(vi) The gases, high voltages, discharge and lasers are switched off and the lights turned on. The two times are noted, as are the transient recorder sensitivity, sweep speed and delay. A photograph of the shock traces is taken and they are stored on paper or magnetic tape. With the replacement of the diaphragm and the pumping out of the driver and test sections the apparatus is ready for another experiment.

Chapter 3

THE ANALYSIS OF DISCHARGE FLOW/SHOCK TUBE DATA

This chapter introduces the kinetic scheme and equations on which the analysis of the shock trace is based. The analysis of the delta dimol emission at 634 nm and of the sigma emission at 762 nm are described in detail. These are used as illustrations of the basic analysis technique and any modifications necessary in order to analyse other emissions are described in the relevant chapter.

Also described are the translation of the theory into a computer programme and its operation on the Hewlett Packard Graphics Terminal. The chapter concludes with a discussion of the errors in the experimental data and analysis.

3.1. Deactivation of $O_2(^1\Delta_g)$ at Room Temperature

Delta is formed in or near the discharge, it is destroyed by quenching (both in the gas phase and at the wall), radiative emission (both single and double molecule) and in the energy pooling reaction.

$$O_2(^1\Delta_g) + M \rightarrow O_2(^3\Sigma_g^-) + M \; ; \; k_q \qquad (1.28)$$

$$O_2(^1\Delta_g) \rightarrow O_2(^3\Sigma_g^-) \; ; \; k_w \qquad (3.1)$$

$$O_2(^1\Delta_g) \rightarrow O_2(^3\Sigma_g^-) + h\nu \; (\lambda = 1270 \text{ nm}) \qquad (1.17)$$

$$O_2(^1\Delta_g) + O_2(^1\Delta_g) \rightarrow O_2(^3\Sigma_g^-) + O_2(^3\Sigma_g^-) + h\nu \; (\lambda = 634 \text{ nm}) \qquad (1.19)$$

$$O_2(^1\Delta_g) + O_2(^1\Delta_g) \rightarrow O_2(^1\Sigma_g^+) + O_2(^3\Sigma_g^-) \; ; \; k_p \qquad (1.20)$$

Compared to the others the radiative processes are slow; the radiative rate constants for the single[25] and double[44] molecule transitions are 2.58×10^{-4} s^{-1} and 0.016 ℓ mol^{-1} s^{-1} respectively. The best value for the energy pooling rate constant[44] is 1.22×10^4 ℓ mol^{-1} s^{-1}, about an order of magnitude greater than that for collisional quenching. However because the energy pooling reaction depends on the meeting of two delta molecules it makes a negligible contribution to the overall decay of delta at the concentration used. This approximation has been confirmed by experiment.[21] In measuring the collisional quenching rate constant for delta some experiments were carried out on oxygen 90% of which was added after the discharge and so had a very low delta concentration. The observed quenching rate constants were identical to those measured under normal conditions.

The rate of change of delta concentration can be written

$$\frac{d[\Delta]}{dt} = -(k_q[\Delta][M] + k_w[\Delta]) \tag{3.2}$$

where $[\Delta] = [O_2(^1\Delta_g)]$

At a constant pressure of oxygen

$$\frac{d[\Delta]}{dt} = -k^*[\Delta] \tag{3.3}$$

where $k^* = k_q[M] + k_w$

In the shock tube there is a decay of excited state molecules down the tube pre-shock. This is due to collisonal quenching and quenching at the shock tube wall. This decay can be measured by monitoring the glow from the flowing gas (in this case at 634 nm) as a function of distance along the shock tube.

The decay constant for the dimol emission at 634 nm, α_ℓ (which is negative) can be determined from the emission intensity ratios (3.4). I_o^{634} is the emission intensity at the observation station and I^{634} is that at any point along the tube at distance ℓ. See figure 3.1 for a sample plot.

$$\ln \frac{I^{634}}{I_o^{634}} = \alpha_\ell \ell \tag{3.4}$$

The relationship between the intensity of the 634 nm emission and the concentration of delta (3.5) has been established by, for example, the work of Whitlow and Findlay[62] on the relative intensities of the 1270 nm and 634 nm emissions at various discharge powers.

$$I^{634} \quad \alpha[\Delta]^2 \tag{3.5}$$

Figure 3.1 Determination of the Decay down the Tube

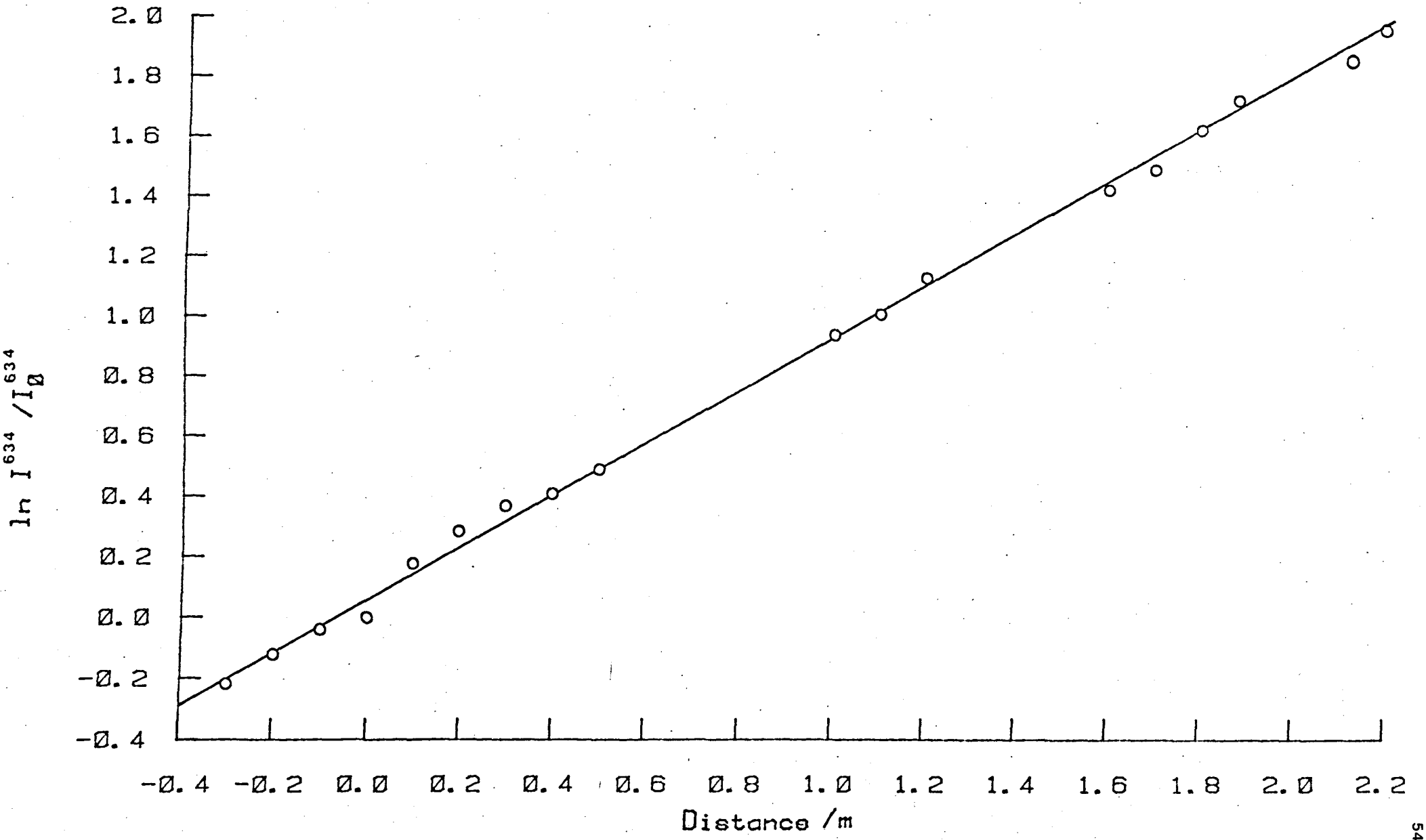

Combining (3.4) and (3.5)

$$\ln \frac{[\Delta]}{[\Delta]_o} = \frac{\alpha_\ell \ell}{2}$$

$$[\Delta] = [\Delta]_o \exp(\alpha_\ell \ell/2)$$

$$\frac{d[\Delta]}{d\ell} = \frac{\alpha_\ell}{2} [\Delta]_o \exp(\alpha_\ell \ell/2)$$

$$\frac{d[\Delta]}{d\ell} = \frac{\alpha_\ell [\Delta]}{2}$$

Now $$\frac{d[\Delta]}{dt} = \frac{d[\Delta]}{d\ell} \frac{d\ell}{dt}$$

where $\frac{d\ell}{dt}$ is the gas flow velocity v. Hence

$$\frac{d[\Delta]}{dt} = \frac{\alpha_\ell v [\Delta]}{2} \qquad (3.6)$$

therefore combining (3.3) and (3.6)

$$k^* = \frac{\alpha_\ell v}{2} \qquad (3.7)$$

The linear gas flow velocity is given by

$$v = \frac{P_o \text{ flow rate}}{P \pi r^2}$$

where P_o is the atmospheric pressure

P is the downstream pressure

r is the tube radius (2.54 cms)

3.1.1. Previous Studies of the Deactivation of $O_2(^1\Delta_g)$ at Room Temperature

The wall and collisional quenching rate constants can be measured in the following way. The decay of the 634 nm emission down the tube is measured, this is converted to a first order decay constant using (3.7). By measuring the decay of delta at various pressures the rate constants for the quenching at the wall and in the gas phase can be obtained by plotting the first order rate constant against concentration. This has been done previously, by Borrell, Borrell and Pedley.[21] They obtained $k_q = 9.4 \pm 0.3 \times 10^2$ ℓ mol^{-1} s^{-1} and $k_w = 0.11$ s^{-1} at 295 K.

This result can be compared with a recent measurement by Schurath et al.[63] of $8.82 \pm 0.3 \times 10^2$ ℓ mol^{-1} s^{-1}. The value obtained in this apparatus is used in the present work.

3.2. Deactivation of $O_2(^1\Delta_g)$ at High Temperatures

The analysis proceeds along the same lines as at room temperature but the rate constants now refer to processes occurring at the high temperature in particle time, t_p (see Appendix 1).

Analagously with (3.2)

$$\frac{d[\Delta]}{dt_p} = -(k_q[\Delta][M] + k_w[\Delta])$$

$$\therefore \quad \frac{[\Delta]_t}{[\Delta]_o} = \exp(-k_q[M]-k_w)t_p \tag{3.8}$$

$[\Delta]_o$ is the concentration of delta at any point in the tube immediately after the shock has passed, $[\Delta]_t$ is that after time t.

What is seen in a shock experiment is a snapshot of the condition of the gas as it is swept back past the observation station (in our apparatus the gas flow and shock are in opposite directions). As explained in the previous section there is a decay of excited state molecules down the tube given by (3.4). Analagously to (3.6) an equation can be written

$$\frac{d[\Delta]}{dt_p} = \frac{\alpha_\ell v_s}{2}[\Delta]$$

where v_s is the gas particle velocity in the shock $= U(^{1-1}\!/_{\rho_{21}})$, U is the shock velocity and ρ_{21} the density ratio (see Appendix 1). Hence

$$\frac{d[\Delta]}{dt_p} = \frac{\alpha_\ell U(1-1/\rho_{21})}{2}[\Delta] = \frac{\alpha_t}{2}[\Delta] \tag{3.9}$$

Consequently the immediate post-shock concentration at any point in the tube $[\Delta]_o$ is related to that immediately post-shock at the observation

station $[\Delta]_{obs}$ by

$$[\Delta]_o = [\Delta]_{obs} \exp(\alpha_t t_p/2) \tag{3.10}$$

Combining (3.8) and (3.10)

$$\frac{[\Delta]_t}{[\Delta]_{obs}} = \exp(-k_q[M] - k_w + \alpha_t/2)t_p$$

To recapitulate; at any point in the tube pre-shock there is a steady concentration of delta molecules, there is a decrease in delta concentration with distance down the tube. The observed post-shock decay will reflect both the decrease in excited state molecule concentration down the tube and any further decay due to quenching in the hot gas.

Now $I^{634} \alpha [\Delta]^2$ hence

$$\frac{I_t^{634}}{I_{obs}^{634}} = \exp(-2k_q[M] - 2k_w + \alpha_t)t_p \tag{3.11}$$

This equation describes how the observed post-shock emission at the observation station evolves with time.

The delta concentration is monitored using the dimol emission

$$O_2(^1\Delta_g) + O_2(^1\Delta_g) \rightarrow O_2(^3\Sigma_g^-) + O_2(^3\Sigma_g^-) + h\nu(\lambda = 634 \text{ nm}) \tag{1.19}$$

At the shock front the density and temperature of the gas increase. The immediate post-shock emission intensity from the heated gas at the observation station I_{obs}^{634} will be related to that from the cool gas I_1^{634} by

$$I_{obs}^{634} = I_1^{634} \rho_{21}^2 T_{21}^{\frac{1}{2}} \tag{3.12}$$

In (3.12) ρ_{21} and T_{21} are respectively the density and temperature ratios of the heated to cool gas, together they account for the increased concentration of delta molecules and collision rate. This relationship will hold if the dimol emission is a simple collisional process, i.e. with no activation energy or dimer formation. A factor K^{634} is introduced (3.13), it will be unity if I^{634}_{obs}, the post-shock glow extrapolated back to the arrival of the shock front is accurately given by (3.12)

$$K^{634} = \frac{I^{634}_{obs}}{I^{634}_{1} \rho_{21}^{2} T_{21}^{\frac{1}{2}}} \qquad (3.13)$$

Combining (3.11) and (3.13)

$$I^{634}_{t} = K^{634} I^{634}_{1} \rho_{21}^{2} T_{21}^{\frac{1}{2}} \exp(-2k_q[M] - 2k_w + \alpha_t)t_p \qquad (3.14)$$

This equation relates the glow observed post-shock at the observation station I^{634}_{t} to that observed pre-shock I^{634}_{1}. It predicts a rapid increase at the shock front followed by a decay, see figure 3.2. The comparison of the observed post-shock behaviour with that predicted is made in chapter 4.

Figure 3.2 The Emission Trace at 634nm

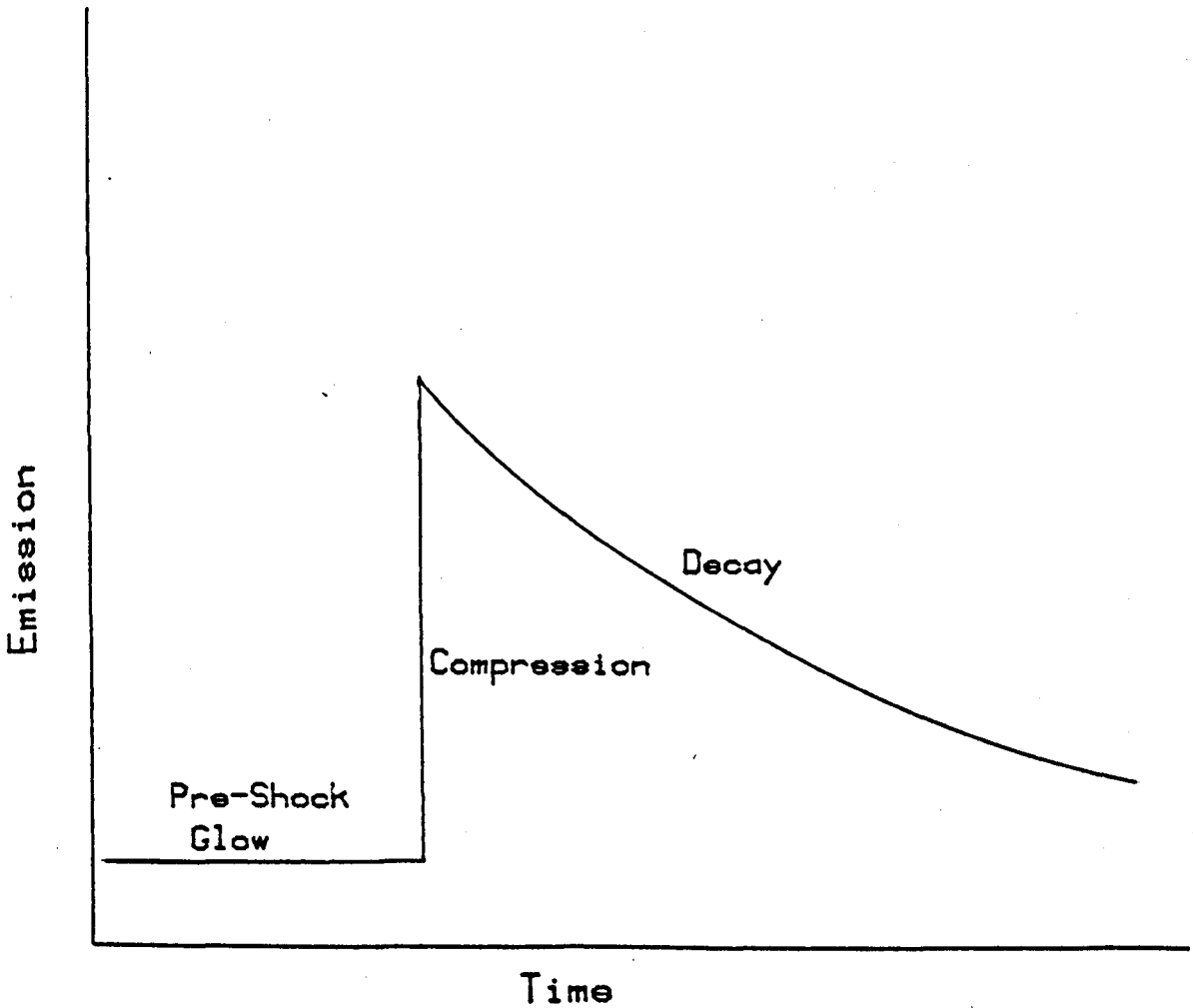

3.3. Deactivation of $O_2(^1\Sigma_g^+)$ at Room Temperature

Sigma is continually formed via the energy pooling reaction and is destroyed by collisonal and wall quenching and radiative emission.

$$O_2(^1\Delta_g) + O_2(^1\Delta_g) \rightarrow O_2(^1\Sigma_g^+) + O_2(^3\Sigma_g^-) \quad ; \quad k_p \tag{1.20}$$

$$O_2(^1\Sigma_g^+) + M \rightarrow O_2(^1\Delta_g) + M \; ; \quad k_q \tag{1.26}$$

$$O_2(^1\Sigma_g^+) \rightarrow O_2(^3\Sigma_g^-) \; ; \quad k_w \tag{3.15}$$

$$O_2(^1\Sigma_g^+) \rightarrow O_2(^3\Sigma_g^-) + h\nu(\lambda = 762 \text{ nm}) \tag{1.18}$$

At a typical pressure of 6.5 torr $k_q[M]$ at room temperature is about 35 s^{-1}, k_w is about 20 s^{-1}. Compared with these processes the radiative emission ($k = 10^{-1}$ s^{-1}) is very slow and so can be ignored, then the rate of change of sigma concentration is given by

$$\frac{d[\Sigma]}{dt} = k_p[\Delta]^2 - k_q[\Sigma][M] - k_w[\Sigma] \tag{3.16}$$

where $[\Sigma] = [O_2(^1\Sigma_g^+)]$

Invoking the steady state approximation at any point in the tube there will be a steady concentration of sigma given by

$$[\Sigma] = \frac{k_p[\Delta]^2}{k_q[M] + k_w} \tag{3.17}$$

3.3.1. Previous Studies of the Deactivation of $O_2(^1\Sigma_g^+)$ at Room Temperature

In pure oxygen, using (3.17) one can write

$$\frac{[\Sigma]}{[\Delta]^2} = \frac{k_p}{k_q[O_2] + k_w}$$

Now

$$I^{762} \propto [\Sigma] \quad \text{and}$$

$$I^{634} \propto [\Delta]^2 \quad \text{hence}$$

$$\frac{I^{762}}{I^{634}} = C\left\{\frac{k_p}{k_q^{O_2}[O_2] + k_w}\right\}$$

where C is a proportionality constant depending on the characteristics of the detection system. The energy pooling rate constant at room temperature is known, the wall quenching rate constant can be calculated as shown below and so the rate constant for the collisional quenching of sigma by oxygen can be determined by measurement of the intensity ratio at various pressures.

Derwent and Thrush[44] have published an equation enabling the wall deactivation rate constant for a flowing gas system to be calculated.

$$k_w = \frac{1}{\frac{r^2(P/Po)}{8Do} + \frac{2r}{\gamma\bar{c}}} \qquad (3.18)$$

where r = radius of tube

P = pressure in tube

Po = atmospheric pressure

γ = probability of surface quenching (10^{-2} for sigma[44])

$\bar{c}$ = mean molecular speed (4.41×10^2 m s^{-1} for O_2 at 295 K)

Do = diffusion coefficient

In this way Pedley[56] has obtained a value for $k_q^{O_2}$ in our apparatus of $(1.07 \pm 0.43) \times 10^5$ ℓ mol^{-1} s^{-1}. This can be compared with a value for dry oxygen[56] (< 2 ppm water) of 2.6×10^4 ℓ mol^{-1} s^{-1}. Taking a best value for the quenching by water[64] of 2.4×10^9 ℓ mol^{-1} s^{-1} this result

indicates the presence of 30 ppm water. This proportion of water is acceptable considering (1) the large volumes of gas passed through, about 5×10^3 ℓ per day; (2) the fact that the apparatus must be regularly opened to the air to facilitate cleaning and replacement of diaphragms. This means that water from the air is continually adsorbed to the walls despite thorough pumping prior to each shock and while the tube is not in use.

Using our value for the room temperature quenching rate constant of sigma by oxygen we find, at a typical pressure of 6.5 torr, $k_q[O_2] = 35\ s^{-1}$. Taking the diffusion coefficient for sigma to be the same as that for delta[65] ($2.01 \times 10^{-5}\ m^2\ s^{-1}$) and Thrush's value[44] for the probability of surface quenching of sigma (1.0×10^{-2} for a pyrex surface) we obtain, using (3.18) $k_w = 21\ s^{-1}$. In other words we find that $k_q[O_2]$ and k_w are of the same order of magnitude.

3.4. Deactivation of $O_2(^1\Sigma_g^+)$ at High Temperatures

Analagously to the room temperature case the formation and removal of sigma post-shock is governed by three reactions leading to (3.19), the rate constants now referring to high temperature reactions occurring in particle time.

$$\frac{d[\Sigma]}{dt_p} = k_p[\Delta]^2 - k_q[\Sigma][M] - k_w[\Sigma] \qquad (3.19)$$

In the shock the concentration of the gas is increased. This means that diffusion to the wall is decreased and consequently so is k_w. On the other hand $k_q[M]$ is increased, hence the wall quenching reactions are insignificant and so we can write

$$\int_{[\Sigma]_o}^{[\Sigma]_t} \frac{1}{k_p[\Delta]^2 - k_q[\Sigma][M]}\, d[\Sigma] = \int_o^{t_p} dt_p$$

$$\ln\left\{\frac{k_p[\Delta]^2 - k_q[M][\Sigma]t_p}{k_p[\Delta]^2 - k_q[M][\Sigma]_o}\right\} = -k_q[M]t_p$$

$$\frac{[\Sigma]t_p}{[\Sigma]_o} = -\left(\frac{k_p[\Delta]^2}{k_q[M][\Sigma]_o}\exp(-k_q[M]t_p)\right) + (\exp(-k_q[M]t_p)) + \left(\frac{k_p[\Delta]^2}{k_q[M][\Sigma]_o}\right)$$

The concentration ratio

$$\frac{[\Delta]^2}{[M][\Sigma]_o}$$

is the same as that pre-shock, all terms being increased by the density

ratio. Using (3.17) the steady state concentration of sigma pre-shock, $[\Sigma]_1$ is given by

$$[\Sigma]_1 = \frac{k_p(T_1)[\Delta]_1^2}{k_q(T_1)[M]_1 + k_w}$$

$$\frac{[\Delta]_1^2}{[M]_1[\Sigma]_1} = \frac{k_q(T_1) + k_w/[M]}{k_p(T_1)}$$

Therefore

$$\frac{[\Sigma]_{t_p}}{[\Sigma]_o} = -(K \exp(-k_q[M]t_p)) + (\exp(-k_q[M]t_p)) + K \qquad (3.20)$$

where $K = \frac{k_p(T_2)}{k_q(T_2)} \cdot \frac{k_q(T_1) + k_w/[M]_1}{k_p(T_1)}$

The concentration of sigma immediately post-shock is that pre-shock multiplied by the density ratio. At the new steady state, after relaxation

$$[\Sigma]_2 = \frac{k_p(T_2)[\Delta]_2^2}{k_q(T_2)[M]_2}$$

Therefore K is the ratio of the enhanced, post-relaxation sigma concentration to that immediately post-shock.

As the emission at 762 nm is from a single molecule the concentration ratio in (3.20) can be replaced by an intensity ratio. Equation (3.20) can then be re-written as (3.21) where $\tau = (k_q(T_2)[M])^{-1}$.

$$\frac{I_t^{762}}{I_o^{762}} = K + (1-K)\exp(-t/\tau) \qquad (3.21)$$

where I_o^{762} is the immediate post-shock emission level and I_t^{762} is that after the t. This curve is sketched out in figure 3.3, two limits may be taken

when t = o

$$\frac{I_t^{762}}{I_o^{672}} = 1$$

when t = ∞

$$\frac{I_t^{762}}{I_o^{762}} = K$$

Between the initial value at t=o of unity the curve rises to K at long times; the rise is characterised by a relaxation time τ.

What is seen in a shock experiment is the conditions of the gas as it is swept back past the observation station. The immediate post--shock glow at any point in the tube is related to the immediate post--shock glow at the observation station I_{obs}^{762} by

$$I_o^{762} = I_{obs}^{762} \exp(\alpha t) \tag{3.22}$$

combining (3.21) and (3.22)

$$\frac{I_t^{762}}{I_{obs}^{762}} = \{K + (1-K)(\exp(-t/\tau))\}\exp(\alpha t) \tag{3.23}$$

The immediate post-shock glow at the observation station is given by

$$I_{obs}^{762} = I_1^{762} \rho_{21} \tag{3.24}$$

Figure 3.3 The 762nm Trace assuming no Decay

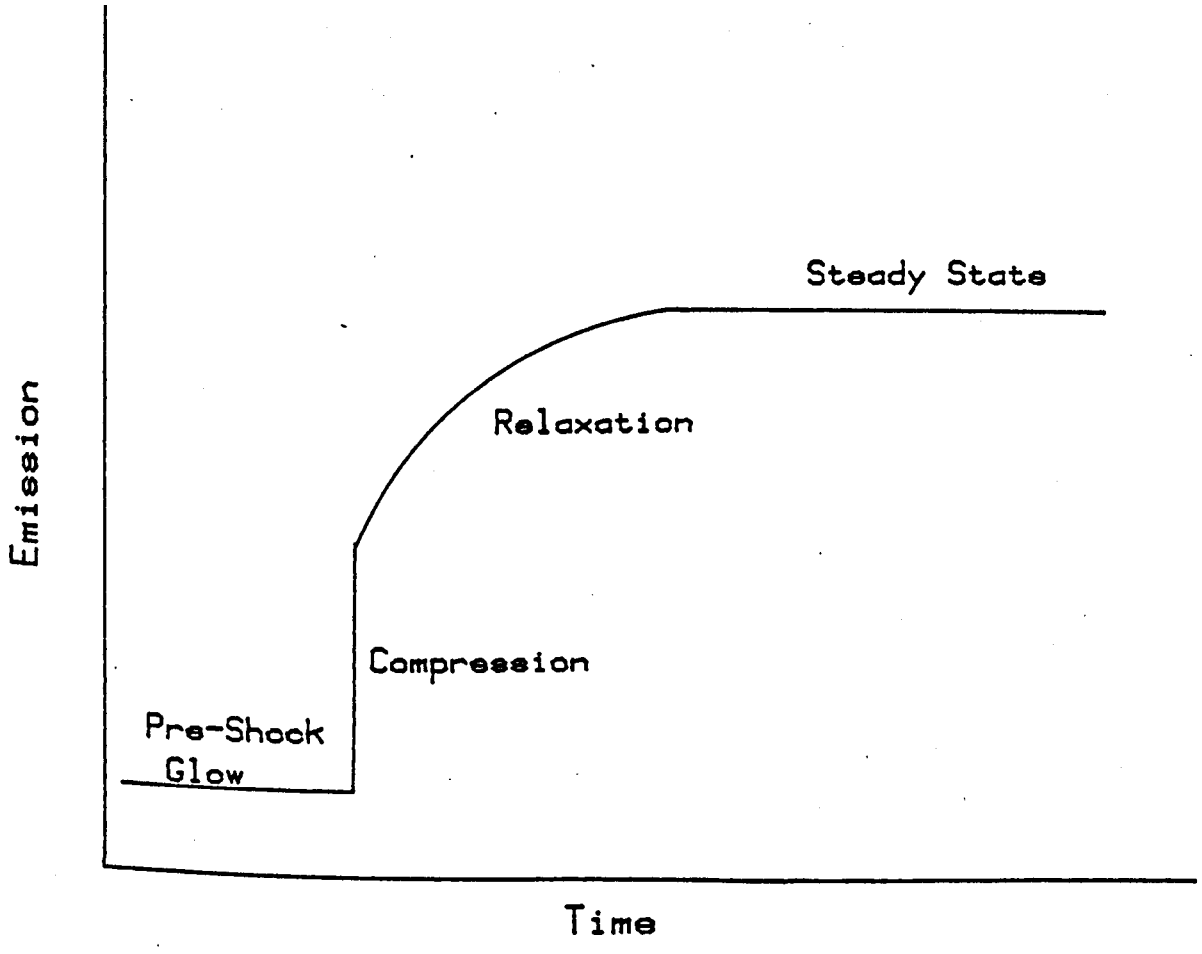

where ρ_{21} is the density ratio and I_1^{762} is the pre-shock glow.

Hence

$$\frac{I_t^{762}}{I_1^{762}\ \rho_{21}} = \{K + (1-K)(\exp(-t/\tau))\}\exp(\alpha t) \qquad (3.25)$$

This curve is sketched out in figure 3.4. Four zones may be distinguished.

1. The steady pre-shock glow from the room temperature steady state concentration of sigma.
2. The rapid rise at the shock front due to compression.
3. The relaxation to the new steady state at the high temperature.
4. The decay due to the fall in sigma concentration down the tube.

Figure 3.4 The 762nm Trace including Decay

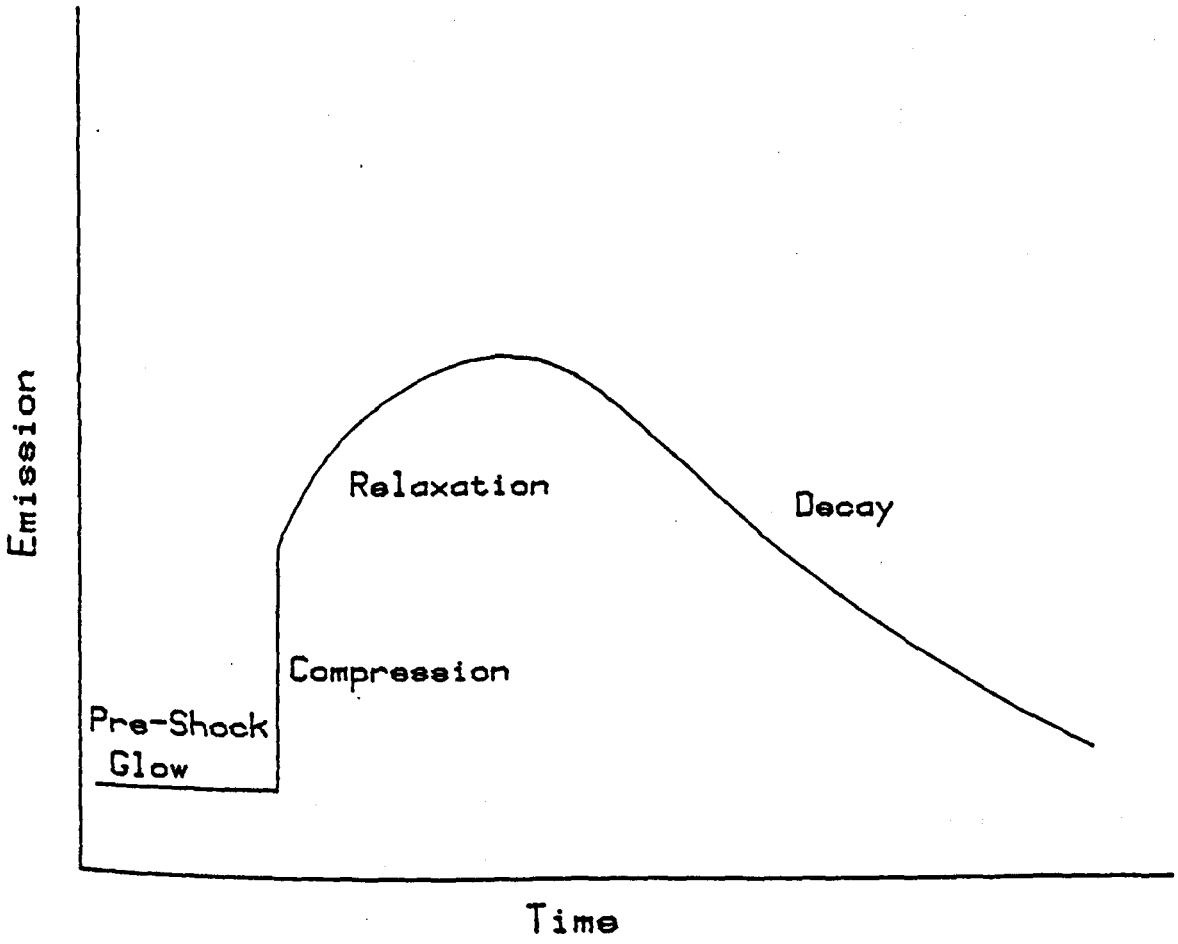

3.5. The Integration Time

Figure 4.1 shows that the rise in emission at the shock front is not instantaneous, i.e. vertical. This arises because of the finite slit width used. The voltage recorded by the transient recorder is an average rather than an instantaneous record at any point. The situation is illustrated in the three diagrams of figure 3.5. The slit (here treated as rectangular) acts as a window and the shaded portions represent the area under the curve that is seen.

To compensate for this equations (3.14) and (3.25) are modified by the introduction of an integration time Δt. For example at any point after the arrival of the shock front the glow at 634 nm is given by

$$I_t^{634} = \frac{1}{\Delta t} \int_{t_p-\Delta t}^{t_p} I_{obs}^{634} K^{634} \exp(\alpha t) dt_p$$

The integrated form of which is

$$I_t^{634} = \left\{ \frac{I_{obs}^{634} K^{634}}{\alpha} \left(\exp(\alpha t)(1-\exp(-\alpha \Delta t)) \right) \right\} / \Delta t$$

A similar expression can be written for the sigma emission

$$I_t^{762} = \frac{1}{\Delta t} \int I_{obs}^{762} \{K + (1-K)\exp(-k_q[M]t)\}\exp(\alpha t) dt_p$$

$$I_t^{762} = \frac{I_{obs}^{762}}{\Delta t} \left\{ \frac{K \exp(\alpha t)}{\alpha}(1-\exp(-\alpha \Delta t) + \frac{(1-K)}{(\alpha + k_q[M])} \exp(\alpha - k_q[M]t) \right.$$
$$\left. (1-\exp(-(\alpha - k_q[M]\Delta t) \right\}$$

In this chapter the kinetic scheme that allows the discharge flow/shock tube data to be analysed has been introduced. The comparison of the observed post-shock behaviour with that predicted is made in the next chapter.

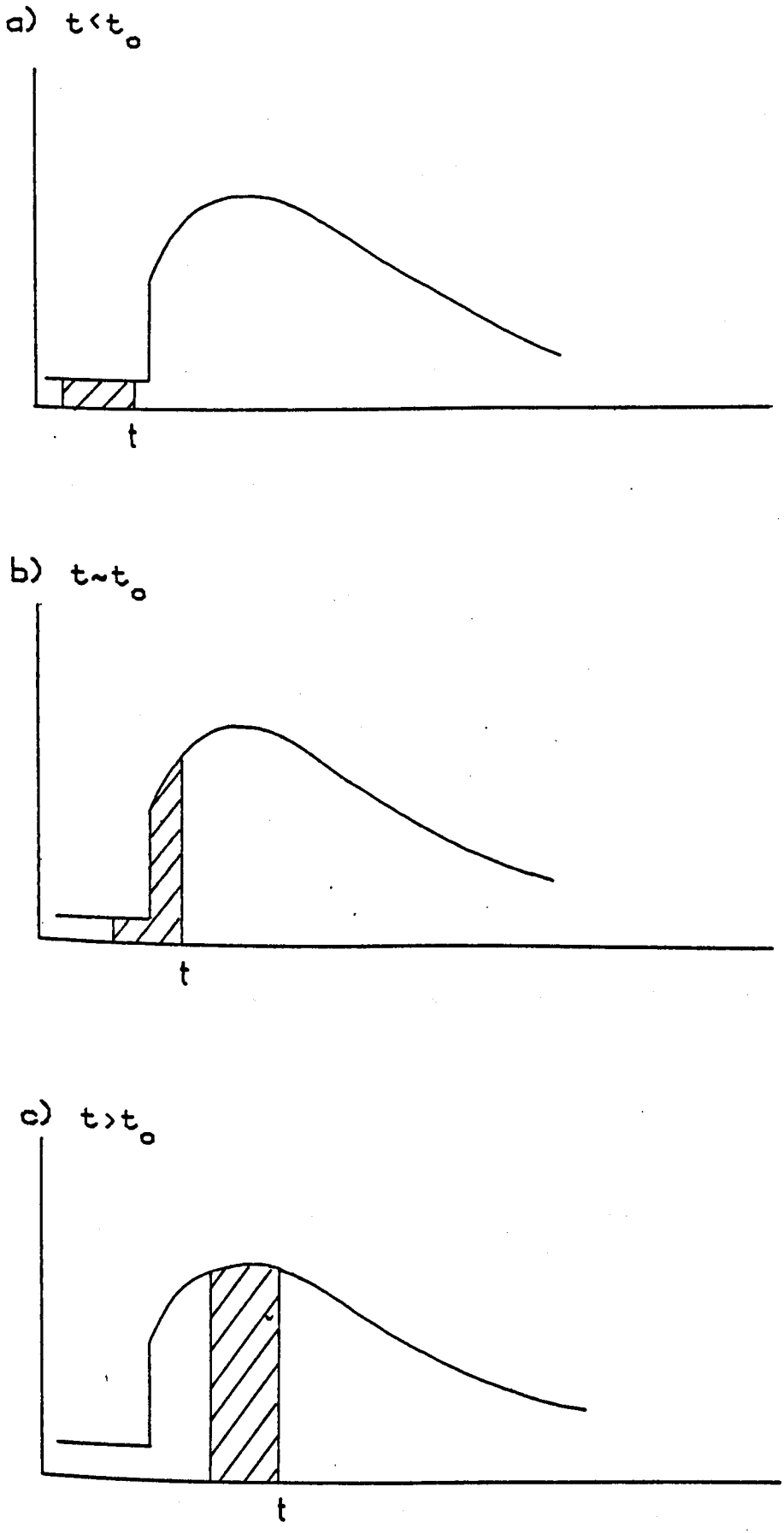

Figure 3.5 Area under curve seen by slit

t_o =time of arrival of shock front

3.6. Analysis by Interactive Computer Graphics

This section describes the translation of the equations derived in the previous sections into an interactive graphical analysis package to run jointly on the HP2647 and GEC4082. It starts with some preliminary remarks on the applicability of interactive graphics to the analysis of kinetic data, and concludes with a description of the program used in this laboratory.

This method possesses several advantages over the traditional, 'blind' method of computer assisted analysis.[66]

i) The operator can observe the progress of the fitting, he thus obtains a feel for and understanding of a multi-stage analysis. In the analysis of discharge flow/shock tube data up to 4 interdependent variables can be fitted to the trace.

ii) After every stage a menu of options is displayed allowing intervention by the operator. This is the interactive part of the analysis; certain parameters can be set visually to the trace thus shortening analysis time, also the operator can intervene if the analysis is heading in an obviously wrong direction.

iii) The input data can be edited prior to analysis. This is much more efficient than the traditional method, a result can be obtained from flawed data that might otherwise have to be discarded. Obviously discretion is needed in the use of such an option, the justifications for its use in the particular case of shock data are given in the next section.

iy) The breaking down of the program into numerous sub-routines that this method of analysis imposes enables modifications to be incorporated quickly.

Figure 3.6 Analysis of Discharge Flow/Shock Tube Data

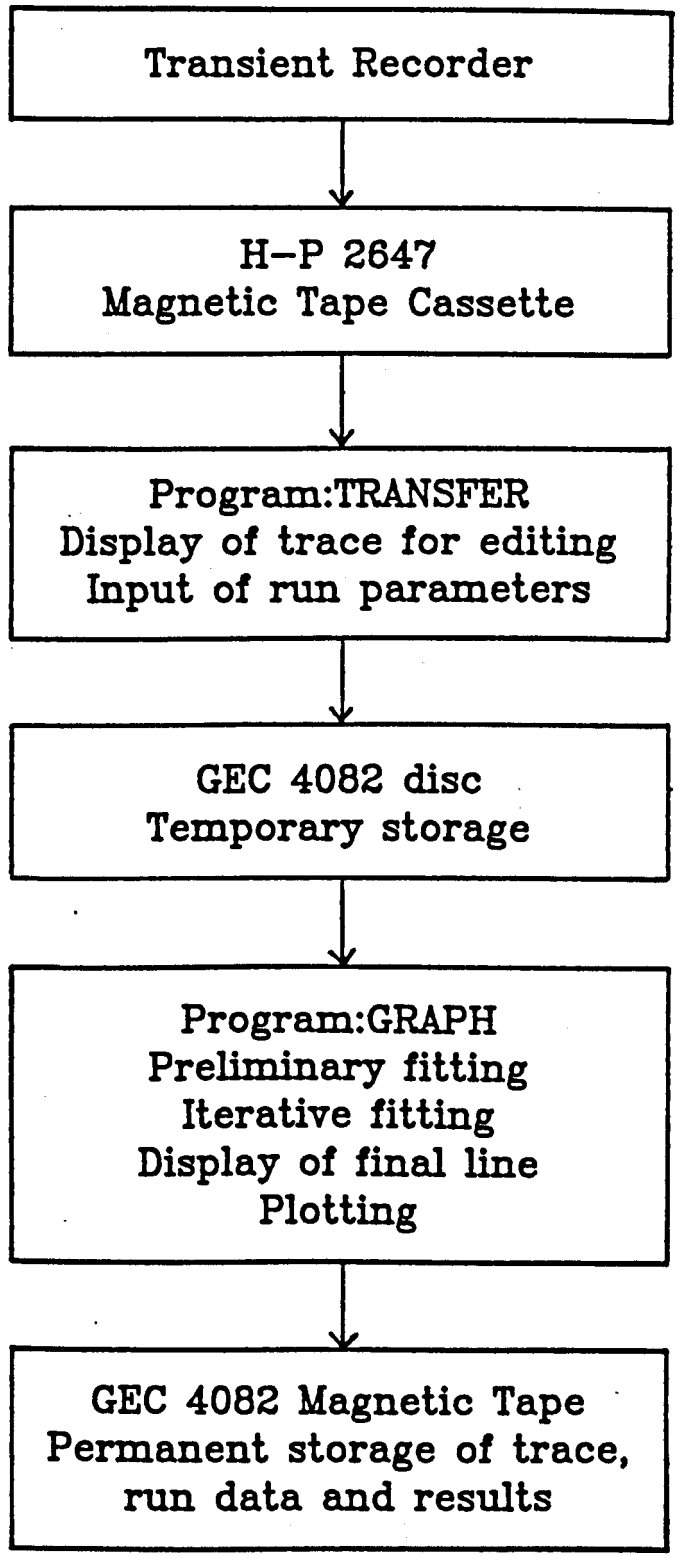

3.6.1. Analysis of Discharge Flow/Shock Tube Data

This section describes in outline the analysis by interactive computer graphics of the shock trace. The majority of the routines were written by Dr. P. Borrell with contributions from Dr. M.D. Pedley and Dr. P.M. Borrell.

A simplified flow chart is given in figure 3.6 the operation of the main sub-routines will now be described.

1. Program TRANSFER

The shock trace is digitized as 1024 points in the transient recorder, it is transferred to the 2647 screen and recorded on magnetic tape, together with the run number, sweep speed and voltage sensitivity.

Using the display facilities of the terminal, including the 16 x zoom, the data is prepared for analysis. Firstly the trace may be edited, if necessary. Random spikes sometimes appear in the trace the origin of which is uncertain but possibilities are reflection from pieces of diaphragm material carried by the shock and combustion of dirt on the tube walls. After editing the arrival of the shock front (ZERO TIME) and end of analysis (XEND) are set using the graphics cursor.

The 2647 is then connected to the 4082 for data transfer; the run parameters, gas composition, initial pressure, temperature and shock conditions etc. can be input and stored on disc.

2. Program GRAPH

This is the main program for analysis of experimental data. It is a multi-stage interactive program during which control passes from the 4082 for processing to the 2647 for display and visual setting of certain parameters. At each sub-routine a series of options is displayed allowing the operator great flexibility in the running of the program.

After initial sub-routines allowing selection of the run and the inputting/changing of run parameters the trace is displayed; ZERO TIME (time of arrival of the shock front), XEND, the pre-shock glow and the afterglow (calculated via 3.12 or 3.24) are also shown.

Using the graphics cursor the start of the decay region is set, this is

(a) After the relaxation zone on 762 nm and 579 nm traces

(b) After the afterglow on 634 nm and 703 nm traces.

A decay line is then displayed over the points; it may be one measured pre-shock using the moveable photomultiplier (3.4) or calculated from the trace by a least squares analysis of ln Y versus time.

By back extrapolation of the decay curve to ZERO TIME K, the ratio of the observed afterglow to that predicted using the pre-shock glow is determined.

After this preliminary setting up control passes to one of two non-linear least squares fitting routines. One, following the method of Moore,[67,68] was written by Dr. K.E. Newman, the other is a NAG library routine (E04GAF).[69]

The parameters to be fitted are now chosen. For 762 nm and 579 nm runs they are K, the integration time, the relaxation and the decay; for 634 nm and 703 nm traces they are K, the integration time and the decay. Each parameter may be included or omitted separately, or a value may be typed in allowing even 'difficult' traces to be analysed. This facility is particularly useful in the analysis of oxygen/carbon dioxide 762 nm traces where the fast relaxation and large K factor meant that the integration time was poorly defined and so generally was not iterated.

RUN NUMBER C216 12 JUN 1980
762. nm SIGMA

RESULTS

fitted	Quenching Const.	:	9.8304E-02	us-1
		:	1.0173E+01	us
	err.	:	1.1011E+01	
fitted	Ratio (K)	:	1.6776E+01	
	err.	:	1.0000E-01	
fitted	Decay Constant	:	-5.0774E-03	us-1
		:	-8.0350E-03	cm-1
	err.	:	1.5834E-01	
	Integration Time	:	2.5886E+00	us

RATE CONSTANTS (in l mol-1 s-1)

fitted	Quenching : kq	:	8.8072E+06	
	err.	:	9.5329E+06	
	log kq	:	6.9448	
fitted	Pooling : kp	:	3.0176E+05	
	err :		1.7988E+03	
	log kp	:	5.4797	

RUN DATA

Oxygen	:	90.000	%
N2O	:	10.000	%
Shock Speed	:	1.361	mm us-1
Initial Pressure	:	6.470	torr
P21	:	21.770	
Initial Temperature	:	296.000	K
T2	:	1130.000	K
Density Ratio, RO21	:	5.643	
Xzero	:	133.300	us
Yzero	:	477.997	mV
Pre-shock glow, PSG	:	16.900	mV
Afterglow	:	95.367	mV

FITTING

Fitted by NAG	:	complete fit.
No. of iterations	:	5
No. of points	:	554
Sum of the Squares	:	8.6424E+06

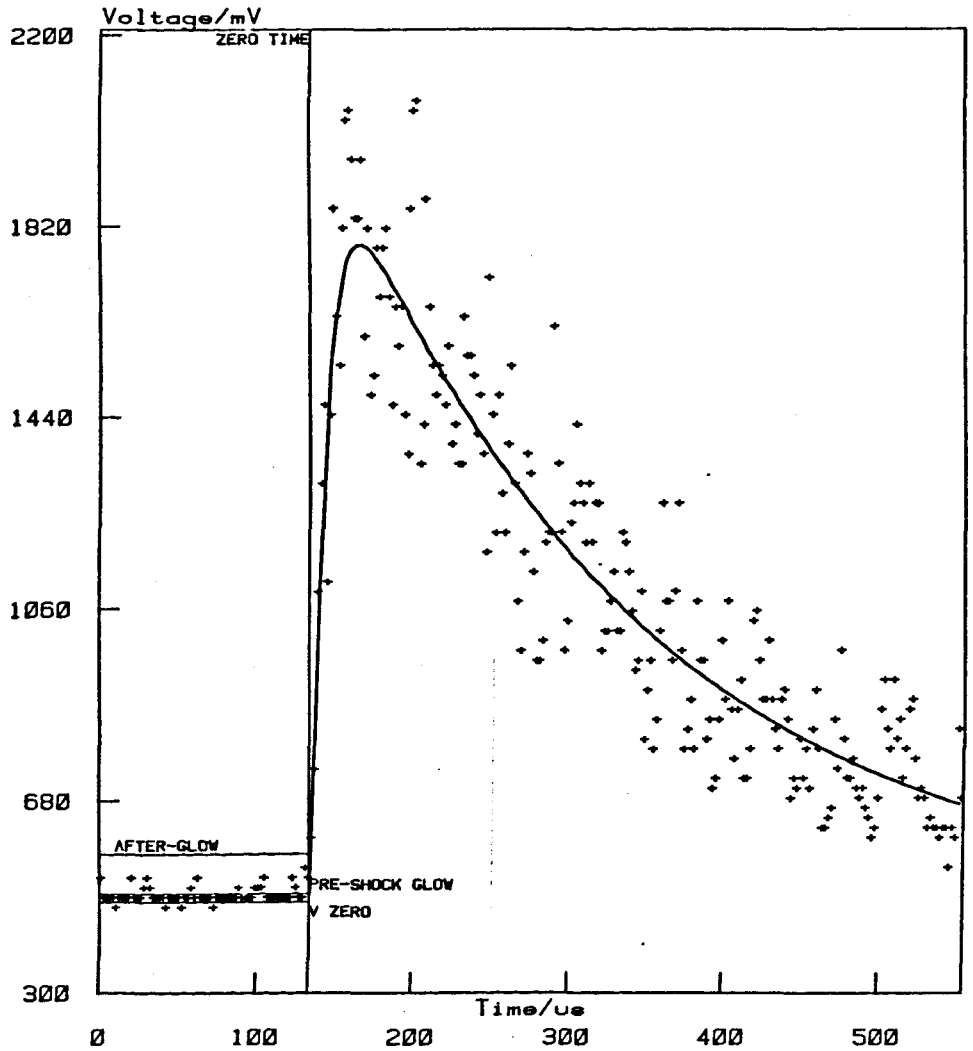

Figure 3.7 Output of Interactive Graphics Fitting

Generally fitting takes between 3 and 10 iterations (5 to 10 minutes in an interactive environment) after which the trace is displayed, together with the fitted line allowing the quality of the fit to be assessed.

After completion the trace, calculated line, results and run parameters are plotted thus providing a permanent visual record of each run (figure 3.7). All this data is recorded with the trace on disc from which it is transferred to magnetic tape for permanent storage. A library of all shocks and results is therefore available for examination.

3.6.2. Accuracy of the Discharge Flow/Shock Tube Results

In assessing the uncertainty in experimental data two terms are used, accuracy and precision. If a series of measurements of a quantity x give a mean value then the accuracy of the experiment is how the mean compares with the true value of x. The precision describes the scatter of individual points about the mean. The precision of an experiment is related to the random errors afflicting the measurements and the accuracy to the systematic errors. The results displayed in figure 5.1 are typical of those in shock tube work, the precision is poor but the accuracy good as will now be shown.

Shock experiments are imprecise because they are necessarily unique. There is a scatter inherent in shocks of nominally the same conditions because of variations in shock deceleration, pressure ratio at diaphragm bursting and gas composition. This, together with the time taken to perform an experiment, preclude data enhancement by signal averaging.

Shock experiments are afflicted by systematic errors due to the flow conditions behind the shock front and this will affect the accuracy of a series of experiments.[11] Boundary layer formation has been shown

to be negligible in this apparatus and so this source of systematic error is eliminated.[56]

This work depends on the measuring of relative voltages as a function of time. Systematic errors could be present in the determination of either. By comparing results from different sources systematic errors become evident. There are no comparable high temperature results but the room temperature quenching rate constants for carbon dioxide and nitrous oxide (see chapter 6) can be compared with values in the literature. The agreement is found to be good. This is good evidence that systematic errors are not afflicting the voltage measurements. The crystal controlled transient recorder time bases were regularly checked against a signal generator so this source of systematic error is eliminated.

Consideration of the measurements that are made enables the magnitude of the random errors in the results to be estimated. There are random errors in the pre-shock measurements. The error in the pre-shock temperature is negligible. The error in the pressure reading, the estimate of which depends on two measurements of height, is larger ± 5%. The error in the pre-shock glow depends on the emission being monitored, a typical error is ± 5%.

The error in the high temperature data, the scatter in the transient recorder points, varies with the relative size of recorded signal and noise. For a slow shock the scatter can be as high as ± 25% but may be as low as ± 5% for a slow shock. The error in the fitted parameters is lower, about ± 5% in K, the relaxation and decay constants.

Error limits are not quoted for individual shocks or shown on graphs. The error in a high temperature rate constant, estimated from the scatter on the graph is typically ± 20%. Where standard

deviations are appropriate the error is quoted as the 95% confidence limit (2 standard deviations). The difference between the sum of the random errors and the error estimated from the graph is due to the non-linear shock effects described above.

Chapter 4

STUDIES OF THE EMISSIONS FROM SINGLET OXYGEN

Table 1 in Chapter 1 lists the dimol transitions from singlet oxygen that have been observed. Those that have been seen in emission form discharged oxygen are marked and of these four are visible in this apparatus, at 634 nm, 703 nm, 579 nm and 405 nm.

This chapter reports work done on the dimol emissions at 634 nm, 703 nm and 579 nm and on the sigma emission at 762 nm.

4.1. Observed High Temperature Behaviour of the Emissions

In the previous chapter the analyses for the shock traces of the dimol emission at 634 nm and the sigma emission at 762 nm were developed. The comparison of the observed shock trace with that predicted by (3.14) and (3.25) is of importance. This section starts with such a comparison. The similarities and differences with the traces at 703 nm and 579 nm are discussed.

In figure 4.1 tracings of the oscilloscope record of the four emissions are given.

a) The 634 nm Emission

$$O_2(^1\Delta_g) + O_2(^1\Delta_g) \rightarrow O_2(^3\Sigma_g^-) + O_2(^3\Sigma_g^-) + h\nu(\lambda = 634\ \text{nm}) \quad (1.19)$$

It was shown in the previous chapter that if the dimol emission at 634 nm is a simple collisional process then the post-shock glow will be related to that pre-shock by

$$I_{obs}^{634} = K_I^{634}\, \rho_{21}\, T_{21}^{\frac{1}{2}} \quad (3.12)$$

The enhancement factor K^{634} is the ratio of the maximum post-shock glow (determined by extrapolation of the decay back to the arrival of the

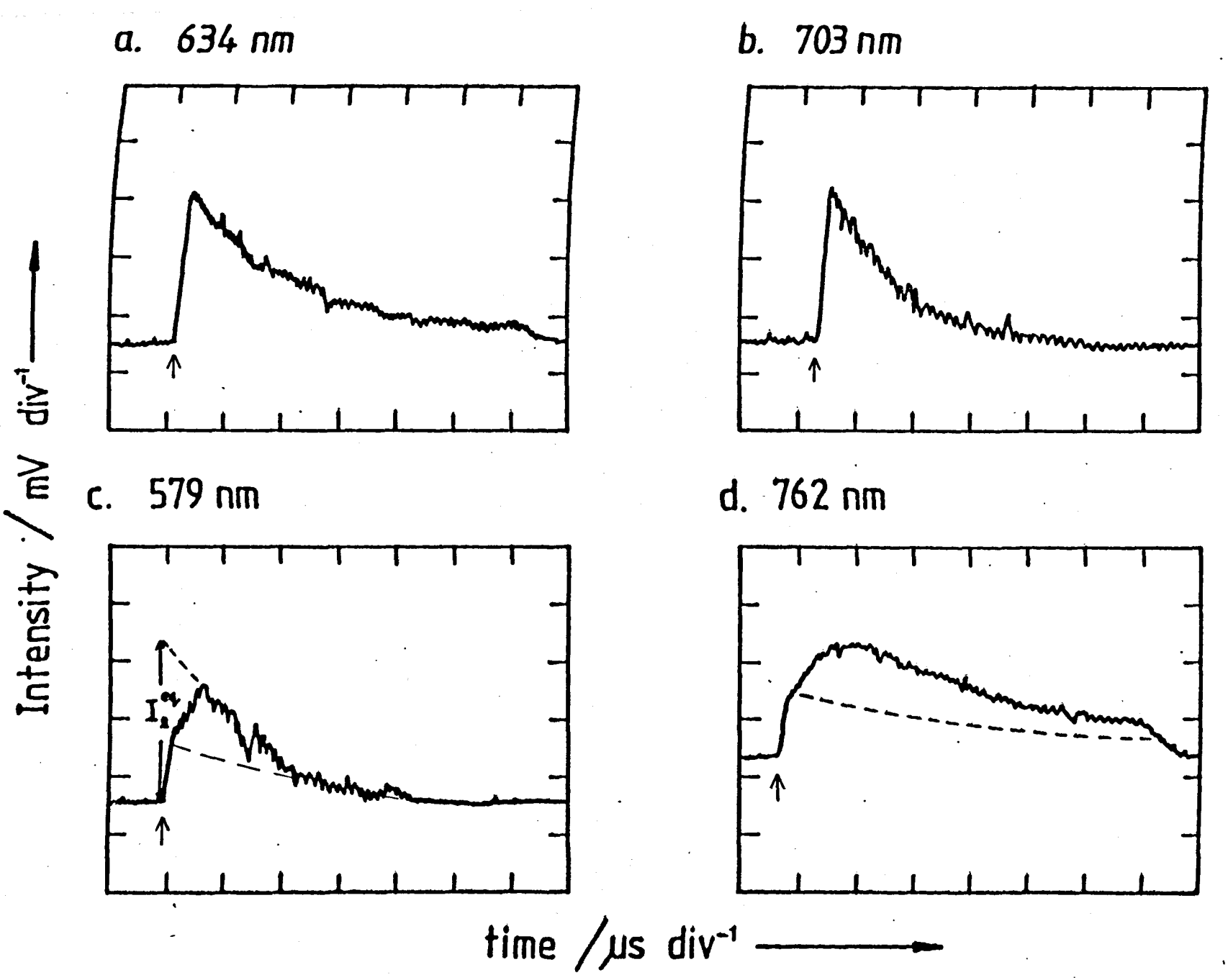

Figure 4.1 Shock Temperature Emission Traces

shock front) to that predicted by (3.12). Hence if (3.12) is accurate it will be unity across the temperature range. Because of the configuration of the apparatus there will be a decay in emission due to the decrease in excited state concentration down the tube.

Figure 4.1a shows an oscilloscope trace of the 634 nm emission from shock heated oxygen, it may be compared with figure 3.2. There are five features to note.

The first zone is the steady emission from the cool, flowing gas. It is recorded because the transient recorders (and hence oscilloscopes see figure 2.3) are triggered before the arrival of the shock front at the observation station. That it is steady shows that at any point in the tube the concentration of delta is steady.

At the arrival of the shock front (which on all traces is marked by an arrow) there is a rapid rise in emission level. This rise is due to shock compression and heating. For a shock into pure oxygen the factor $(\rho_{21}^{2}\, T_{21}^{\frac{1}{2}})$ is about 30 at 1000K and 70 at 1500 K. The rise is not instantaneous (i.e. vertical) because of the finite slit width and rise time of the detection system.

The immediate post-shock emission level is approximately given by (3.12), i.e. K = 1 across the temperature range. There is a slight enhancement of K^{634} with temperature, it rises to 1.3 at 1500 K in pure oxygen. This is discussed in the subsequent section.

There is no relaxation zone visible on the emission trace i.e. no curvature up to the peak (c.f. 579 nm and 762 nm traces). This confirms that the emission is from two ground vibrational state molecules.

After the peak there is a decay in emission intensity. This has been found to be identical to the measured pre-shock decay down the tube. This can be explained by the sizes of the various terms in (3.14).

$$I_t^{634} = K^{634} I_1^{634} \rho_{21}^2 T_{21}^{\frac{1}{2}} \exp(-2k_q[M] - 2k_w + \alpha_t)t_p \quad (3.14)$$

A typical value for the post-shock decay α_t (that due to the decay down the tube) is 10^3 s^{-1}; at room temperature the wall and collisional quenching rate contacts are about the same 10^{-1} s^{-1}. To obtain the high temperature collisional quenching rate constant from a comparison of pre- and post-shock decays it would therefore have to increase markedly with temperature. This is not found to be the case, many studies[22] including this one have shown the pre- and post-shock decays to be identical.

Therefore

$$\alpha_t >> (-2k_q[M] - 2k_w)$$

and hence (3.14) reduces to

$$I_t^{634} = K^{634} I_1^{634} \rho_{21}^2 T_{21}^{\frac{1}{2}} \exp(\alpha_t t_p)$$

Because of the similarity of the measured pre- and post-shock decays it is only possible to put an upper limit on k_q at the highest temperature studied, Borrell, Borrell and Pedley[22] obtaining 3.8×10^4 ℓ mol^{-1} s^{-1} at 1650 K.

All these observations are in accordance with the model. Therefore the attribution (1.19) and the kinetic scheme are confirmed. The 634 nm traces are analysed by interactive computer graphics as outlined in chapter 3 to yield values for the integration time, the enchancement factor and the decay.

b) The 703 nm Emission

Arnold et al[64] first suggested that the 703 nm emission was a dimol transition from two delta molecules, one of the ground state

molecules so formed being left in the first vibrational level

$$O_2(^1\Delta_g) + O_2(^1\Delta_g) \rightarrow O_2(^3\Sigma_g^-) + O_2(^3\Sigma_g^-)v=1 + h\nu(\lambda = 703 \text{ nm}) \qquad (4.1)$$

If this is correct then an equation similar to that for the 634 nm emission can be written

$$I_t^{703} = K^{703} I_1^{703} \rho_{21}^2 T_{21}^{\frac{1}{2}} \exp(\alpha_t t_p) \qquad (4.2)$$

where I_1^{703} is the pre-shock glow and I_t^{703} is the post-shock glow at time t.

In figure 4.1b a tracing of the 703 nm emission from shock heated oxygen is given. It can be seen to be very similar to the 634 nm trace. There is a steady glow followed by a rapid rise at the shock front. The rise at the shock front is found to be that which would be expected for a bimolecular emission, dependent on $\rho_{21}^2 T_{21}^{\frac{1}{2}}$. The enhancement factor K^{703} is found to behave in a similar way to that at 634 nm, to be approximately unity but to show a slight rise with temperature (up to 1.3 at 1500 K). Again no relaxation zone is visible showing that the partners are not vibrationally excited. After the peak there is a decay. The decay is found to be identical to that measured for the 634 nm emission, as would be expected if the emissions come from the same partners.

These findings are in agreement with the attribution (4.1), a dimol emission from two ground vibrational state delta molecules. Consequently (4.2) is applicable and the 703 nm shock traces are analysed in a similar manner to those at 634 nm. (4.2) is integrated to allow for the slit width and rise time of the detection system and the traces are analysed by interactive computer graphics.

c) The 579 nm Emission

The 579 nm emission is attributed to a delta dimol with one partner in the first vibrational level.[28]

$$O_2(^1\Delta_g)v=1 + O_2(^1\Delta_g) \rightarrow O_2(^3\Sigma_g^-) + O_2(^3\Sigma_g^-) + h\nu(\lambda = 579 \text{ nm}) \qquad (4.3)$$

Figure 4.1c shows the high temperature behaviour of this emission. It is markedly different to those at 634 nm and 703 nm.

There is a measurable glow at room temperature (typically 10 mV) and at the shock front there is a rise given by $\rho_{21}^2 T_{21}^{\frac{1}{2}}$. This is consistent with the bimolecular origin of the emission. Unlike the other dimol traces the 579 nm emission then displays a relaxation zone, that is a gradual rise to an enhanced level of emission. The dashed line indicates the shape of the emission trace that would be seen if the 579 nm emission behaved as the other dimol emissions studied. The enhancement factor K^{579} in this case rises from 3 at 1000 K to 6 at 1500 K, markedly different to those for the other dimol emissions. It is shown in chapter 5 that the peak emission level corresponds to the Boltzmann equilibrium at the high temperature and consequently that the relaxation zone is due to vibrational relaxation. This shows the attribution (4.3) is correct.

The kinetic scheme for the analysis of the 579 nm trace is developed in Chapter 5. Suffice to say here that the analysis allows the initial rise, relaxation zone and decay to be fitted as in the case of the 762 nm emission from sigma.

d) The 762 Emission

$$O_2(^1\Sigma_g^+) \rightarrow O_2(^3\Sigma_g^-) + h\nu(\lambda = 762 \text{ nm}) \qquad (1.18)$$

A 762 nm shock trace, figure 4.1d can be compared with the predicted behaviour, figure 3.4. The two can be seen to be in agreement.

At the shock front there is an increase that is accurately given by (3.24)

$$I_{obs}^{762} = I_1^{762} \rho_{21} \qquad (3.24)$$

This shows that the emission is from a single molecule. After this rise there is a further gradual increase to an enhanced level of emission. The dashed line indicates what would be seen if no relaxation zone was visible. This enhancement is due to the room temperature steady state concentration of sigma adjusting to the new value at the high temperature. The ratio of the enhanced emission level to that predicted by (3.24) varies with the gas composition because it depends on the temperature dependence of the reactions forming and removing sigma.

After relaxation there is a decay. This has been found to be identical to that measured for the decay of delta. This shows that sigma is formed from delta and the two concentrations are in step along the tube.

The 762 nm emission trace is analysed by interactive computer graphics as outlined in Chapter 3. The fitted parameters are the integration time, the relaxation zone, the enhancement factor and the decay. From the relaxation zone the quenching rate constant at the high temperature can be determined, using this value and the enhancement factor the energy pooling rate constant can be calculated. The procedure is

discussed more fully in Chapter 6. The essential result for the purposes of this chapter is the value of the enhancement factor K^{762}, that is the the ratio of the post-relaxation glow to that predicted by (3.24). Use of this enables an emission intensity to be calculated which can be compared to that at 634 nm.

It was mentioned in Chapter 2 that when a shock is run into undischarged pure oxygen no emission is visible at any of the four wavelengths. The observations made in this section (together with those in Chapter 5 for the 579 nm emission) are consistent with the attribution of the four emissions (1.19), (1.18), (4.1) and (4.3). The shape of the shock traces at 634 nm and 762 nm are found to be in agreement with the predictions of Chapter 3, confirming the kinetic models. The shock traces at 703 nm and 579 nm confirm the bimolecular nature and vibrational characteristics of the emissions.

4.2. Comparative Studies of the Dimol Emissions

As noted in the previous section the dimol emissions at 703 nm and 579 nm are visible in the apparatus. As little has been published on these dimol emissions a comparative study with the 634 nm emission seemed worthwhile.

4.2.1. Experimental

In this work the object was to obtain a comparable series of shocks at various speeds at each of the three wavelengths. In order to do this the experimental technique described in chapter 2 was modified.

One photomultiplier (in the Oxford Instruments housing) was used to provide a standard at 634 nm. The other photomultiplier was then used to obtain a series of shock traces at each wavelength. Once the photomultipliers had been positioned they were clamped and care was taken to ensure that they were not moved during the changing of the filters. The experiments comprised three shocks at each of the temperatures 1150, 1400, 1450 and 1500 K. Prior to each shock the glows were taken to provide room temperature emission ratios. The shock traces were analysed by computer graphics as outlined in Chapter 3, the analysis of the 579 nm emission is described in detail in the next chapter. The run parameters are listed in Appendix 4.

4.2.2. Results

The intensity recorded depends on several factors, for example the 634 nm emission intensity can in general be represented by

$$I^{634} = g\, f^{634}\, p^{634}\, [\Delta]^2\, k^{634} \qquad (4.4)$$

where g is a geometry factor depending on the position of the photomultiplier

f^{634} is a filter factor depending on the transmission of the filter at 634 nm and the overlap with the emission band

p^{634} is a photomultiplier factor depending on the sensitivity of the photomultiplier at 634 nm

k^{634} is the rate constant for the emission at 634 nm

In these experiments dimol emission intensity ratios are determined using the same photomultiplier. Consequently the geometry factor cancels.

In order that the results at different wavelengths be comparable it is necessary to determine what portion of each emission band is transmitted by the relevant filter. Each of the filters was found to have a maximum transmittance of 40 ± 2% and a half-width of 10 nm. However the maximum was not always at the peak of the emission band so the transmitted intensity of each band was calculated.

This was done by matching the published dimol spectrum with the filter transmission curve and calculating the area of overlap. Filter transmission curves were obtained on a Perkin-Elmer spectrophotometer. Dimol spectra were obtained from the following sources; the 579 nm band from the gas absorption spectrum of Khan and Kasha[70] and the 634 nm and 703 nm bands from the spectrum of discharged oxygen published by Bader and Ogryzlo.[30] Figure 4.2 shows the 579 nm band with the transmission curve of the filter superimposed. The transmitted intensity was then calculated as a percentage of the incident intensity; in all cases the filters were found to transmit 24 ± 3% of the incident intensity. This figure is not very sensitive to the position of the filter maximum because the dimol emissions are broad and structureless (half-width

Figure 4.2 Overlap of 579nm Band and Filter

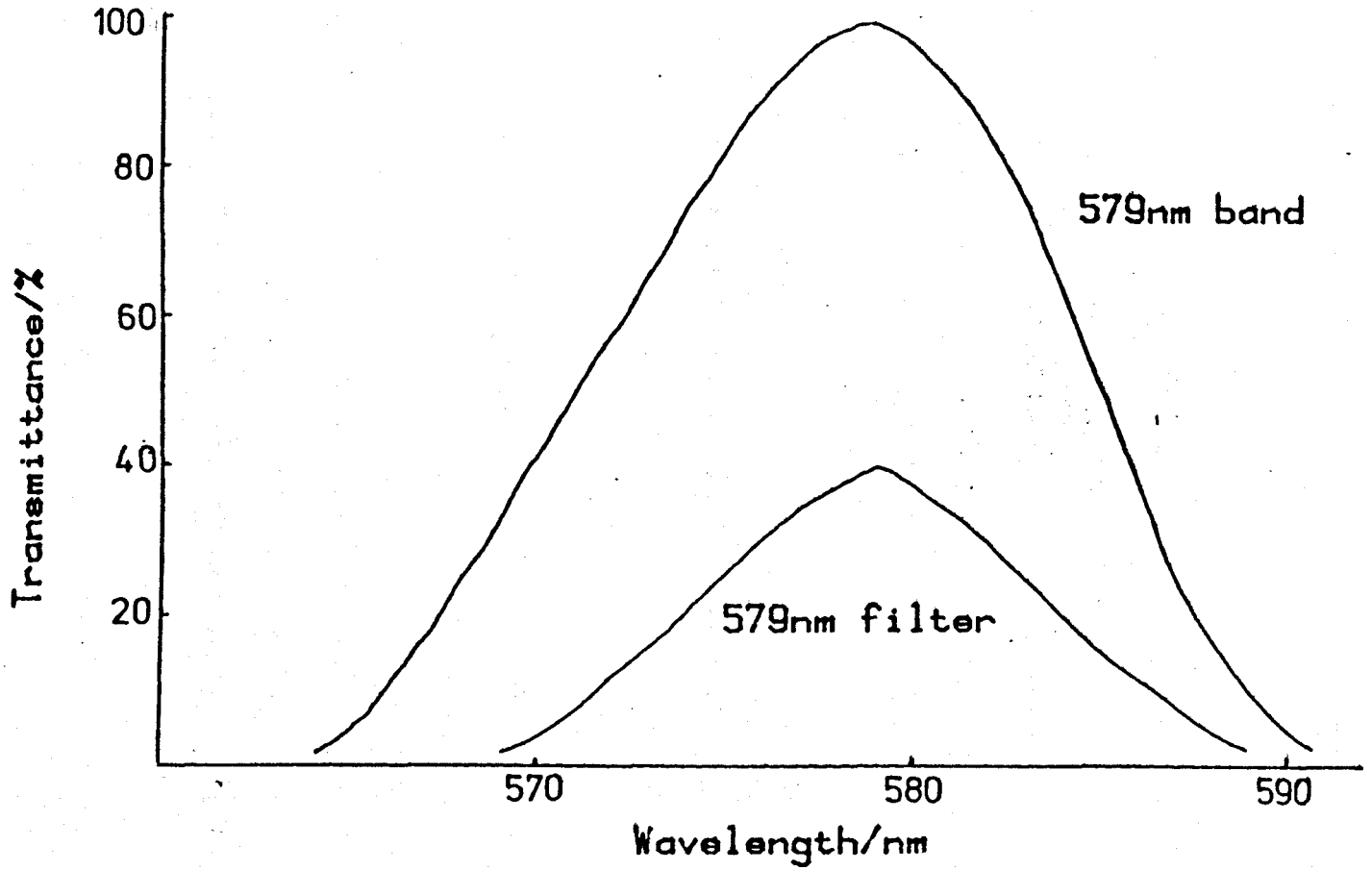

typically 14 nm).

Two 634 nm filters were used in this work, denoted in the Tables by A and C. In order for the results to be comparable the intensity ratios are quoted relative to the 634 C filter. In a series of experiments at room temperature to ratio of the recorded intensities for the filters was found

$$\frac{I(634\ A)}{I(634\ C)} = 1.27$$

Corrections were made for the differing photomultiplier sensitivity at the different wavelengths using the manufacturer's published curves of quantum efficiency.[61] For a 9658B photomultiplier

Quantum efficiency at 579 nm = 14.6%

Quantum efficiency at 634 nm = 11.2%

Quantum efficiency at 703 nm = 7.8%

Comparative post-shock glows were obtained in the following way. Using (4.5) the post-shock glow $I^{\lambda}(t = o)$ at each wavelength was obtained

$$I^{\lambda}(t = o) = K^{\lambda} . I_1{}^{\lambda} . \rho_{21}{}^{2} . T_{21}{}^{\frac{1}{2}} \qquad (4.5)$$

To compensate for fluctuating delta concentration each post-shock glow was then normalised to the standard at that temperature. The standards are denoted in Table 4.1 by an asterisk. These normalised post-shock glows were then corrected for the other factors in (4.4) as described above. In this way high temperature emission ratios were obtained.

Because of the large voltages measured in the shocks at 1450 K and for the 579 nm emission at 1500 K, which caused the voltage follower to approach saturation, no high temperature ratios were calculated for

Table 4.1
Relative Intensities of Dimol Emissions
All runs 100% O_2, 100 W, 28 ml s^{-1}

No.	λ /nm	Pre-Shock Glow /mV	Room Temp. Ratio	ρ_{21}	T_{21}	Ratio K	Corr AFGL	Shock Temp. Ratio	Corr Ratio
C132A	634A	44.7		5.381	3.912	0.95			
C132	579	7.3	0.13	5.381	3.912	3.17	1247	0.42	0.42
*C134A	634A	41.4		5.356	3.867	0.98	2289		
C134	634C	40.2		5.356	3.867	0.93	2109		
C135A	634A	39.3		5.381	3.916	1.00			
C135	703	49.7	1.87	5.381	3.916	0.84	2431	1.66	1.66
C133A	634A	42.7		5.797	4.808	1.18			
C133	579	6.9	0.13	5.797	4.808	4.25	2377	0.48	0.48
* 12	634A	45.5		5.808	4.836	1.21	4084		
12A	634C	41.1		5.808	4.836	1.16	3795		
C136A	634A	38.6		5.761	4.719	1.06			
C136	703	49.3	2.03	5.761	4.719	1.06	5216	1.97	1.97
4	634C	30.0		5.857	4.963	1.23			
4A	579	14.2	0.13	5.857	4.963	4.94			
* 6	634C	27.5		5.799	4.812	1.32			
6A	634A	98.1		5.799	4.812	1.09			
5	634C	27.5		5.852	4.949	1.24			
5A	703	99.2	1.84	5.852	4.949	1.11			
1	634C	31.4		5.910	5.081	1.31			
1A	703	76.0	1.65	5.910	5.081	1.20	5544	1.54	1.96
* 2	634C	28.8		5.789	4.740	1.19	2500		
2A	634A	76.9		5.789	4.740	0.92	5162		

these experiments. Room temperature ratios were however obtained.

a) The 634 nm Emission

The process that gives rise to the glow at 634 nm is now taken to be a two molecule-one photon simultaneous transition from a pair of colliding delta molecules.

$$O_2(^1\Delta_g) + O_2(^1\Delta_g) \rightarrow O_2(^3\Sigma_g^-) + O_2(^3\Sigma_g^-) + h\nu(\lambda = 634 \text{ nm}) \qquad (1.19)$$

Many studies,[22,64,71] including this one, have shown this to be the only tenable interpretation. For example Huestis et al,[71] studying the decay of emission after laser excitation, found the decay constant to be twice that for the single molecule transition down to 78 K. Their work also indicated that it was a simple collisional process with no activation energy.

If the emission were dependent simply on the collision rate then (3.12) should hold and the enhancement factor K would be unity across the temperature range.

$$I_2^{634}(t = o) = K^{634} I_1^{634} \rho_{21}^2 T_{21}^{\frac{1}{2}} \qquad (3.13)$$

While this is found to be generally true, there is a slow increase in K^{634} with temperature above 1100 K. Figure 4.3 shows the values of K for pure oxygen shocks plotted against temperature.

The collisional nature of the interaction allows radiative rate constants at the shock temperature to be calculated. Using (4.6) and the room temperature value measured by Derwent and Thrush[44]

$$k_2^{634} = K^{634} k_1^{634} \left(\frac{T_2}{T_1}\right)^{\frac{1}{2}} \qquad (4.6)$$

Figure 4.3 K^{634} versus Temperature

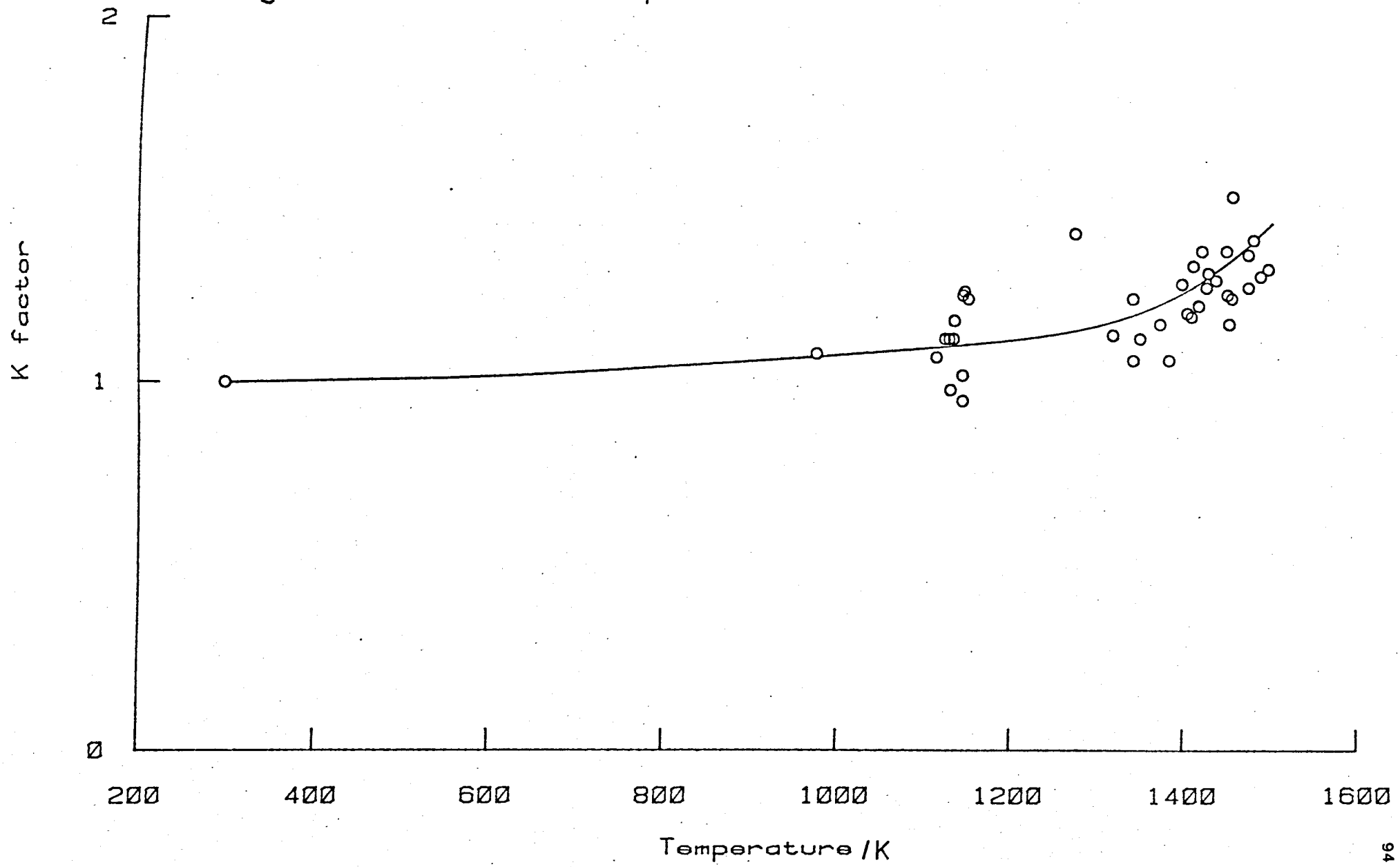

Table 4.2

Relative Intensities and Rate Constants

	Temperature/K			
	295	1150	1400	1500
K^{634}	1.00	1.10	1.24	1.30
k^{634}/l mol^{-1} s^{-1}	0.016	0.035	0.043	0.047
I^{703}/I^{634}	1.85	1.66	1.97	1.96
k^{703}/l mol^{-1} s^{-1}	0.030	0.058	0.085	0.091
I^{579}/I^{634}			0.48	
k^{579}/l mol^{-1} s^{-1}	0.047	0.111	0.121	0.140

where $k_1^{634} = 0.016\ \ell\ mol^{-1}\ s^{-1}$

The values are listed in Table 4.2.

b) The 703 nm Emission

The shape of the high temperature 703 nm emission trace is very similar to that at 634 nm and confirms the attribution (4.1).

$$O_2(^1\Delta_g) + O_2(^1\Delta_g) \rightarrow O_2(^3\Sigma_g^-) + O_2(^3\Sigma_g^-)v=1 + h\nu(\lambda = 703\ nm) \qquad (4.1)$$

The enhancement factor K^{703} shows the same slight increase with temperature as does that at 634 nm. Consequently after normalisation and correction for all filter and photomultiplier effects.

$$\frac{I^{703}}{I^{634}} = \frac{k^{703}[\Delta]^2}{k^{634}[\Delta]^2} \qquad (4.7)$$

Using (4.7) rate constants for the 703 nm emission at the various temperatures can be calculated relative to the 634 nm rate constants. They are listed in Table 4.2.

Across the temperature range the 703 nm emission is found to be more intense than that at 634 nm by a factor of 1.86.

The measured intensity ratios can also be used to calculate relative transition probabilities.

The intensity of a spectral line in emission is given by[23]

$$I_{nm}^{em} = N_n\ h\ c\ \omega\ A_{nm} \qquad (4.8)$$

In (4.8) N_n is the number of molecules in the upper state, ω is the wavenumber of the emitted radiation and A_{nm} is the Einstein transition probability for spontaneous emission - the Einstein A factor. When comparing the intensities of different transitions the A factors should

be used, that is the intensity per unit population measured as number of quanta emitted. The factor N_n becomes important when comparing transitions from different vibrational levels, as in the case of the 634 nm and 579 nm emissions.

In absorption a similar equation can be used (4.9), this assumes the same radiation density and thickness of absorbing layer at the wavelengths compared

$$I_{mn}^{abs} = N_m B_{mn} h c \omega \tag{4.9}$$

Here B_{mn} is the Einstein transition probability of absorption.

The A and B factors for a given transition are related by

$$A_{nm} = 8\pi\, h\, c\, \omega^3\, B_{mn} \tag{4.10}$$

Table 4.3 lists the A factors calculated from the measured intensity ratios and compares them with the previous estimates.

c) The 579 Emission

The emission at 579 nm from discharged oxygen is attributed to the transition

$$O_2(^1\Delta_g)v{=}1 + O_2(^1\Delta_g) \rightarrow O_2(^3\Sigma_g^-) + O_2(^3\Sigma_g^-) + h\nu(\lambda = 579\ nm) \tag{4.3}$$

As noted in the previous section the 579 nm shows a markedly different form to the other dimol emissions. The post-shock emission can be obtained using (4.5) but here the enhancement factor K is the ratio of the glow after relaxation to that predicted using (3.12). It rises to about 6 at 1850 K.

At the high temperature, after relaxation, there is the Boltzmann equilibrium across the vibrational levels of delta. The Boltzmann

equation[72] in it's most general form is

$$\frac{N_j}{N} = g_j \exp(-\varepsilon_j/kT)/q \qquad (4.11)$$

where N_j is the population of level j

N is the total population

g_j is the degeneracy of level j

ε_j is the energy of level j

q is the partition function.

$$q = \Sigma_j g_j \exp(-\varepsilon_j/kT)$$

The term for the zero point energy in (4.11) cancels and for a simple harmonic oscillator the partition function can be approximated by

$$q = (1 - \exp(-hc\omega/kT))^{-1} \qquad (4.12)$$

For delta

$$\frac{hc\omega}{k} = 2130 \text{ K}$$

Therefore

$$\frac{[\Delta^1]}{[\Delta^0]} = \exp(-2130/T)/(1 - \exp(-2130/T))^{-1}$$

Now

$$\frac{I^{579}}{I^{634}} = \frac{k^{579}}{k^{634}} \frac{[\Delta^0][\Delta^1]}{[\Delta^0][\Delta^0]} \qquad (4.13)$$

where I^{579} is the corrected post-relaxation emission intensity. Hence the 579 nm radiative rate constant can be calculated, relative to the 634 nm rate constant at that temperature. This has been done using the intensity ratio measured at 1400 K.

Rate constants at the other temperatures can be obtained using that calculated at 1400 K and (4.14).

$$k^{579}(T) = \frac{K^{634}(T)}{K^{634}(1400)} k^{579}(1400) \left(\frac{T}{1400}\right)^{\frac{1}{2}} \qquad (4.14)$$

This analysis assumes that there is the same enhancement in K at 579 nm as there is at 634 nm. As this is seen to be true for the 703 nm emission the assumption seems reasonable.

Using the ratio at 1400 K the intensity ratio for unit population can be calculated, the result is shown in Table 4.3. It can be compared with that obtained by Khan and Kasha[70] from absorption studies, which has been converted using (4.10).

Preliminary work showed that the glow from the cool flowing gas at 579 nm was much greater than that which would come from vibrational equilibrium population of delta at room temperature. Using (4.13) an estimate of the vibrational temperature at the obversation station can be made. Using the measured room temperature emission ratio (0.13) and the constants at 295 K from Table 4.2 we find

$$\frac{[\Delta^1]}{[\Delta^o]} = 0.045$$

This is the Boltzmann equilibrium population that would be expected for delta at 700 K.

Table 4.3

Intensity Ratios for unit population measured as number of quanta emitted

703nm/634nm	579nm/634nm	References
2.06	2.74	this work
1.05		11
2.50		73
1.17		64
1.11		71
	1.44	70
From Franck-Condon Factors for single molecule transitions		
0.0068	0.022	74

4.2.3. Discussion

4.2.3.1. Emission Intensity Ratios

Relative A factors, calculated from the emission intensities are listed in Table 4.3.

As well as the errors in discharge flow/shock tube work in general discussed in Chapter 3 there are several other sources of error that could afflict these measurements. In particular they relate to the comparison of intensities at different wavelengths measured during separate experiments. Clamping the photomultipliers in place minimized errors due to positioning and using the same photomultiplier ensured there were no geometry errors. The largest source of error remaining is the comparison of emissions at different wavelengths which depends on the accuracy of the manufacturer's data and also on our estimates of filter transmittance. Taking these sources of error into account we estimate a 95% confidence level at ± 25% of the values listed in Tables 4.2 and 4.3.

Our value for the 703 nm/634 nm ratio lies between the previous estimates. The highest value is that of Seliger,[73] estimated from solution phase chemiluminescence. Like us both Whitlow and Findlay[62] and Ogryzlo et al[64] studied the emissions from discharged oxygen. However as we have been able to work at higher concentrations due to shock compression we prefer our estimate.

There has been only one previous estimate of the 579 nm/634 nm ratio, that of Khan and Kasha[70] who estimated it from gas phase absorption measurements. Our value is about twice theirs. However again we have been able to work with higher concentrations, in this case because of shock compression and heating and so again we have confidence in our measurement.

Also shown in Table 4.3 are the single molecule ratios calculated from the Franck-Condon factors.[74] The A factor is related to the transition moment R_{nm} by

$$A_{nm} = c\ \omega^3 |R_{nm}|^2$$

where c is a constant.[23] The transition moment can be separated into electronic and vibrational parts, in (4.15) q is the square of the vibrational overlap integral, the Franck-Condon factor

$$A_{nm} = c\ \omega^3 |R_e|^2 q \qquad (4.15)$$

The vibrational overlap integral is

$$\int \psi_n\ \psi_m\ dr \qquad (4.16)$$

where ψ_n and ψ_m are the initial and final nuclear (vibrational) wavefunctions. The low ratios obtained using the Franck-Condon factors for the (0,1) and (1,0) single molecule transitions indicate that the internuclear separations in the ground and first excited states are very similar.

The situation for the dimol transitions is illustrated in figure 4.4. In these diagrams the dimol complex is considered in diatomic terms. The upper curve represents a potential surface between two delta molecules and the lower curve that between two ground state molecules. The vibrational wavefunctions for the first two vibrational levels of each state are also shown. These represent cases in which one molecule only has vibrational excitations.

In the first diagram the curves are drawn with the same equilibrium separation. In such a case the strongest emission (or absorption) will be the (0,0) transition (i.e. at 634 nm). This is due to overlap of

Figure 4.4 Potential Energy Curves for Dimol Emissions

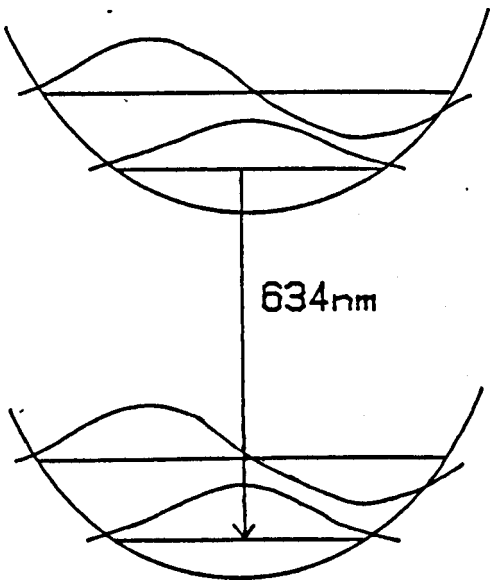

a) No Displacement

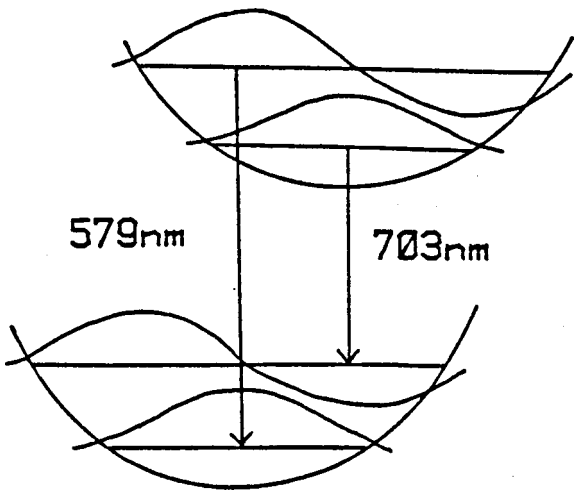

b) Displacement

vibrational wavefunctions. For the (0,0) transition the vibrational overlap integral is positive, in the case of the (0,1) transition for each individual positive contribution there is an equal negative contribution and so the integral (4.16) is zero. This is the quantum mechanical formulation of the Franck-Condon principle. In figure 4.4.b the curves are drawn with a larger equilibrium separation in the upper state. In this situation the (0,1) transition (at 703 nm) and the (1,0) transition (at 579 nm) will be allowed and so intense.

The results in Table 4.3 show that the (1,0) and (0,1) transitions are favoured over the (0,0). This indicates that the separations in the upper and lower states must differ.

Implicit in this interpretation of the results is the existence of $(O_2)_2$ complexes sufficiently long lived to have defined vibrational structure. Our studies and those of Ogryzlo[64] show that the $(O_2)_2$ complex is not bound. If the dimol emission were from a bound complex then the emission would decrease with temperature as the formation of the complex became less favoured. The only evidence for the existence of O_4 dimers comes from work done on solid oxygen in a neon host at 3 K.[75]

The dimol emissions themselves provide information about the nature of the emitting complex. Figure 4.5 illustrates a phenomenon similar to the dimol emissions of oxygen, the formation of an excimer and it's emission.

Many organic substances are known to form excimers.[76] Their existence is indicated by the development of a new emission band at longer wavelengths then the single molecule emission.

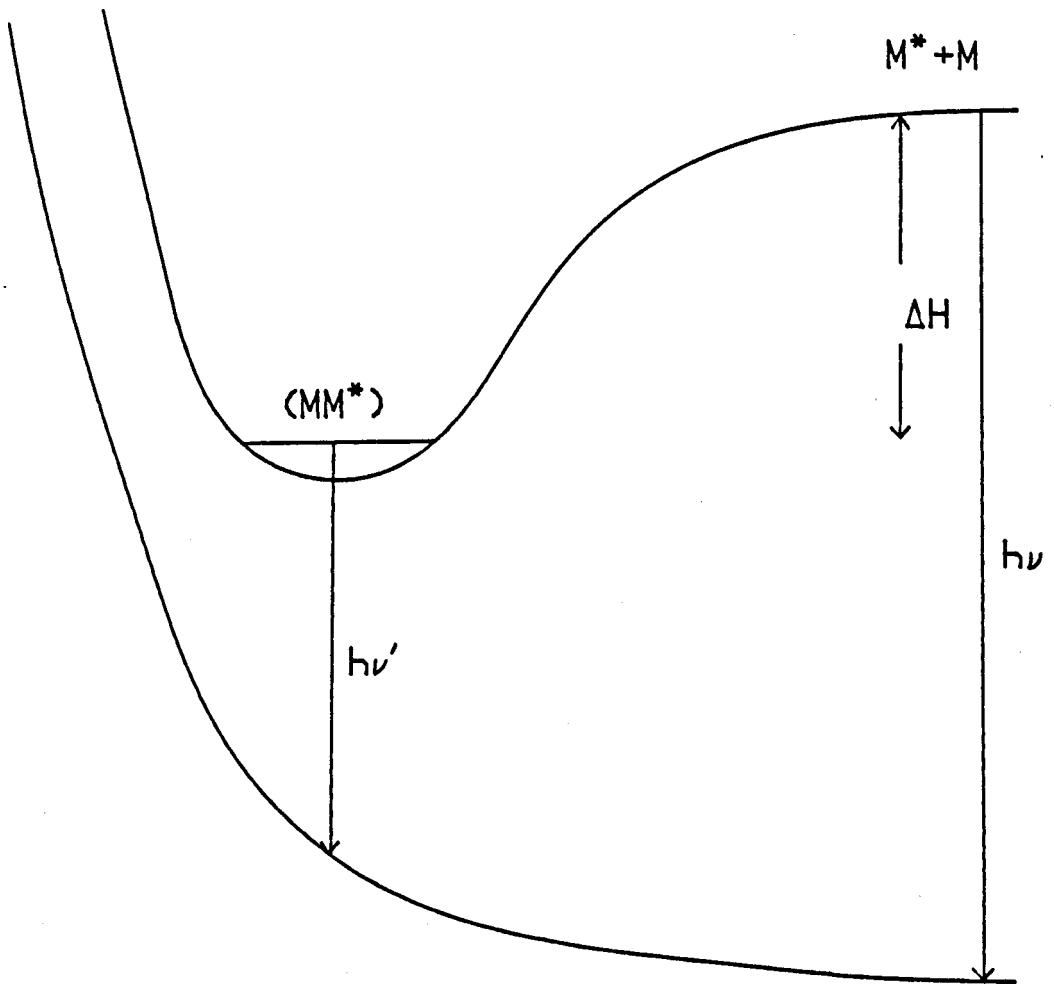

Figure 4.5 Excimer Formation and Emission

$$M + h\nu \rightarrow M^* \xrightarrow{M} (MM)^* \rightarrow M + M + h\nu'$$

excimer — excimer emission

As this emission occurs to a repulsive potential surface it is broad and structureless. The shift to lower energies is due to the stabilization of the excimer with respect to the separated components. This is the 'binding energy' of the excimer and is represented on figure 4.5 by ΔH.

The dimol emissions are similar but they represent cases in which both partners are excited. The broad, structureless nature of the emission indicates that it occurs to a repulsive potential energy surface. The emission wavelength is exactly half that of the single molecule emission. This lack of energy shift indicates that the emitting complex is only weakly bound and so is not a dimer. For example assume the dimol complex had a binding energy 1 kJ mol^{-1} (100 cm^{-1}). Even this feeble binding energy would cause an appreciable shift in emission wavelength, from 634 nm (15764 cm^{-1}) to 638 nm (15664 cm^{-1}). It is therefore very unlikely that dimers could exist in liquid or gaseous oxygen where kT would greatly exceed their low binding energy. This is in accordance with our experimental observations.

Given the weak interactions the lifetime of the dimol complex need be little more than the time for an allowed electronic transition $\sim 10^{-12}$ s.

4.2.3.2. The Temperature Dependence of the Dimol Emissions

These studies have confirmed the bimolecular nature of the emissions. All three emissions show an increase at the shock front consistent with this model over the temperature range 600 - 1500 K. The fact that the enhancement factor K does not decrease with increasing temperature shows

that the emitting species cannot be considered as a dimer. This is in keeping with the findings of the other temperature dependent study. Indeed figure 4.3. shows that there is an increase in emission intensity with temperature beyond that due to the increased collision rate. Considering the temperature range studied this enhancement is not large, a factor of 1.3 between 300 and 1500 K (the factor $T_{21}^{\frac{1}{2}}$ is 2.25 at 1500 K). A reaction with a more ordinary temperature dependence (Arrhenius type, ΔE = 50 kJ mol^{-1}) could be expected to show an increase in rate constant of several orders of magnitude across such a range. Also the temperature dependence is not simple, the enhancement factor does does not increase steadily with temperature but more rapidly at higher temperatures. Several explanations are possible for this effect.

The first is that the delta concentration post-shock is increased beyond that due to compression by heating i.e. translational-electronic energy transfer. Using a simplified form of the Boltzmann equation

$$\frac{N_u}{N_l} = \frac{g_u}{g_l} \exp(-\Delta E/RT)$$

where g_u and g_l are the degeneracies (2 for delta and 3 for the ground state) and the subscripts denote the upper and lower states. The energy gap between delta and the ground state is 93.8 kJ mol^{-1}; at 1500 K

$$\frac{N_u}{N_l} = 3.3 \times 10^{-4}$$

This small population in the upper state cannot account for the enhancement of the emissions.

Other mechanisms for the selective production of excited species is the shock, for example by atom recombination will also be negligible. This is because at these temperatures dissociation of oxygen into atoms

Figure 4.6 Arrhenius Plot for Dimol Emission at 634nm

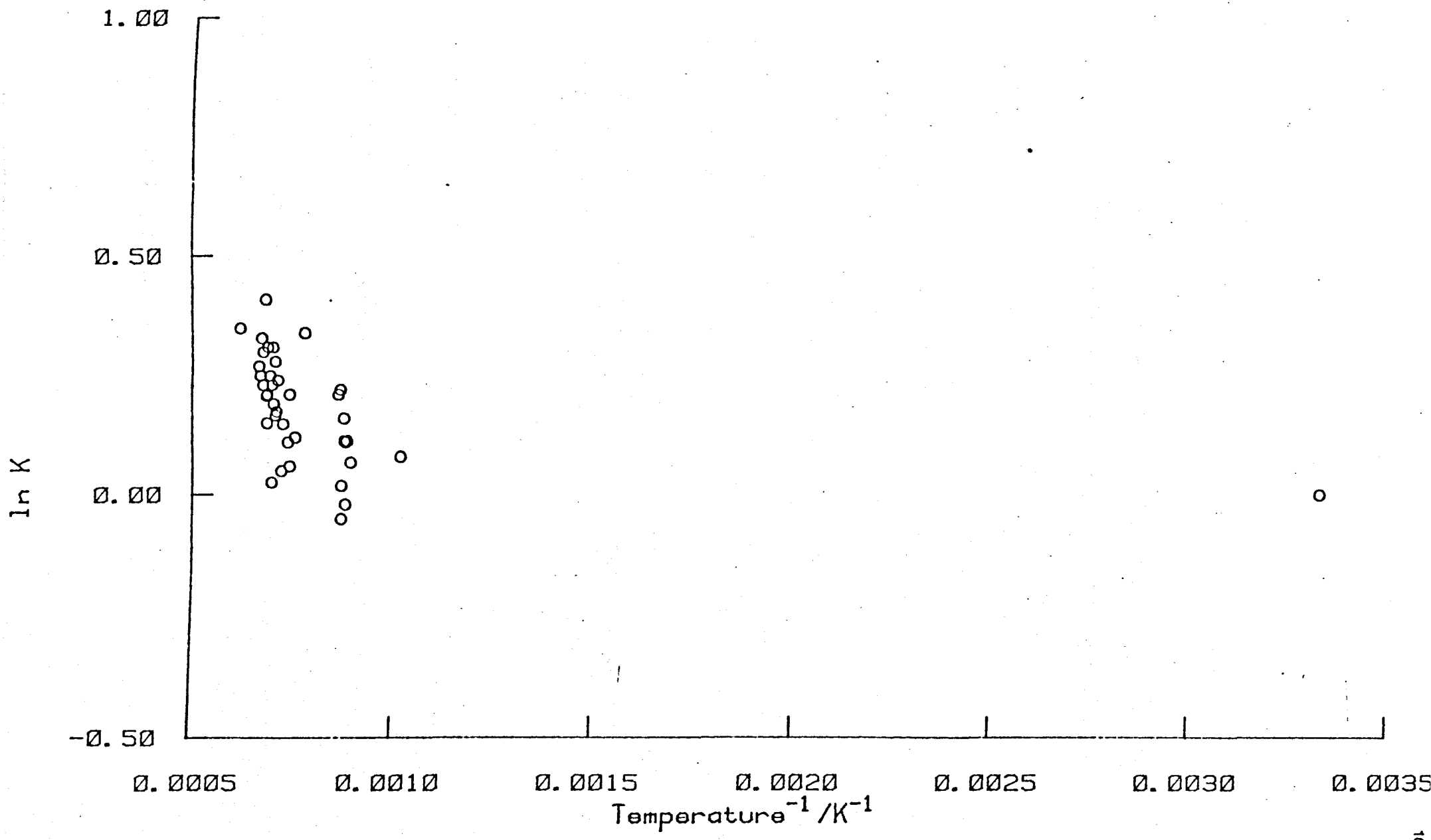

is negligible.

The effect seen in figure 4.3 could therefore be due to (1.19) having an activation energy, a temperature dependent transition probability or to some other emission process becoming operative.

If (1.19) had an activation energy then an Arrhenius plot using K would be linear. Such a plot is shown in figure 4.6. The plot is evidently non-linear showing that the Arrhenius approach is not applicable.

Another possible explanation is that the dimol transition probability increases for higher energy collisions, of which there are more at higher temperatures. This explanation requires that the transition probability be greater for collisions on the repulsive part of the intermolecular potential. This would have the effect of making the Arrhenius plot non-linear and so is in agreement with 4.6. However the temperature dependence of the transition probability is strange in that it does not appear from 4.3 to change steadily across the temperature range but abruptly beyond 1100 K. Such behaviour has no analogue in single molecule transitions.

A third explanation is that another emission process is becoming important at higher temperatures. One possibility for this process is hot band emission, i.e. transitions from upper vibrational levels which become populated in the shock. The similarity of vibrational spacing in the ground and excited states means that combinations of vibrational excitation other than (1.19), (4.1) and (4.3) may give rise to emission at approximately the same wavelengths. Ignoring combinations involving v=2 which are unlikely the hot band emissions near each of the three wavelengths will be

$$O_2(^1\Delta_g)v=1 + O_2(^1\Delta_g) \rightarrow O_2(^3\Sigma_g^-)v=1 + O_2(^3\Sigma_g^-) + h\nu(\lambda = 637\ nm)$$

$$O_2(^1\Delta_g)v=1 + O_2(^1\Delta_g)v=1 \rightarrow O_2(^3\Sigma_g^-)v=1 + O_2(^3\Sigma_g^-) + h\nu(\lambda = 582\ nm)$$

$$O_2(^1\Delta_g)v=1 + O_2(^1\Delta_g) \rightarrow O_2(^3\Sigma_g^-)v=1 + O_2(^3\Sigma_g^-)v=1 + h\nu(\lambda = 707\ nm)$$

In the following discussion the emissions above are referred to as hot bands and the three dimol emissions studied as fundamentals.

The fact that the filters have bandwidths of about 10 nm opens the possibility that these transitions will be important, particularly at higher temperatures. The filters transmit 17%, 17% and 23% respectively of these bands. Though the 582 nm transition depend on the meeting of two vibrationally excited molecules it could still be significant. This is because the ratio of the population of each hot band to it's fundamental is the same in each case. The relative populations will change with temperature and the intensities will depend on the population and the emission rate constants.

If these hot bands are significant there will be a relaxation zone in which the population of vibrationally excited delta increases to the Boltzmann equilibrium at the high temperature. No such relaxation zones are visible on the 634 nm or 703 nm emission traces. An estimate of the effect on the results at 634 nm can be obtained in the following way.

In the studies of the quenching of sigma one of the additives used was carbon dioxide (see Chapter 6). As well as the sigma emission at 762 nm the dimol emission at 634 nm was monitored in these experiments. In such a mixture with carbon dioxide vibrational relaxation will be very fast. Consequently the enhancement factor K^{634} will be an accurate representation of the total emission. The equilibrium emission I_{eq}

is given by

$$I_{eq} = k^{634}[\Delta^o]^2 + k^{637}[\Delta^o][\Delta^1]$$

where k^{634} and k^{637} are the high temperature emission rate constants and $[\Delta^o]$ and $[\Delta^1]$ are the concentrations in the zeroth and first vibrational levels.

Immediately post-shock

$$I = k^{634}[\Delta]^2$$

assuming that all delta molecules are in the zeroth level at room temperature. This is a reasonable approximation in the presence of carbon dioxide.

$$K^{634} = \frac{I_{eq}}{I} = \frac{[\Delta^o]^2}{[\Delta]^2}\left(1 + \frac{k^{637}}{k^{634}}\frac{[\Delta^1]}{[\Delta^o]}\right)$$

Using the partition function for the first term

$$K^{634} = (1 - \exp(-hc\omega/kT)^2(1 + \frac{k^{637}}{k^{634}}\exp(-hc\omega/kT))$$

$$\therefore \quad \ln\left(\frac{K^{634}}{(1 - \exp(-2130/T))^2} - 1\right) = \ln\left\{\frac{k^{637}}{k^{634}}\right\} - \frac{2130}{T} \qquad (4.17)$$

Therefore a plot of the left hand side of (4.17) against T^{-1} will be a straight line, gradient 2130 K from which the rate constant ratio may be obtained from the slope. Such a plot is shown in figure 4.7. for shocks into oxygen/carbon dioxide mixtures. The run parameters may be found in Appendix 6.

As can be seen the points fit the theoretical line quite well. The scatter is larger at the lower end of the temperature range where the enhancement factors become nearer unity. The rate constant ratio

Figure 4.7

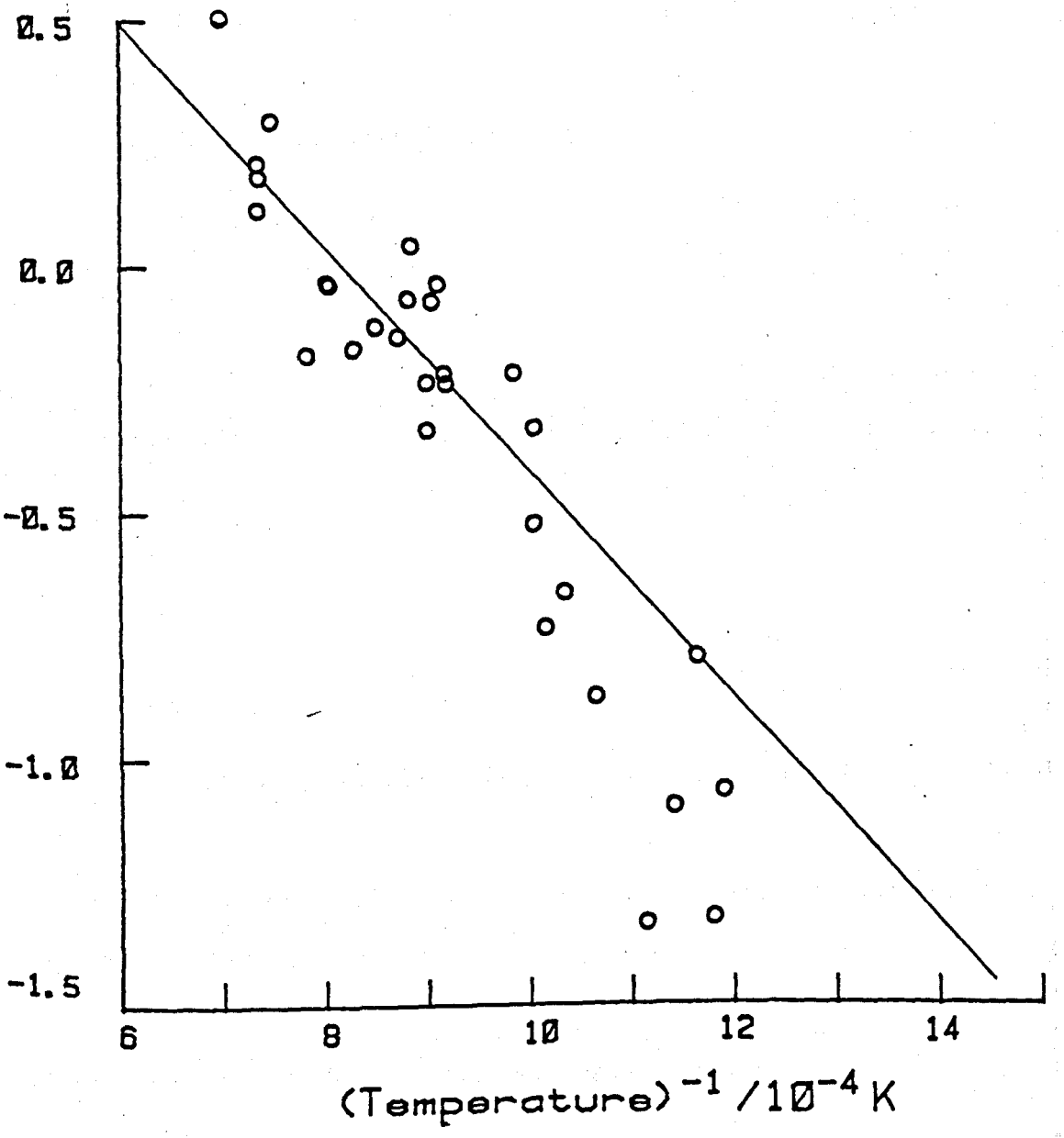

obtained from the intercept is 6. At 1500 K

$$\frac{[\Delta^1]}{[\Delta^o]} = 0.2$$

therefore using (4.4), assuming the same quantum efficiency at the two wavelengths.

$$\frac{I^{637}}{I^{634}} = \frac{k^{637}[\Delta^1]\ f^{637}}{k^{634}[\Delta^o]\ f^{634}} = 0.9$$

We find that the 637 nm and 634 nm emissions will be of similar intensity.

The 637 nm transition is written as

$$O_2(^1\Delta_g)v=1 + O_2(^1\Delta_g) \rightarrow O_2(^3\Sigma_g^-)v=1 + O_2(^3\Sigma_g^-) + h\nu(\lambda = 637\ nm)$$

which does not specify the changes in vibrational excitation of any one molecule. However the rate constant ratio calculated above allows the vibrational changes within the transition to be clarified. In figure 4.8 the possible vibrational states of each molecule during the simultaneous transition are shown.

Dealing first with the 637 nm transition in case a. Here the transitions of the individual molecules are (0,0) and (1,1). Arguments based on the relative emissivities of the 579 nm and 703 nm transitions indicated that the potential energy surfaces were arranged as in figure 4.4b i.e. displaced with respect to one another. In such a case the (0,0) and (1,1) transitions would have unfavourable Franck-Condon factors. This would have the effect of making the 637 nm emission rate constant similar to that for the 634 nm transition. This is not found to be the case. If however the component transitions were as in figure 4.8b then the Franck-Condon factors, given the potential surfaces in figure 4.4b would be favourable. Consequently the transition would

Figure 4.8

Vibrational Components of Dimol Transitions

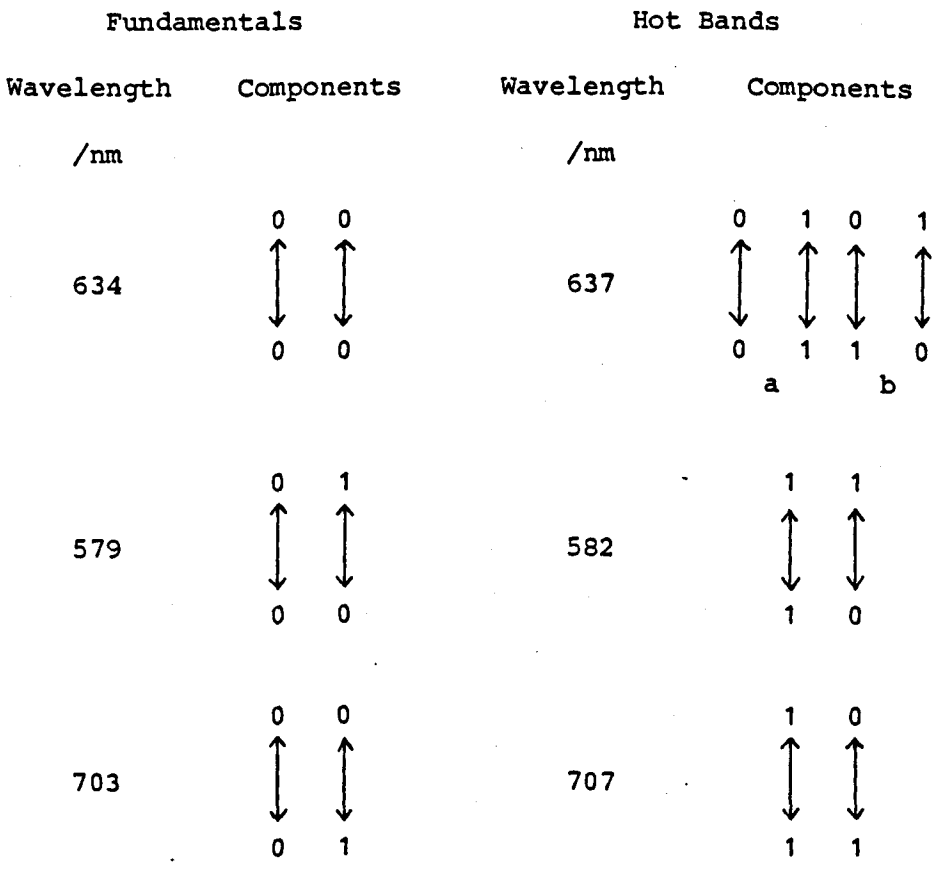

be intense compared to that at 634 nm. This is consistent with the results obtained from figure 4.7. Furthermore the rate constant ratio obtained above is consistent with the intensities of the 579 nm and 703 nm transitions. Relative to the (0,0) transition the (0,1) and (1,0) transitions are found to have rate constants greater by factors of 1.86 and 2.74 respectively. This leads to the conclusion that the 634 nm transition, if composed of a (0,1) and (1,0) transition would have a rate constant greater than the 634 nm transition ((0,0) and (0,0)) by a factor of about 5. This is in agreement with our estimate from figure 4.7.

The components of the 582 nm and 703 nm bands are also shown in figure 4.8. They can only be combinations of a (1,0) or (0,1) transition with the (1,1) respectively. The fundamental can likewise only be a combination of a (1,0) or (0,1) with a (0,0). The (0,0) and (1,1) transitions will be equally disfavoured on the basis of Franck-Condon factors and so the hot bands will be expected to have similar rate constants as their fundamentals. The observed intensity depends on the emission rate constant and the population and so they will be of lesser intensity than their fundamentals because of the lower population of the upper vibrational levels. The effect of these hot bands on their traces would therefore be of lesser importance than at 634 nm.

There is however evidence that the hot band emissions are not important. If these emissions were important one would expect relaxation zones, in which the Boltzmann population across the vibrational levels at the high temperature was achieved, to be evident on the emission traces. This is not the case, see figure 4.1a (634 nm) and figure 4.1b (703 nm) and compare with figure 4.1c (579 nm).

In conclusion the attribution of the dimol emissions at 634 nm, 703 nm and 579 nm have been confirmed. They are found to be bimolecular processes with no activation energy. The relative intensities have been measured and it is found that the 703 nm and 579 nm transitions are more intense than that at 634 nm. This leads to the conclusion that the separations in the upper and lower levels differ and hence indicates that the emitting complex is more than just two adjacent molecules. There is however evidence against dimer formation. The Arrhenius plot is non-linear and a small enhancement of intensity with temperature is found. Two possible explanations are forwarded for this, a temperature dependent transition probability or the addition of hot band emission. The answer as to which is the correct explanation must await further experiments.

4.2.3.3. The Mechanism of the Dimol Emissions

Using the rate constants in Table 4.2 it is possible to determine the probability of a collision between delta molecules resulting in emission. The collision number for like molecules is given by[72]

$$Z = \frac{\pi\sigma^2 \bar{c}\, L\, 10^3}{\sqrt{2}}$$

where σ is the collision diameter of the oxygen molecule (2.9×10^{-10} m)

$\bar{c}$ is the mean molecular speed

L is Avogadro's number

At 295 K this gives a value of 5×10^{10} ℓ mol^{-1} s^{-1}. Therefore the dimol emissions have a probability, defined by (4.19) of 10^{-13} i.e. only one collision is 10^{13} results in radiation.

$$\text{Probability} = \frac{k}{Z} \qquad (4.19)$$

where k is the second order rate constant for emission

Z is the collision number

The increase in rate constant with temperature beyond that due to collision i.e. the increase seen in K, is negligible on this scale. The probability increases by a factor of 1.3 between 300 and 1500 K. This can be compared with the behaviour of another energy transfer reaction involving delta, the energy pooling reaction

$$O_2(^1\Delta_g) + O_2(^1\Delta_g) \rightarrow O_2(^1\Sigma_g^+) + O_2(^3\Sigma_g^-) \qquad (1.20)$$

The similarity between the energy pooling reaction and the dimol emissions might suggest a common mechanism. The probability for the energy pooling reaction has been determined (see Chapter 6) and it is plotted against temperature in figure 4.9. It displays a quite different form to that of the dimol emissions. At room temperature the probability is much greater, 10^{-7}. A positive temperature dependence is seen, the probability increases by a factor of 45 between 300 and 1500 K. So the dimol emissions and the energy pooling reaction evidently proceed by different mechanisms.

One mechanism for the dimol emissions, intensity borrowing, has been proposed by Robinson.[77] He suggests that the dimol transitions borrow intensity from the strongly allowed Schumann-Runge transition $^3\Sigma_g^- - {}^3\Sigma_u^-$. This transition is so intense that a small interaction, $\sim 5\ cm^{-1}$ can account for the observed intensity. Such a small interaction would be in accordance with our observations. Also as the emission depends on the perturbation caused by a collision an increase in

Figure 4.9 Probability of Energy Pooling Reaction

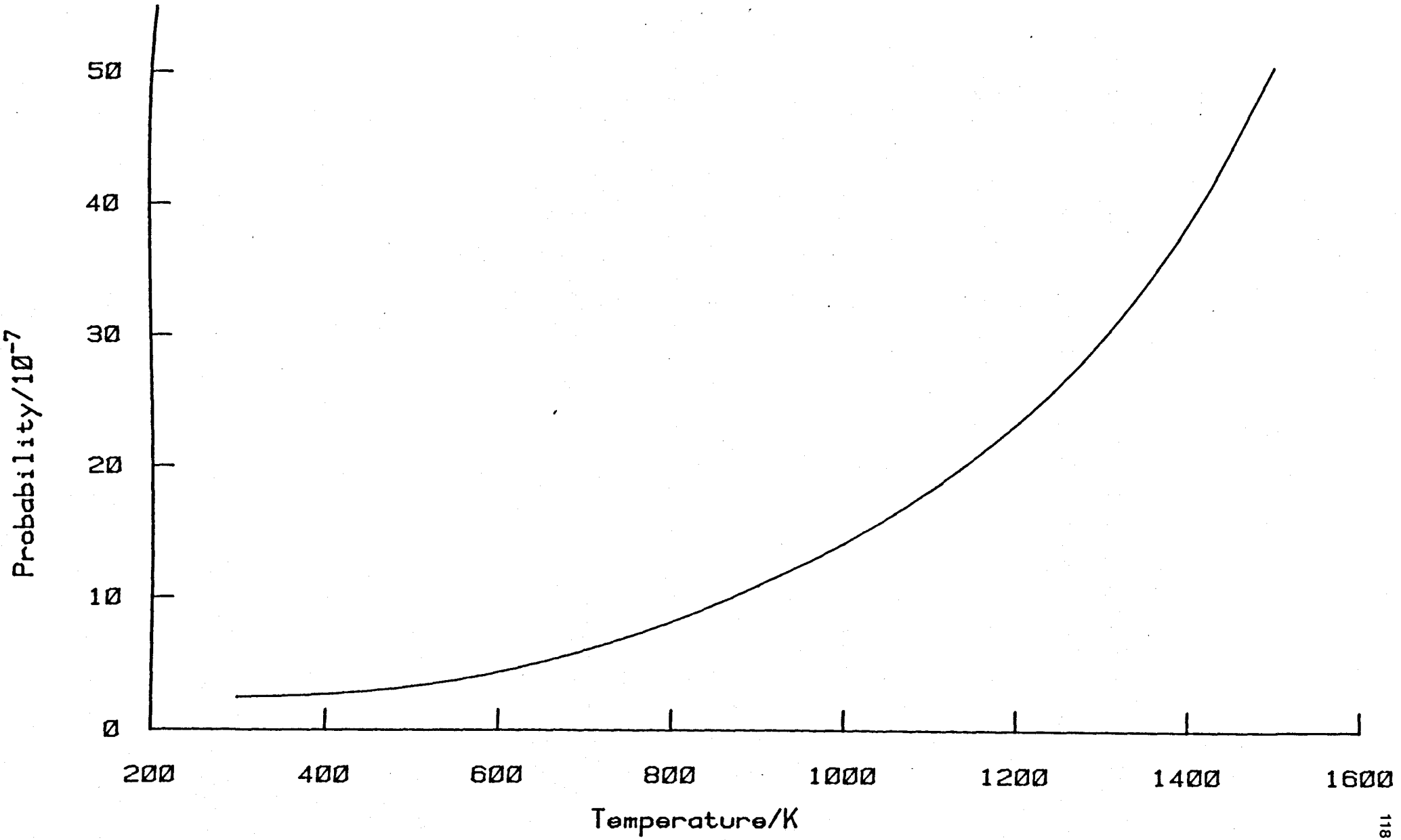

emission intensity with temperature is possible, as the strength of collision increases. This could explain the enhancement of K with temperature (figure 4.3). However there is a problem with the theory in that it predicts that the transitions will vary in intensity with the single molecule Franck-Condon factors. This is not found to be the case.

The precise nature of the interaction that leads to the dimol emissions is uncertain. What is certain is that the emissions do not display the temperature dependence expected of a chemical reaction, an Arrhenius type. They also display a different temperature dependence and probability to that of the energy pooling reaction which suggests different mechanisms. The observed high temperature behaviour is that expected of a pure collisional reaction but beyond this there is little temperature dependence. In this the dimol emissions behave as single transitions.

4.3. Studies of the Sigma Emission

By comparing the intensities of the sigma emission at 762 nm and the dimol emission at 634 nm an estimate of the proportion of sigma is the discharged gas can be made. This is done both at low and high temperatures.

4.3.1. Experimental

The experimental procedure was the same as that for the study of the dimol emissions. One photomultiplier being used to monitor the emission at 762 nm and the corrected intensity compared to that recorded by the other at 634 nm. Firstly the proportion of the 762 nm band that is transmitted by the 762A filter has to be determined.

There is rotational structure associated with the 762 nm band. There are P and R branches degraded towards the red with the Q branch missing as would be expected for a Σ-Σ transition of a diatomic molecule. The maximum in intensity lies in the R branch, between the band head at 759·3 nm and the band origin. Using the published spectrum of Khan and Kasha[70] the proportion of the band transmitted by the three filters was calculated, see figure 4.10. The filter transmittance is broad compared to the band envelope and was found to transmit 40 ± 5% of the incident intensity.

The quantum efficiencies of the 9658B photomultiplier at 762 nm and 634 nm are 5% and 11.2% respectively.[61]

Figure 4.10 Overlap of 762nm Band and Filter

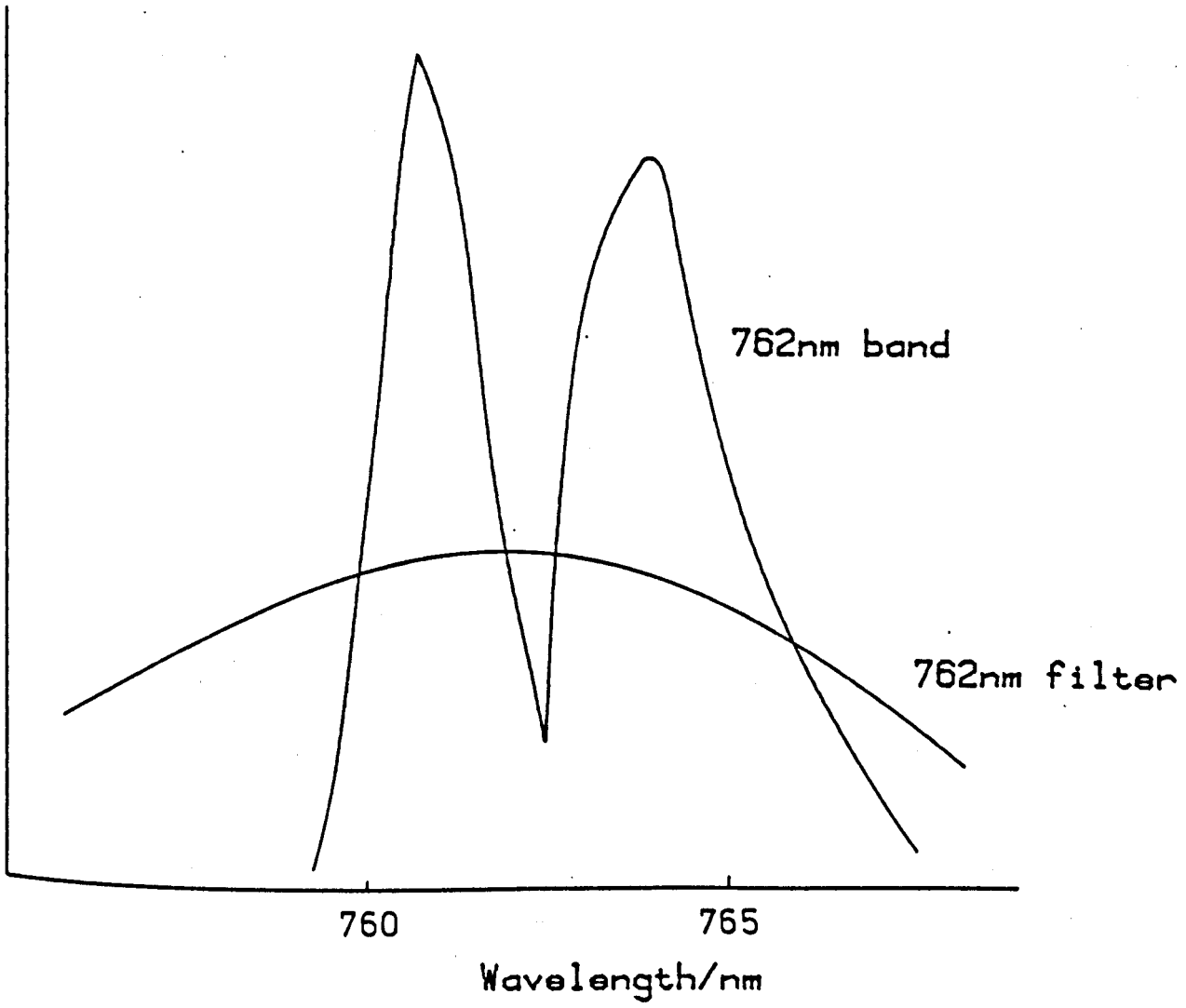

4.3.2. Results

The intensity ratio of the 762 nm and 634 nm transitions, measured by the same photomultiplier is given by

$$\frac{I^{762}}{I^{634}} = \frac{f^{762} p^{762} [\Sigma] k^{762}}{f^{634} p^{634} [\Delta]^2 k^{634}} \qquad (4.20)$$

where the symbols have their usual meaning. At room temperature the radiative rate constants are[44]

$$k^{762} = 0.077 \ s^{-1}$$

$$k^{634} = 0.016 \ \ell \ mol^{-1} \ s^{-1}$$

The filter and photomultiplier quantum efficiency factors are also known. Hence using the intensities (corrected for delta concentration) it is possible to calculate the ratio of sigma to delta in the flow, if the proportion of delta is known.

Many studies[78,79,80] have shown that the delta concentration in discharged oxygen is about 10% of the total flow. Using this value the percentage of delta in the flow at the observation station can be estimated, knowing the decay of delta and the distance from the discharge (170 cm).

A typical decay constant for the dimol emission at 634 nm is 0.008 cm^{-1}

$$\alpha^{634} = -0.008 \ cm^{-1} = \frac{\ln \frac{I_o}{I}}{170}$$

where I_o is the intensity and I is that at the discharge. Inserting a typical value for I_o(25 mV) the glow at the discharge can be found.

Table 4.4

Relative Intensity of 762nm emission at Room Temperature

Filter	Intensity /mV	Ratio	Corrected Ratio	$[\Sigma]/[\Delta]$ /%
762A	895	183	521	0.12
634A	4.9			
762A	869	140	398	0.09
634A	6.2			
762A	857	179	509	0.11
634A	4.8			
762A	1068	178	506	0.11
634A	6.0			
762A	1074	199	566	0.13
634A	5.4			
762A	5020	192	546	0.12
634A	26.2			
762A	4540	223	500	0.11
634A	20.4			
762A	959	196	558	0.12
634A	4.9			
762A	890	182	518	0.12
634A	4.9			
762A	527	108	307	0.07
634A	4.9			

At the discharge

$$I = c(0.1)^2 \qquad (4.21)$$

where c is a constant.

Equation (4.21) also holds at any point in the tube and so the proportion of delta at the observation station, corresponding with 10% at the discharge can be found. The proportion calculated is 5%.

Using this value of 5% as the percentage of delta in the flow at the observation station (4.20) can be used to calculate the proportion of sigma to delta. Table 4.4 lists the measured intensity ratios and the calculated percentages of sigma.

The mean of these values is 0.1% which is in reasonable agreement with the only other estimate, that of Wayne et al[80] who found sigma to be 0.2% of the delta concentration. This level of agreement is quite acceptable considering the nature of the calculation. The proportion of sigma can be doubled by assuming only 5% of delta in the flow at the discharge.

Similar calculations on the porportion of sigma in the discharged gas can be done at the shock temperature. Three shocks into pure oxygen were performed to yield the emission intensity ratios at 1430 K. They are listed in Appendix 4. The post-shock glow at 762 nm was obtained using

$$I^{762}_{(t=o)} = K^{762}\, I_1^{762}\, \rho_{21}$$

where I_1^{762} is the pre-shock glow

K^{762} is the enhancement factor for the 762 emission

The 762 nm emission, being a single molecule transition, would not be expected to show a temperature dependence. Consequently the room temperature rate constant was used. A rate constant for the emission

at 634 nm was obtained from (4.6).

$$k_2^{634} = K^{634} \cdot k_1^{634} \left(\frac{T_2}{T_1}\right)^{\frac{1}{2}} \qquad (4.6)$$

using the value of K^{634} at 1430 K taken from figure 4.3. The calculated value is 0.044 ℓ mol^{-1} s^{-1}.

Using (4.20) the proportion of sigma in the flow was calculated, the results are listed in Table 4.5. They are found to be in agreement with those obtained at room temperature, confirming that sigma is formed from delta present in the flow at both temperatures.

The emission intensity ratios and percentages calculated in this section cannot be very precise. The assumptions made about the concentration of delta and it's decay prevent this. The concentration of sigma in the flow is very sensitive to the presence of oxygen atoms and to all estimates depend on the removal of atoms and the establishment of a steady state. Wayne et al[80] used silver wire to remove oxygen atoms in contrast to the more common mercury system used here. Both groups find a similar proportion of sigma in the flow which suggests both methods are satisfactory.

Table 4.5

Relative Intensity of 762nm emission at Shock Temperature

No.	Filter	Pre-Shock Glow /mV	ρ_{21}	T_{21}	Ratio K	Corr AFGL	Shock Temp. Ratio	Corr Ratio	$\frac{[\Sigma]}{[\Delta]}$ /%
8	634C	26.0	5.891	4.798	1.26				
8A	762A	866.5	5.891	4.798	1.28	6707	20.7	58.9	0.2
9	634C	26.7	5.823	4.789	1.29				
9A	634A	4.9	5.823	4.789	0.89	324			
11	634C	42.7	5.834	4.851	1.28				
11A	762A	663.5	5.834	4.851	1.35	3260	10.1	28.6	0.1

Chapter 5

STUDIES OF THE VIBRATIONAL RELAXATION OF $O_2(^1\Delta_g)$

5.1. Introduction

As described in the previous chapter the dimol emission at 579 nm is observable in our apparatus

$$O_2(^1\Delta_g)v=1 + O_2(^1\Delta_g) \rightarrow O_2(^3\Sigma_g^-) + O_2(^3\Sigma_g^-) + h\nu(\lambda = 579\ nm)$$

While the vibrational relaxation of ground state oxygen is well characterised[12] there have only been two studies of the excited states; both Parker and Ritke[40] and Collins and Husain[81] observing the relaxation of delta in its first vibrational level. Both studies were at room temperature and the two groups came to conflicting conclusions concerning V-V exchange with the ground state.

The work described in this chapter is a study of $O_2(^1\Delta_g)v=1$ using the 579 nm emission at both high and low temperatures.

5.2. Room Temperature Studies

It was shown in Chapter 3 that a measurement of the decrease of the emission intensity at 634 nm down the tube allowed the room temperature wall and collisonal quenching rate constants for $O_2(^1\Delta_g)v=0$ to be determined. By a comparison of the pre-shock decays at 579 nm and 634 nm the collisional quenching rate constant for the v=1 level was obtained.

5.2.1. Experimental

In the standard procedure for determining the pre-shock decay intensity measurements are taken at 10 cm intervals over a distance of 2.5 m. However because of the lower glow at 579 nm about 10% of that at 634 nm, the experimental technique was modified. Intensity measurements were taken at only two points which were sufficiently near the discharge for the 579 nm emission to be measured accurately yet far enough apart for a decay to be estimated. Two series of experiments were performed, the observation points being either 90 or 50 cms apart.

The aim was to obtain comparable decays for the 634 nm and 579 nm emissions. The experimental procedure was as follows. The shock tube was thoroughly cleaned. The oxygen was allowed to flow, the pressure adjusted and the discharge and photomultiplier switched on; the system was then allowed to come to a steady state. With the photomultiplier at one observation point an intensity reading at one wavelength was taken. Without moving the photomultiplier the filter was changed and an intensity reading at the other wavelength taken. The photomultiplier was then moved to the other observation point and another reading taken, the filter was changed and a final reading taken. In this way two directly comparable decays were obtained and errors due

to the positioning of the photomultiplier were minimized. The pressure was then changed and the system again allowed to settle before another experiment was performed.

After a series of experiments at various pressures zero readings, that is a measure of the stray light intensity at each observation point and wavelength were taken. Ideally a zero would be a measure of the intensity with no excited oxygen present but with the discharge on, as the discharge is the main source of stray light. However a zero obtained with no oxygen flowing but the discharge on is erroneously high because of the brightness of the discharge. Consequently the zeros were obtained with the oxygen flowing but being pumped away before it entered the shock tube. It is essential that the zero be measured as accurately as possible because it becomes comparable with the 579 nm intensity at higher pressures (about 10 mV at 12 torr) and so has a marked effect on the calculated decay (see later).

5.2.2. Results

In a series of 17 comparable experiments at pressures between 4.5 and 12 torr (temperature 295 ± 1 K) the decay of the 579 nm emission with distance, α^{579} and that of the 634 nm emission α^{634} were obtained (see Table 5.1). The ratio of the two decays was found to be

$$\frac{\alpha^{579}}{\alpha^{634}} = 0.93 \pm 0.2 \qquad (5.1)$$

where the error represents the 95% confidence limit.

Table 5.1

Comparison of Observed Decays Down Tube

Pressure /torr	Delta Decay $/m^{-1}$	Delta* Decay $/m^{-1}$	Ratio Delta*/Delta
4.10	0.970	0.941	0.97
4.57	0.570	0.667	1.17
5.10	0.472	0.406	0.86
5.27	0.502	0.411	0.82
5.73	0.736	0.676	0.92
5.82	0.727	0.671	0.92
6.15	0.662	0.598	0.90
6.65	0.640	0.496	0.78
6.76	0.888	0.849	0.96
7.62	1.320	1.100	0.83
7.66	1.016	0.941	0.93
7.66	1.008	0.957	0.95
7.78	1.050	1.183	1.13
7.85	0.804	0.772	0.96
8.70	0.830	0.726	0.87
9.80	1.116	1.050	0.94
12.00	1.354	1.245	0.92

5.2.3. Discussion

The deactivation processes for the v=0 state are

$$O_2(^1\Delta_g)v=0 + O_2 \rightarrow O_2(^3\Sigma_g^-) + O_2 \; ; \; k_1$$

$$O_2(^1\Delta_g)v=0 \xrightarrow{\text{wall}} O_2(^3\Sigma_g^-) \; ; \; k_2$$

Hence

$$\frac{d[\Delta^o]}{dt} = -(k_1[O_2] + k_2)[\Delta^o]$$

$$\ln \frac{[\Delta^o]}{[\Delta^o]_o} = -kt$$

where $k = (k_1[O_2] + k_2)$

It was shown in Chapter 3 that

$$\frac{\alpha^{634}v}{2} = k$$

where v is gas flow velocity.

The deactivation processes for the v=1 state are

$$O_2(^1\Delta_g)v=1 + O_2 \rightarrow O_2(^3\Sigma_g^-) + O_2 \; ; \; k_3$$

$$O_2(^1\Delta_g)v=1 \xrightarrow{\text{wall}} O_2(^3\Sigma_g^-) \; ; \; k_4$$

$$O_2(^1\Delta_g)v=1 + O_2 \rightarrow O_2(^1\Sigma_g)v=0 + O_2 \; ; \; k_5$$

A further probable reaction is intersystem crossing

$$O_2(^1\Delta_g)v=1 + O_2 \rightarrow O_2(^3\Sigma_g^-)v=0 + O_2(^3\Sigma_g^-)v=n \qquad (5.2)$$

which could also occur for the delta v=0 state

$$O_2(^1\Delta_g)v=0 + O_2 \rightarrow O_2(^3\Sigma_g^-)v=0 + O_2(^3\Sigma_g^-)v=m \qquad (5.3)$$

In their study Parker and Ritke[40] used a laser spectrophone to follow the deactivation of delta v=1. They were, by addition of efficient vibrational quenchers (e.g. helium) and observation of the effect on the signal, to deduce which partner was vibrationally excited. They found no evidence for reactions (5.2) or (5.3) occurring. Therefore

$$\frac{d[\Delta^1]}{dt} = -(k_3[O_2] + k_4 + k_5[O_2])[\Delta^1]$$

$$\ln\frac{[\Delta^1]}{[\Delta^1]_o} = -Kt$$

where $K = (k_3[O_2] + k_4 + k_5[O_2])$

Analagously to (3.4) the decay of the 579 nm emission down the tube α^{579} can be related to the first order decays of delta v=0 and 1.

$$\ln\frac{I^{579}}{I_o^{579}} = \alpha^{579}\ell = \ln\frac{[\Delta^o]\,[\Delta^1]}{[\Delta^o]_o[\Delta^1]_o} = \ln\frac{[\Delta^o]}{[\Delta^o]_o} + \ln\frac{[\Delta^1]}{[\Delta^1]_o}$$

Therefore

$$\alpha^{579} = \frac{K}{y} + \frac{k}{y}$$

It is found experimentally that

$$\frac{\alpha^{579}}{\alpha^{634}} = 0.93$$

Therefore substituting the terms and eliminating the gas flow velocity

$$\left(k_3 + \frac{k_4}{[O_2]} + k_5\right) + \left(k_1 + \frac{k_2}{[O_2]}\right) = 0.93\left(2k_1 + \frac{2k_2}{[O_2]}\right) \quad (5.4)$$

It is a reasonable assumption that the wall reaction occurs at the same rate for the two vibrational levels[21] i.e. $k_2 = k_4 = 0.11\ s^{-1}$. The collisional quenching rate constant has been measured by Borrell et al;[21] $k_1 = 9.4 \times 10^2\ \ell\ mol^{-1}\ s^{-1}$. Parker and Ritke[40] obtained a value for the vibrational relaxation rate constant (k_5) of $6.9 \times 10^2\ \ell\ mol^{-1}\ s^{-1}$. Therefore using (5.4) a value for k_3 can be obtained. At a typical pressure of 6.5 torr

$$k_3 = 7.4 \times 10^1\ \ell\ mol^{-1}\ s^{-1}$$

Hence

$$\frac{k_3}{k_1} = 0.08$$

The large error limits in the ratio (5.1) mean that the error in k_3 is correspondingly large. The lower limit is zero, meaning that no delta v=1 is quenched directly to the ground state; the upper limit is about $5.6 \times 10^2\ \ell\ mol^{-1}\ s^{-1}$. These large errors arise because of the low level of emission at 579 nm and the difficulty of measuring accurately the zero level. Most of the measured ratios in (5.1) were less than one. A small change in the zero of ± 0.1 mV could make a large difference, raising the ratio to 1.3 and thus making k_3 comparable with k_1. However the large number of experiments performed give us confidence in the result quoted in (5.1).

Also Parker and Ritke[40] have previously studied this system and obtained

$$\frac{k_3}{k_1} = 0.09$$

a result in very good agreement with ours. They do not give an error in their result but quote their rate constants to three decimal places.

This is certainly optimistic. A more reasonable estimate of the error would be ± 10% at least.

What is observed in our experiments is the rate of cooling of the zeroth and first vibrational levels of delta by measuring the 579 nm and 634 nm intensities at two points in the tube. These decays are then compared to yield the ratio in (5.1). This ratio is then used, together with the rate constants for the reactions causing the removal of the two levels, to allow the rate constant for the collisional quenching of the v=1 level to be calculated. Using their laser spectrophone Parker and Rîtke[40] were able to conclude that the vibration--vibration (V-V) process (5.5) is very slow

$$O_2(^1\Delta_g)v=1 + O_2(^3\Sigma_g^-) \rightarrow O_2(^1\Delta_g) + O_2(^3\Sigma_g^-)v=1 \qquad (5.5)$$

Our results do not allow us to confirm or refute this.

If reaction (5.5) occurred then the vibrational relaxation reaction occurring would be

$$O_2(^3\Sigma_g^-)v=1 + O_2 \rightarrow O_2(^3\Sigma_g^-)v=o + O_2 \; ; \; k_6$$

The rate constant for this reaction has been found to be very similar to that for the delta v=1 level,[40] $k_6 = 7.5 \times 10^2$ ℓ mol^{-1} s^{-1}. Using this value in (5.4) would yield a value for k_3 of 1.5×10^1 ℓ mol^{-1} s^{-1}. Thus, given the accuracy of our estimate of the ratio (5.1), we are unable to say whether V-V exchange is occurring or not.

The conclusion to be drawn from this part of the work is that the rate constant for the collisional quenching of delta v=1 is small compared to those for vibrational relaxation and quenching of v=o. The value we obtain is 7.4×10^1 ℓ mol^{-1} s^{-1}. The results do not allow us to say if V-V exchange is occurring.

5.3. High Temperature Studies

5.3.1. Introduction

As mentioned in Chapter 4 the appearance of the 579 nm emission trace is different to those of the other dimol emissions studied. There is a measurable glow at room temperature and so at the shock front there is a rapid increase due to the increased density and temperature of the shocked gas. It is found to be that which would occur for a dimol emission and is given by

$$I_2^{579}(t=o) = I_1^{579} \rho_{21}^{2} T_{21}^{\frac{1}{2}} \qquad (5.6)$$

This confirms the bimolecular nature of the emission process. After this there is a gradual increase to an enhanced level of emission. The traces at 634 nm and 703 nm do not show this (see figure 4.1). The ratio of the enhanced emission level to that predicted by (5.6) rises from 3 at 1000 K to 6 at 1850 K. Following the enhancement there is a decay.

In this section the enhancement observed on the traces is shown to be due to vibrational relaxation. The analysis of the 579 nm traces is developed and vibrational relaxation times obtained.

5.3.2. Experimental

A series of shock experiments in 100% oxygen were carried out between 1000 and 1850 K. During each shock the emission was monitored at two wavelengths, 634 nm and 579 nm. The results of the analysis at 634 nm were reported in the previous chapter, the enhancement factors being plotted against temperature in figure 4.3. The 579 nm traces were analysed by interactive computer graphics using the model developed in the next section.

5.3.3. The Theory of the Analysis of the 579 nm Shock Traces

In the two state model the molecule has only two vibrational levels, the ground and the first and so the relaxation process is

$$O_2 + O_2(^1\Delta_g)v=o \underset{k'_{10}}{\overset{k'_{01}}{\rightleftharpoons}} O_2 + O_2(^1\Delta_g)v=1$$

Hence

$$\frac{d[\Delta^1]}{dt} = k'_{01}[\Delta^o][O_2] - k'_{10}[O_2][\Delta^1]$$

$$\frac{d[\Delta^1]}{dt} = k_{01}[\Delta^o] - k_{10}[\Delta^1]$$

where $k_{01} = k'_{01}[O_2]$

$k_{10} = k'_{10}[O_2]$

$$\frac{d[\Delta^1]}{dt} = k_{01}([\Delta] - [\Delta^1]) - k_{10}[\Delta^1]$$

where $[\Delta]$ = total delta concentration

$$\frac{d[\Delta^1]}{dt} = k_{01}[\Delta] - (k_{01} + k_{10})[\Delta^1]$$

After integrating and re-arranging one obtains

$$\frac{[\Delta^1]_t}{[\Delta^1]_o} = K + (1-K)(\exp - t/\tau) \qquad (5.7)$$

where $K = \dfrac{[\Delta^1]_\infty}{[\Delta^1]_o}$

and $\tau = (k_{10} + k_{01})^{-1}$

$[\Delta^1]_o$ is the immediate post-shock concentration of delta v=1 and $[\Delta^1]_t$ is that after time t.(5.7) has exactly the same form as (3.22) for the analysis of sigma emission. The dimol emission at 579 nm is being monitored.

Hence

$$I^{579} = k^{579} [\Delta^o][\Delta^1] \tag{5.8}$$

continuing (5.7) and (5.8)

$$\frac{I_t^{579}}{I_o^{579}} = (K + (1-K)\exp(-t/\tau))\frac{[\Delta^o]_t}{[\Delta^o]_o} \tag{5.9}$$

where I_o^{579} is the immediate post shock emission and I_t^{579} is that after time t. As the emission is from a dimol

$$I_o^{579} = I_1^{579} \rho_{21}^2 T_{21}^{\frac{1}{2}}$$

where I_1^{579} is the pre-shock emission. The final term in (5.9) describes the post-shock change in concentration of ground state delta. After relaxation the concentrations of delta v=o and 1 are at a steady state and so the post-shock decay of delta v=1 will mirror that of delta v=o.

The full expression is therefore

$$\frac{I_t^{579}}{I_1^{579} \rho_{21} T_{21}^{\frac{1}{2}}} = \{K + (1-K)\exp(-t/\tau)\}\exp(\alpha_t t_p) \tag{5.10}$$

This equation can be seen to have the same form as (3.24) for the 762 nm emission, however in this case a dimol emission is being monitored. The shock trace is predicted to show four zones:

1. The steady pre-shock glow from the cool flowing gas.
2. The rapid rise at the shock front due to shock compression and heating.
3. The relaxation to the new vibrational equilibrium population at the high temperature.
4. The decay due to the fall in excited state concentration down the tube.

These predictions can be seen to be borne out by the observed post-shock behaviour, (figure 4.1c). After the introduction of the integration time (5.10) is fitted by interactive computer graphics to the trace. The fitted parameters are the integration time, the relaxation zone, the enhancement factor K^{579} and the decay.

5.3.4. Results

5.3.4.1. The Equilibrium Emission at 579 nm

If the relaxation zone observed on the 579 nm traces is due to vibrational relaxation then the peak concentration reached should be that predicted by the Boltzmann equation.

At equilibrium, after relaxation

$$I_{\infty}^{579} = K^{634} k^{579} T_2^{\frac{1}{2}} [\Delta^o]_{\infty} [\Delta^1]_{\infty} \qquad (5.11)$$

where k^{579} is the temperature independent term in the rate constant. This analysis assumes that there is the same enhancement in the 579 nm with temperature as in the 634 nm emission; this was found to be true in the case of the 703 nm emission.

From the Boltzmann equation (4.11)

$$[\Delta^1]_{\infty} = [\Delta] \exp(-\epsilon_1/kT)/q \qquad (5.12)$$

$$[\Delta^o]_{\infty} = [\Delta] \exp(-\epsilon_o/kT)/q \qquad (5.13)$$

where [Δ] is the total concentration of delta.

Therefore combining (5.11), (5.12) and (5.13)

$$I_{\infty}^{579} = K^{634}\, k^{579}\, T_2^{\frac{1}{2}}\, [\Delta]^2 \exp(-(\varepsilon_o + \varepsilon_1)/kT)/q^2$$

Now

$$I_{\infty}^{579} = K^{579}\, I_1^{579}\, \rho_{21}^{\ 2}\, T_{21}^{\frac{1}{2}}$$

The total post-shock concentration of delta is given by

$$[\Delta]_2^{\ 2} = [\Delta]_1^{\ 2} \rho_{21}^{\ 2}$$

Hence

$$\frac{K^{579}\, I_1^{579}}{K^{634}\, [\Delta]_1^{\ 2}\, T_1^{\frac{1}{2}}} = k^{579} \exp(-(\varepsilon_o + \varepsilon_1)/kT)/q^2 \qquad (5.14)$$

Now

$$I_1^{634} = k^{634}\, [\Delta]_1^{\ 2}\, T_1^{\frac{1}{2}} \qquad (5.15)$$

as most of the delta molecules are in the ground vibrational level at room temperature.

Hence combining (5.14) and (5.15)

$$\frac{K^{579}\, I_1^{579}}{K^{634}\, I_1^{634}} = \frac{k^{579}}{k^{634}} \exp(-(\varepsilon_o + \varepsilon_1)/kT)/q^2$$

Eliminating the zero-point energy

$$\frac{K^{579}\, I_1^{579}}{K^{634}\, I_1^{634}} = \frac{k^{579}}{k^{634}} \exp(-h\nu/kT)(1-\exp(-h\nu/kT)^2 \qquad (5.16)$$

The left hand side of (5.16) consists of measured quantities and the exponential terms can be calculated. If vibrational relaxation is being observed a plot of the experimentally measured quantities against the

Figure 5.1 Plot of Equation (5.16)

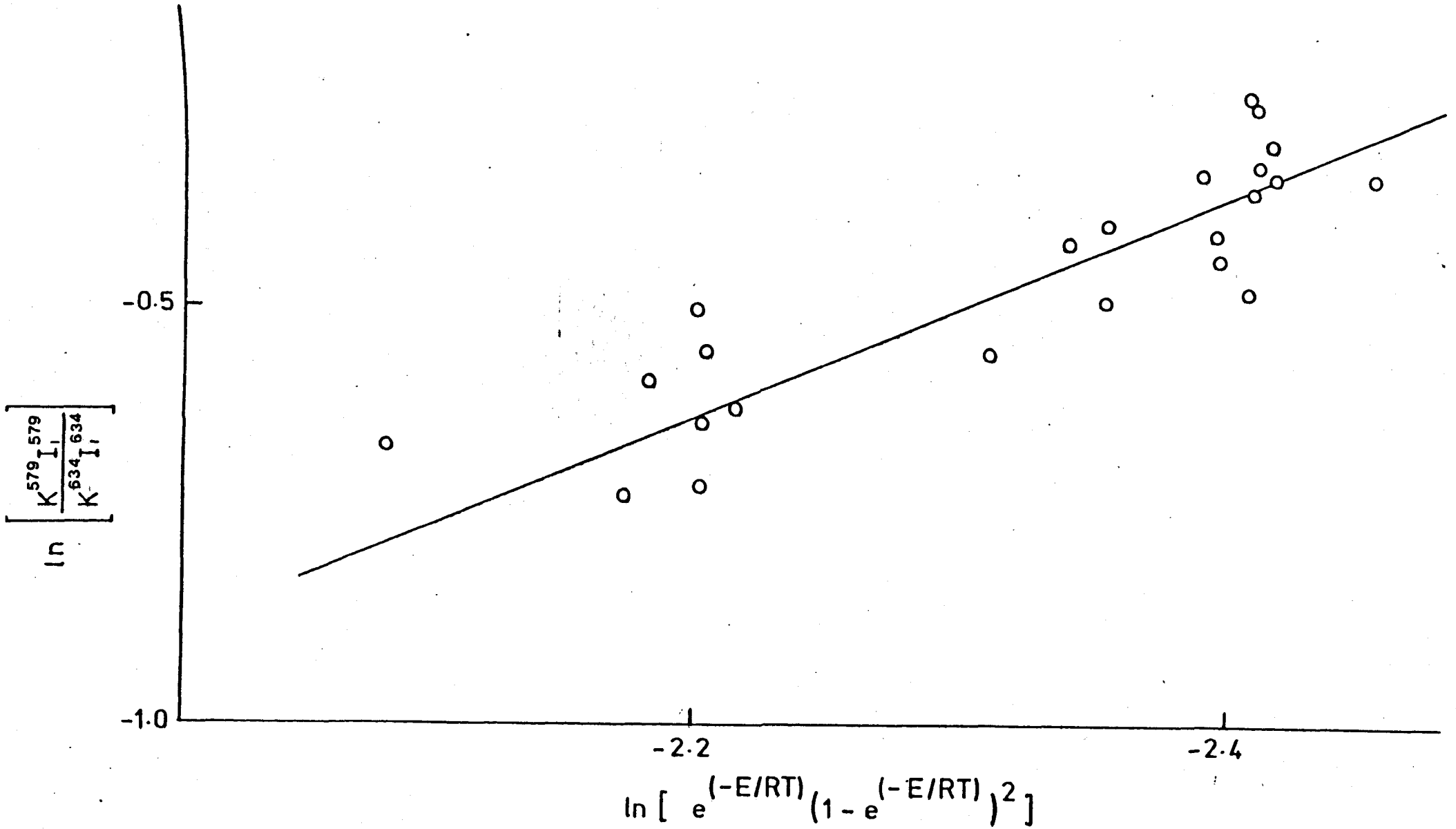

temperature dependent terms should be linear. Such a plot is shown in figure 5.1.

The linearity of the plot shows that the Boltzmann equilibrium over the vibrational levels is achieved after the relaxation zone and so the relaxation times measured are characteristic of vibrational relaxation.

This result, together with the observations of the shock trace made in chapter 4 confirm the attribution of the 579 nm emission from discharged oxygen (4.3).

$$O_2(^1\Delta_g)v=1 + O_2(^1\Delta_g) \rightarrow O_2(^3\Sigma_g^-) + O_2(^3\Sigma_g^-) + h\nu(\lambda = 579\ nm) \quad (4.3)$$

The high temperature behaviour of the emission trace is consistent with it being a dimol emission of singlet delta with one partner vibrationally excited. Hence measurement of the relaxation constant would allow vibrational relaxation to be followed.

5.3.4.2. The Vibrational Relaxation Times

Vibrational relaxation is a bimolecular process, the relaxation time is therefore pressure dependent. The relaxation time referred to standard pressure is called the Napier Time. Table 5.2 lists the results of 32 shocks into pure oxygen, the Napier times being calculated from the relaxation constants obtained by fitting the relaxation zone. The run parameters and results of the graphical analysis are listed in Appendix 5. All the runs were analysed using the 4130 version of GRAPH which operated in particle time, consequently the Napier times were obtained using

$$\text{Napier time/atm s} = \tau \rho_{A1} \frac{P_1}{760}$$

Table 5.2

Napier Times

No.	P_{A1}	τ /atm us	T_A /K
C54	28.72	18.46	1685
C57	28.12	13.10	1656
C58	27.49	11.42	1625
C59	27.95	13.30	1647
C60	20.49	28.66	1282
C61	27.25	10.80	1613
C62	26.66	10.57	1585
C63	25.24	15.48	1515
C64	23.60	12.38	1435
C65	25.24	10.36	1515
C67	24.68	13.48	1488
C68	25.44	14.06	1525
C69	28.94	6.31	1696
C70	28.02	11.00	1651
C71	28.94	13.00	1696
C72	32.01	6.00	1846
C73	28.58	9.88	1678
C94	20.04	19.36	1260
C95	20.58	39.47	1287
C96	20.19	15.29	1268
930A	20.43	28.53	1279
931A	27.39	10.49	1620
934A	20.46	28.64	1281
935A	20.46	21.71	1281
936A	28.23	13.64	1661
938A	19.80	21.35	1249
939A	17.98	36.29	1160
940A	16.30	64.47	1078
941A	20.79	22.06	1297
Runs C74-945A:100% O_2,Discharge Power 80 W			
C74	21.68	15.22	1308
C75	20.97	17.99	1290
943A	26.87	19.40	1595
945A	23.34	10.00	1422
Runs 958A-959A:25% O_2added after Discharge			
958A	27.77	10.58	1639
959A	26.94	11.49	1598

where τ is the relaxation constant

ρ_{Al} is the frozen density ratio

P_1 is the initial pressure in torr

A Landau-Teller plot, the logarithm of the Napier time versus $T_A^{-1/3}$ is shown in figure 5.2. The full line is that predicted using (5.17) which is the best line for ground state oxygen.[12]

$$\log_{10}\tau/\text{atm s} = 54.7T^{-1/3} - 9.535 \qquad (5.17)$$

The dashed line is that obtained by a least squares analysis of the 100% discharged oxygen, 100 W experimental points.

$$\log_{10}\tau/\text{atm s} = 56.45T^{-1/3} - 9.8 \qquad (5.18)$$

Some experiments were carried out on mixtures containing a reduced proportion of delta. This was achieved by using a discharge power of 80 W or by discharging only 75% of the total gas flow. The results are also plotted in figure 5.2. These experiments were inconclusive, no change in relaxation time being observed. However the scatter in the experimental points is such that any deviation is probably masked (see Discussion).

As can be seen from figure 5.2 the least squares line through the experimental points lies below that for ground state oxygen, for a sample of 10 points around 1270 K a mean and a standard deviation can be calculated. Student's t test[57] indicates whether the mean of this sample is significantly different from the mean of the parent group, in this case taken to be the ground state oxygen value at 1270 K found using (5.17).

Figure 5.2 Landau-Teller Plot

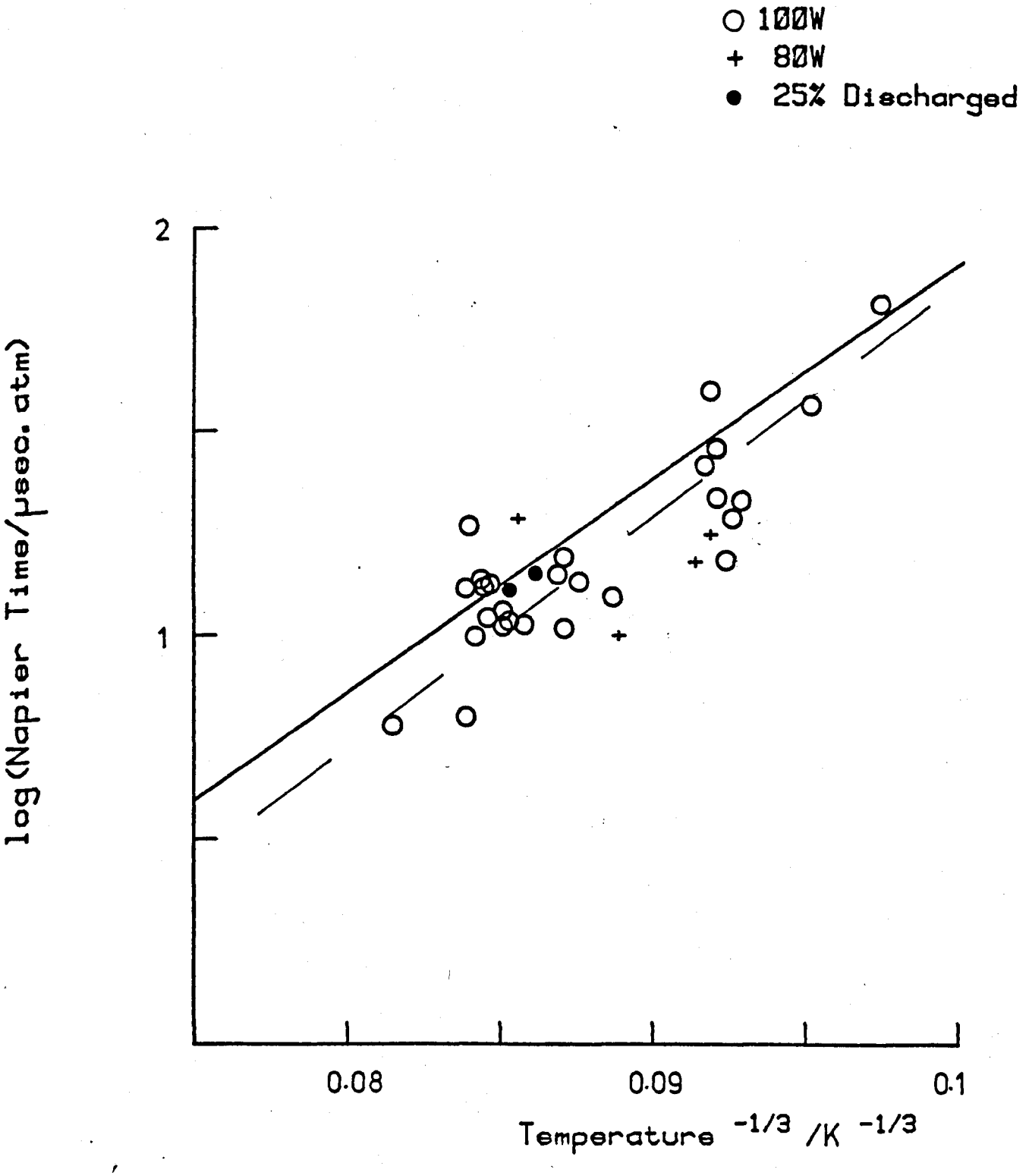

$$\text{Student's } t = \frac{\sqrt{n}(X - x)}{\sigma}$$

where n = number of points in sample

x = mean of sample

σ = standard deviation of sample

X = mean of parent group

This test indicates that the difference seen in figure 5.2 between the ground state oxygen line and the experimental points is highly significant (the probability of it occurring by chance < 0.01).

5.3.5. Discussion

The phenomenon of vibrational relaxation behind a shock front can be described as follows. Before the shock arrives the three degrees of freedom of the gas translational, rotational and vibrational are in equilibrium. They have the same temperature. After the passage of the shock front the translational and rotational temperatures increase rapidly. Vibrational relaxation is the return of the vibrational degree of freedom to equilibrium with the other two. In this case what is monitored is the increase in $O_2(^1\Delta_g)v=1$ concentration to the equilibrium value at the high temperature - the Boltzmann population. However this vibrational relaxation is occurring in a bath of ground state oxygen molecules which are also undergoing vibrational relaxation. In a shock experiment one would not in general expect to observe the relaxation of one component separately. However the experimental points are seen to fall below the line for the relaxation of the bulk gas. This deviation has been shown to be significant i.e. vibrational relaxation is occurring slightly faster in our system than for ground state oxygen. The possible causes of this effect will now be discussed.

The presence of impurities can cause an acceleration in the rate of vibrational relaxation, water in particular is a troublesome impurity in this context. Water has a bending mode (ω = 1596 cm^{-1}) which is very nearly in resonance with oxygen (ω = 1556 cm^{-1}) and so vibration-vibration transfer (V-V) would be expected to be rapid. The theory of relaxation in a mixture of two relaxing gases has been developed by Bauer and Schotter[82,83] and the effect of water will be discussed after in a description of their approach.

5.3.5.1. Bauer and Schotter Theory of Coupled Vibrational Relaxation

The following scheme lists the five interactions possible between two relaxing gases A and B.

1. $A^* + A \rightleftharpoons A + A$ (V-T) ; k_1
2. $A^* + B \rightleftharpoons A + B$ (V-T) ; k_2
3. $A^* + B \rightleftharpoons A + B^*$ (V-V) ; k_3
4. $B^* + B \rightleftharpoons B + B$ (V-T) ; k_4
5. $B^* + A \rightleftharpoons B + A$ (V-T) ; k_5

Using this scheme the following equation is obtained

$$\left[\frac{1}{\tau} - (1 + (X_{A1}/X_{AO}))(k_1(1-X) + \left\{k_2 + \frac{k_3}{1+(X_{B1}/X_{BO})}\right\}X)\right]$$

$$\left[\frac{1}{\tau} - (1 + \frac{X_{B1}}{X_{BO}})\left\{(k_5 + \left\{\frac{k_3}{1 + (X_{A1}/X_{AO})}\right\})(1-X) + k_4X\right\}\right]$$

$$- k_3 k_{-3} (1-X)X = 0$$

where τ = observed relaxation time of mixture

X = mole fraction of component B

X_{AO}, X_{A1} = concentrations in zeroth and first level of A respectively

X_{BO}, X_{B1} = concentrations in zeroth and first level of B respectively

k_{-3} = rate constant for reverse of reaction 3 =

$$k_3 \left\{\frac{X_{A1}}{X_{AO}}\right\} \left\{\frac{X_{BO}}{X_{B1}}\right\}$$

This can be simplifed to

$$\left[\frac{1-X}{\tau_{AA}} + \frac{X}{\tau_{AB}} - \frac{1}{\tau}\right]\left[\frac{1-X}{\tau_{BA}} + \frac{X}{\tau_{BB}} - \frac{1}{\tau}\right] - k_3\, k_{-3}(1-X)X = 0 \quad (5.19)$$

where τ_{AA}, τ_{BB} = vibrational relaxation times for pure components

τ_{AB}, τ_{BA} = vibrational relaxation times for one molecule of A (or B) in pure B (or A).

When vibration-vibration transfer does not take place i.e. $k_3 = k_{-3} = 0$ (5.19) reduces to the equations describing parallel relaxation. This scheme is shown diagramatically in figure 5.3. Each component relaxes separately with a composition dependence given by (5.20) and (5.21).

$$\frac{1-X}{\tau_{AA}} + \frac{X}{\tau_{AB}} = \frac{1}{\tau} \quad (5.20)$$

$$\frac{1-X}{\tau_{BA}} + \frac{X}{\tau_{BB}} = \frac{1}{\tau} \quad (5.21)$$

Each relaxation time varies linearly with gas composition. If B were a non-relaxing gas e.g. a noble gas then the relaxation of A would also be described by (5.20).

If V-V transfer does take place then this picture will be altered. Figure 5.3 also illustrates the situation in which V-V transfer does occur. The vibrational populations of A and B are now coupled by the V-V exchange process 3. What occurs depends on the relative rates of

Figure 5.3

Schemes for the Vibrational Relaxation of a Binary Mixture

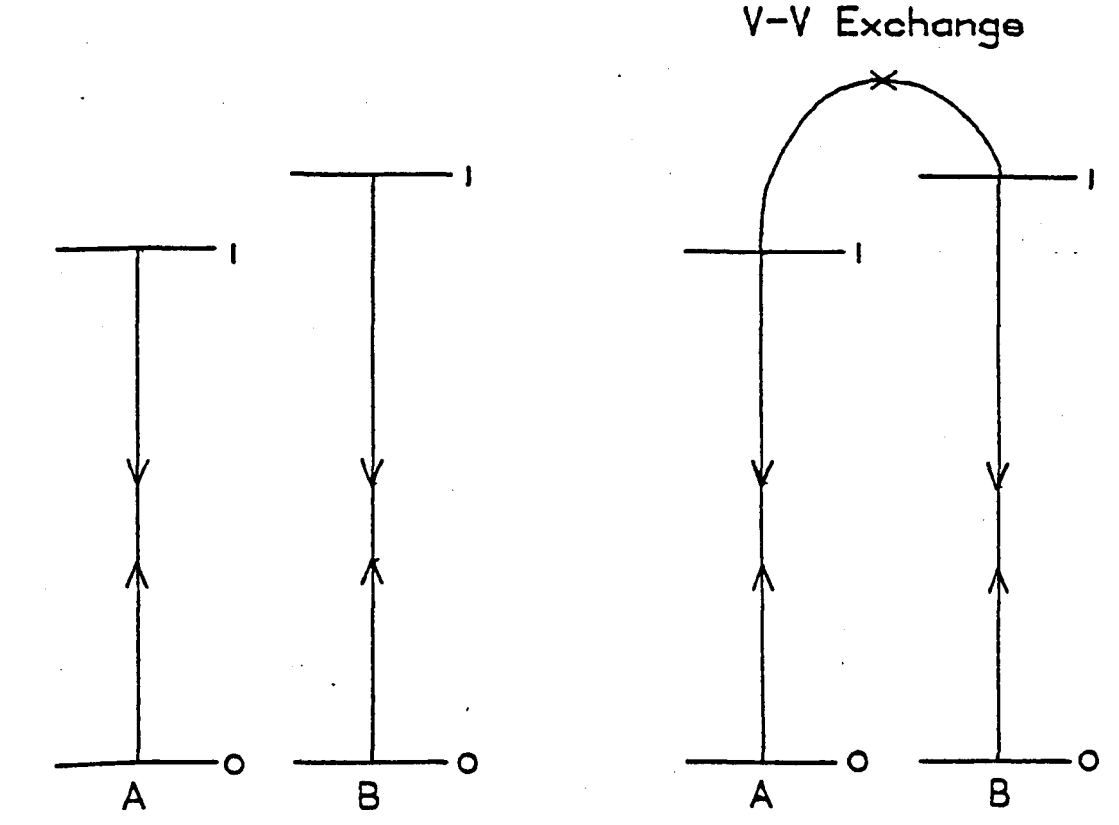

Parallel Relaxation

Coupled Relaxation

the V-V and various V-T transfer processes. For example if pure A relaxes slowly and pure B rapidly and if V-V exchange is rapid then a single relaxation time would be observed, that of B. In other cases a double relaxation may occur. Whether such processes are seen depends on the experimental technique and on the gases used.

For small mole fractions of additive B (5.19) can be expanded to give[83]

$$\frac{1}{\tau} = \frac{1}{\tau_{AA}} + w_1 X_B + w_2 X_B^2 + \ldots\ldots \qquad (5.22)$$

where $w_1 = (k_2 - k_1) + \left(\frac{k_3 k_5}{k_{-3} + k_5}\right)$

5.3.5.2. Effect of Impurities on Observed Vibrational Relaxation Time

It was mentioned in chapter 3 that from a measurement of the sigma quenching rate constant for oxygen it was deduced that 30 ppm water were present in the flowing gas. Using (5.22) the effect of this proportion of water on the observed vibrational relaxation time can be assessed.

The possible reactions are

1. $O_2^* + O_2 \rightleftharpoons O_2 + O_2$
2. $O_2^* + H_2O \rightleftharpoons O_2 + H_2O$
3. $O_2^* + H_2O \rightleftharpoons O_2 + H_2O^*$
4. $H_2O^* + H_2O \rightleftharpoons H_2O + H_2O$
5. $H_2O^* + O_2 \rightleftharpoons H_2O + O_2$

The rate constants for these reactions can be obtained from the reciprocals of the Napier times.

A Napier time for reaction 1, the vibrational relaxation of pure oxygen can be obtained from the literature,[12] τ = 86 atm μs at 1000 K.

Reaction 2 is the vibrational relaxation of oxygen on collison with water via a V-T mechanism. An estimate of the Napier time for this process can be obtained using the Millikan and White correlation.[84] This is an empirical equation (5.23) relating the relaxation time to the reduced mass of the collision partners μ and the characteristic temperature of the vibration.

$$\log_{10} \tau/\text{atm s} = 5 \times 10^{-4} \mu^{\frac{1}{2}} \theta^{4/3} (T^{-1/3} - 0.015\ \mu^{1/4}) - 8 \qquad (5.23)$$

where $$\mu = \frac{m_1\ m_2}{m_1 + m_2}$$

and $$\theta = \frac{hc\omega}{k}$$

(5.23) has been shown to hold for several diatomic molecules in collision with various partners.

In the case of the vibrational relaxation of oxygen a more accurate form of the correlation is

$$\log_{10} \tau/\text{atm s} = (4.78 \times 10^{-4}) \mu^{\frac{1}{2}} \theta^{4/3} (T^{-1/3} - 0.015\ \mu^{1/4}) - 8.0 \qquad (5.24)$$

This correlation gives the same relaxation times as the best fit equation (5.17). At 1000 K the vibrational relaxation time calculated using (5.24) for oxygen on collision with water is 25 atm μs.

An estimate of the vibrational relaxation time for water on collision with oxygen, reaction 5, can be made using (5.23); τ = 50 atm μs at 1000 K.

Before (5.22) can be used an estimate of the rate of V-V exchange between oxygen and water is needed. Lambert[9] quotes a collision probability Z_{vv} for V-V transfer between ground state oxygen and water of 80 at 300 K. This is related to the relaxation time by

$$\tau = \frac{Z_{vv}}{Z} \qquad (5.25)$$

where Z is the collision number. Assuming that the rate of V-V exchange does not change much with temperature (this is known to be the case for vibrational relaxation of water[9]) then an estimate of the rate of reaction 3 can be obtained from (5.25). Uzing $Z = 6ns^{-1}$ atm^{-1} at 300 K in (5.25) we obtain $\tau = 0.01$ atm μs.

If the difference between the vibrational spacings of oxygen and water is used to calculate a characteristic temperature then the general Millikan and White correlation (5.23) can also be used to estimate the rate constant for reaction 3. The relaxation time obtained in this way is also about 0.01 atm μs. This indicates that the Millikan and White correlation can be used to give reasonable estimates of V-V as well as V-T processes.

The relaxation times for the various reactions are listed in Table 5.3. Using the Bauer and Schotter equation it is now possible to estimate the effect of 30 ppm water on the observed relaxation time of oxygen. It is found that the decrease in vibrational relaxation time is negligible, less than 0.05% which is certainly not observable. It would take water concentrations of about 10% to account for the deviation observed in figure 5.2. The relaxation time in Table 5.3 are estimates. They can be changed considerably, by an order of magnitude, without changing the result that the effect of 30 ppm water is negligible.

Also present in the gas is nitrogen, about 0.05% of the gas flow. This molecule has a large vibrational spacing ($\omega = 2360$ cm^{-1}) and so is far from resonance with oxygen. Mixtures of oxygen and nitrogen have been found to relax separately[85] therefore the presence of nitrogen

Table 5.3

Relaxation Times at 1000K

O_2/H_2O System

Reaction	τ/atm us	Reference
1	86	(5.24)
2	25	(5.24)
3	0.01	(5.25 and 5.24)
4	0.001	9
5	50	(5.23)

cannot account for the observed relaxation times.

The conclusion to be drawn from these calculations is that the presence of impurities cannot account for the deviation observed between the experimental results and the behaviour of ground state oxygen.

5.3.5.3. The Observed Relaxation Times

We are observing the relaxation of delta in a bath of ground state oxygen that is also relaxing. The measured relaxation times are shorter than those for ground state oxygen. Delta has a similar vibrational spacing as the ground state, 1484 cm^{-1} compared to 1556 cm^{-1}. Therefore V-V exchange would be expected to be fast. The processes occurring are then

1. $O_2^* + O_2 \rightleftharpoons O_2 + O_2$
2. $O_2^* + O_2(^1\Delta_g) \rightleftharpoons O_2 + O_2(^1\Delta_g)$
3. $O_2^* + O_2(^1\Delta_g) \rightleftharpoons O_2 + O_2(^1\Delta_g)^*$
4. $O_2(^1\Delta_g)^* + O_2(^1\Delta_g) \rightleftharpoons O_2(^1\Delta_g) + O_2(^1\Delta_g)$
5. $O_2(^1\Delta_g)^* + O_2 \rightleftharpoons O_2(^1\Delta_g) + O_2$

Using (5.22) an estimate of the observed relaxation time if V-V exchange occurs can be made. Firstly the rate of the four V-T processes are needed. The rates of vibrational relaxation of each species will be the same regardless of whether the relaxation occurs on collision with a delta or ground state molecule. This is because as collision partners delta and the ground state are identical. Hence the relaxation times of reactions 1 and 2 and also of 4 and 5 are the same. Napier times for these processes can be obtained using (5.17) (ground state) or (5.24) (delta).

It was shown in the discussion of the effect of water on the observed relaxation time that the Millikan and White correlation (5.23) provided a

Table 5.4

Relaxation Times

Delta/Ground State Oxygen System

Temp /K	Ground State /atm us	Delta /atm us	Experimental /atm us	Calculated /atm us
1000	86	47	70	73
1200	41	23	33	36
1500	18	10	14	16
Reference	(5.17)	(5.24)	this work	(5.22)

Figure 5.4

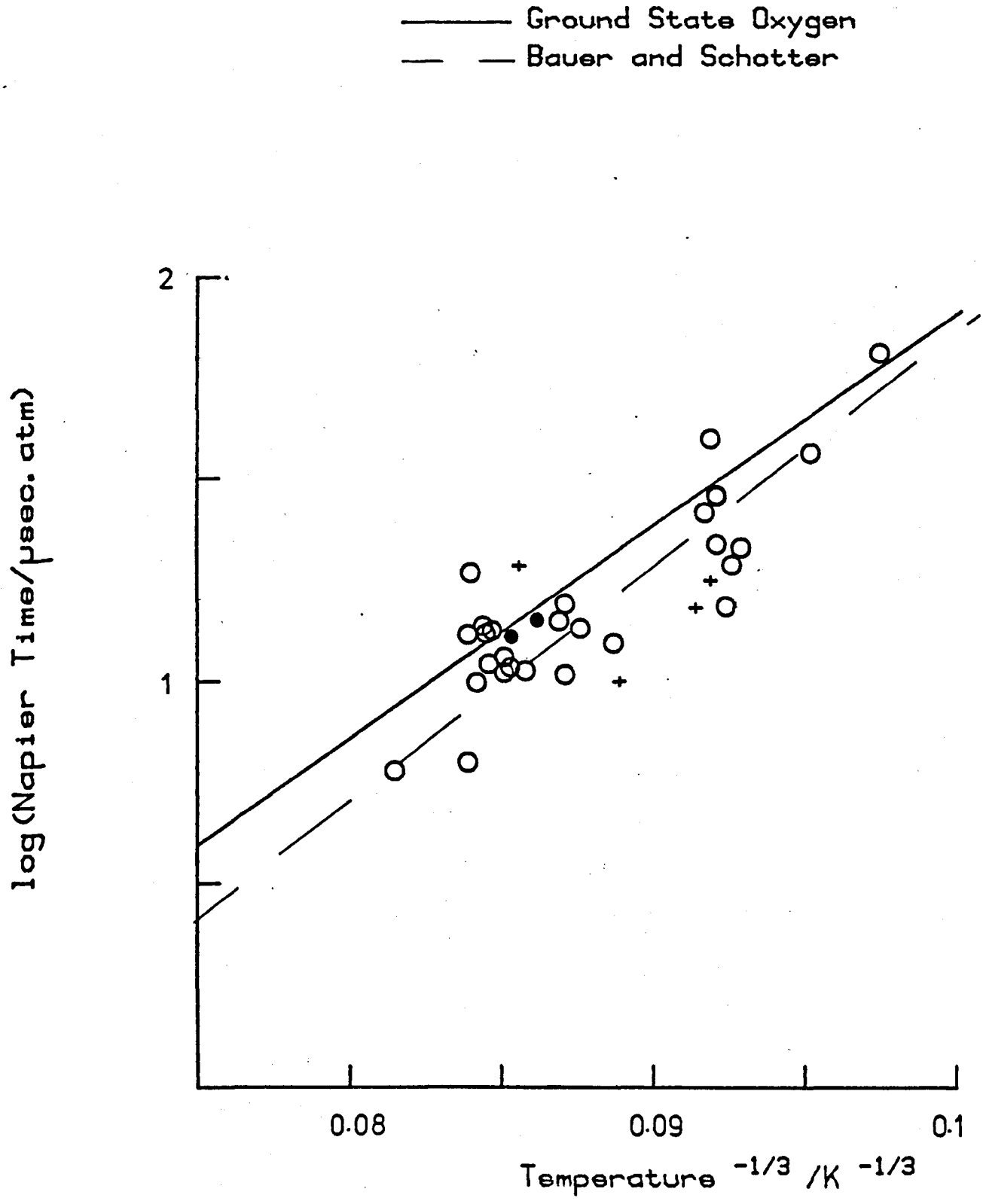
Ground State Oxygen
Bauer and Schotter
log (Napier Time/μsec. atm)
2
1
0.08
0.09
0.1
Temperature -1/3 /K -1/3

reasonable estimate of the rate of V-V exchange. In this case the characteristic temperature is calculated using the difference between the vibrational spacings of delta and ground state oxygen (72 cm^{-1}). These estimates, together with the values for the other processes are listed at three temperatures in Table 5.4. Inserting these values in (5.22) and assuming a delta concentration of 10% of the total the relaxation time for a mixture can be calculated. These calculated vibrational relaxation times and those observed are also listed in Table 5.4.

The experimental results with the relaxation times calculated using the Bauer and Schotter equation (5.22) are shown in figure 5.4. The observed and calculated relaxation times are found to be in very good agreement at all temperatures. This indicates that V-V exchange is important at high temperatures.

If a delta concentration of 5% is assumed then the calculated relaxation times at the three temperatures are 79, 38 and 17 atm μs and the agreement is still good. This shows why the experiments with a reduced delta concentration were inconclusive. The change in relaxation time for a halved delta concentration is very small and insignificant compared to the scatter of the experimental points. The effect on the delta concentration of reducing the discharge power by 20% or of discharging only 75% of the total flow is probably less than this. Consequently the effect on the relaxation time will be negligible and too small to measure.

So it appears that V-V exchange is occurring at the high temperature. We were unable to say if it occurred at room temperature but the results of Parker and Ritke[40] indicated that it did not. This is a surprising result and is in contrast with the work of Collins and Husain.[81] The Millikan and White correlation predicts that V-V exchange will still

be very rapid at 300 K, τ = 0.01 atm μs. This is very much faster than the V-T processes at this temperature and so would be expected to dominate. In contrast at high temperatures V-V exchange does appear to be important. The experimental results are significantly different from the relaxation times of both pure ground state or delta (Table 5.4). If this is so it is in keeping with the general experience in this field, that V-V exchange is rapid between states near resonance. Delta and ground state oxygen are such a system. To resolve this conflict more experiments are needed.

Firstly a study over a wider concentration range. Our experiments with a reduced delta concentration were inconclusive. If a mixture nearer 50/50 in composition could be studied then the results might indicate whether V-V exchange was occurring. In such a mixture if V-V exchange were rapid one would expect the relaxation of the faster relaxing component to dominate and so a single relaxation time of one component to be seen. The problem here is experimental, the vibrational relaxation times of delta and the ground state are similar and so it would not be easy to differentiate between them. Certainly the cases where V-V exchange occurs and a single relaxation time for one component has been observed are systems where the relaxation times of the pure components are markedly different.[9]

Further work following the relaxation of both components simultaneously would be useful. The disadvantage of the present technique is that only the relaxation of delta can be followed. Collins and Husain have observed the simultaneous relaxation of both states but were only able to work at room temperature. Our results indicate that the effect of V-V exchange changes with temperature and so a temperature dependent study seems necessary.

Other useful experiments would involve the following of the vibrational relaxation of one component in isolation. A disadvantage of the shock tube method is that it causes the relaxation of both states. The laser stimulated Raman excitation method of Ducuing[86] appears sufficiently discriminating to be used to follow the relaxation of one component separately. This technique also lends itself to a temperature dependent study by the use of a thermostatted cell.

In summary the vibrational relaxation of $O_2(^1\Delta_g)v=1$ has been followed using the dimol emission at 579 nm. A good linear Landau--Teller plot has been obtained for results between 1000 and 1850 K. The observed relaxation is found to be faster than that for ground state oxygen. This is interpreted as being due to V-V exchange between ground state oxygen and delta.

At room temperature the rate constant for the collisonal quenching of delta v=1 has been obtained, 7.4×10^1 ℓ mol^{-1} s^{-1}. This is slow compared to the other reactions involving this state. It could not be ascertained whether V-V exchange was important at this temperature or not.

Chapter 6

THE EMISSION FROM $O_2(^1\Sigma_g^+)$ AT HIGH TEMPERATURES

6.1. Introduction

Data on the reactions of sigma is obtained from the high temperature behaviour of the emission at 762 nm

$$O_2(^1\Sigma_g^+) \rightarrow O_2(^3\Sigma_g^-) + h\nu(\lambda = 762\ nm) \qquad (1.18)$$

As described in Chapter 4 the emission trace displays the four zones that were predicted by the model developed in Chapter 3. It is from the relaxation zone and the enhancement factor that the experimental results are obtained. The analysis yields rate constants for the energy pooling reaction which forms sigma

$$O_2(^1\Delta_g) + O_2(^1\Delta_g) \rightarrow O_2(^1\Sigma_g^+) + O_2(^3\Sigma_g^-) \qquad (1.20)$$

and for the collisional quenching reaction which removes it

$$O_2(^1\Sigma_g^+) + M \rightarrow O_2(^1\Delta_g) + M \qquad (1.32)$$

Of the gas phase reactions of singlet oxygen one of the most intensively studied is the quenching of sigma[1]. Several contradictory trends have been observed. Kear and Abrahamson[50] have found a relationship between the quenching rate constant and the vibrational frequency of the quencher. This contrasts with the work of Thomas and Thrush[51] who found that resonant quenching processes were not the exclusive mechanism. If resonant quenching is occurring there are two distinct theroetical approaches to the problem, differing in the nature of the interaction which induces the transition[50,54]. The

quenching of sigma is thus a fruitful field of study.

As the high temperature behaviour of the quenching reaction may indicate the nature of the interaction that leads to energy transfer the principal experimental aim of this work is to determine the temperature dependence of the quenching reaction with various partners. The essential first step is to determine the behaviour of the quenching by oxygen itself. Next a systematic study with other quenchers is undertaken.

The quenching rate constants which can be measured in this apparatus are in the range $10^5 - 5 \times 10^8$ ℓ mol^{-1} s^{-1}. The lower limit is determined by the maximum hot-flow time that can be recorded. The upper limit is set by the shortest relaxation time that can be followed and also by the requirements of a measurable glow at room temperature. This limits the choice of additives. The possible information to be gained is then taken into account after which practical considerations such as toxicity, reactivity and stability determine which are chosen. For the reasons stated later in the chapter the quenching of sigma by nitrogen, argon, carbon dioxide and nitrous oxide were studied. The practical aspects of the work and the determination of the results are described in this chapter. The results are discussed in the next chapter.

6.2. Studies of Oxygen/Nitrogen Mixtures.

The behaviour of the collisional quenching and energy pooling reactions in pure oxygen are first determined. As Thrush[5] has suggested that the quenching of sigma by oxygen may be a special case it is compared to that of a similar diatomic molecule, nitrogen.

The method of analysis to yield the results is described. In Table 6.1 are listed the results of the analysis of the 762 nm shock trace in a 90% O_2, 10% N_2 mixture. These results complement those obtained in mixtures containing 0, 10, 27.9, 53.7 and 75% nitrogen by Dr. P.M. Borrell[87] and Dr. M.D. Pedley.

Results.

The Shock Trace and Method of Analysis.

In Chapter 4 the shape of the 762 nm emission trace from a shock into pure oxygen was described (see figure 4.1d). In figure 6.1 a typical shock trace from a 90% O_2, 10% N_2 mixture is shown. It can be seen to display the same behaviour as that from pure oxygen; a rapid rise at the shock front, relaxation to an enhanced emission level and subsequent decay. The degree of enhancement is greater than in pure oxygen, in such a mixture K^{762} rises from 1.3 at 650 K to 3.3 at 1477 K.

It was shown in Chapter 3 that the high temperature emission trace at 762 nm has a relaxation zone due to the different temperature dependencies of the formation and removal reactions of sigma. The collisional quenching rate constant at the high temperature can be obtained from the relaxation constant τ using

$$k_q(T_2) = (\tau \cdot \rho_{21} \cdot [M])^{-1} \qquad (6.1)$$

where [M] is the total concentration of the gas at the high temperature and τ is determined in particle time or

$$k_q(T_2) = (\tau \cdot \rho_{21}^2 \cdot [M])^{-1} \qquad (6.2)$$

where τ is determined in laboratory time.

The enhancement factor K^{762} is measured experimentally. It is the ratio of the post-relaxation glow to that predicted using the pre-shock glow. The post-relaxation glow is determined by back extrapolation of the decay to the time of arrival of the shock front.

$$K^{762} = \frac{I^{762}(t = o)}{I_1^{762} \rho_{21}}$$

where $I^{762}(t = o)$ is the post-relaxation glow

I_1^{762} is the pre-shock glow

It was shown in Chapter 3 that the enhancement factor is given by the ratio of the rate constants for the reactions forming and removing sigma at the two temperatures

$$K^{762} = \frac{k_p(T_2)}{k_p(T_1)} \cdot \frac{k_q(T_1) + k_w/[M]}{k_q(T_2)} \qquad (6.3)$$

The room temperature rate constants in (6.3) are known, the quenching rate constant at the high temperature can be obtained from the relaxation constant and the enhancement factor is measured for each shock. Consequently the rate constant for the energy pooling reaction at the high temperature can be obtained, re-arranging (6.3)

$$k_p(T_2) = \frac{K^{762} k_p(T_1) k_q(T_2)}{k_q(T_1) + k_w/[M]} \qquad (6.4)$$

Figure 6.1

The Shock Emission at 762nm

Run C7 90% O_2. 10% N_2

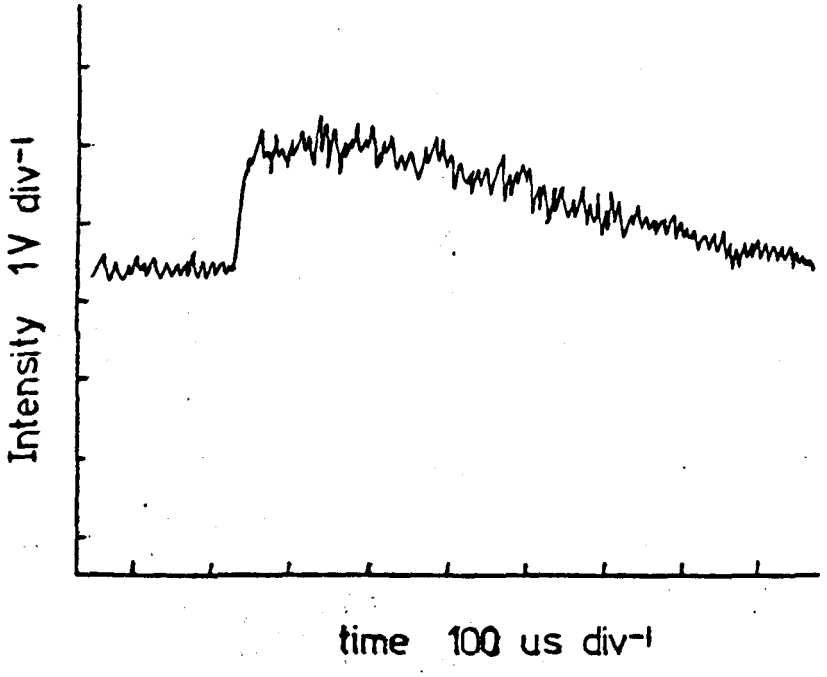

Table 6.1

Analysis of 762nm Emission

All runs 90% O_2, 10% N_2; 28ml s^{-1}; 100W

Run No.	T /K	k_p /l mol^{-1} s^{-1} 10^5	k_q(obs) /l mol^{-1} s^{-1} 10^6
C4	661	1.10	1.69
C4A	661	0.81	1.17
C5	642	0.77	1.29
C5A	642	0.66	1.02
C6	720	1.05	1.71
C6A	720	1.18	1.73
C7	718	1.31	1.98
C7A	718	1.15	1.88
C8	714	1.19	1.92
C8A	714	1.08	1.65
C9	1345	7.12	5.56
C9A	1345	4.72	3.48
C10	1477	16.29	12.64
C10A	1477	12.33	8.53

The high temperature emission traces were analysed by computer graphics to yield values for the integration time, the relaxation constant, the enhancement factor and the decay. From these results the rate constants in Table 6.1 were calculated.

In this apparatus two emission traces can be recorded from any one shock; generally the emission is monitored at two wavelengths. The form of the 634 nm emission trace from these mixtures was exactly similar to that described in Chapter 4 for shocks into pure oxygen. This would be expected given that the origin of the 634 nm emission from two delta molecules has been established.

The Collisional Quenching of $O_2(^1\Sigma_g^+)$ by Oxygen and Nitrogen.

In an oxygen/nitrogen mixture the two quenching reactions are

$$O_2(^1\Sigma_g^+) + O_2 \rightarrow O_2(^1\Delta_g) + O_2; \quad k_q(O_2) \qquad (6.5)$$

$$O_2(^1\Sigma_g^+) + N_2 \rightarrow O_2(^1\Delta_g) + N_2; \quad k_q(N_2) \qquad (6.6)$$

The quenching is known to occur to delta for the reasons given in Chapter 2. At room temperature these reactions have markedly different rate constants $k_q(O_2) = 1.0 \times 10^5$ ℓ mol^{-1} s^{-1} and $k_q(N_2)$[88] $= 1.3 \times 10^6$ ℓ mol^{-1} s^{-1}. By a high temperature study at several concentrations the temperature dependencies of the reactions can be determined.

The observed quenching rate constants in a 90% O_2, 10% N_2 mixture, obtained using (6.2) are plotted against temperature in figure 6.2. In such a binary mixture the observed quenching rate constant should be the sum of two contributions

$$k_q = k_q(O_2)X_{O_2} + k_q(N_2)X_{N_2} \qquad (6.7)$$

Figure 6.2 Quenching Rate Constant in 90% O_2, 10% N_2 mixture

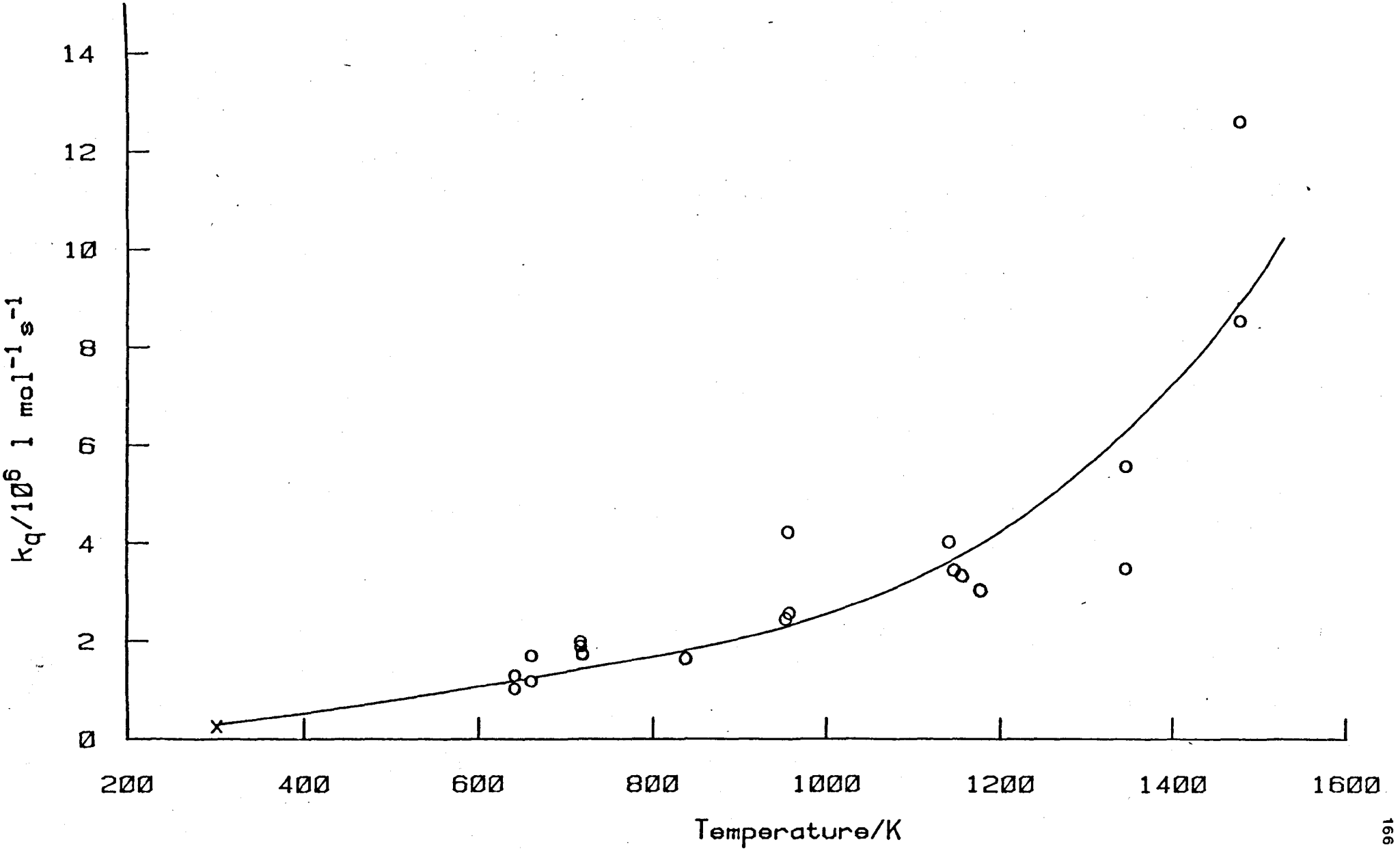

where the rate constants refer to the high temperature processes and X_{O_2} and X_{N_2} are the mole fractions. By plotting the rate constants at any temperature against composition the two pure gas rate coefficients can be obtained. In figure 6.3 such plots are shown, they include the 90% O_2, 10% N_2 rate constants cited in Table 6.1 and values from other mixtures.

Straight lines are drawn through the points and from the intercepts at either end of the mole fraction scale the rate coefficients at that temperature can be determined. While the data give a good straight line at lower shock temperatures (< 1100 K) a slight curvature is noticeable at higher temperatures. This can be put down to the experimental method. As the temperature increases the relaxation zone becomes smaller (if the quenching rate constants increase) and hence the rate constants are less accurately determined. At either end of the composition scale the experimental error is greater because of either low K values (at low N_2 mole fractions) or low emission levels (at high N_2 mole fractions). But it can be seen that the plots in figure 6.3 confirm the model (6.7) and enable rate constants for the quenching reactions (6.5) and (6.6) to be determined. These values are plotted against temperature in figure 6.4.

In Table 6.2 values of the rate constants taken from figure 6.4 are displayed. The errors are taken from the scatter about the best line through the points and correspond to 2σ limits (approximately ± 20%).

From figure 6.4 it can be seen that the curves, when extrapolated back, agree well with the literature room temperature values[89]. Recently another group of workers, Kohse-Hoinghaus and Stuhl[43] have measured the quenching rate constants for nitrogen (and other gases) as a function of temperature. They used the method of time resolved

Figure 6.3 Variation of Quenching Rate Constant with Mole Fraction of Oxygen at Various Temperatures

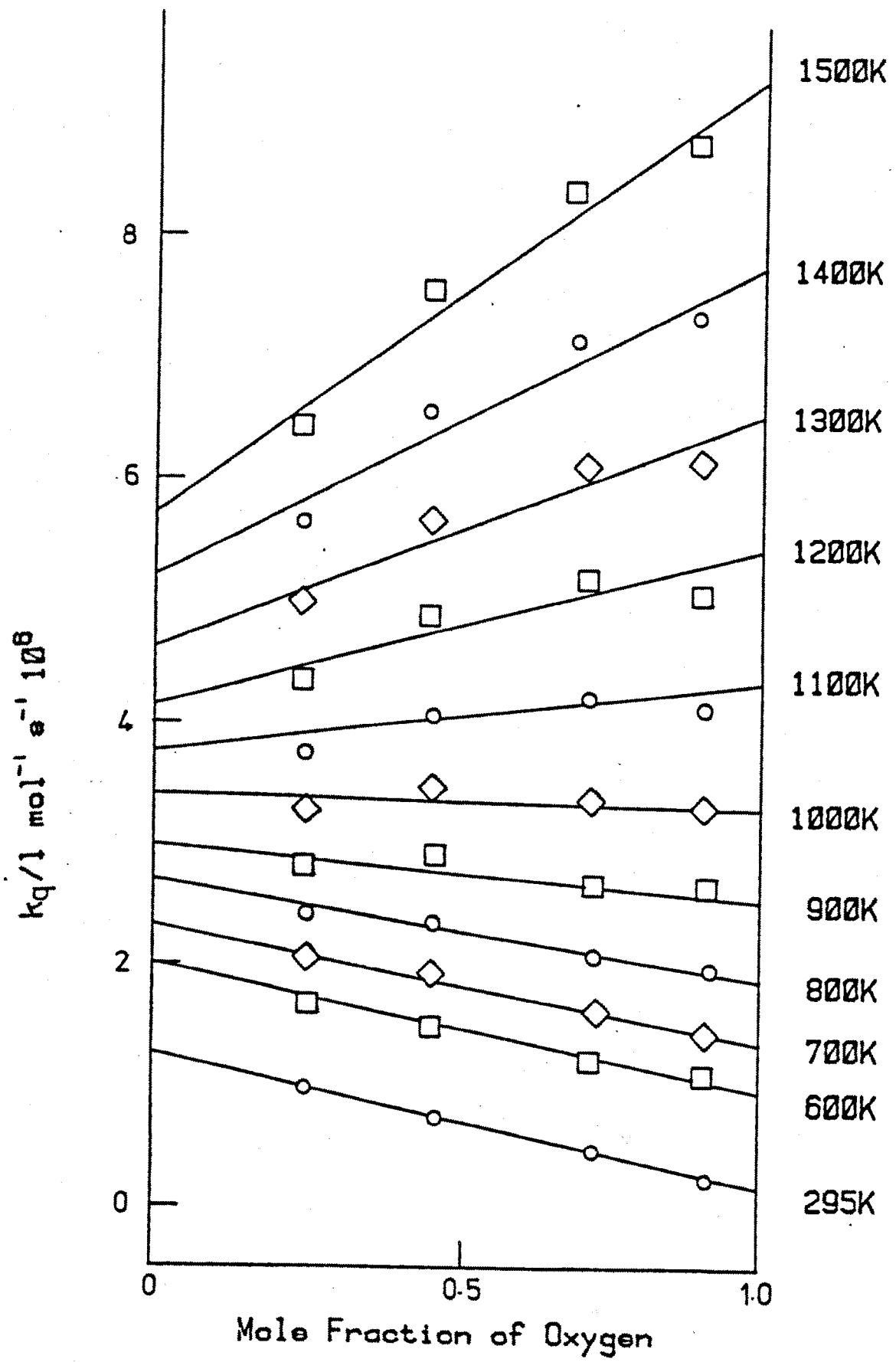

Table 6.2

Best Values for Quenching Rate Constants

Temperature /K	$k_q(O_2)$ /l $mol^{-1} s^{-1} 10^6$	$k_q(N_2)$ /l $mol^{-1} s^{-1} 10^6$
295	0.10±.01	1.30±0.1
700	1.25±0.1	2.30±0.1
1000	3.25±0.5	3.30±0.5
1300	6.40±0.8	4.65±0.8
1500	9.20±1.5	5.70±1.5

Figure 6.4 Best Lines for Quenching by Oxygen and Nitrogen

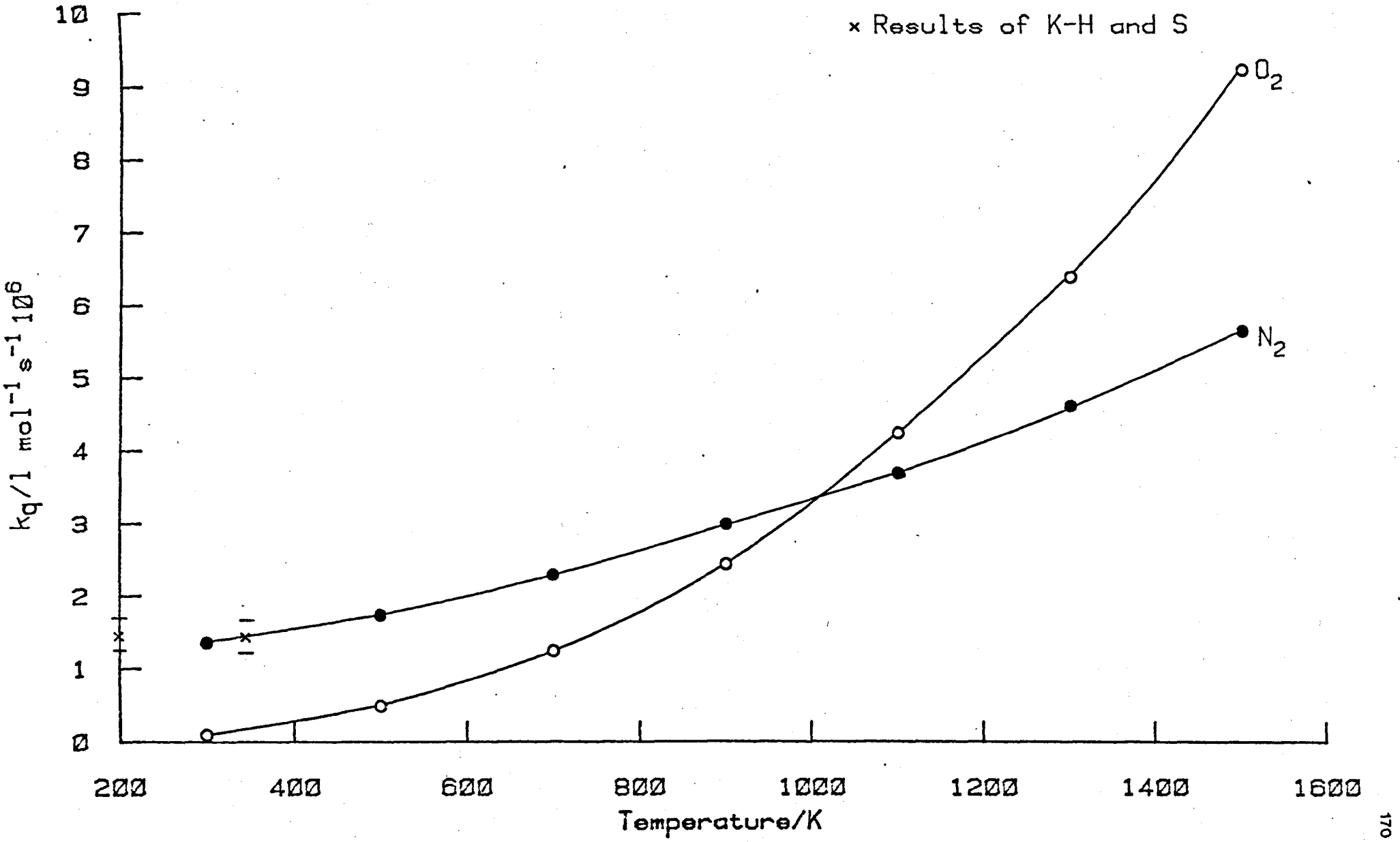

laser induced fluorescence between 200 and 350 K. Because of their experimental method they were able to achieve greater precision than we can, though over a smaller temperature range. Their values, with their error limits (3σ), are also shown in figure 6.4. They can be seen to agree well with our extrapolations. These observations give us confidence in the accuracy of the present work.

It can be seen that the quenching reactions by oxygen and nitrogen show a similar gross temperature dependence in that both increase. However quenching by oxygen increases faster than that by nitrogen and the curves cross at 1100 K. These temperature dependencies are discussed in Chapter 7.

The Energy Pooling Reaction.

$$O_2(^1\Delta_g) + O_2(^1\Delta_g) \rightarrow O_2(^1\Sigma_g^+) + O_2(^3\Sigma_g^-) \qquad (1.20)$$

The rate constants at the high temperature are obtained from the results of the graphical analysis using (6.4).

For example for shock C9

$$P_1 = 6.63 \text{ torr, } [M] = 3.63 \times 10^{-4} \text{ mol } l^{-1}$$

$$k_q(T_1) = 2.2 \times 10^5 \text{ } l \text{ mol}^{-1} \text{ s}^{-1}, \; k_w = 21.5 \text{ s}^{-1}$$

$$T_2 = 1345 \text{ K}, \; \rho_{21} = 5.580$$

The computer fitting yields the results

$$K^{762} = 2.93, \; \tau = 88.9 \; \mu s$$

Using (6.1) $k_q(T_2) = 5.56 \times 10^6 \text{ } l \text{ mol}^{-1} \text{ s}^{-1}$

Therefore using (6.4)

$$k_p(T_2) = 7.12 \times 10^5 \text{ } l \text{ mol}^{-1} \text{ s}^{-1}$$

The rate constants obtained in this way in a 90% O_2, 10% N_2 mixture are plotted in figure 6.5. The reaction was studied in other mixtures and the results from all mixtures are plotted in figure 6.6. The line is the best line drawn by eye through the points.

It can be seen that there is no composition dependence. This would be expected from (1.20) and so confirms the nature of the energy pooling reaction and the correctness of the model.

The reason for the low enhancement factors in pure oxygen shocks (they rise to 2.2 at 1500 K c.f. other mixtures) is also evident by comparing figure 6.4 and 6.6. The enhancement factor depends on the different temperature dependencies of the reactions forming and removing sigma, the rate constants for the energy pooling reaction and for the quenching by oxygen rise by approximately the same amount between 300 and 1500 K, consequently K^{762} given by (6.3) is small. The quenching by nitrogen increases more slowly with temperature consequently the enhancement factors in oxygen/nitrogen mixtures are larger.

Figure 6.5 Energy Pooling Reaction Rate Constant in 90% O_2, 10% N_2 mixture

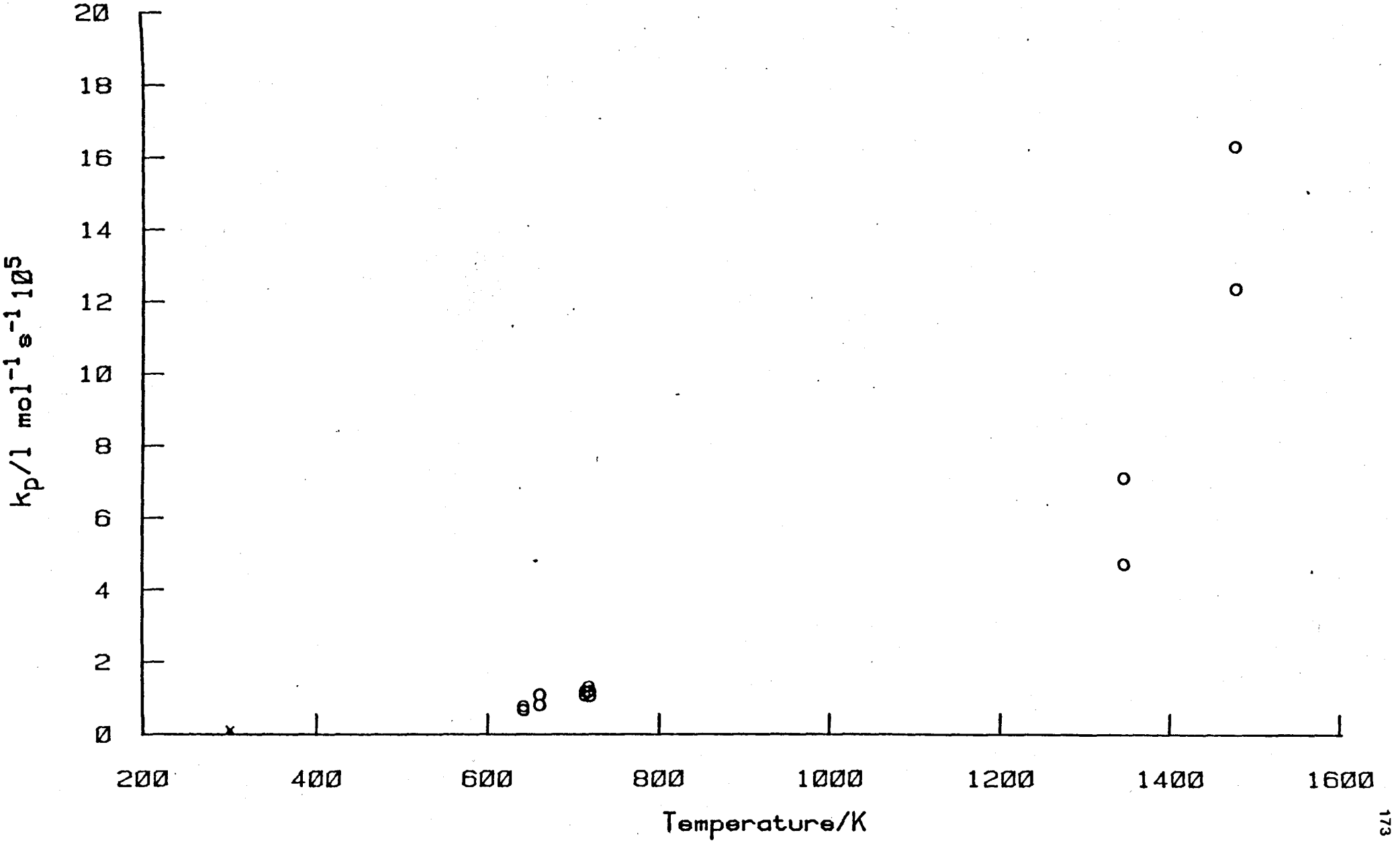

Figure 6.6 Energy Pooling Reaction Rate Constants

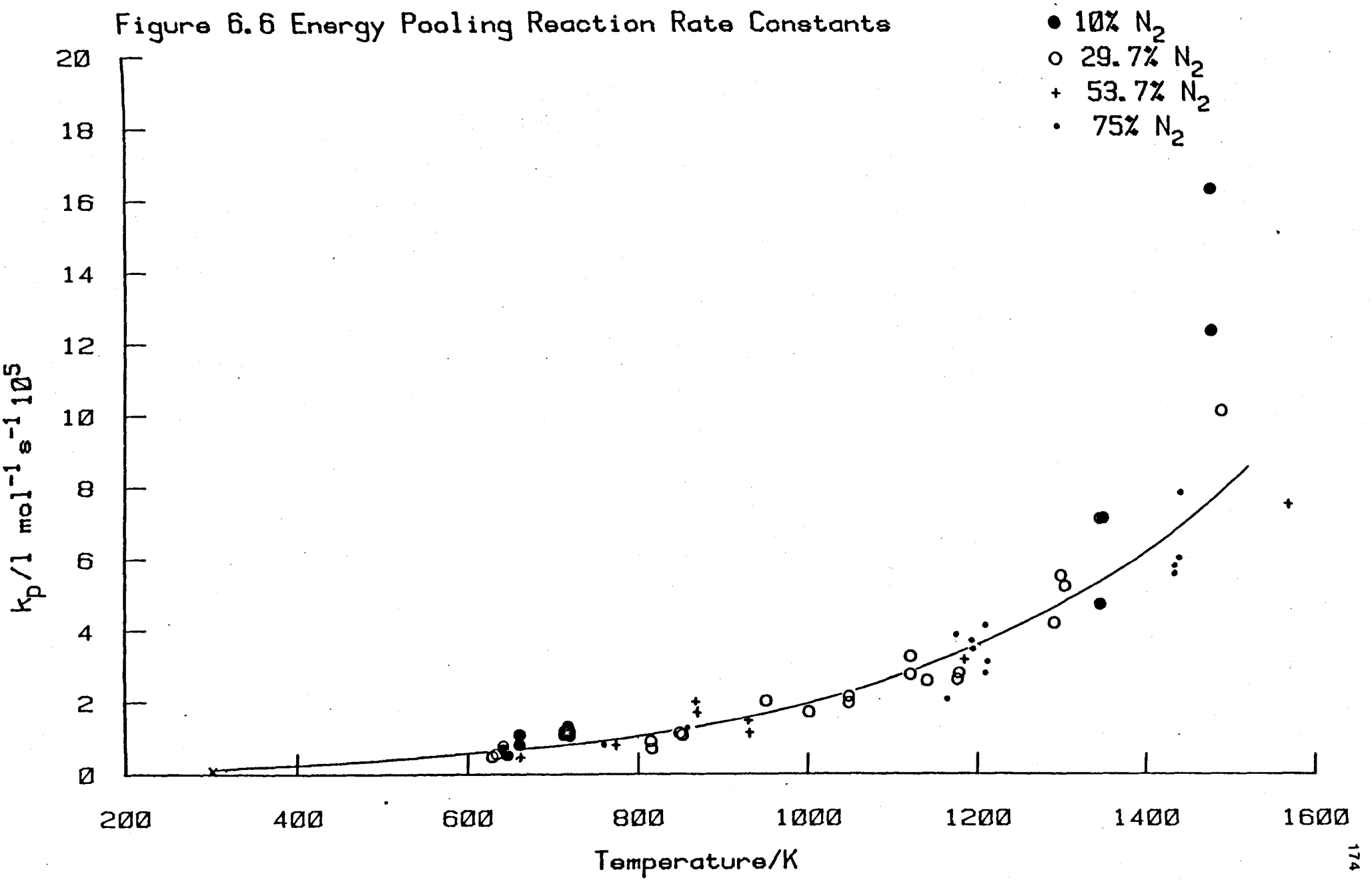

6.3. Studies of Oxygen/Nitrogen/Argon Mixtures.

After the initial determination of the temperature dependence of the energy pooling reaction and of the collisional quenching by oxygen and nitrogen the next step was to extend the work with other quenchers. As was mentioned in the introduction there is some controversy as to the participation of vibrational excitation of the quencher in the quenching process. A noble gas quencher would be unable to become vibrationally excited and so would be a useful subject for investigation. Argon was chosen as an additive.

A series of shocks were performed into 30/30/40 and 45/45/10 mixtures of oxygen, nitrogen and argon. Mixtures containing nitrogen were chosen for two reasons, firstly to reduce the high temperature quenching rate. Argon is known to be an inefficient quencher at room temperature[89] ($k_q = 9 \times 10^3$ ℓ mol^{-1} s^{-1} at 295 K) and so it's contribution to the measured quenching rate constant would probably not be large. Secondly the enhancement factors in oxygen/nitrogen mixtures are large, this improves the signal to noise ratio.

Results.

The Shock Trace.

The 762 nm emission trace from a shock into a 30/30/40 oxygen/nitrogen/argon mixture is shown in figure 6.7. Compared to figure 4.1d (pure oxygen) and figure 6.1 (oxygen/nitrogen) the relaxation zone is very long. This indicates a slow relaxation and hence a low quenching rate constant. This is also evidenced from the enhancement factors which for a 30/30/40 mixture rise from 2.0 at 760 K to 15.0 at 1850 K. The same effect could be seen in oxygen/nitrogen mixtures where the slow increase in quenching rate constant for nitrogen caused the enhancement factor to increase with mole fraction of nitrogen.

Figure 6.7

The Shock Emission at 762nm
Run C139 30% O_2, 30% N_2, 40% Ar

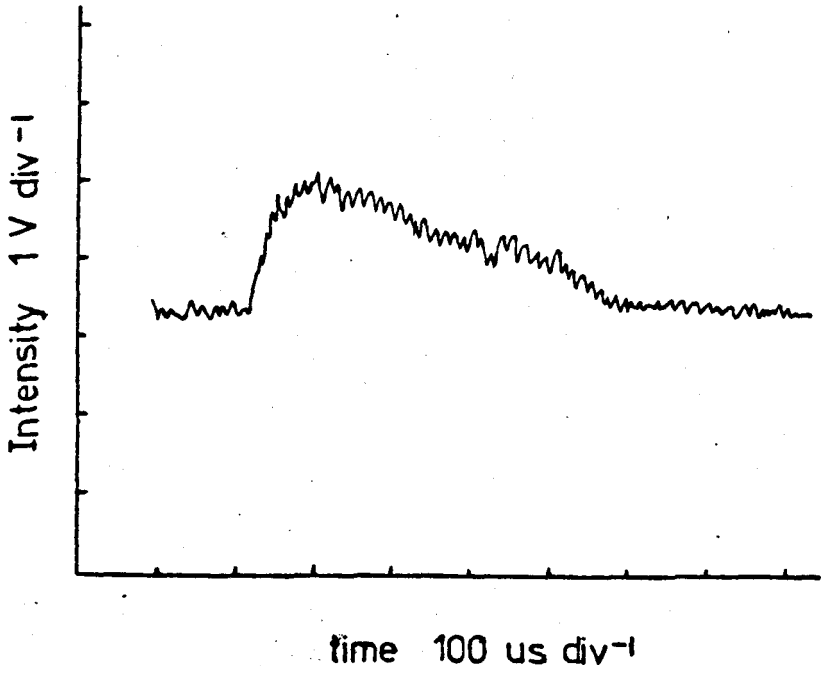

Table 6.3

Analysis of 762nm Emission

45% O_2,45% N_2,10% Ar;28ml s^{-1};100W

Run No.	T /K	k_p /l mol^{-1} s^{-1} 10^5	k_q(obs) /l mol^{-1} s^{-1} 10^6
C121A	1258	3.55	3.31
C123A	1293	3.92	3.43
C124	1341	5.15	4.39
C124A	1341	5.06	4.68
C125	1303	4.55	4.02
C125A	1303	4.35	3.82
C126	1259	3.57	3.34
C126A	1259	3.64	3.45
991A	1620	14.55	8.45
992	1589	9.31	5.51
992A	1589	8.51	4.42
993	1586	8.40	5.79
993A	1586	12.33	8.05
994	685	0.51	1.21
994A	685	0.49	1.15
995	755	0.77	1.82
995A	755	0.85	1.89
996	743	0.69	1.42
996A	743	0.89	1.96
30% O_2,30% N_2,40% Ar;28ml s^{-1};100W			
C138	1491	5.30	2.37
C139	1504	8.30	4.82
C140	1491	7.38	3.39
C141	1767	17.76	5.84
C142	1817	20.43	5.38
C142A	1817	17.34	6.59
C143	1832	19.25	5.60
C143A	1832	18.36	6.78
C144	1644	9.54	4.65
C144A	1644	8.36	4.53
C145	1628	11.96	4.67
C145A	1628	6.94	3.49
C146	1177	4.00	3.47
C146A	1177	1.91	1.81
C147	1178	2.65	1.41
C147A	1178	2.11	1.17
C148	1195	2.59	1.57
C148A	1195	3.17	2.62
C149	743	0.85	1.53
C149A	743	1.00	1.69
C150	755	0.63	1.18
C150A	755	1.16	2.22
C151	748	0.88	1.45
C151A	748	0.79	1.43

The high temperature emission traces were analysed as described previously to yield values for the energy pooling reaction and overall collisional quenching rate constants. The results are listed in Table 6.3 and the run parameters in Appendix 6.

As in oxygen/nitrogen mixtures the emission at 634 nm was monitored as well as that at 762 nm. The form of the dimol emission was again identical to that described in Chapter 4.

The Collisional Quenching of $O_2(^1\Sigma_g^+)$ by Argon.

The observed quenching rate constants for the two mixtures are plotted against temperature in figures 6.8 and 6.9. The lines are the best lines through the points judged by eye.

The results in oxygen/nitrogen mixtures showed that the observed quenching rate constant displayed the expected composition dependence. Therefore by extension the quenching rate constant in an oxygen/nitrogen/argon mixture is given by

$$k_q = k_q(O_2)X_{O_2} + k_q(N_2)X_{N_2} + k_q(Ar)X_{Ar} \qquad (6.8)$$

where the symbols have their usual meaning. The overall quenching rate constant at the high temperature can be obtained from the relaxation constant. Rate constants for the quenching by oxygen and nitrogen can be obtained from the best lines on figure 6.4. Hence it is possible to determine $k_q(Ar)$ at the high temperature.

On figures 6.8 and 6.9 the best lines through the points lie very close to the values calculated using (6.8) with the appropriate high temperature rate constants for the quenching by oxygen and nitrogen and the room temperature value for argon. Consequently it is not possible to measure the argon quenching rate constant. Because the quenching rate constant for argon at the high temperature is too

Figure 6.8 Quenching Rate Constant in 30% O_2, 30% N_2, 40% Ar mixture

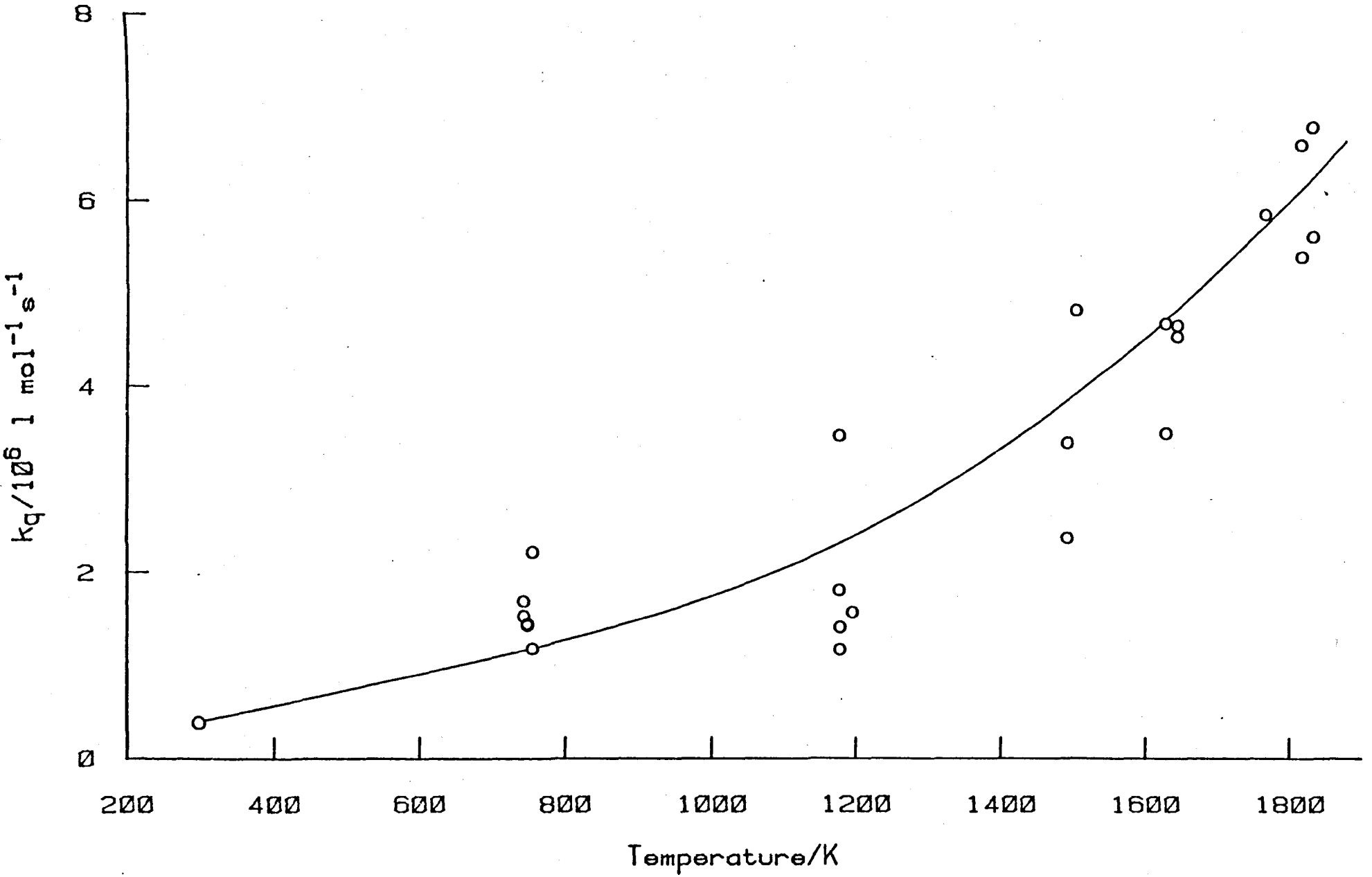

Figure 6.9 Quenching Rate Constants in 45% O_2, 45% N_2, 10% Ar mixture

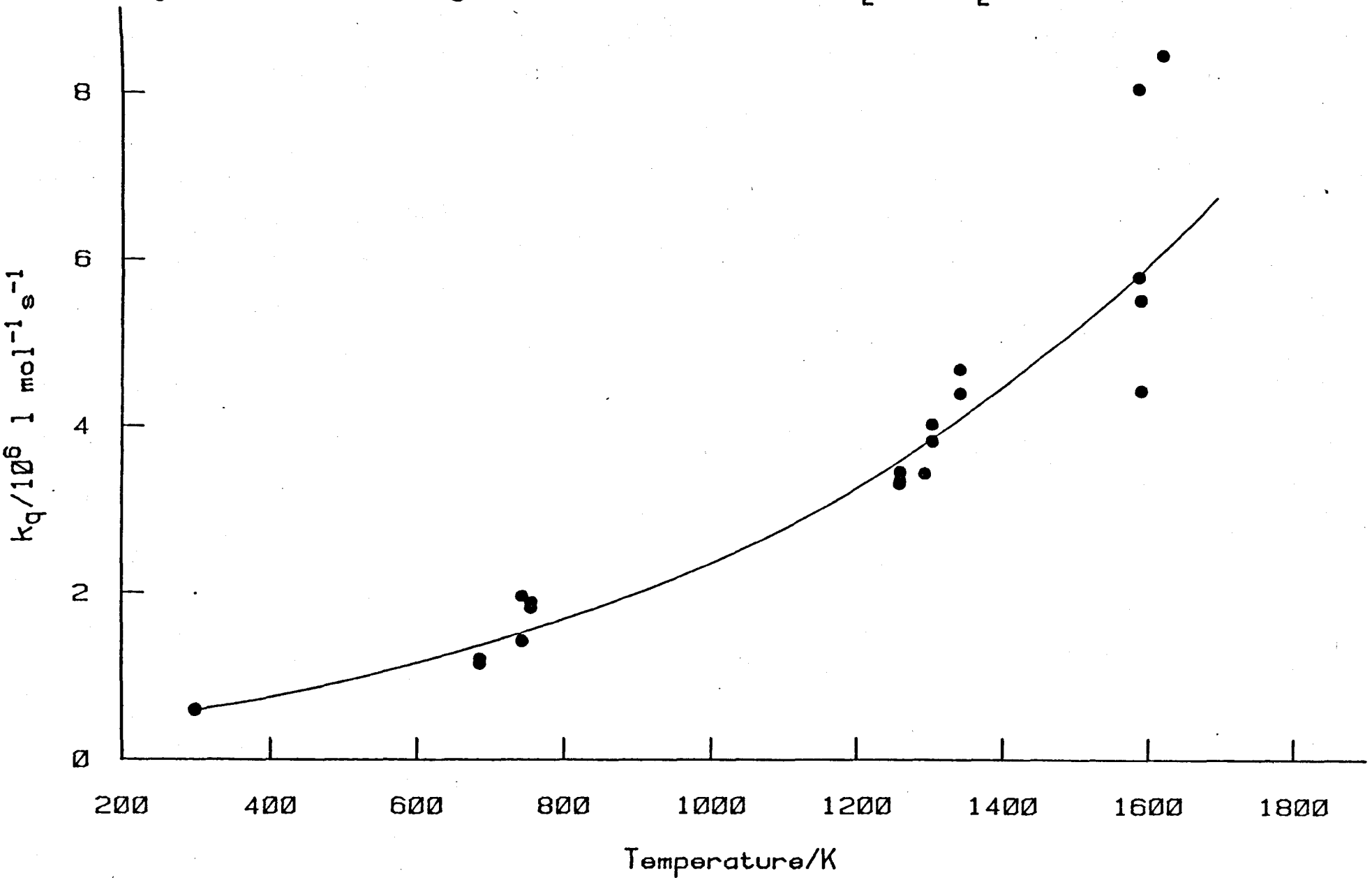

low to be measured by this method only an upper limit can be obtained, in the following way.

Estimates of the upper limits of the overall quenching rate constants at 800, 1200 and 1500 K were made. These corresponded to the best values from figures 6.8 and 6.9 plus 25%. Using the rate constants for the quenching by oxygen and nitrogen from figure 6.4 and the mole fractions and upper limit for the quenching rate constant for argon was made. The lowest value obtained was at 1500 K, $k_q(Ar) = 8 \times 10^5$ ℓ mol^{-1} s^{-1}.

On the inclusion of argon there is a rise in the maximum shock temperature reached (it rises from 1500 K to 1850 K). This is due to the change in partition of energy between translation and vibration on the inclusion of a monatomic gas. Although for the mixture containing 40% argon the scatter in experimental points becomes less beyond 1500 K, reliable estimates of the oxygen and nitrogen quenching rate constants have only been obtained up to this temperature. Consequently this was the highest temperature at which an estimate of the argon quenching rate constant was made.

The Energy Pooling Reaction.

In order to determine the rate constant for the energy pooling reaction at the high temperature it is necessary only to know the overall quenching rate constant, not the individual contributions. Hence rate constants for the energy pooling reaction could be obtained in both mixtures, they are plotted in figure 6.10.

The line drawn through the points is the best line through previous measurements in oxygen/nitrogen mixtures. It can be seen that the points lie on or very close to the line up to it's limit at 1500 K. Because of the higher temperature reached in shocks into

Figure 6.10 Energy Pooling Reaction Rate Constants

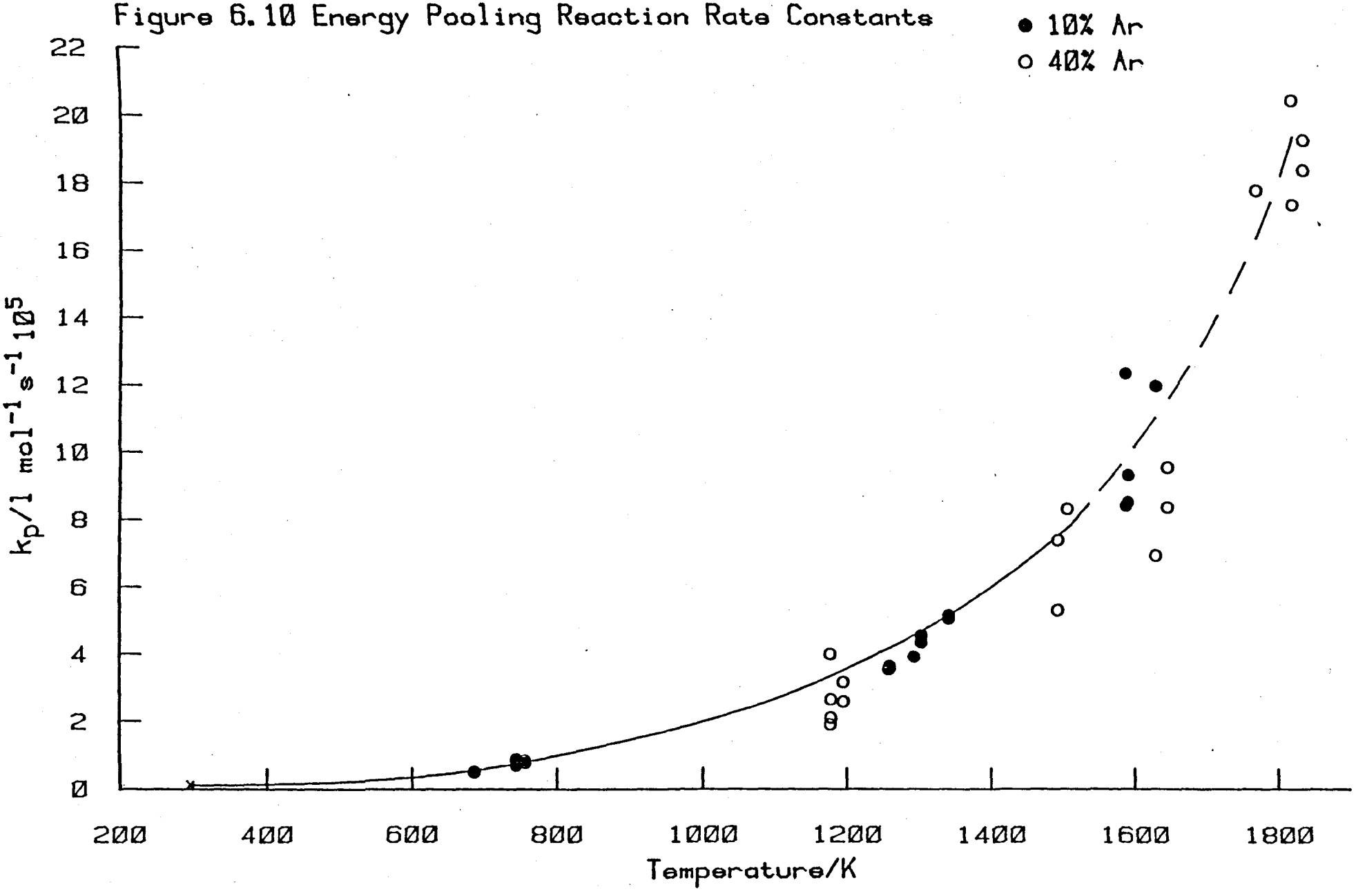

mixtures containing argon results were obtained up to 1850 K. These are also plotted in figure 6.10. It can be seen that they agree very well with the extrapolation of the line from lower temperatures. In Table 6.4 are listed some of the values of the rate constant for the energy pooling reaction taken from figure 6.10, the error limits are taken from the scatter about the best line.

Though we were unable to determine the temperature dependence of the quenching of sigma by argon the results from these mixtures for the energy pooling reaction are most encouraging. The striking agreement between the previous measurements and the current work in different mixtures indicates the validity of the kinetic scheme and the nature of the energy pooling reaction. The agreement found between the highest temperature results in argon and the extrapolation of previous measurements underlines the accuracy of the analysis.

The confirmation of the absence of any composition dependence is significant and the consequences for the method of analysis adopted in the case of oxygen/carbon dioxide and oxygen/nitrous oxide mixtures described in the next section.

Table 6.4

Best Values for Energy Pooling Rate Constant

Temperature /K	k_p /l mol^{-1} s^{-1} 10^5
295	0.12±0.02
700	0.7 ±0.15
1000	1.9 ±0.3
1300	4.5 ±0.7
1500	7.6 ±1.0
1800	17.7 ±2.5

6.4. Studies of Oxygen/Carbon Dioxide Mixtures.

The temperature dependence of the quenching by oxygen and nitrogen has been established. Both show a positive temperature dependence but of different type, quenching by nitrogen increasing more slowly with temperature. Quenching by argon has been investigated and found to be inefficient at all temperatures. It has been suggested that vibrational excitation of the quencher is important in the quenching mechanism[50]. In order to test this a quencher that is near resonance is needed, there are several possibilities for example HCl, HBr or a variety of polyatomic molecules.

Ogryzlo et al[55] have previously investigated the temperature dependence of the quenching by HBr, they found very little change in rate constant up to 400 K. As the temperature dependence of the quenching can indicate the mechanism by which it occurs this does not seem a suitable choice, even though we are able to work up to 1500 K and so are more likely to discern a trend. It seems likely that the quenching by HCl will be similar to that by HBr. These two diatomic molecules also possess the disadvantage of being corrosive. Consequently a polyatomic molecule, carbon dioxide, was chosen as the next additive. This molecule is able to come close to resonance by the simultaneous excitation of several vibrational modes.

6.4.1. Determination of the Room Temperature Quenching Rate Constant for Carbon Dioxide.

Before (6.4) can be used to calculate a rate constant for the energy pooling reaction the overall quenching rate constant at room temperature must be known. For a mixture of carbon dioxide and oxygen this is given by (6.9) so an accurate estimate of $k_q(CO_2)$ is required.

$$k_q = k_q(O_2)X_{O_2} + k_q(CO_2)X_{CO_2} \qquad (6.9)$$

It was shown in Chapter 3 that from a comparison of the 762 nm and 634 nm emission intensities with and without added gas a quenching rate constant for the additive could be determined (6.10)

$$\frac{I^{762}/I^{634}}{(I^{762}/I^{634})'} = \frac{k_q(O_2)[O_2] + k_q(CO_2)[CO_2] + k'_w}{k_q(O_2)[O_2] + k_w} \qquad (6.10)$$

where $(I^{762}/I^{634})'$ is the ratio in the presence of carbon dioxide and k'_w is the wall quenching rate constant at that pressure. The rate constants for quenching at the wall can be calculated at any pressure using (3,18). In this apparatus at 295 K this reduces to

$$k_w/s^{-1} = \frac{1}{4{,}01(P/P_o) + 0{,}0115} \quad \text{for sigma at 295 K}$$

The rate constant for the quenching by oxygen at this temperature is 1.0×10^5 ℓ mol^{-1} s^{-1}.

Intensity ratios were measured in the following way. The photomultipliers were clamped in position opposite one another. One was equipped with a 634 nm filter, the other to monitor the 762 nm emission. The first measurement was taken in pure oxygen, the pressure was set and after the flow had steadied the intensities measured. The desired proportion of carbon dioxide was then added and after the flow had stabilized the new pressure and intensities were noted.

Ten experiments were perfomed at pressures of about 6,5 torr adding 5% carbon dioxide to the flow. The results are listed in Table 6,5. These give an average of $2{,}18 \pm 0{,}34 \times 10^8$ ℓ mol^{-1} s^{-1}

Table 6.5

Determination of Room Temperature Quenching Rate Constant for Carbon Dioxide

Pressure /torr	Intensity Ratio	$k_q(CO_2)$ /l mol^{-1} s^{-1} 10^8
6.40	68.6	
6.64	0.93	2.22
6.55	71.7	
6.80	0.93	2.37
6.55	71.2	
6.80	0.91	2.32
6.64	40.5	
6.84	0.65	1.87
6.72	44.2	
6.96	0.63	2.15
6.80	38.3	
6.96	0.58	2.00
6.80	70.7	
7.17	0.93	2.26
6.80	70.0	
7.17	0.88	2.34
6.80	70.0	
7.17	0.87	2.36
6.80	37.8	
6.96	0.58	1.95

Table 6.6

Carbon Dioxide Quenching Rate Constants

Value /l mol^{-1} s^{-1} 10^8	Reference
2.5	50
1.8	90
1.8	91
2.6	92
1.2	93
2.7	94
2.18	this work

at 295 K where the error is the 95% confidence limit.

In this part of the work the results can be compared with those of other workers obtained by different methods. These previous estimates are listed in Table 6.6. Our results can be seen to be in very good agreement with them. The value of $k_q(CO_2)$ obtained by us depends on the values of $k_q(O_2)$ used. The measure of agreement found between our estimate of $k_q(CO_2)$ and previous determinations provides additional confirmation of our value of $k_q(O_2)$ and hence of the water content of the gas.

6.4.2. High Temperature Studies of Oxygen/Carbon Dioxide Mixtures.

A series of shocks into mixtures containing 1.7,5,10 and 21% carbon dioxide were performed. The run parameters are listed in Appendix 6.

Results.

The Shock Trace.

A typical high temperature emission trace from a mixture containing carbon dioxide is shown in figure 6.11. The four regions expected can be seen; the steady glow from the cool gas, the rapid rise at the shock front, the relaxation zone and the decay. It can be seen from figure 6.11 that the relaxation zone is small. What is not readily apparent is the size of the enhancement factor. For a mixture containing 21% carbon dioxide this rises from 16 at 979 K to 149 at 1276 K, the corresponding values in pure oxygen are 1.1 and 1.3 respectively.

Work in nitrogen and argon mixtures has established that the energy pooling rate constant increases by a factor of 35 between 300 and 1500 K. The very large enhancement factors in the presence of carbon dioxide indicate that the quenching rate constant must decrease with temperature.

The work described in the previous section has established that

Figure 6.11

The Shock Emission at 762nm

Run C200 95% O_2, 5% CO_2

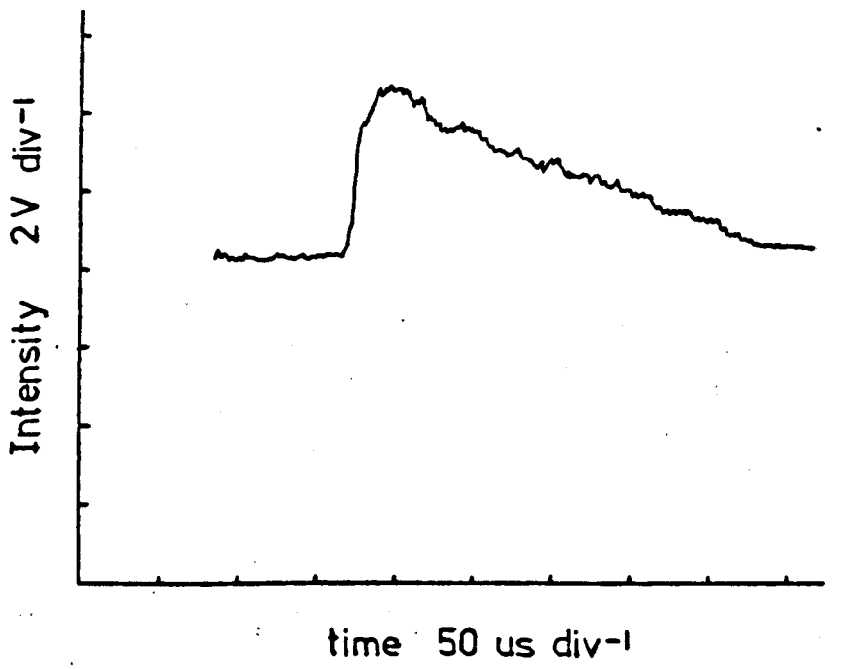

the quenching by carbon dioxide is rapid at room temperature. The fact that the relaxation zone is small on all traces, even at the highest temperature, shows that the rate constant is still large despite the decrease with temperature. The shortness of the relaxation zone means that there are few points from which the relaxation constant can be determined. This factor, coupled with the size of the enhancement factor, has consequences for the quality of the fitting of the relaxation zone.

The 634 nm emission from shock heated mixtures containing carbon dioxide was also monitored. The traces had the expected shape and were fitted by interactive computer graphics as described in Chapters 3 and 4. These results were used in the investigation of the hot band emission at 637 nm as described in Chapter 4.

The Collisional Quenching of $O_2(^1\Sigma_g^+)$ by Carbon Dioxide.

High temperature rate constants for the collisional quenching in the various mixtures were calculated from the fitted relaxation constant using (6.3). They are plotted for the mixtures containg 5 and 21% carbon dioxide in figure 6.12. Also shown are the room temperature rate constants calculated using

$$k_q = k_q(O_2)X_{O_2} + k_q(CO_2)X_{CO_2} \qquad (6.11)$$

where $k_q(O_2) = 1 \times 10^5$ ℓ mol^{-1} s^{-1} at 295 K

$k_q(CO_2) = 2.18 \times 10^8$ ℓ mol^{-1} s^{-1} at 295 K.

The temperature dependence of the quenching by oxygen has previously been established (figure 6.4) therefore (6.11) can be used to determine the quenching rate constants for carbon dioxide at any temperature. The values so obtained are plotted for the mixtures in figure 6.13. It can be seen that while the results fall

Figure 6.12 Quenching Rate Constants

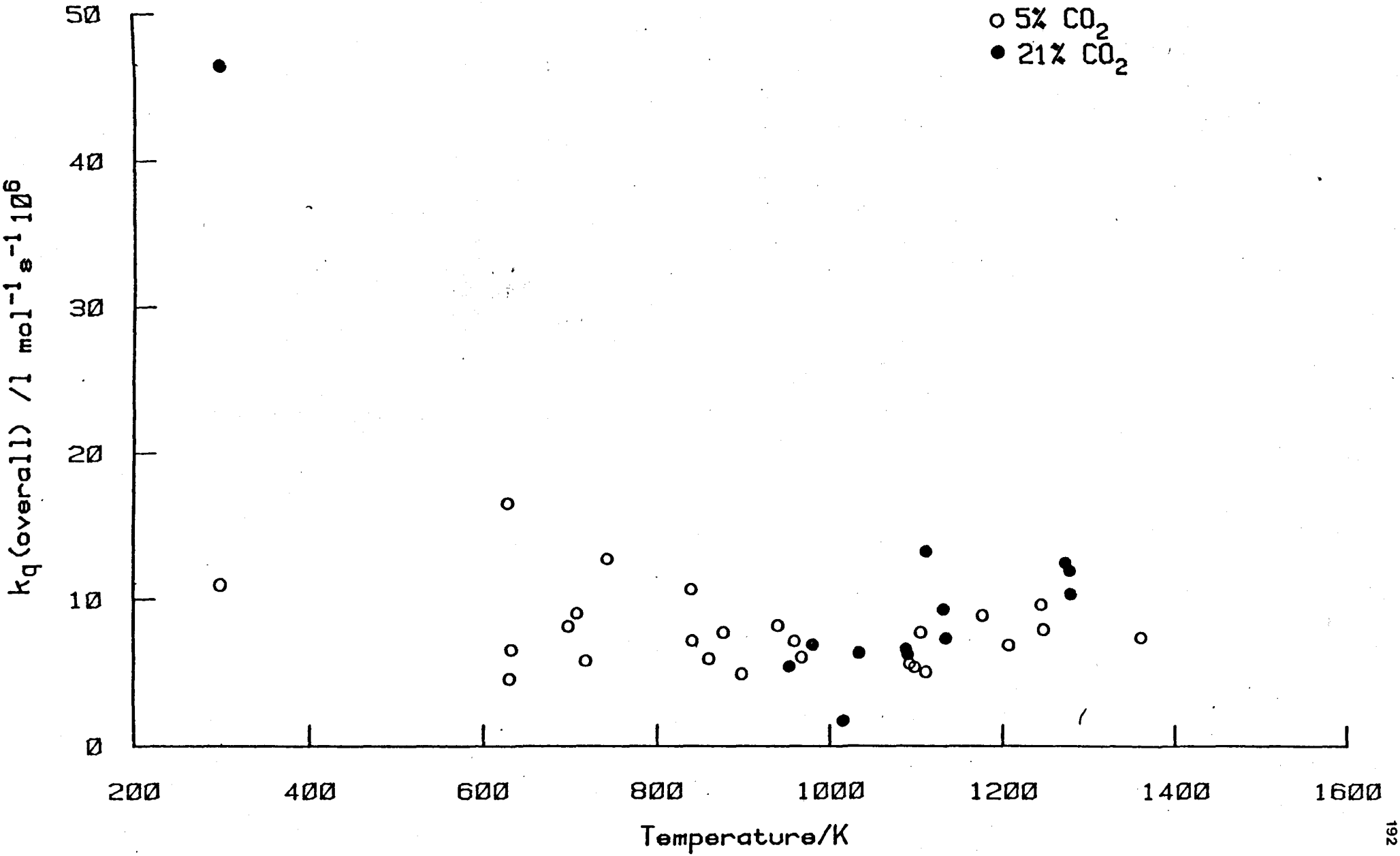

Figure 6.13 Quenching Rate Constants for Carbon Dioxide

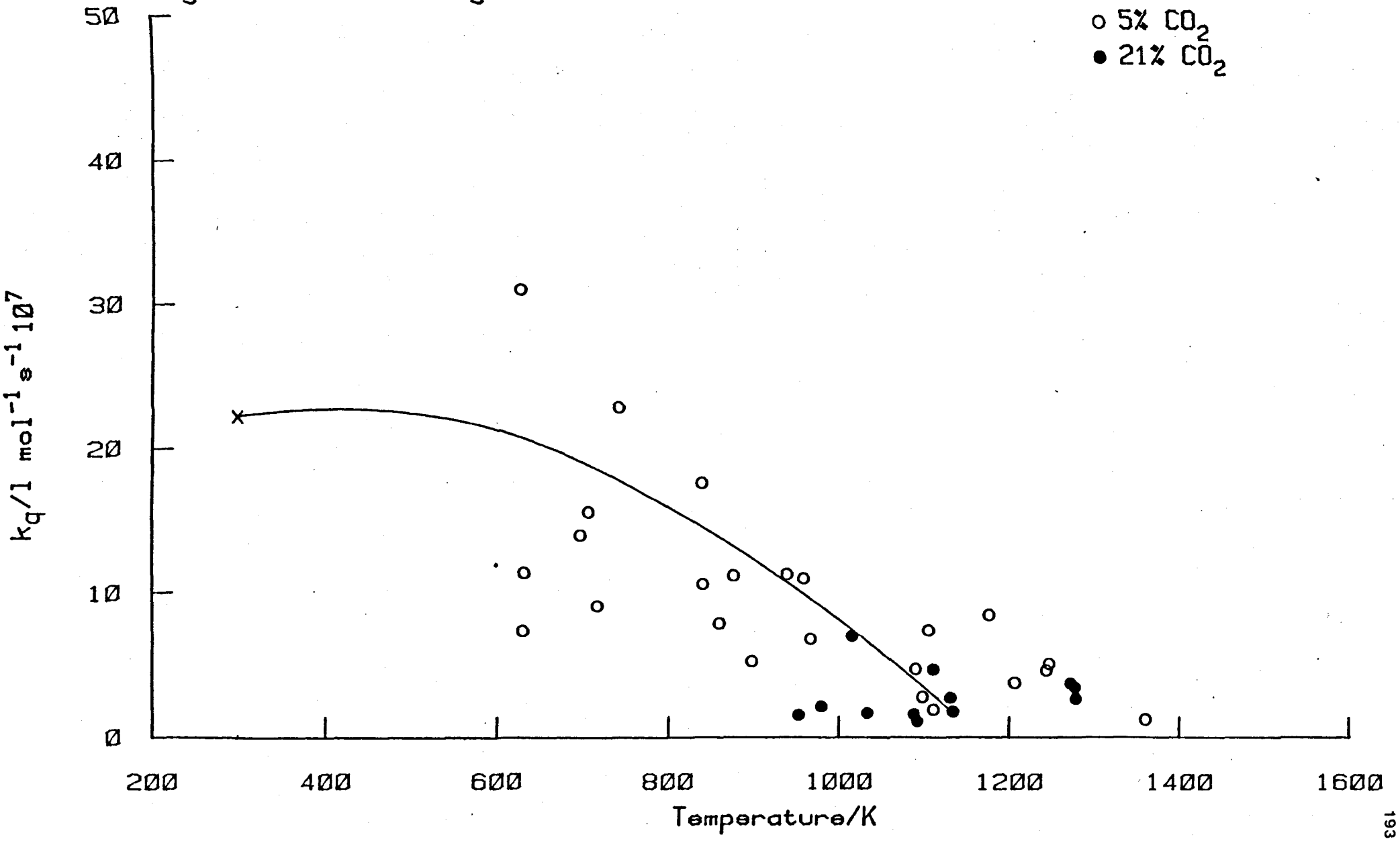

on one line, confirming the composition dependence (6.11) the points are scattered. This scatter is larger than usual for such measurements, compare figure 6.13 with for example figure 6.8. The origin of this scatter will be discussed shortly.

The Energy Pooling Reaction.

The rate constants for the energy pooling reaction can be calculated from the quenching rate constants using (6.4). The values are plotted against temperature in figure 6.14, the line is the best line through previous results in oxygen, nitrogen and argon.

The temperature dependence of the energy pooling reaction was initially determined in oxygen/nitrogen mixtures. The results obtained with argon as an additive confirmed the temperature dependence and that there was no composition dependence. The high temperature behaviour of the energy pooling reaction is thus well characterised. Figure 6.14 shows that the present measurements, while falling near the best line, are less accurate than previous results. In particular there is a marked tendency for the points around 1000 K to fall below the line. The cause of this deviation from expected behaviour will now be discussed.

The rate constants plotted in figure 6.14 are calculated from the quenching rate constants. The quenching rate constants were determined from the relaxation constant which was in turn obtained by fitting the relaxation zone. Thus the accuracy of the energy pooling reaction rate constants depends on the accuracy of the fitting of the relaxation zone. Where relaxation is very fast, as it is in the presence of carbon dioxide, the fitting can be affected by other features of the shock trace, notably the integration time.

Because of the finite slit width used and the rise time of the

Figure 6.14 Energy Pooling Reaction Rate Constants

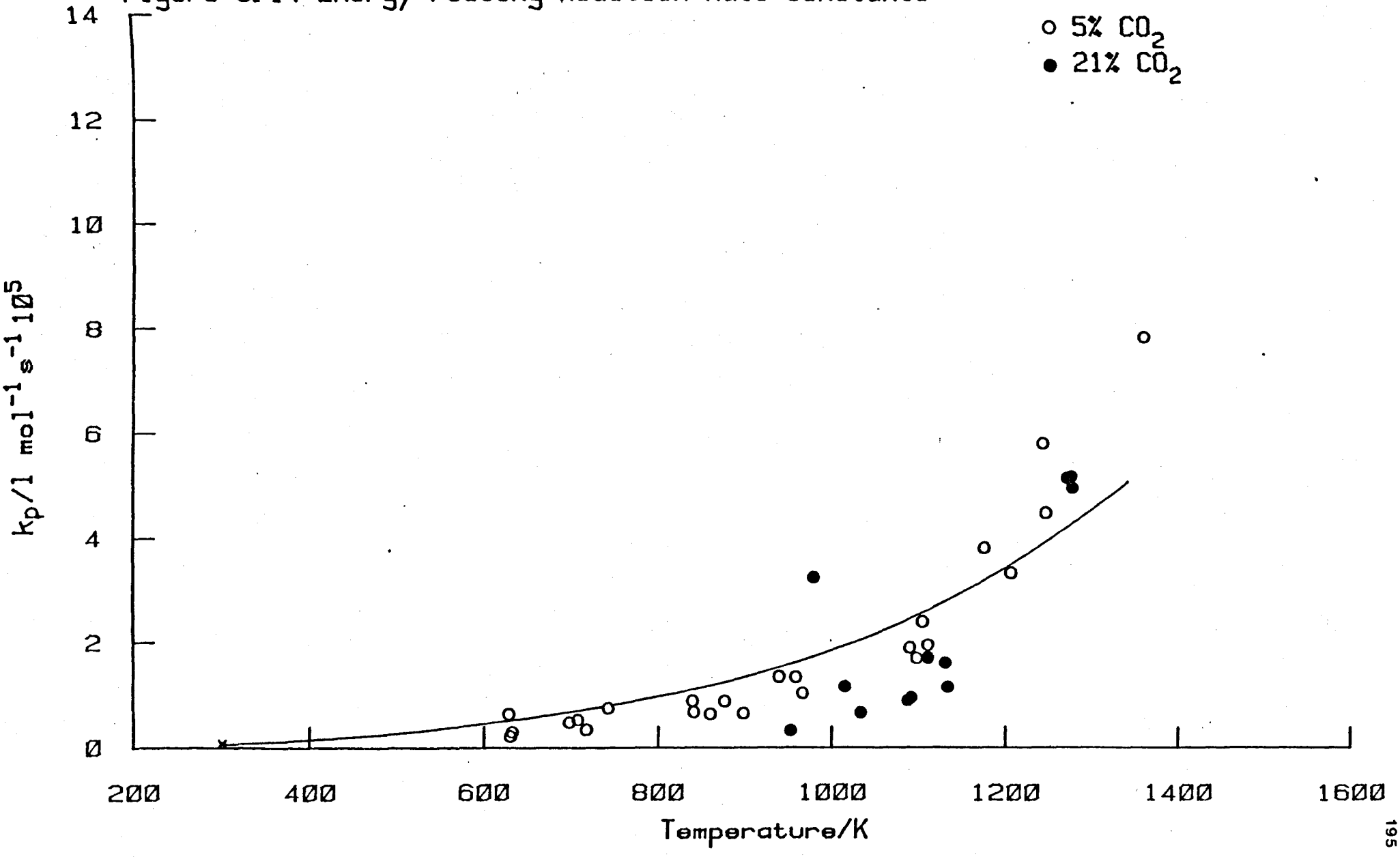

electronics there is a response time of the detection system, this is called the integration time. In discussing the integration time in Chapter 3 a square slit was assumed, this is not the case in practice. However this approximation is not significant if the relaxation time is large compared to the integration time. Thus the integration time effectively puts a lower limit on the relaxation times that can be measured. The integration time depends on the experimental conditions of slit width and shock speed but a typical value for these experiments is 10-15 μs (laboratory time).

The relaxation times of two typical shocks are (in laboratory time)

Run C192; T_2 = 708 K, τ = 17 μs

Run C199; T_2 = 1206 K, τ = 12 μs

As the temperature of the shock increases the slit width is narrowed because of the increased post-shock glow. Consequently the integration time decreases. Hence the relaxation time and integration time are always comparable and so much of the relaxation is lost in the integration time. This, coupled with the fact that there are few points in the relaxation zone anyway because of it's rapidity, mean that the determination of the relaxation constant is poor.

The results do fall near the best line and show the same general trend with temperature. Therefore they show that the energy pooling reaction is occurring at the same rate in the present mixture as in other mixtures studied. Thus the deviation of the experimental points from the best line in figure 6.14 is due to the inaccuracy in the determination of the relaxation constant.

The Collisional Quenching of $O_2(^1\Sigma_g^+)$ by Carbon Dioxide.

The rapidity of relaxation in the presence of carbon dioxide causes the relaxation constant to be inaccurately measured. This is the origin of the large scatter seen in the measured quenching rate

constants and the deviation seen in the energy pooling rate constants. As the energy pooling reaction is found to be occurring at the same rate as in other mixtures it is reasonable to take rate constants for the energy pooling reaction from the best line (figure 6.10) and to calculate more accurate quenching rate constants using

$$k_q(T_2) = \frac{k_p(T_2)}{k_p(T_1)} \cdot \frac{k_q(T_1) + k_w/[M]}{K^{762}} \qquad (6.12)$$

The energy pooling rate constant can be obtained from figure 6.10, the room temperature rate constants are known or can be calculated, this leaves the enhancement factor K^{762}. This factor is determined by back extrapolation of the decay to the time of arrival of the shock front. Thus it is determined from points which are unaffected by the rapid relaxation and so is accurately measured.

The quenching rate constants calculated in this way are plotted for two mixtures in figure 6.15. These results were obtained using the experimentally measured value of K^{762} in (6.12). From the group of three results around 630 K an estimate of the random error afflicting the measurement of K^{762} can be obtained. Assuming that the error in the measurement of shock speed is negigible (experience shows this to be the case) the scatter of the points indicates that K^{762} can be measured to ± 10%.

These results can be compared with those of figure 6.12 calculated from the relaxation constant. The improvement is readily apparent, the scatter is reduced and the points lie on two well defined lines.

Assuming the usual dependence of the quenching rate constant on composition the quenching rate constants for carbon dioxide can be calculated. These are listed in Table 6.7 and plotted in figure 6.16. The points for all mixtures are seen to fall on the same line

Figure 6.15 Quenching Rate Constants

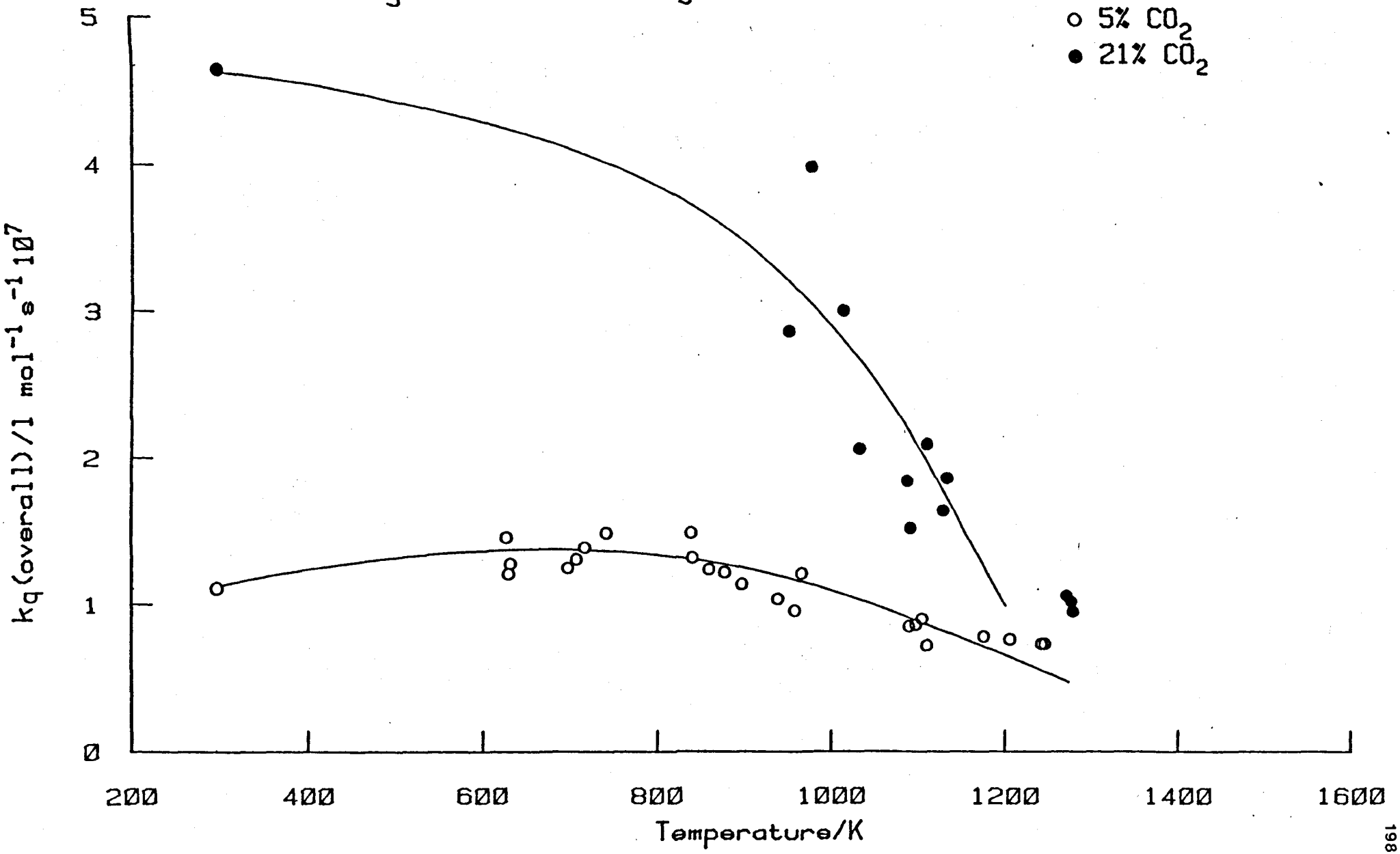

Table 6.7

Analysis of 762nm Emission

Run No.	T /K	k_p(obs) /l mol^{-1} s^{-1} 10^5	k_q(calc) /l mol^{-1} s^{-1} 10^7	$k_q(CO_2)$ /l mol^{-1} s^{-1} 10^7
		79% O_2,21% CO_2;28ml s^{-1};100W		
C152A	1130	1.61	1.64	6.10
C153A	1092	0.95	1.52	5.67
C154A	1088	0.90	1.84	7.20
C155A	1111	1.71	2.09	8.31
C156A	1278	4.95	0.95	2.20
C157A	1276	5.16	1.02	2.55
C158A	1271	5.13	1.06	2.77
C159A	1134	1.15	1.86	7.14
C160A	979	0.32	3.98	17.80
C161A	1015	1.16	3.00	13.00
C162A	1033	0.67	2.06	8.47
C163A	952	0.32	2.86	12.50
		95% O_2,5% CO_2;28ml s^{-1};100W		
C178A	1105	2.39	0.90	9.75
C179A	1098	1.70	0.86	9.09
C180	1111	1.95	0.72	6.08
C181	939	1.35	1.04	15.6
C182	958	1.34	0.96	13.5
C186	630	0.21	1.21	22.5
C187	628	0.61	1.46	27.5
C188	632	0.29	1.28	23.9
C189	839	0.88	1.49	26.0
C190	718	0.34	1.39	25.2
C191	698	0.48	1.25	22.6
C192	708	0.53	1.31	23.7
C193	743	0.75	1.49	27.0
C194	840	0.67	1.32	22.5
C195	966	1.03	1.21	18.5
C196	897	0.64	1.14	18.2
C197	859	0.65	1.24	20.7
C198	877	0.88	1.22	20.0
C199	1206	3.32	0.76	5.03
C200	1242	5.79	0.73	3.74
C201	1090	1.90	0.85	9.20
C202	1176	3.79	0.78	6.18
C203	1246	4.46	0.73	3.70
		90% O_2,10% CO_2;28ml s^{-1};100W		
C204	1357	5.42	0.78	1.60
C205	1338	3.49	0.67	0.52
		98.3% O_2,1.7% CO_2;28ml s^{-1};100W		
C208	847	0.90	0.54	19.7

Figure 6.16 Quenching Rate Constants for Carbon Dioxide

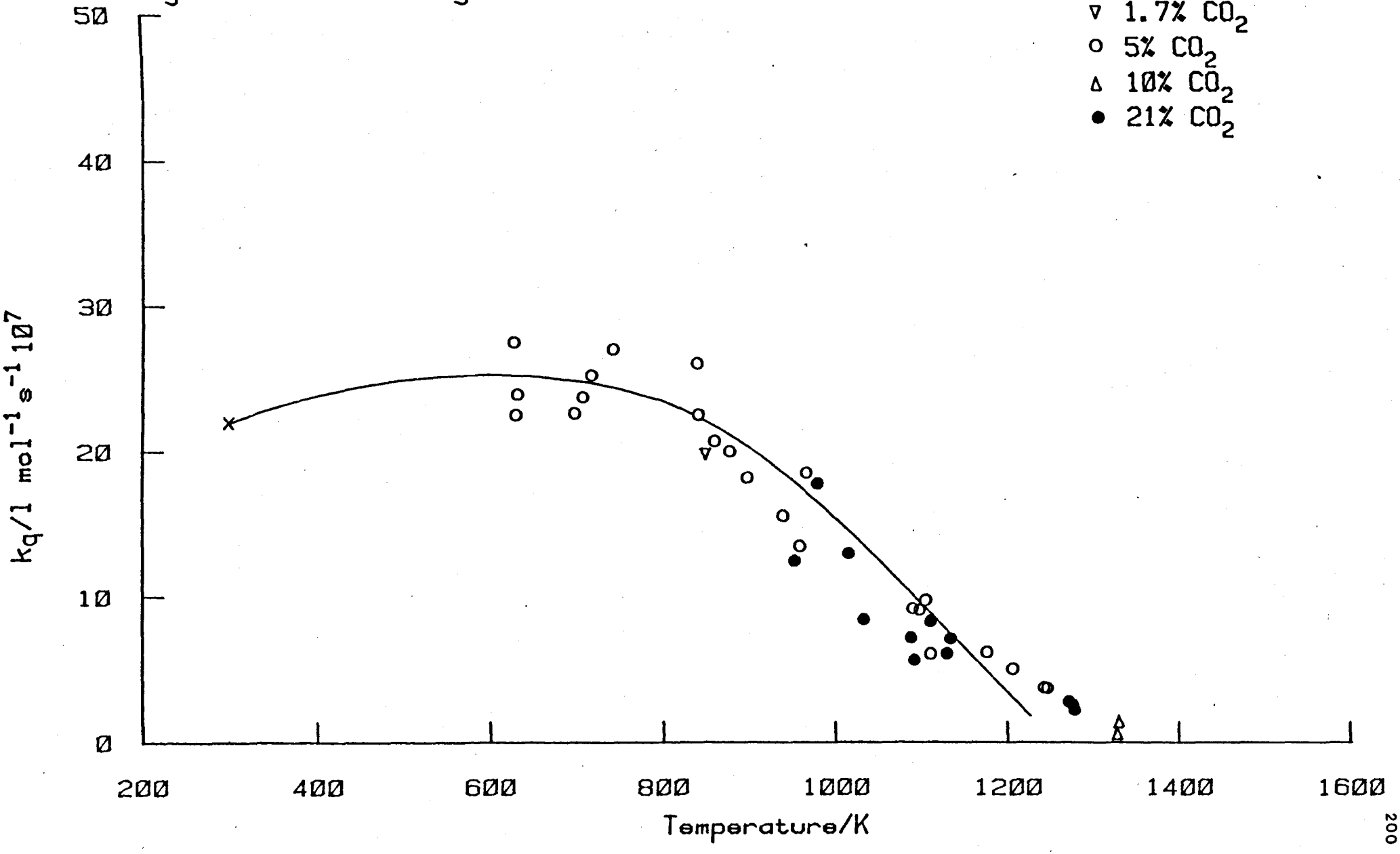

confirming the assumptions about the composition dependence (6.11).

The quenching rate constants for carbon dioxide and oxygen are plotted together in figure 6.17, note the scale is logarithmic to accommodate the range. There are obvious differences in behaviour: the rate constants for carbon dioxide reach a maximum at about 700 K and then decrease, the oxygen rate constants increase throughout the temperature range. Over the 1200 K temperature range the oxygen rate constant increases by two orders of magnitude while that for carbon dioxide decreases by a factor of about twenty (mostly in the range 1200 - 1400 K). For a reaction showing typical Arrhenius behaviour (ΔE = 50 kJ mol^{-1}) the rate constant can double for a 10 K rise in temperature. In such cases the increase in rate constant due to the increase in number of collisions is insignificant compared to the effect of the activation energy. In the case of the quenching of sigma however there is little temperature dependence and so the effect of the changing collision rate is significant. It is corrected for in the following way.

The second order rate constant k can be seen as the product of Z_{AB}, the number of collisions occurring per unit concentration per unit time and P, the probability that any one collision will lead to quenching.

$$k = Z_{AB} P$$

In a mixture of two gases A and B the number of collisions occurring in the gas in a volume per second is[72]

$$Z = \pi\sigma^2 \left\{\frac{8RT}{\pi M}\right\}^{\frac{1}{2}}$$

Figure 6.17 Quenching Rate Constants for Oxygen and Carbon Dioxide

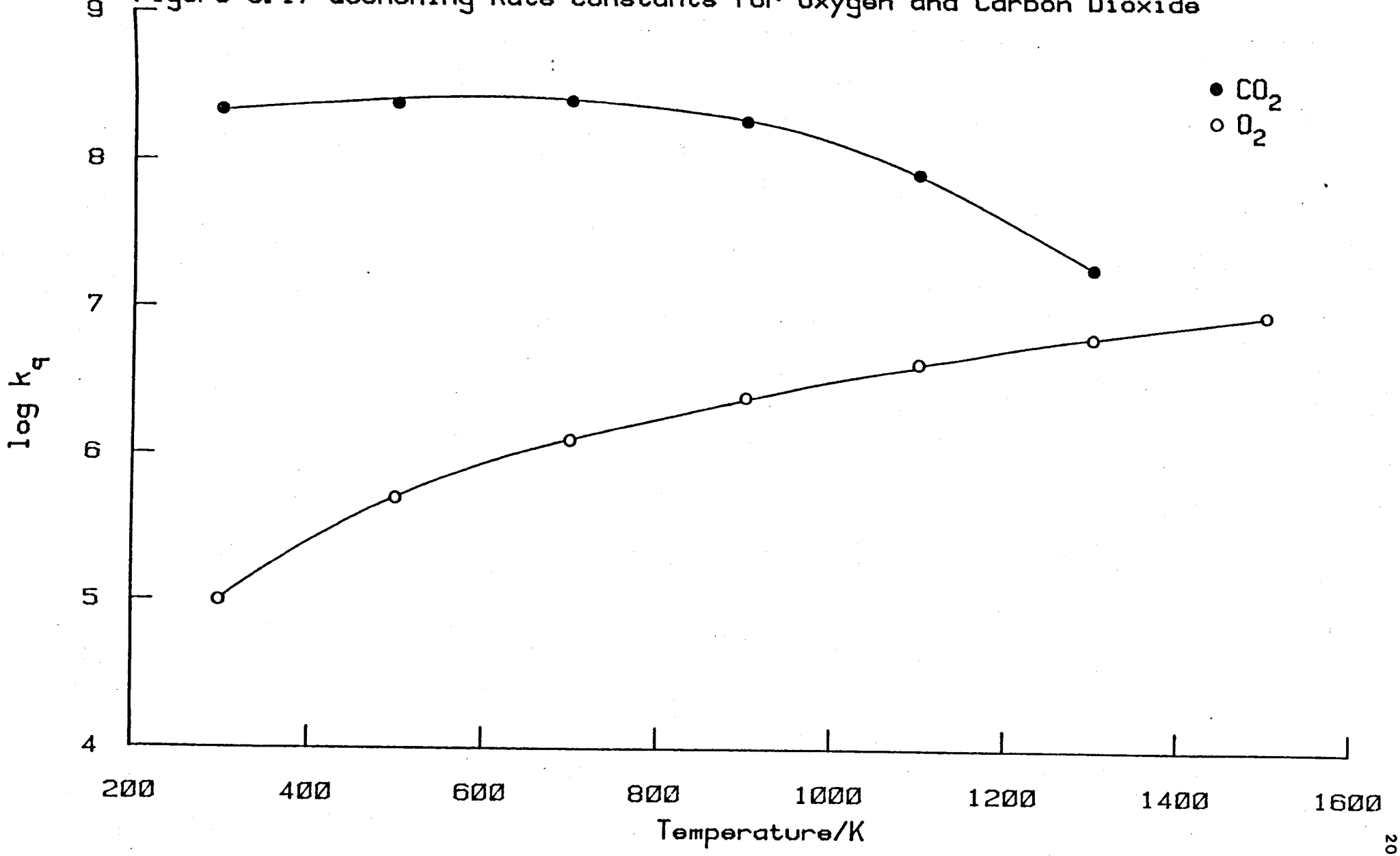

where M is the reduced molar mass ($\equiv \mu \times 10^{-3}$ kg)

σ is the mean collision diameter

From which the collision number in units of $\ell\ mol^{-1}\ s^{-1}$ is given by

$$Z_{AB} = \pi\sigma^2 \left\{\frac{8RT}{\pi M}\right\}^{\frac{1}{2}} L\ 10^3$$

where L is Avogardro's number.

The molecular diameters, obtained from viscosity measurements[72] are listed in Table 6.8. Using this data to calculate collision numbers the quenching probabilities for carbon dioxide have been calculated, they are plotted in figure 6.18. This may be compared with figure 6.16 which shows the rate constants.

The probability plot illustrates the effect of the changing collision rate on the rate coefficients of reactions with little temperature dependence, there is now no maximum and the descent at higher temperatures is steeper. It also indicates the peril of attempting to discern a temperature dependence from a study over a small temperature range. Measurement of the quenching rate constant for carbon dioxide up to 700 K would have shown an apparently positive temperature dependence while in fact the opposite is true.

Table 6.8

Molecular Diameters

Molecule	Diameter /nm
Oxygen	0.29
Nitrogen	0.31
Carbon Dioxide	0.46

Figure 6.18 Quenching Probabilities for Carbon Dioxide

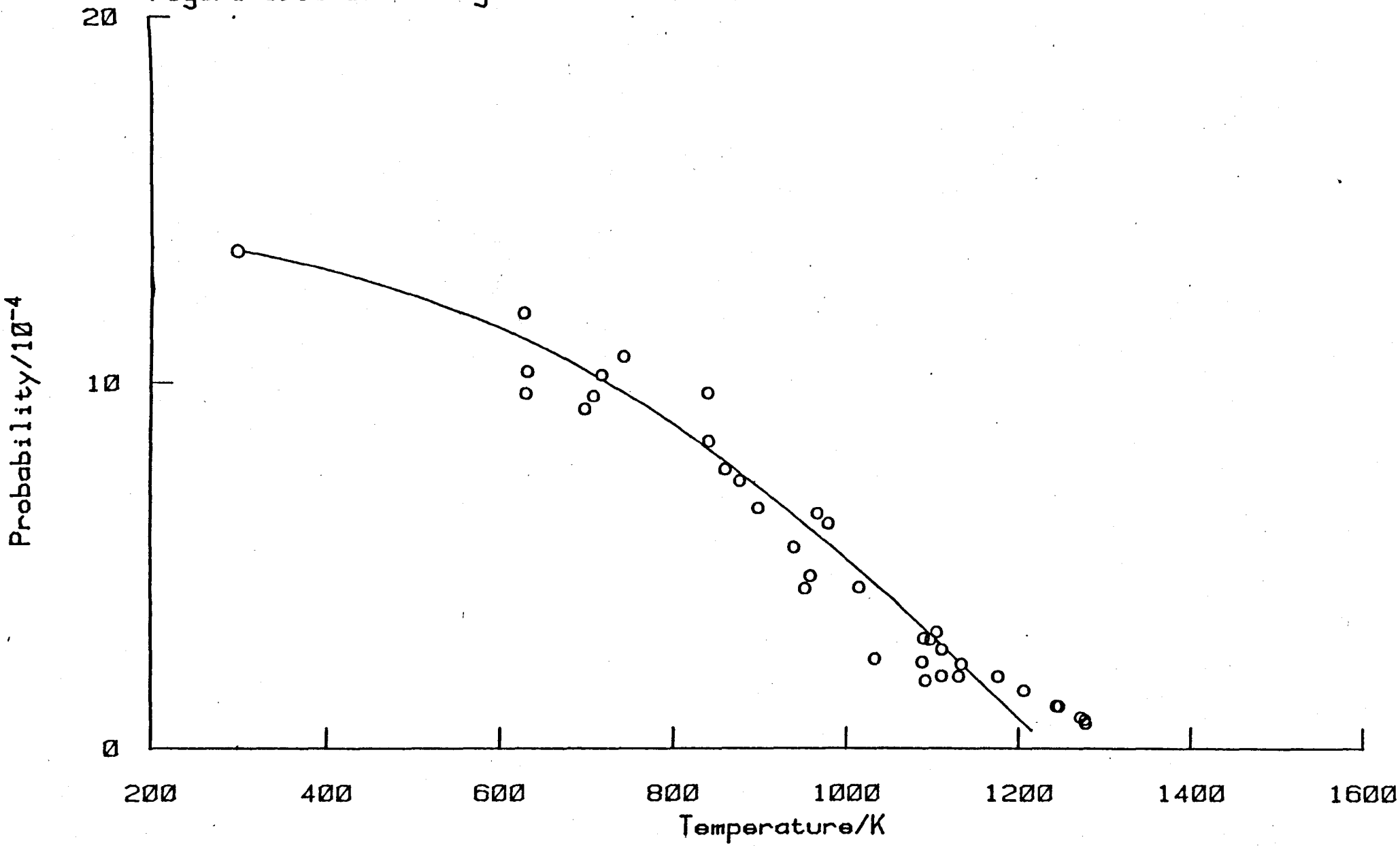

6.5. Studies of Oxygen/Nitrous Oxide Mixtures

After the work on carbon dioxide the next additive chosen was nitrous oxide. It is a triatomic molecule similar in size and bonding to carbon dioxide. The investigation would show whether the quenching by carbon dioxide was an instance of a specific interaction or indicative of a general mechanism.

6.5.1. Determination of the Room Temperature Quenching Rate Constant for Nitrous Oxide.

The quenching rate constant at room temperature for nitrous oxide was determined in a slightly different way to that for carbon dioxide, by a graphical method.

From (3.16) in pure oxygen

$$\frac{I^{634}}{I^{762}} = I = k \left\{ \frac{k_q[O_2] + k_w}{k_p} \right\}$$

where k is a constant.

In a mixtures of nitrous oxide and oxygen

$$\frac{I^{634}}{I^{762}} = I' = k \left\{ \frac{k_q[N_2O] + k_q[O_2] + k'_w}{k_p} \right\}$$

$$(I' - I) = \frac{1}{k_p} \left\{ k_q[N_2O] + (k'_w - k_w) \right\}$$

At a constant partial pressure of oxygen

$$\frac{I' - I}{I} = \frac{k_q[N_2O] + (k'_w - k_w)}{(k_q[O_2] + k_w)}$$

Re-arranging

$$\left\{ \frac{I' - I}{I} (k_q[O_2] + k_w) \right\} - (k'_w - k_w) = k_q[N_2O] \qquad (6.13)$$

Table 6.9

Determination of Room Temperature Quenching Rate Constant for Nitrous Oxide

Pressure /torr	$I^{'}$	I $/10^{-2}$	L.H.S.	$[N_2O]$ $/mol\ l^{-1}\ 10^{-5}$
4.71	0.19			
4.87		1.23	769	1.33
5.20	0.19			
5.37		1.22	788	1.47
6.72	0.23			
7.00		1.19	1063	1.90
8.20	0.28			
8.48		1.30	1293	2.32
5.16	0.43			
5.63		1.20	1881	3.08
6.06	0.49			
6.55		1.27	2180	3.58
7.50	0.59			
8.10		1.31	2664	4.43
8.44	0.65			
9.16		1.32	3082	5.00

Figure 6.19

Room Temperature Quenching

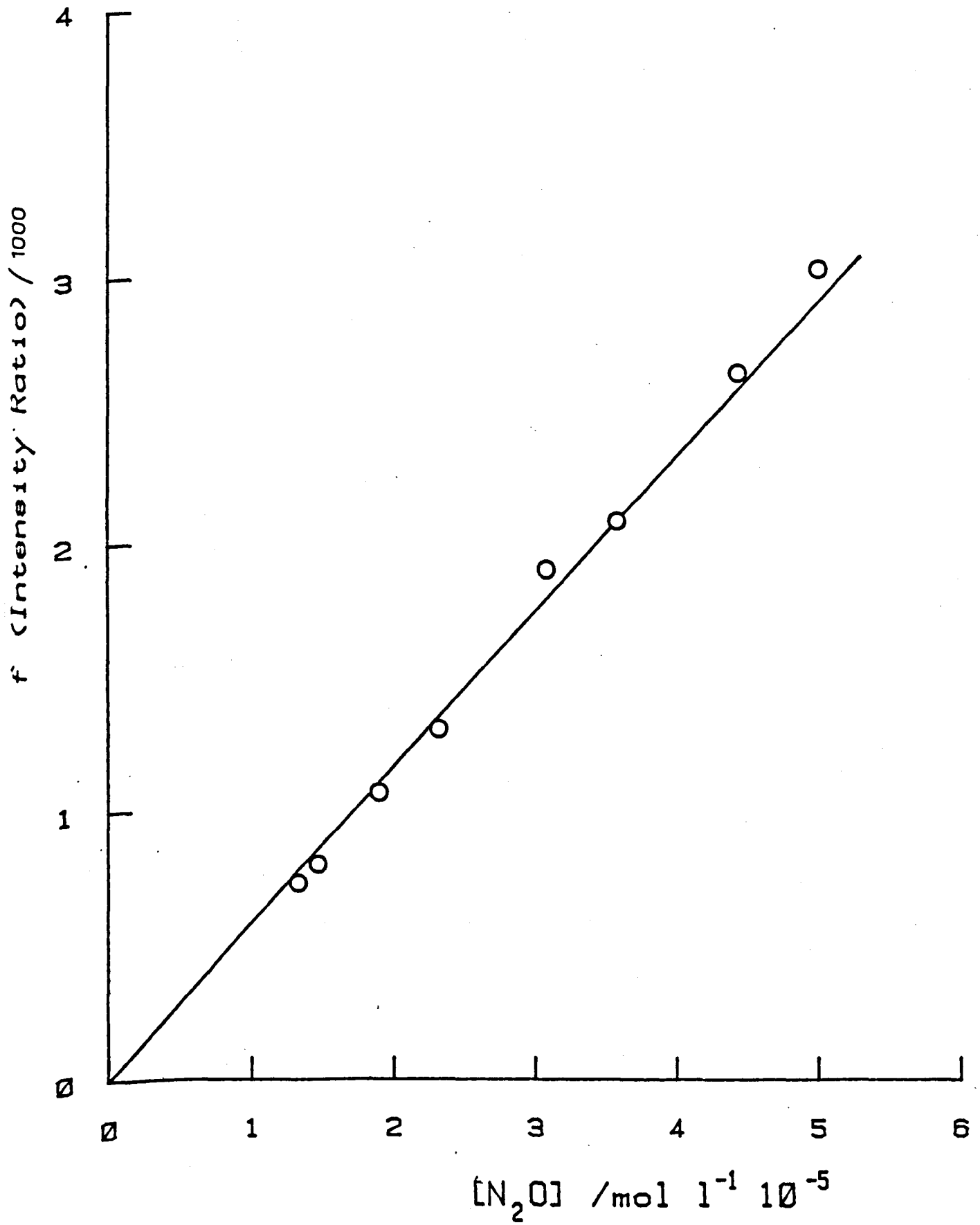

Table 6.10

Nitrous Oxide Quenching Rate Constants

Value /l mol^{-1} s^{-1} 10^7	Reference
4.2	95
8.1	50
4.5	96
5.88	this work

Of the terms on the left had side of (6.13) $k_q(O_2)$ is known, k_w and k'_w can be calculated at any pressure using (3.18) and the intensity ratios can be measured. Hence the quenching rate constant for nitrous oxide can be determined from a plot of the left hand side of (6.13) against concentration of nitrous oxide.

Intensity ratios were monitored in the same way as in the case of oxygen/carbon dioxide mixtures. In this case the pressure varied between 4 and 10 torr, the results are listed in Table 6.9 and plotted in figure 6.19. The rate constants obtained from the gradient is $5.88 \pm 0.3 \times 10^7$ ℓ mol^{-1} s^{-1} where the error is two standard deviations. This results can be seen to agree well with the previous estimates in Table 6.10.

The linearity of the plot indicates the stability of the room temperature conditions. Most experiments in this apparatus are carried out at pressures of about 6.5 torr. The results of the relative emission studies reported in Chapter 4 showed that atomic oxygen was being removed efficiently at this pressure. As the pressure changes the efficiency of removal of atomic oxygen changes, becoming less efficient at lower pressures as the gas is swept faster past the mercury surface. The fact that the plot is linear shows that the mercury surface is effective in removing oxygen atoms across this pressure range.

6.5.2. High Temperature Studies of Oxygen/Nitrous Oxide Mixtures.

A series of shock experiments were performed on mixtures containing 5 and 10% nitrous oxide. The emission at 634 nm and 762 nm were monitored, the behaviour of the 762 nm emission is described below, that of the 634 nm emission in the next section.

Figure 6.20

The Shock Emission at 762nm

Run C214 90% O_2. 10% N_2O

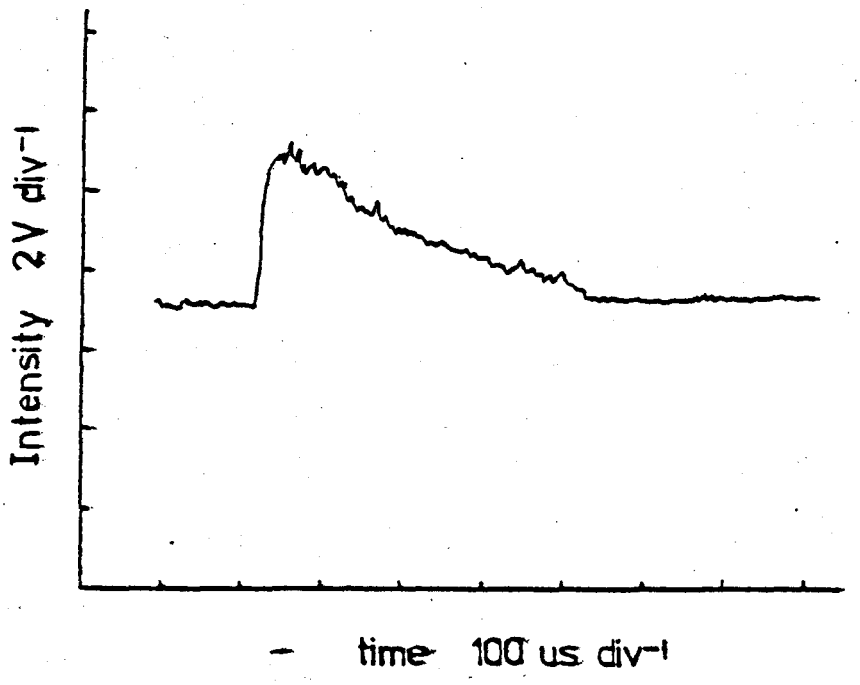

Results

The Shock Trace

The emission trace at 762 nm from a mixture of oxygen and nitrous oxide is shown in figure 6.20. It can be seen to display the expected shape and to be similar to that obtained from carbon dioxide mixtures. In this case the enhancement factor K^{762} rises from 8.7 at 917 K to 37.8 at 1383 K in mixtures containing 10% nitrous oxide.

The rate constant for quenching by nitrous oxide at room temperature is about half that of carbon dioxide. The size of the enhancement factor shows that the overall quenching rate constant increases slightly with temperature. The relaxation zones are therefore about the same size as for oxygen/carbon dioxide mixtures.

The Collisional Quenching of $O_2(^1\Sigma_g^+)$ by Nitrous Oxide

The overall quenching rate constants calculated from the fitted relaxation constants are plotted against temperature in figure 6.21. The points are scattered with no separation between the different mixtures.

The observed quenching rate constants are about the same as for the carbon dioxide mixtures, about 10^7 ℓ mol^{-1} s^{-1}. Therefore the relaxation time and integration time are again comparable. This means that again the relaxation constants are not accurately measured.

The Energy Pooling Reaction

The rate constants for the energy pooling reaction, determined from the quenching rate constants are plotted in figure 6.22. Once again the line is the best line established by previous work.

The effect of the rapid relaxation is apparent. At lower temperatures (> 1200 K) the measured rate constants agree well with the previous results. Above 1200 K, where the relaxation is faster

Figure 6.21 Quenching Rate Constants

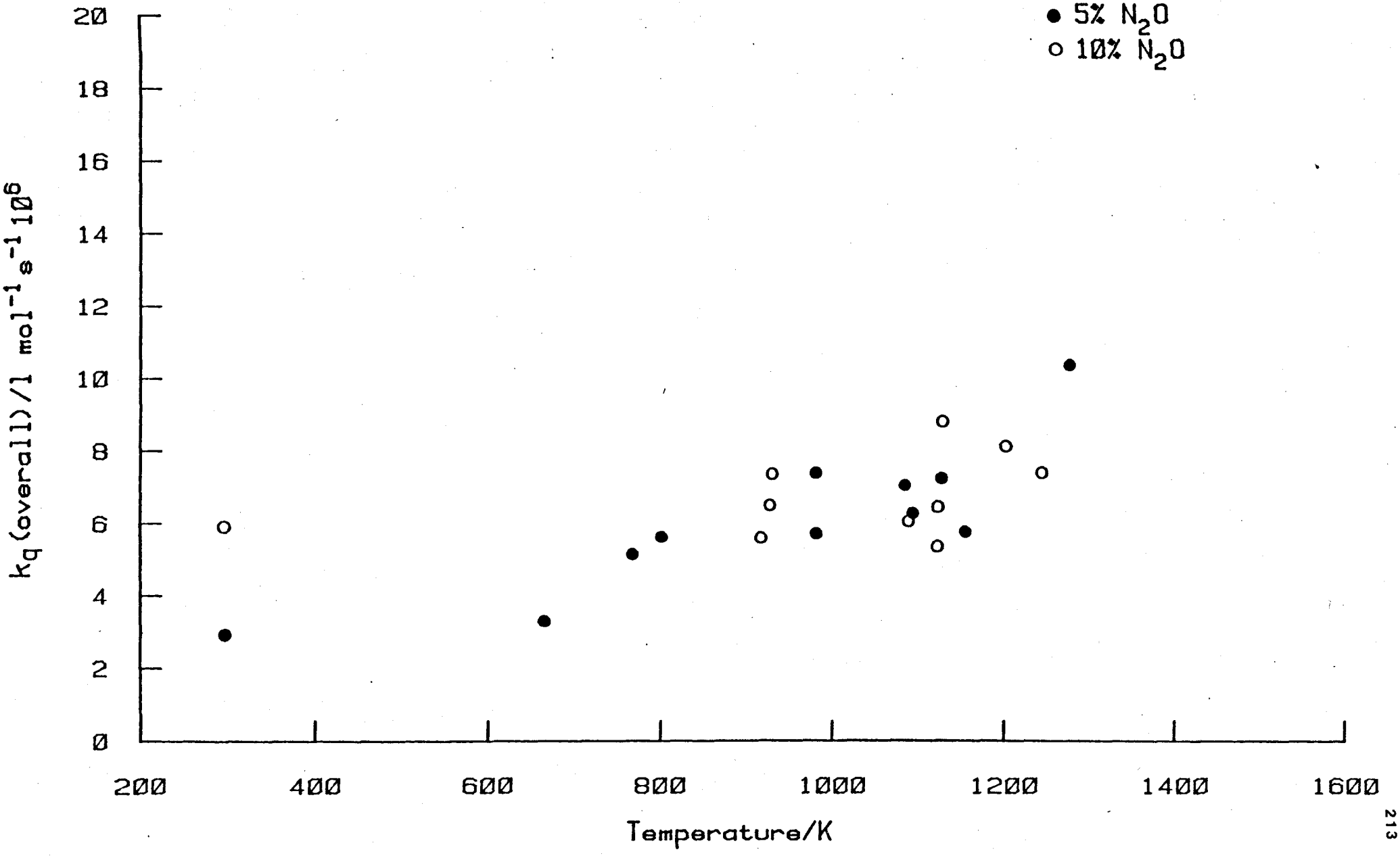

Figure 6.22 Energy Pooling Reaction Rate Constants

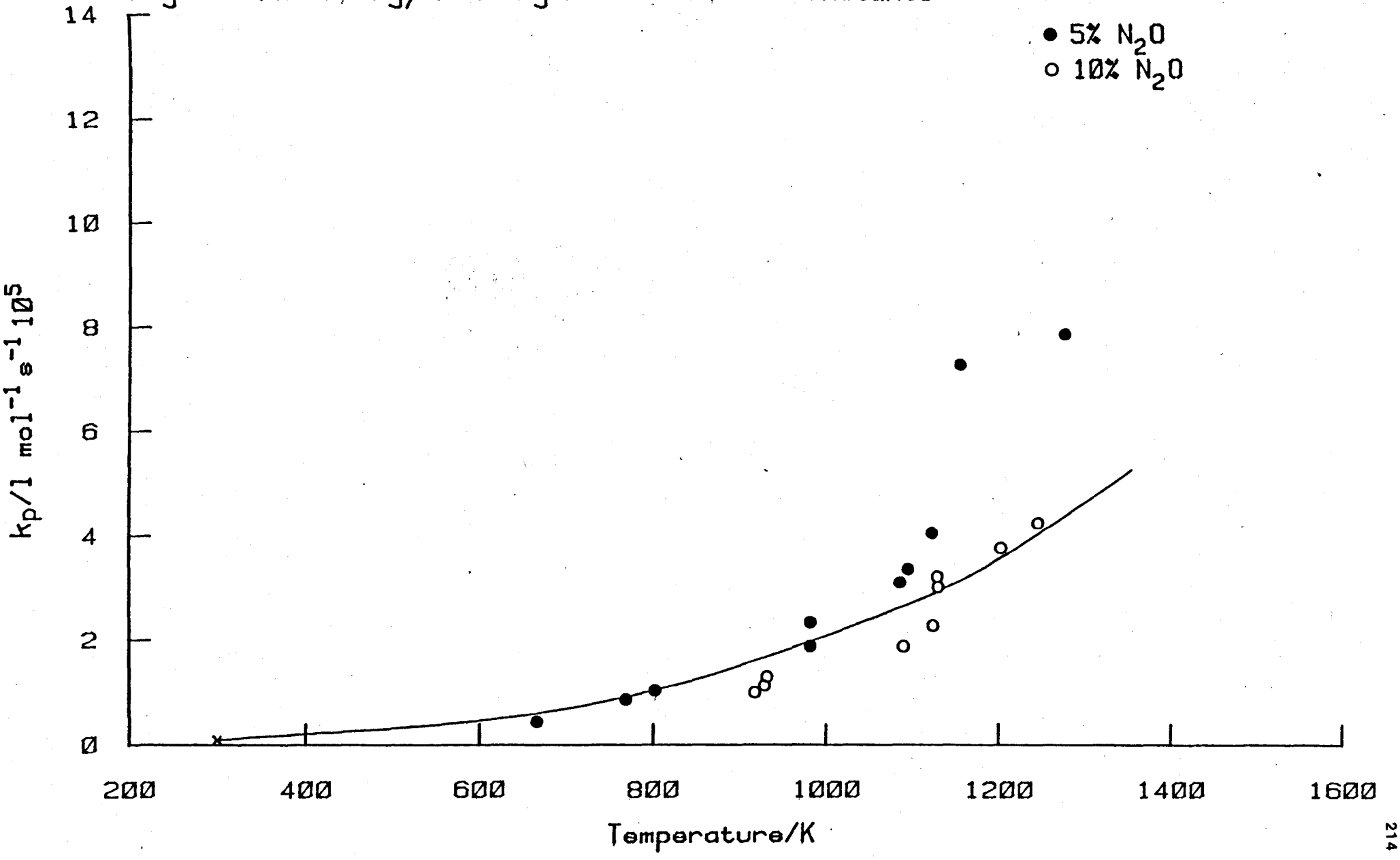

because of the larger quenching rate constant (see figure 6.21) the measured values start to become more scattered. These results do show however that the energy pooling reaction is occurring at the same rate as in other mixtures, as would be expected from the previous work in nitrogen, argon and carbon dioxide mixtures.

The Collisional Quenching of $O_2(^1\Sigma_g^+)$ by Nitrous Oxide.

The results in figure 6.22 show that the energy pooling reaction is occurring at the same rate as in previous mixtures. The deviation is due to the inaccuracy in the determination of the quenching rate constants from the fitted relaxation constant. It is therefore justifiable to calculate quenching rate constants using the measured enhancement factor and taking the value of the energy pooling rate constant from the best line. This procedure was also adopted in the case of oxygen/carbon dioxide mixtures.

The results obtained by this method are plotted in figure 6.23. It can be seen that, compared to figure 6.21, the scatter is less and the data fall on two separate lines. Lines are drawn through the points from the room temperature values.

Using (6.14) the rate constants for quenching by nitrous oxide can be calculated from the results for the two mixtures

$$k_q = k_q(O_2)X_{O_2} + k_q(N_2O)X_{N_2O} \qquad (6.14)$$

These rate constants are listed in Table 6.11 and plotted in figure 6.24. It can be seen that they fall on one line, confirming the composition dependence (6.14). The rate constant is found to increase to a maximum at 800 K and then to decrease. Similar behaviour was seen in the case of carbon dioxide.

As the quenching reaction again shows a small temperature dependence hence quenching probabilities were calculated. In order to calculate

Figure 6.23 Quenching Rate Constants

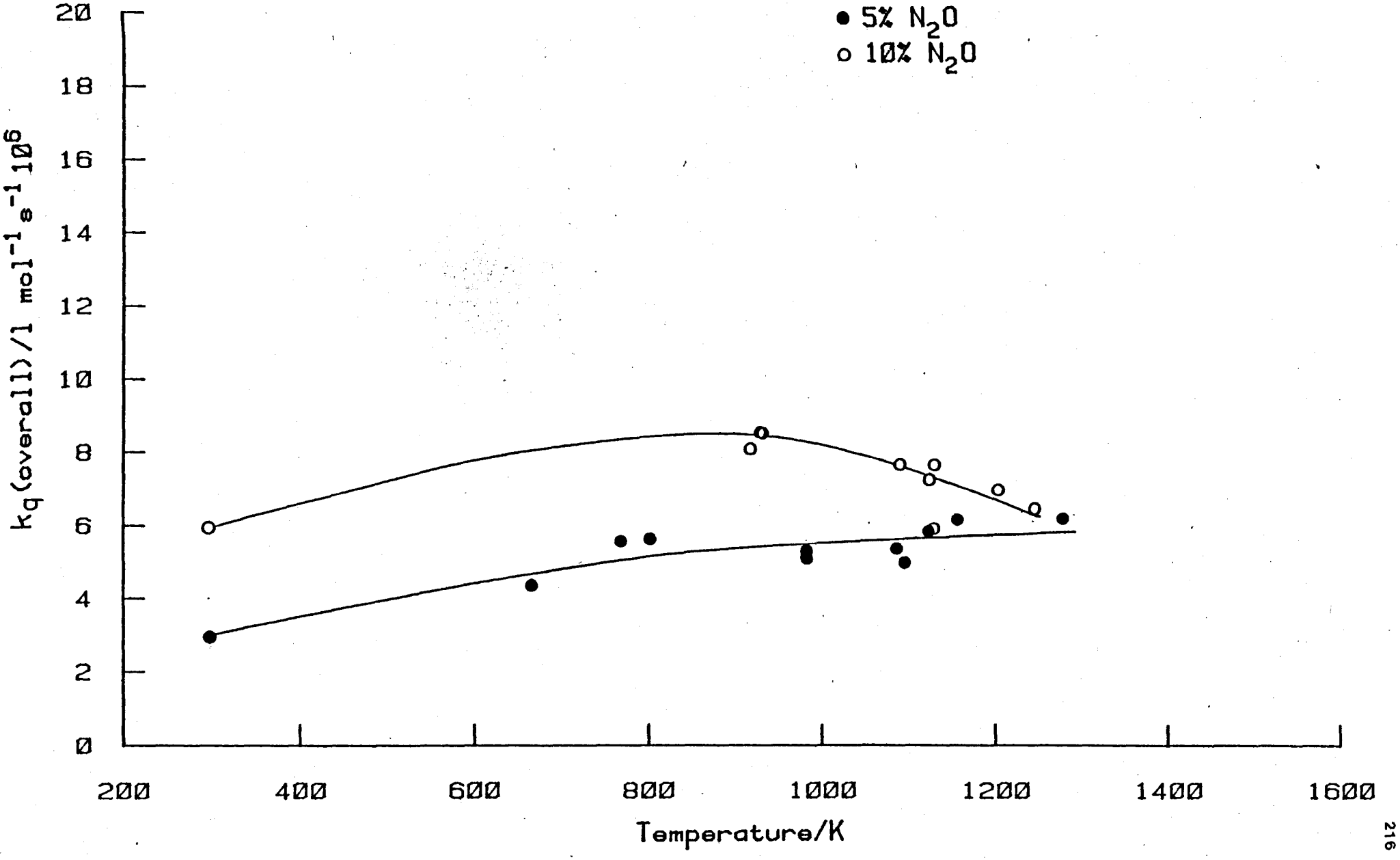

Table 6.11

Analysis of 762nm Emission

90% O_2, 10% N_2O; 28ml s^{-1} ; 100W

Run No.	T /K	k_p(obs) /l mol^{-1} s^{-1} 10^5	k_q(calc) /l mol^{-1} s^{-1} 10^6	$k_q(N_2O)$ /l mol^{-1} s^{-1} 10^7
C214	1129	3.21	5.91	1.83
C215	1090	1.88	7.65	3.91
C216	1130	3.01	7.64	3.57
C217	917	1.00	8.09	5.75
C218	931	1.30	8.51	6.08
C219	928	1.13	8.53	6.20
C223	1124	2.28	7.24	3.19
C226	1203	3.77	6.96	2.24
C227	1193	6.54	7.10	2.42
C228	1245	4.25	6.46	1.29
	95% O_2, 5% N_2O; 28ml s^{-1} ; 100W			
16A	1095	5.36	4.77	2.56
17A	1086	3.11	5.29	2.79
24A	982	1.89	5.12	4.35
25A	982	2.35	5.31	4.73
26A	666	0.44	4.38	6.73
27A	1123	4.06	5.84	3.23
28A	1156	7.29	6.36	3.60
29A	1277	7.87	6.19	0.79
31A	769	0.87	5.59	8.14
32A	802	1.04	5.65	7.88

Figure 6.24 Quenching Rate Constants for Nitrous Oxide

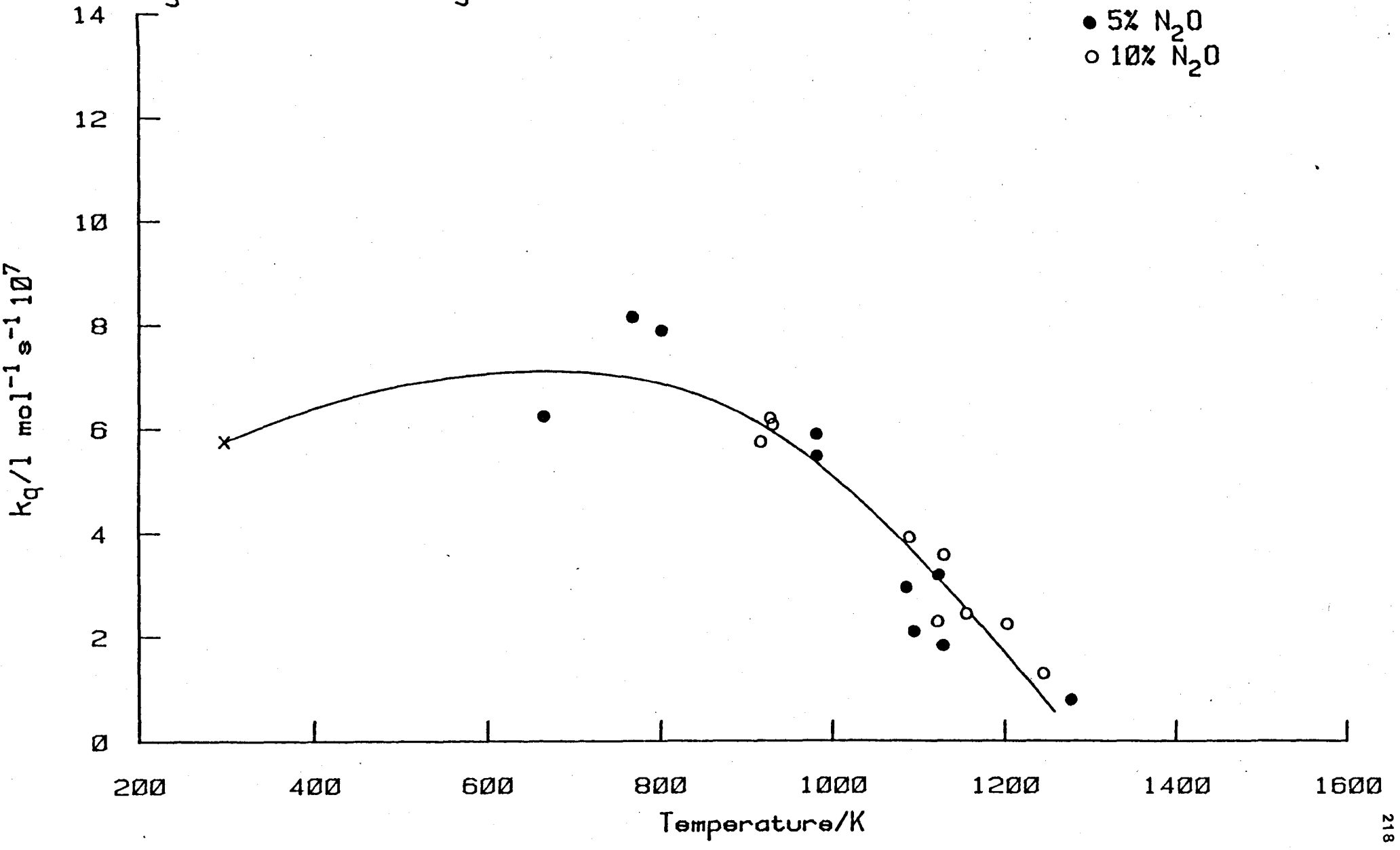

Figure 6.25 Quenching Probabilities for Nitrous Oxide

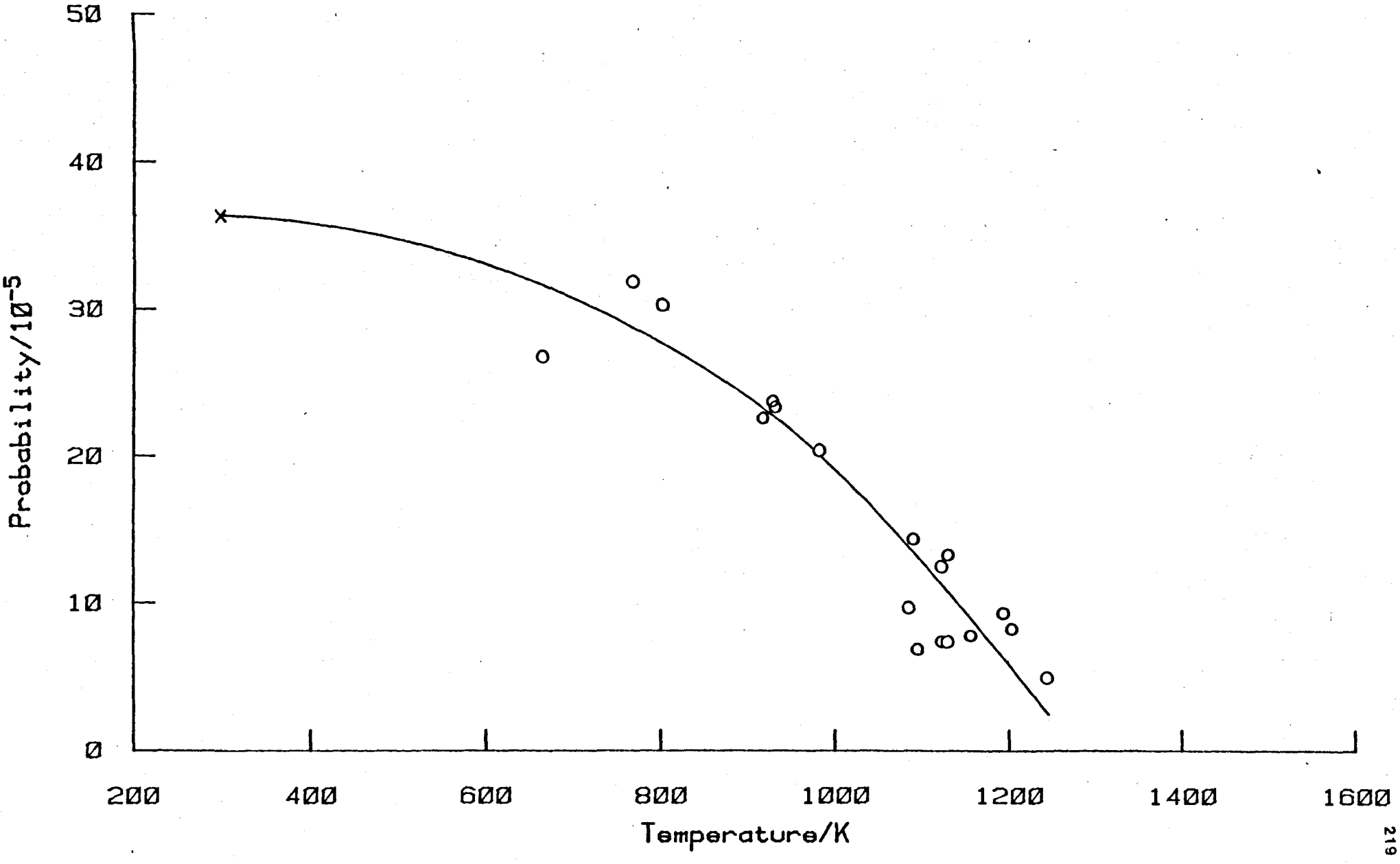

collision numbers it is necessary to know the molecular diameter. This was calculated for nitrous oxide using data that was available for carbon dioxide. Viscosity is a property that depends on molecular diameter[72] hence

$$\sigma(N_2O) = \sigma(CO_2) \left\{ \frac{\eta(N_2O)}{\eta(CO_2)} \right\}^{\frac{1}{2}}$$

where $\sigma(CO_2) = 0.46$ nm

$\eta(N_2O) = 1.51 \times 10^{-5}$ Pa s

$\eta(CO_2) = 1.46 \times 10^{-5}$ Pa s

This yields a value for the molecular diameter of nitrous oxide of 0.47 nm. This value is directly comparable with those for oxygen and nitrogen which were also obtained from viscosity data.

Using this value for the molecular diameter of nitrous oxide collision numbers and hence quenching probabilities were calculated. These are plotted against temperature in figure 6.25. This graph may be compared with that for the rate constant, figure 6.24. The probability curve does not show a maximum and has a steeper descent at higher temperatures.

6.5.3. The Dissociation of Nitrous Oxide in the Shock.

In this chapter the form of the 762 nm emission trace from various mixtures has been described. These traces have then been analysed to yield data on the quenching and energy pooling reaction of sigma. As two emission traces can be captured from each shock the dimol emission at 634 nm was generally recorded as well. This was the source of the results in carbon dioxide mixtures discussed in relation to the hot band emission in Chapter 4. In all mixtures previously mentioned the 634 nm emission has been found to behave in exactly the same way as in pure oxygen, to show the form described in Chapter 4. However

Figure 6.26

a) The Shock Emission at 634nm
Run C221 90% O_2, 10% N_2O

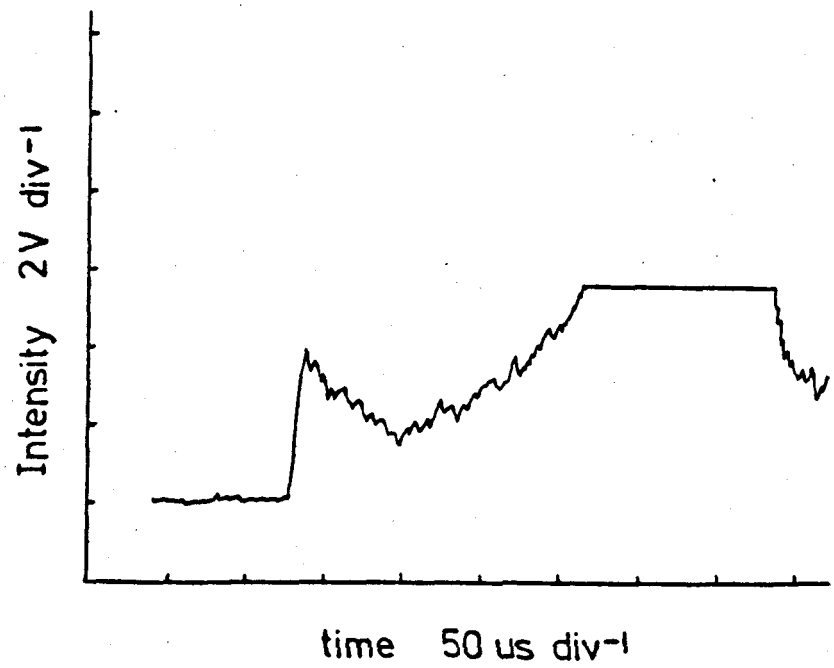

The Shock Emission with Discharge off
Run C224 90% O_2, 10% N_2O

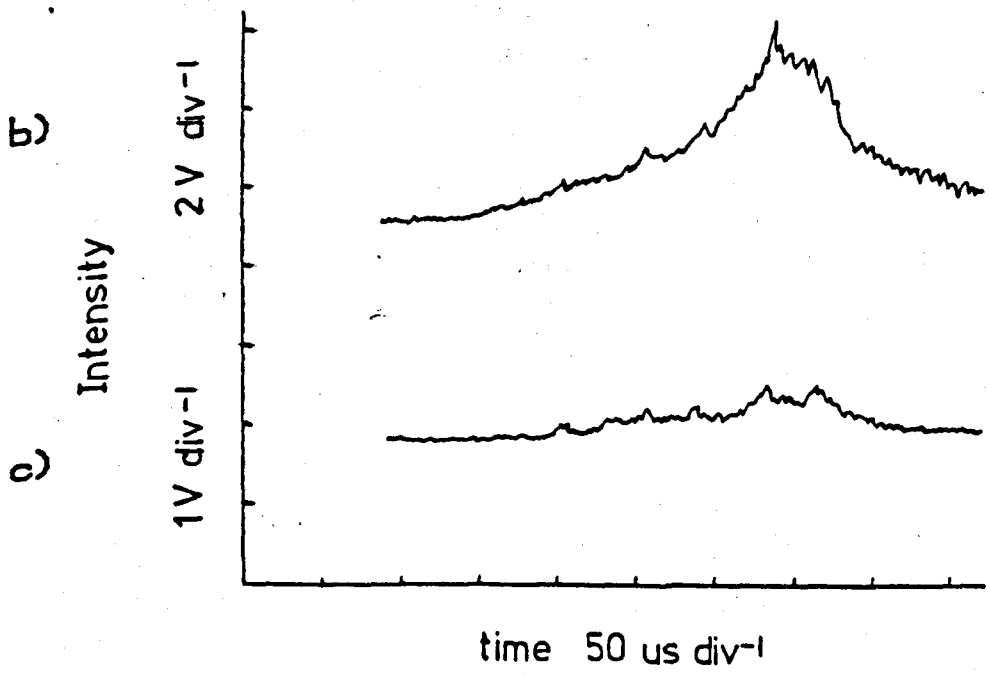

the 634 nm traces from nitrous oxide mixtures at temperatures above 1200 K showed a different form to that expected. While the increase at the shock front and the decay were apparent the emission intensity increased rapidly towards the end of the trace generally causing saturation of the transient recorder (see Figure 6.26a).

Two features were immediately noted about this spurious emission. Firstly it showed a marked temperature dependence, it was not visible on 634 nm traces below 1200 K. Secondly it was not visible on 762 nm traces at any temperature.

To help identify the source of the glow some shock experiments were performed on undischarged oxygen/nitrous oxide mixtures, a resultant 634 nm trace is shown in figure 6.26b. It can be seen that the emission becomes apparent 100 μs after the arrival of the shock front and then increases in intensity. The rapid decrease marks the end of hot-flow time. A 762 nm trace from the same shock is shown in figure 6.26c. The negligible level of emission at this wavelength is apparent (figures 6.26b and 6.26c also show that the 634 nm and 762 nm emissions are absent when the discharge is off).

The conclusions to be drawn from these observations are that the extra emission does not depend on the presence of singlet oxygen, but does on the presence of nitrous oxide. That it shows a marked temperature dependence, an incubation time and has a maximum in intensity to the shorter wavelength side of 762 nm.

One candidate which fits all these criteria is the chemiluminescent associative reaction

$$NO + O \rightarrow NO_2 + h\nu \qquad (6.15)$$

This reaction is widely used to detect oxygen atoms[1]. It gives rise to a broad band emission with a maximum at 630 nm. This maximum

emphasises the need for the removal of oxygen atoms when studying singlet oxygen, particularly delta, in a discharge flow system. The small amount of nitrogen present in cylinder oxygen may lead to the formation of nitrogen atoms in the discharge and hence to nitric oxide.

The fact that the glow is not visible in the absence of singlet oxygen eliminates such energy transfer processes as

$$NO_2 + O_2(^1\Delta_g) \rightarrow NO_2^* + O_2(^3\Sigma_g^-)$$

So the most likely source is the reaction (6.15). This would necessitate the prior dissociation of nitrous oxide.

Monat, Hanson and Kruger[97] have studied the dissociation of nitrous oxide is a shock tube. Using their dissociation scheme the reaction sequence giving rise to the emission would be

1.	$N_2O + M \rightarrow N_2 + O + M$;	k_1
2.	$N_2O + O \rightarrow 2NO$;	k_2
3.	$N_2O + O \rightarrow N_2 + O_2$;	k_3
4.	$NO + O \rightarrow NO_2 + h\nu$;	k_4

They determined following expressions for the rate constants (in $\ell\ mol^{-1}\ s^{-1}$); energies are in $kJ\ mol^{-1}$.

$$k_1 = 1.42 \times 10^{11} \exp(-214.7/RT)$$
$$k_2 = k_3 = 6.23 \times 10^{10} \exp(-102.7/RT)$$

At 1400 K these yield the following rate constants

$$k_1 = 1.38 \times 10^3\ \ell\ mol^{-1}\ s^{-1}$$
$$k_2 = k_3 = 9.1 \times 10^6\ \ell\ mol^{-1}\ s^{-1}$$

Reaction 1 starts the reaction sequence. The oxygen atoms so formed react via reaction 2 to form nitric oxide which combines with an oxygen atom in the chemiluminescent reaction 4. Reaction 1 is slow compared to 2 and 3 and so is rate determining. The incubation time seen in figure 6.26b is due to the time taken for reaction 1 to produce an appreciable concentration of oxygen atoms.

The expression for the change in nitrous oxide concentration is

$$\frac{-d[N_2O]}{dt} = k_1[N_2O][M] + (k_2 + k_3)[N_2O][O]$$

At early times the only reaction which proceeds significantly is 1, because of the low oxygen atom concentration. Therefore

$$\frac{-d[N_2O]}{dt} = k_1[N_2O][M]$$

Assuming an initial pressure of 6.5 torr. At 1400 K $\rho_{21} = 6$ therefore $[M] = 2.1 \times 10^{-3}$ mol l^{-1}

At 300 μs after the arrival of the shock front

$$\frac{-d[N_2O]}{[N_2O]} = k_1[M]t$$
$$= 8.7 \times 10^{-4}$$

Therefore after 300 μs less than 0.1% of the nitrous oxide has dissociated. As well as this negligible effect on the concentration of nitrous oxide this result shows that the production of atomic oxygen is also negligible. This is significant because of the known effect of atomic oxygen on singlet oxygen kinetic measurements.

The conclusions are that the dissociation of nitrous oxide, though it gives rise to a noticeable emission at 634 nm has no effect on the analysis of 762 nm traces. The emission level at 762 nm is

negligible, even at long times. The removal of nitrous oxide (and concomitant production of atomic oxygen) is negligible during the time of study. Consequently the 762 nm traces from shock heated oxygen/nitrous oxide mixtures were analysed in the usual way and the effect on the results of the dissociation of nitrous oxide is negligible.

Chapter 7

THE COLLISIONAL QUENCHING OF $O_2(^1\Sigma_g^+)$

7.1. Introduction

In this chapter the temperature dependences and possible mechanism of the quenching reactions

$$O_2(^1\Sigma_g^+) + O_2 \rightarrow O_2(^1\Delta_g) + O_2 \qquad (6.5)$$

$$O_2(^1\Sigma_g^+) + N_2 \rightarrow O_2(^1\Delta_g) + N_2 \qquad (6.6)$$

$$O_2(^1\Sigma_g^+) + Ar \rightarrow O_2(^1\Delta_g) + Ar \qquad (7.1)$$

$$O_2(^1\Sigma_g^+) + CO_2 \rightarrow O_2(^1\Delta_g) + CO_2 \qquad (7.2)$$

$$O_2(^1\Sigma_g^+) + N_2O \rightarrow O_2(^1\Delta_g) + N_2O \qquad (7.3)$$

and of the energy pooling reaction

$$O_2(^1\Delta_g) + O_2(^1\Delta_g) \rightarrow O_2(^1\Sigma_g^+) + O_2(^3\Sigma_g^-) \qquad (1.20)$$

are discussed. Initially the general mechanism of quenching and energy transfer are reviewed. This follows the format of the reviews adopted by Cundall,[98] Callear and Lambert[99], Callear[100] and Lenont and Flynn[101] in that two extreme cases of electronic-translation (E-T) energy transfer and electronic-vibration/translation (E-V,T) energy transfer are illustrated; resonant and non-resonant. As the circumstances of E-T energy transfer (quenching by atoms) and E-V,T energy transfer (quenching by molecules) are similar they are dealt with together. Firstly the case of E-T energy transfer where the potential energy surfaces are continuously separated by approximately the same energy.

Figure 7.1 Diagram of E-T Energy Transfer

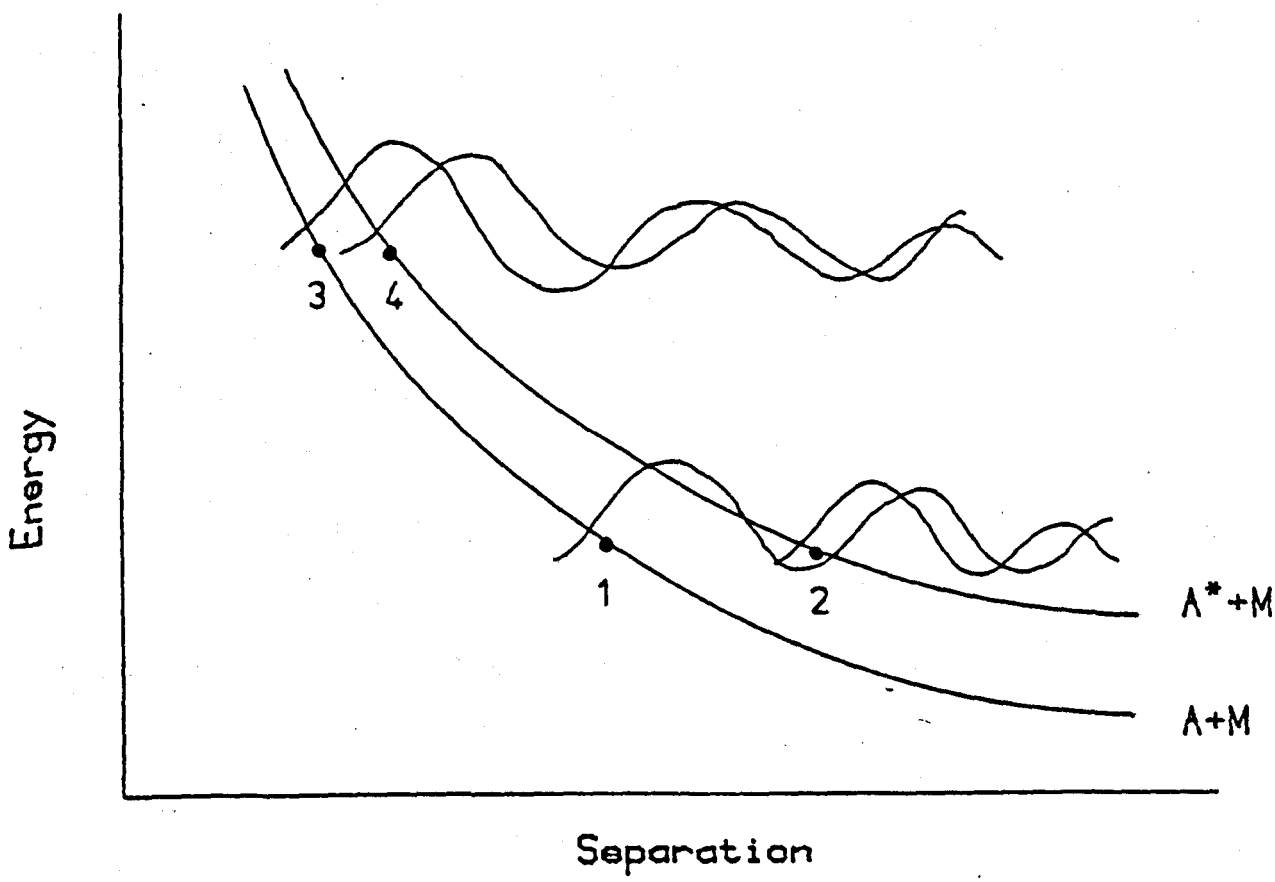

7.2. Resonant Mechanism for E-V,T Energy Transfer

The quenching process under consideration is

$$A^* + M \rightarrow A + M$$

where A^* represents the excited species and M the quenching atom. In figure 7.1 the one dimensional potential energy surfaces are drawn. These curves represent the interaction between the excited or ground state species with the quencher as the separation changes. The turning points occur where the intermolecular repulsion equals the kinetic energy of approach. The efficiency of quenching is dependent on the overlap of translational wavefunctions at the turning points which are also shown in figure 7.1.

At room temperature the turning points 1 and 2 are reached. The degree of overlap of translational wavefunctions at this separation is small and so the quenching process is inefficient. At a higher temperature the turning points 3 and 4 are reached. Here, though the separation in energy of the surfaces is constant the degree of overlap is greater, hence the quenching process is more efficient. Thus for quenching by this mechanism a positive temperature dependence would be expected.

The case of resonant E-V,T energy transfer (resonant quenching) is similar to that described above. The potential energy surfaces are again separated by a constant amount. In figure 7.2 the potential energy curves representing the interaction between the excited or ground state species A with the quencher M are shown. The curve representing the interaction between the ground state species and the quencher in it's first vibrational level is separated from that with the quencher in it's zeroth vibrational level by a constant energy. The overlaps of the translational wavefunctions at any given kinetic energy are shown.

Figure 7.2 Diagram of Resonant E-V,T Energy Transfer

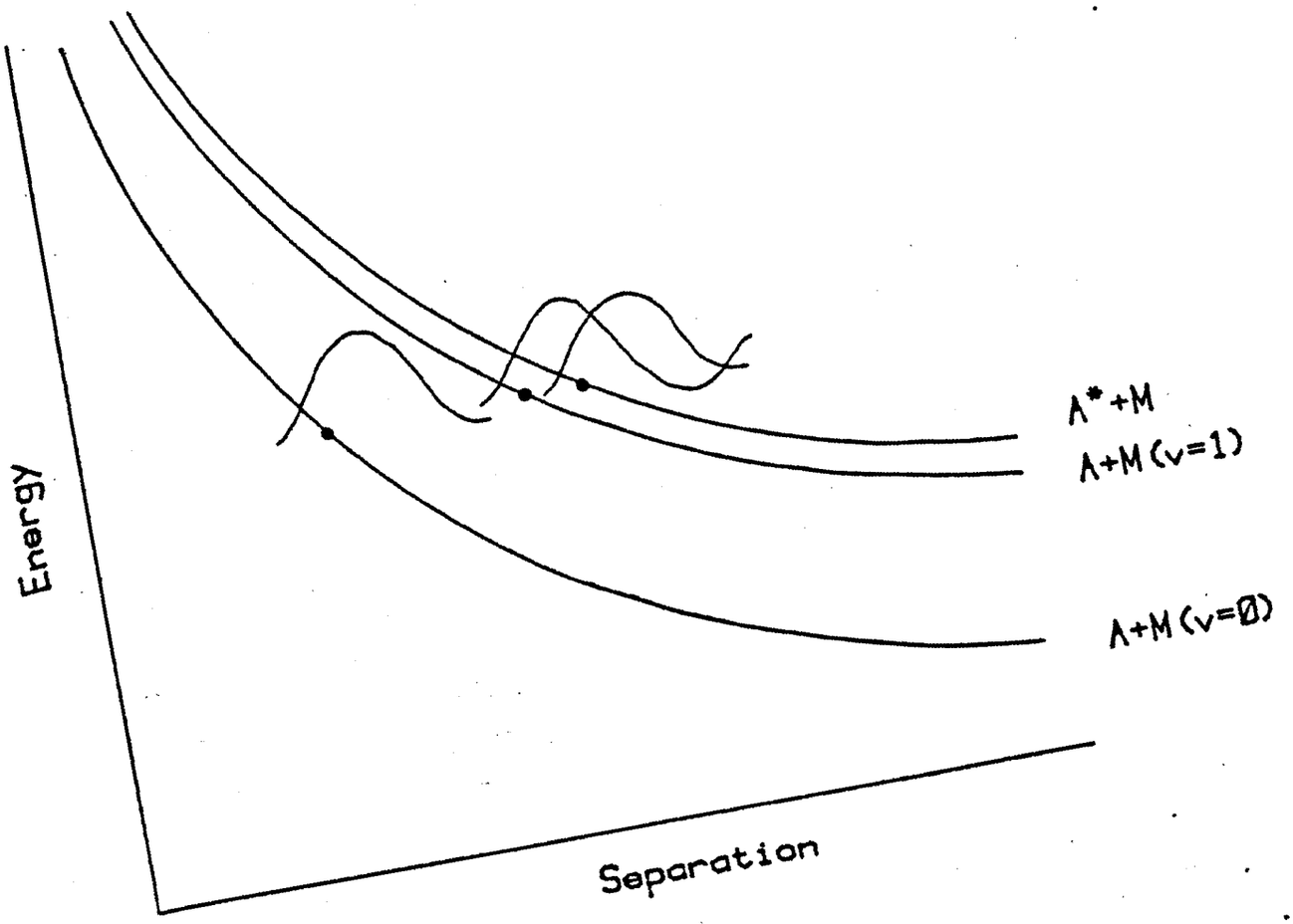

It can be seen that the degree of overlap for the v=1 level is greater than that for the v=o level, consequently the probability of quenching to the v=1 level is greater. This explains the common observation that if quenching occurs by this mechanism one vibrational level of the quencher is predominantly excited.[99] Furthermore as this reaction takes place on the repulsive part of the potential curve the reaction would show a positive temperature dependence.

There is considerable evidence in favour of the importance of vibrational excitation of the quencher in the quenching of sigma. The work of Thomas and Thrush[51] described in Chapter 2 has shown that quenching occurs to delta and not to the ground state. If delta v=o is formed this means there is 62.6 kJ mol^{-1} (5238 cm^{-1}) of energy to be distributed amongst the product molecules.

Kear and Abrahamson[50] have found a correlation between the room temperature quenching rate constant and the highest fundamental vibrational frequency of the quencher. The correlation is of the form

$$\log_{10} k_q = \frac{K\Delta E}{\omega} + C$$

where K and C are constants

ΔE is the sigma-delta energy gap

ω is the quencher vibrational frequency.

Using the data in the literature[89] for the quenching rate constants and vibrational frequencies the correlation is shown for two molecular types in figures 7.3 and 7.4. The relation also holds for a series of substituted alkanes.

Further support for the participation of vibrational excitation comes from the observation that deuteration decreases the quenching rate constant.[1] This isotope effect has been observed for all types of quenchers, diatomic and triatomic molecules as well as alkanes.

Figure 7.3

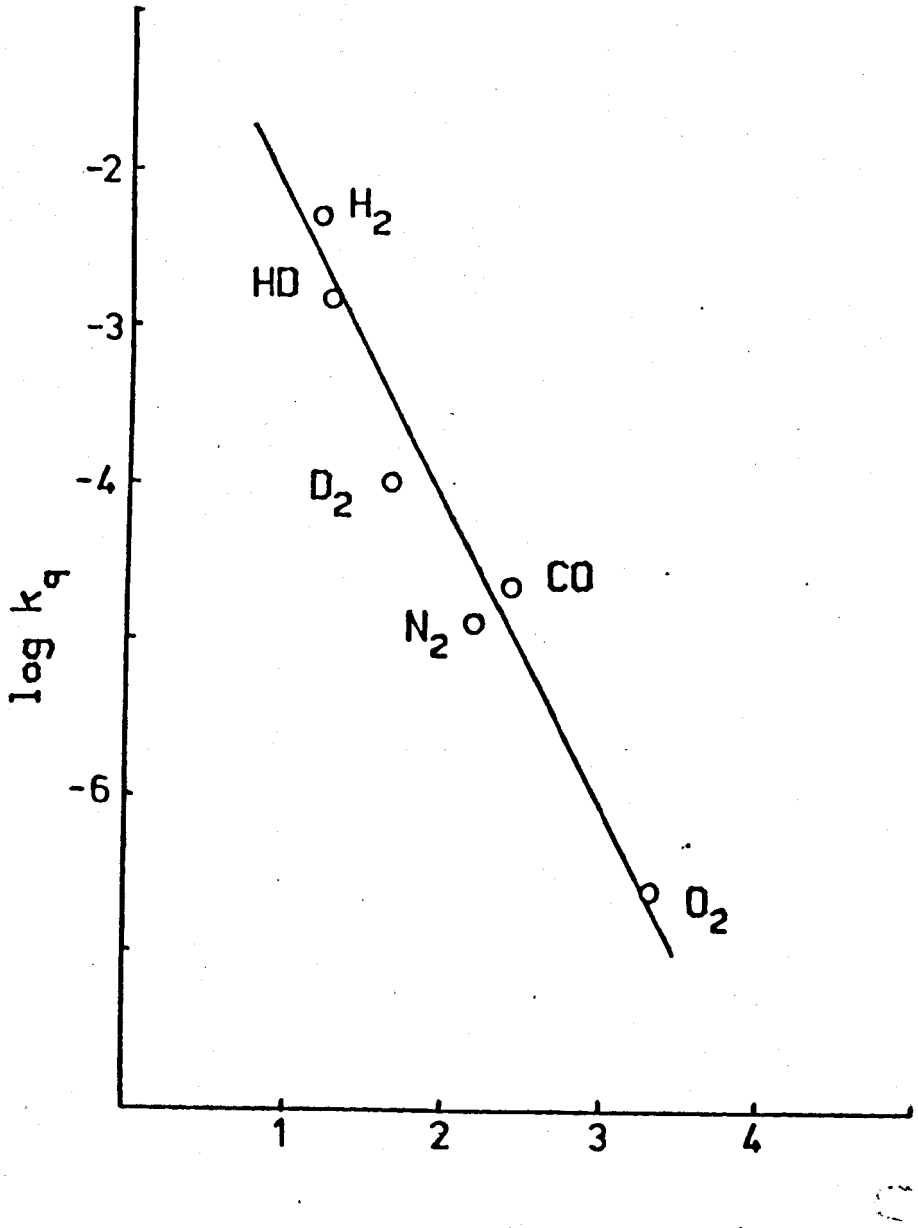

Figure 7.4

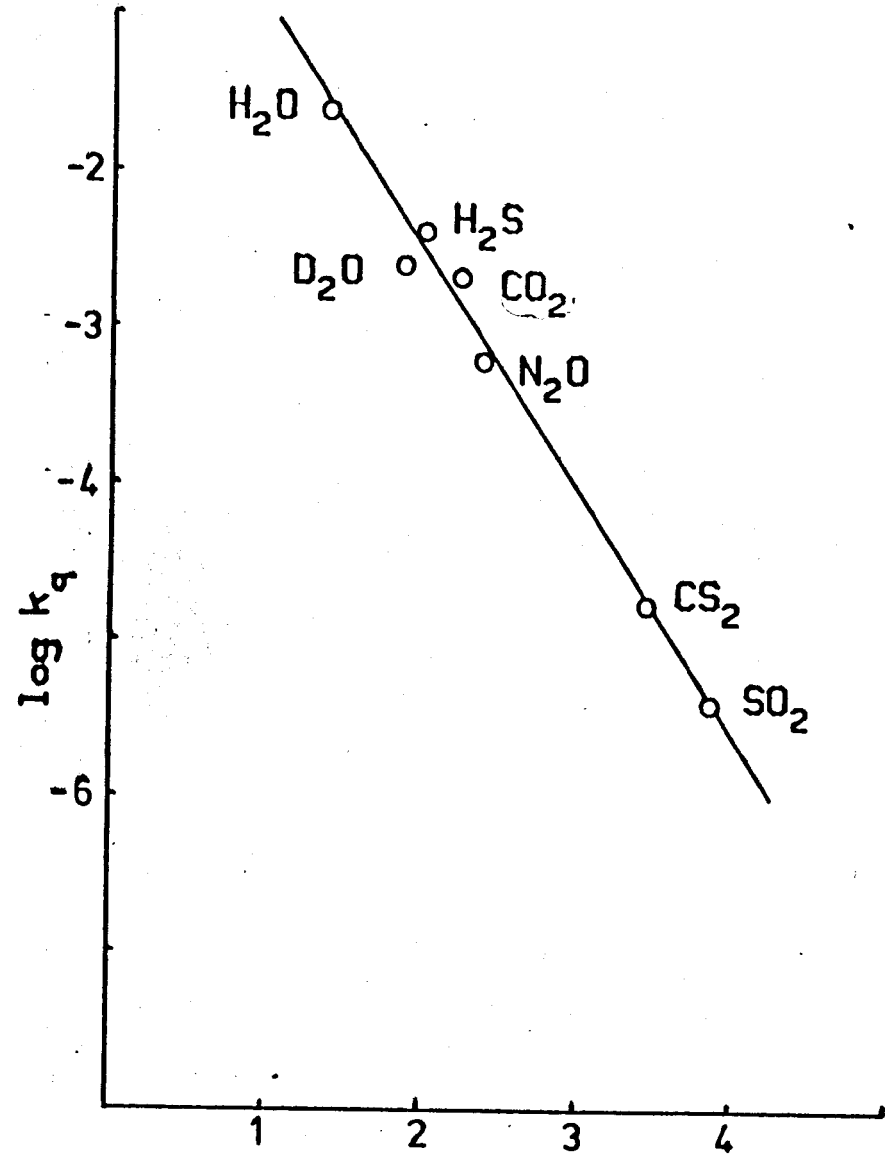

It has been ascribed to a Franck-Condon effect on the oxygen transition.[54] In the quenching by hydrogen and deuterium Ogryzlo et al[54] identified the following reactions

$$O_2(^1\Sigma_g^+) + H_2 \rightarrow O_2(^1\Delta_g) + H_2(v=1) \qquad (7.4)$$

$$O_2(^1\Sigma_g^+) + D_2 \rightarrow O_2(^1\Delta_g)v=1 + D_2(v=1) \qquad (7.5)$$

The lower vibration frequency of deuterium (2990 cm^{-1} compared to 4160 cm^{-1}) allows the v=1 level of oxygen to be excited. The bond length in the sigma and delta states is the same consequently the (0,1) transition has an unfavourable Franck-Condon factor. This leads to less efficient quenching by deuterium, a prediction borne out by the rate constants.

Though there is a tendency for energy to appear as vibration in the quencher the link between this and the quenching rate cannot be simply related to the ability of the quencher to become vibrationally excited optically. Homonuclear diatomic molecules can be efficient quenchers, e.g. hydrogen, yet show no intrinsic infra-red absorption. Therefore attempts to relate the quenching rate constant to the extinction coefficient of the quencher at 5238 cm^{-1} (the (0,0) transition $^1\Sigma_g^+ - {}^1\Delta_g$) cannot be correct.[102] Such correlations have however been successful in interpreting the quenching of delta in solution.[1]

Two theoretical models which stress the conversion of electronic energy into vibrational energy have been proposed. The first approach, that of Kear and Abrahamson,[50] was based on the assumption that the interaction that lead to quenching occurred at short range i.e. on the repulsive part of the intermolecular potential. In their calculations

they assumed a value for the electric dipole matrix element for the sigma-delta transition of unity. As this transition is forbidden this value represents an upper limit, consequently the calculated rate constants do also. The vibrational matrix elements were calculated for oxygen and the quenching molecule from Franck-Condon factors and harmonic oscillator wavefunctions respectively. Some values calculated the short range interaction theory (SRIT) are listed in Table 7.1. They can be seen to be an order of magnitude too low.

Ogryzlo and co-workers[6,54,55] have approached the modelling of the quenching of sigma from a different direction. They assumed that the dominant interaction in the process occurred at long range, an interaction between the transition quadrupole for the transition of oxygen and the transition dipole or quadrupole on the quencher. The results of their calculations are also listed in Table 7.1. The values can again be seen to be generally low but nearer the experimental values than those calculated using SRIT. In the case of the quenching by HD and D_2 the estimates are very accurate.

Ogryzlo et al[6] also made the first temperature dependent studies of the quenching of sigma. The temperature dependence might reveal which interaction is dominant in the reaction with a particular quencher. Figure 7.2 shows that the short range interaction will lead to a positive temperature dependence as the turning points come closer together higher up the repulsive wall of the potential surface. Conversely if quenching occurs via a long range mechanism a negative temperature dependence will be observed as the velocity through the interaction region increases.

Table 7.1

Comparison of Experimental and Calculated Sigma Quenching Rate Constants

Quencher	Experimental	Calculated	
		S.R.I.	L.R.I.
		k /l mol^{-1} s^{-1}	
H_2	6.0×10^8	1.8×10^8	3.6×10^8
HD	1.5×10^8	3.0×10^6	1.0×10^8
D_2	1.2×10^7	9.2×10^5	1.2×10^7
NO	3.0×10^7		9.3×10^6
CO	2.0×10^6	3.1×10^4	2.5×10^6
HBr	2.3×10^8	1.2×10^8	1.2×10^8

Quenching by hydrogen was the first reaction investigated

$$O_2(^1\Sigma_g^+) + H_2 \rightarrow O_2(^1\Delta_g) + H_2(v=1) \qquad (7.4)$$

In the temperature range studied, 173-393 K the rate constant was found to increase. However the rate constants calculated using the two models also increased. It is suggested that this is due to the fact that (7.4) is not near resonance (ΔH = 12.8 kJ mol^{-1}, 1078 cm^{-1}). Rotational excitation of the quencher allows the reaction to come closer to resonance. Ogryzlo et al had modified the long and short range theories to take rotational changes in oxygen and the quencher into account. As the degree of rotational excitation increases with the temperature both calculated rate constants were found to as well.

Following this Ogryzlo and co-workers[55] next chose to study a quencher nearer resonance, hydrogen bromide.

$$O_2(^1\Sigma_g^+) + HBr \rightarrow O_2(^1\Delta_g) + HBr(v=2)$$

Again they determined the quenching rate constant in the temperature range 173-393 K and compared it to values calculated using the two models, figure 7.5. It was found that the measured rate constant increased slightly with temperature. The rate constant calculated using the SRIT increased with temperature while that for the LRIT decreased. Both predictions were low and it was found that the experimental behaviour was bestreproduced by the addition of the two contributions. This would apparently indicate that both quenching mechanisms were operative. However these results, because of the narrow temperature range studied are inconclusive. It can be seen from figure 7.5 that the change in experimentally measured rate constant is not large, being scarcely more than the experimental error. This lack of a marked temperature dependence for HBr was a reason for it's rejection

in favour of carbon dioxide and nitrous oxide in this study.

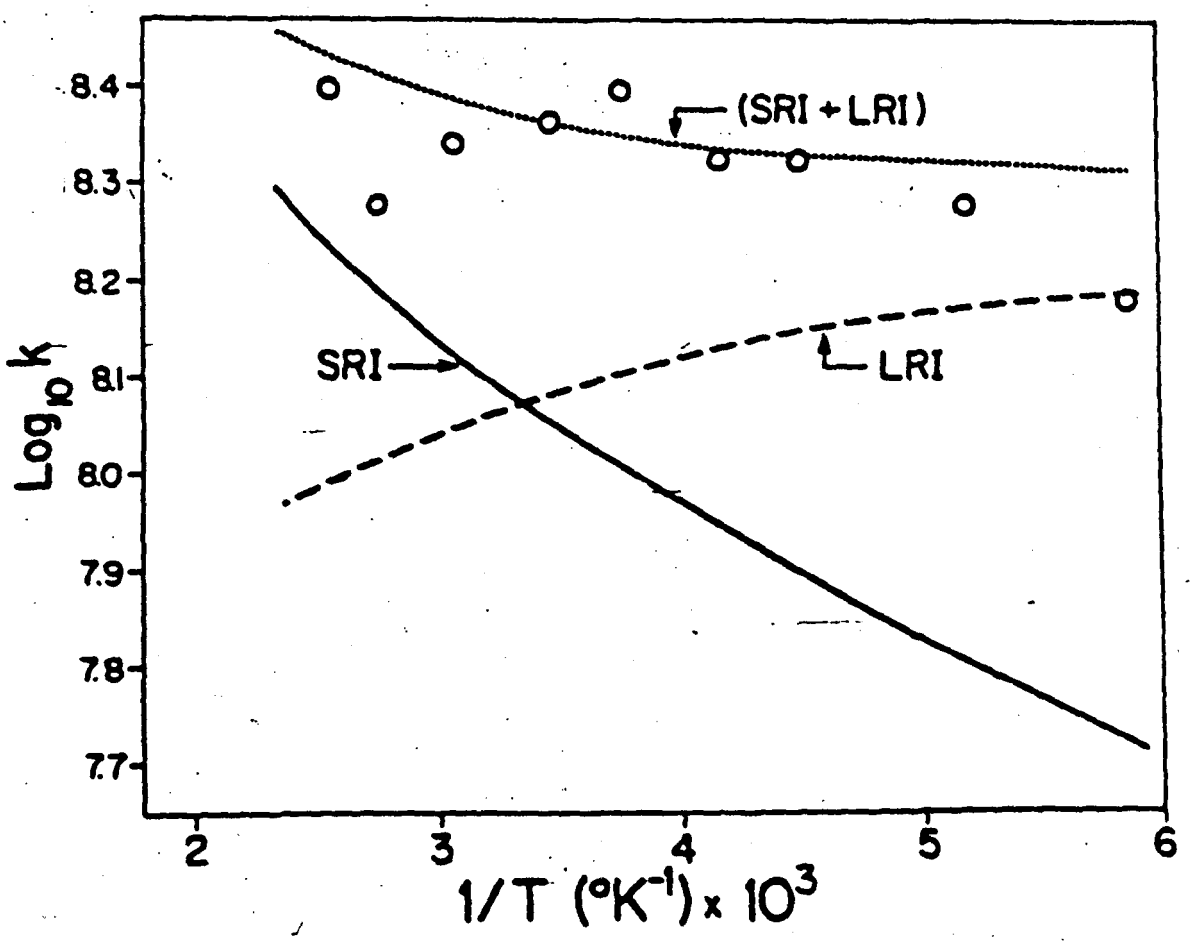

Figure 7.5 Results of Ogryzlo et al

7.3. Curve Crossing Mechanism for E-V,T Energy Transfer

In the previous section quenching was interpreted using potential surfaces that had a constant separation. The other extreme of E-V,T energy transfer is via surfaces that come close or cross. Predictions of quenching rate constants in such circumstances are usually made with Landau-Zener[76] theory and so this section contains a brief introduction to it. Again the model can be applied equally to quenching by atoms or molecules. Because of the relative simplicity of the process the quenching by atoms will be dealt with first.

According to Landau-Zener theory the probability of a surface jump at a critical nuclear configuration r_c (see figure 7.6) where the potential surfaces come close is given by

$$P(\text{Probability of surface jump at } r_c) = \exp - \frac{\Delta E}{V \delta S} \qquad (7.5)$$

where ΔE is the energy splitting between the surfaces

V is the velocity of nuclear motion in the region of r_c

δS is the difference in slopes of the surfaces if no splitting occurred (the dotted lines in figure 7.6)

Assuming that the crossing point is accessible this equation shows that the surface jump is favoured by

1. Low energy separation between the surfaces
2. High velocity in the region of r_c
3. Large difference in slopes.

The energy separation between the surfaces depends on the characteristics of the states giving rise to the surfaces, for example spin multiplicity. If on figure 7.6 ψ_1 were a singlet state and ψ_2 a triplet then the energy separation would be small and hence a surface jump (staying on ψ_1) would be favoured - leading to a reaction without

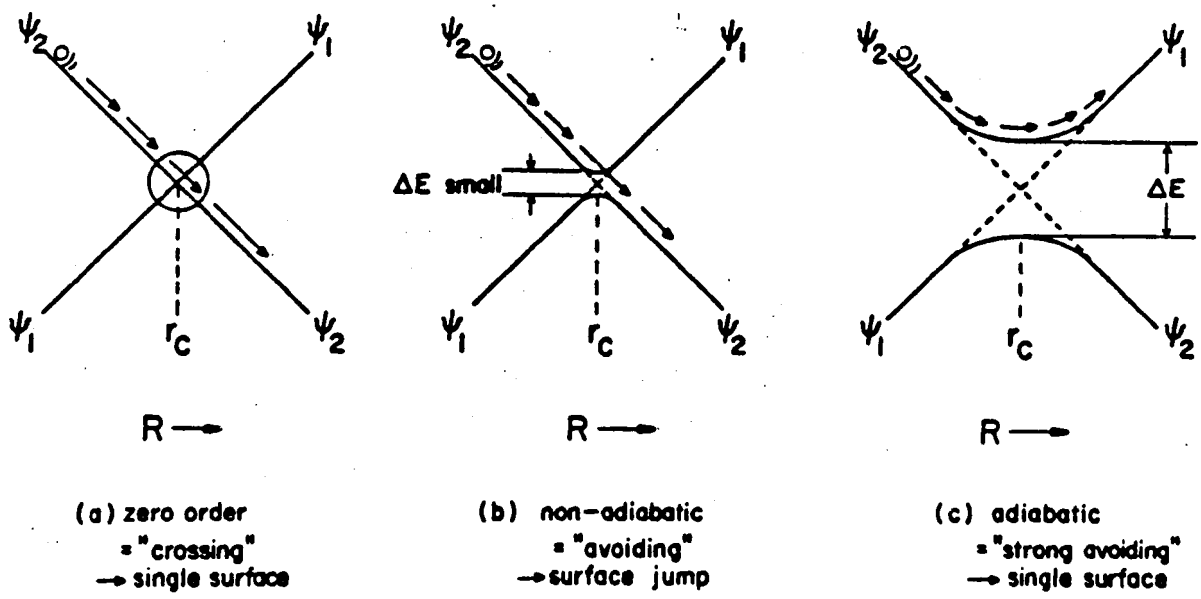

Figure 7.6 Trajectory of a Representative Point

Figure 7.7 Potential Energy Surfaces Relevant to certain Quenching Reactions

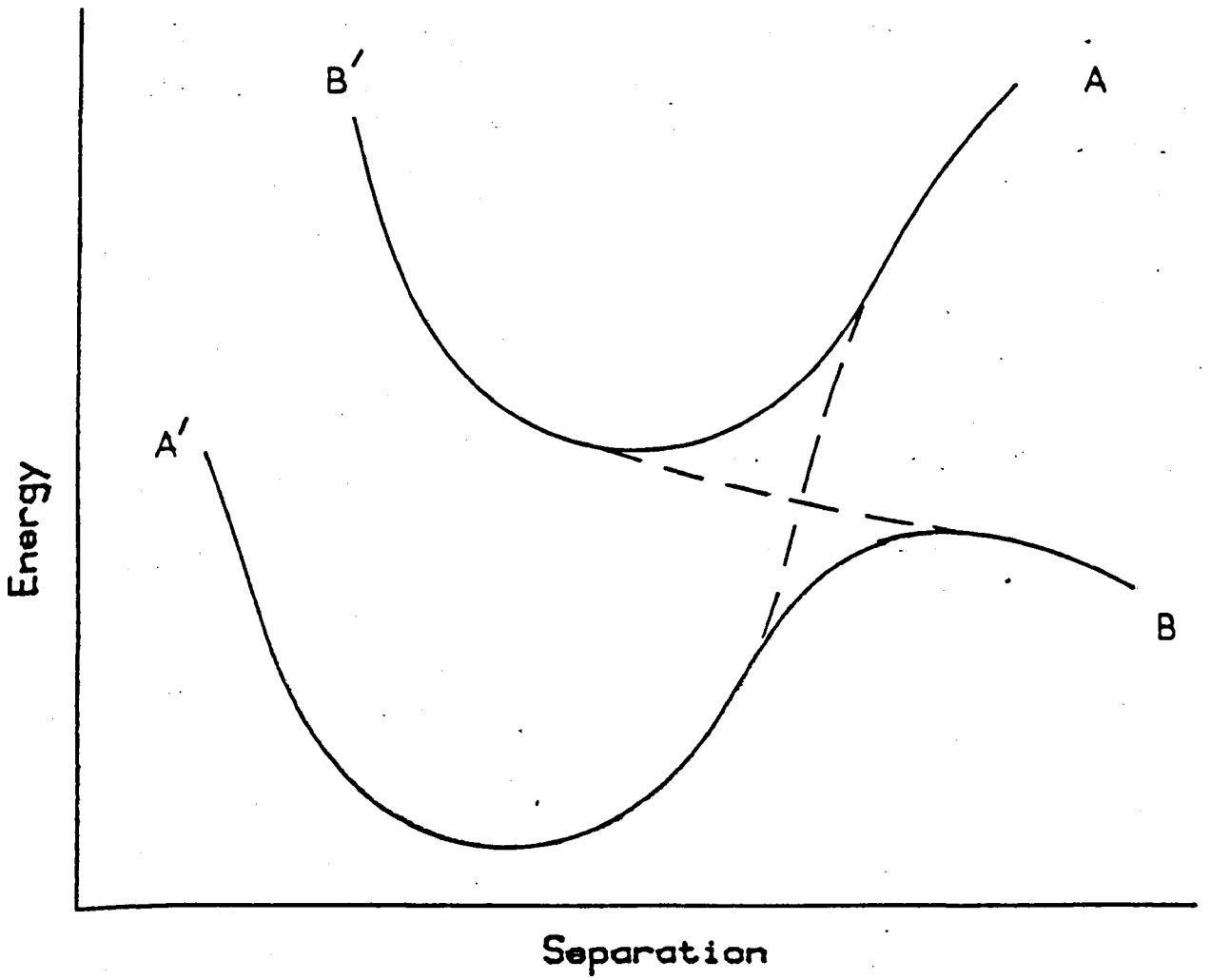

change of spin. This is in accordance with the Wigner Spin Conservation Law.

The velocity of travel along the surface depends on the kinetic energy and hence on the temperature.

Assuming the quenching reaction under consideration is

$$A + M \rightarrow B + M$$

then the probability of quenching can be calculated as follows. The excited species A is considered to approach the quencher M along the surface A of figure 7.7. If it exits on A it has been elastically scattered, if on B it has been quenched. There are two paths to B; either a surface jump from A to A′ and then reflection along the surface to B or travel along the upper surface to B′ followed by a surface jump to B. The probability of a surface jump is P, that of staying on the surface (1-P). Therefore the total quenching probability for both paths is 2P(1-P). This factor has a maximum value when P = 0.5 and decreases for either very low or very high probabilities of surface jumping. As the factors ΔE and δS in (7.5) are constant for a given quenching reaction this means that the probability of quenching depends on the nuclear velocity and hence temperature. These considerations will now be applied to some real quenching reactions.

In figure 7.8 are shown the potential energy surfaces for the $O(^1D)$ - noble gas system.[103] The quenching reaction under consideration is

$$O(^1D) + M \rightarrow O(^3P) + M \qquad M = Ne, Ar, Kr, Xe$$

It can be seen that there are two crossing points for the $O(^1D)$ and $O(^3P)$ surfaces. The one at smaller internuclear separation varies from being far out on the attractive part of the surface in the case of

Figure 7.8 Potential Energy Surfaces for the O (^{1}D)/Noble Gas System

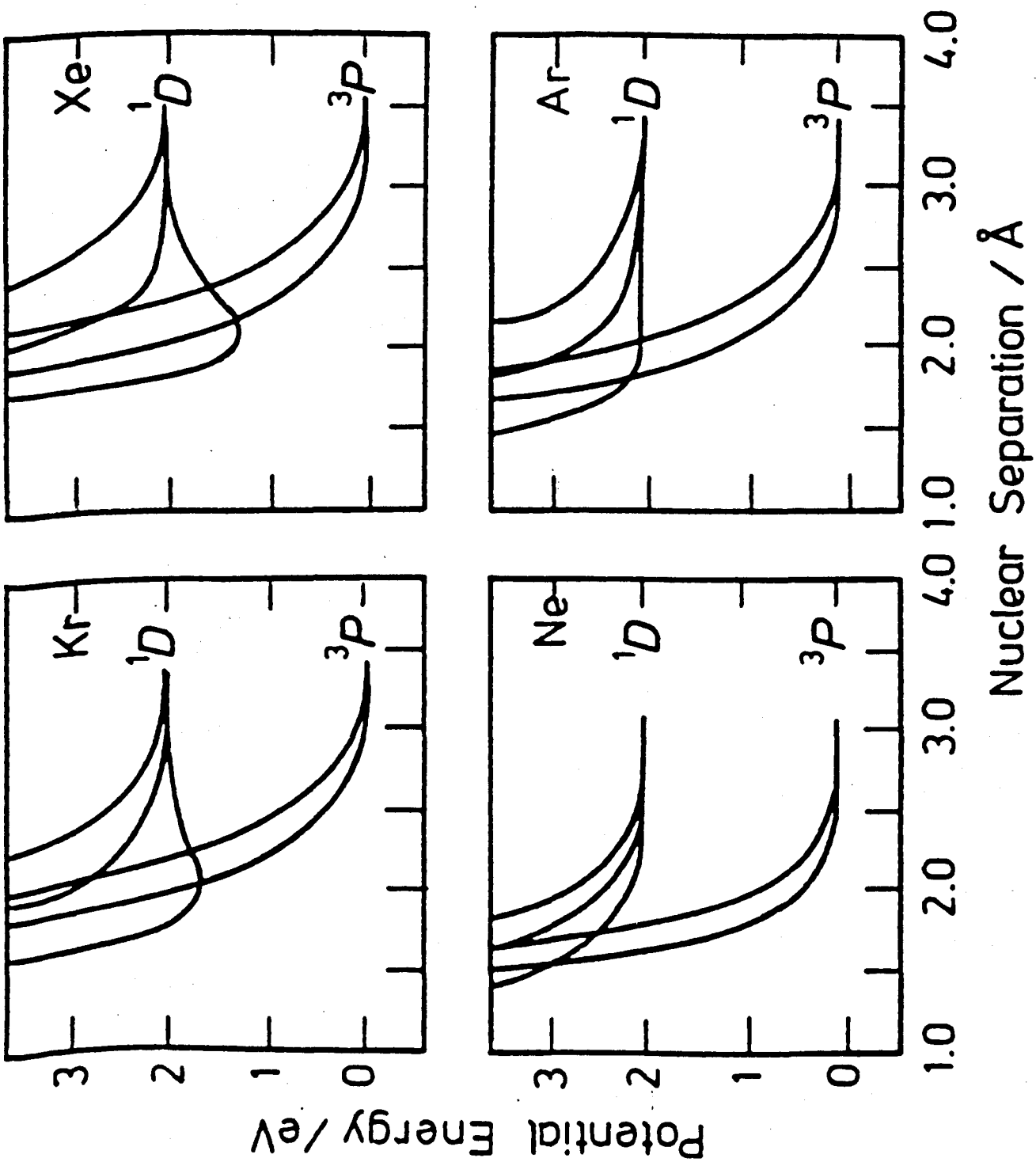

Xe + O (-0.37 eV relative to the separated atoms) to high on the repulsive wall in the case of Ne + O (+0.39 eV). At 300 K the factor kT is 0.026 eV thus the accessibility of the crossing point has an effect on the quenching rate. Figure 7.8 suggests that the quenching rate constants at room temperature should increase with increasing weight of noble gas and this is indeed found to be the case. The effect of increasing temperature would be to increase the quenching rate constant in the case of argon and decrease it in the case of xenon. Argon, which has a crossing point at 0.03 eV might show a maximum in rate constant as the crossing point was first reached and then passed. However there is a second factor to be taken into consideration in such a quenching reaction involving a change of spin, the size of the spin-orbit coupling. Recent results[104] suggest that where the crossing occurs on the attractive part of the potential (i.e. Kr and Xe) the difference in rate constants is mainly due to this effect.

Quenching reactions involving polyatomic excited state molecules or quenchers are more complicated in that there is not one surface but several, corresponding to the various vibrational levels. Consequently there is a grid of surface crossings as indicated in figure 7.9. This potential energy diagram is based on one for the quenching of excited sodium atoms by diatomic quenchers due to Bauer, Fisher and Gilmore.[105] The surfaces describing the interaction of the ground or excited state atom and the quencher are crossed by one for the ionic complex $Na^+ X^-$. This crossing of surfaces due to the formation of a complex is a feature of such quenching reactions.[100] However evidence for complex formation in the case of the quenching of sigma is sparse.

There is no correlation between the quenching rate constant and the saturation or unsaturation of the quencher. For example ethane, ethylene and acetylene all show similar quenching rate constants. Correlations

Figure 7.9 Quenching Involving a Polyatomic Molecule

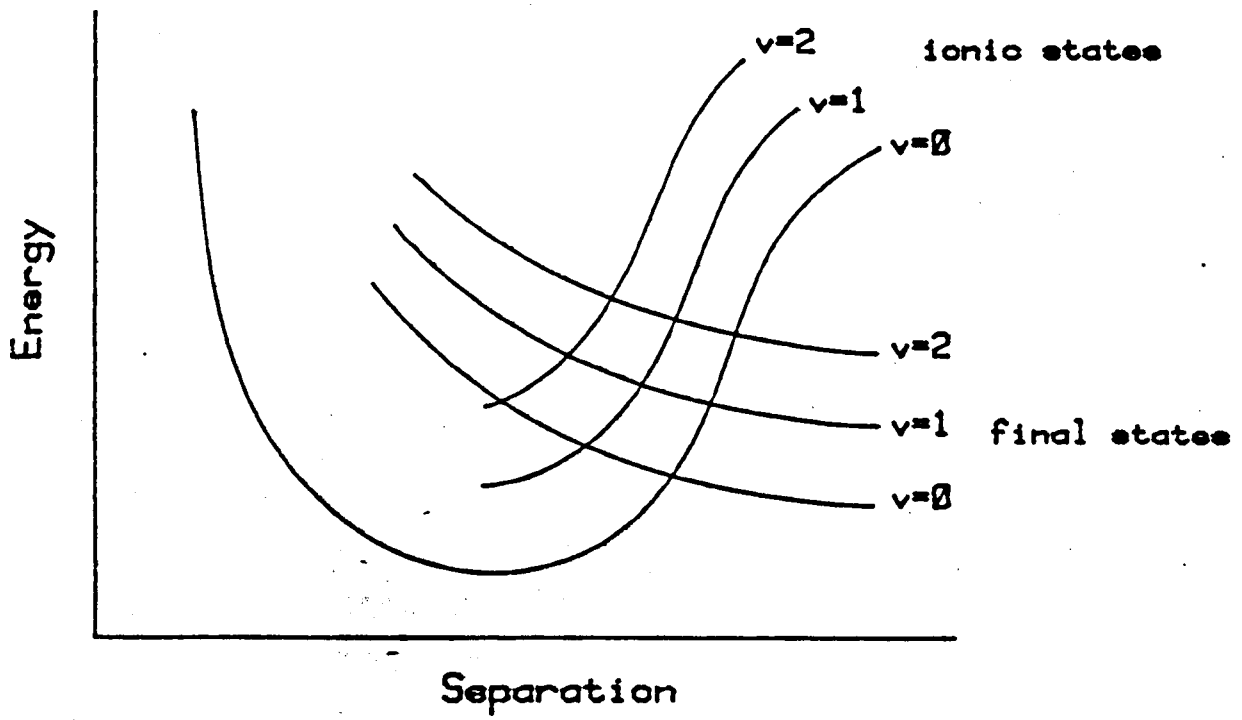

with ionization potential or electron affinity are also absent.[1]

This introduction has briefly reviewed the main theories of quenching of electronically excited species and has also presented some of the previous work on the quenching of sigma. In the next section the temperature dependencies determined in this study are discussed in the light of them.

7.4. The Temperature Dependence of the Quenching of $O_2(^1\Sigma_g^+)$

As the potential surfaces for the quenching of sigma are unknown the mechanism of quenching can only be inferred from the measured temperature dependences of the reactions. In this section the observed temperature dependencies (figure 7.10) are discussed.

The investigation of the quenching of sigma by argon (7.1) did not allow the exact form of the temperature dependence to be ascertained, the increase with temperature was too slow.

$$O_2(^1\Sigma_g^+) + Ar \rightarrow O_2(^1\Delta_g) + Ar \qquad (7.1)$$

However an upper limit of 8×10^5 $\ell\ mol^{-1}\ s^{-1}$ at 1500 K was obtained, the value at 300 K is 9×10^3 $\ell\ mol^{-1}\ s^{-1}$. This rise with temperatures indicates that the quenching occurs on the repulsive part of the intermolecular potential but whether by a curve crossing mechanism or not is unclear. The fact that the quenching of $O(^1D)$ by argon proceeds via a curve crossing on a repulsive potential surface might make this the most likely possibility.

It is known that the rate constants for the quenching of sigma increase with the relative molecular mass of the quencher. This could indicate that the polarizibility of the quencher is important leading to the formation of a complex and so the converging of the potential surfaces. However this increase could also be due to the quenching reaction (7.6) becoming important due to increased spin orbit interactions with the heavier quenchers

$$O_2(^1\Sigma_g^+) + M \rightarrow O_2(^3\Sigma_g^-) + M \qquad (7.6)$$

Figure 7.10 Temperature Dependence of Sigma Quenching Reactions

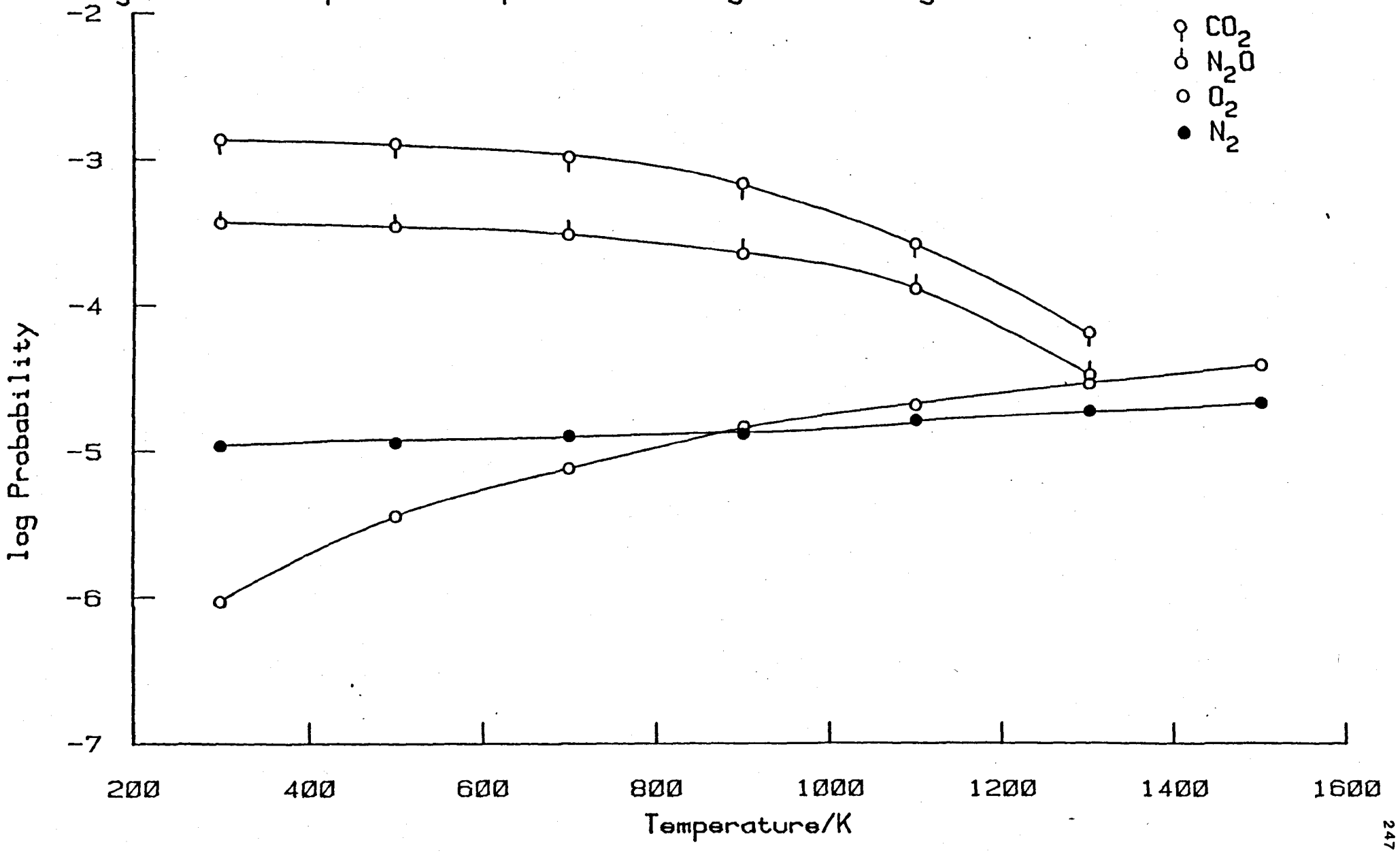

The quenching probabilities for oxygen, nitrogen, carbon dioxide and nitrous oxide are plotted on a logarithmic scale in figure 7.10. There are apparently three distinct types of behaviour. The quenching by oxygen rises with temperature as does that by nitrogen. However in the case of oxygen the rise is more rapid at higher temperatures. The quenching reactions of carbon dioxide and nitrous oxide display an apparently similar dependence; they decrease rapidly in probability at higher temperatures. How can such diverse behaviour in quite similar molecules be explained?

One of the most commonly found temperature dependencies for chemical reactions is the Arrhenius type. The reactants are thought to have to surmount an energy barrier to proceed to the products. Consequently a positive temperature dependence is predicted. Arrhenius plots using the quenching probabilities for oxygen and nitrogen are shown in figure 7.11. It can be seen that for neither is the plot linear, the closest to linearity being that for nitrogen but even here the curvature is distinct.

Kohse-Hoinghaus and Stuhl[43] have made a study of the quenching of sigma by nitrogen, hydrogen chloride, methane and ammonia and their deuterated analogues using a laser fluorescence method. The rate constants obtained agree well with the literature values where available and are generally of better precision. Within their temperature range (200-350 K) they obtained linear Arrhenius plots for all the quenchers, including nitrogen (figure 7.12). In most cases positive activation energies were obtained varying from 6.7 kJ mol^{-1} (561 cm^{-1}) in the case of deuterium to 0.7 kJ mol^{-1} (59 cm^{-1}) for ammonia. These they correlated with the endothermicities of the reactions and hence deduced the vibrational changes in the reaction. For example they obtained an activation energy for the quenching of

Figure 7.11 Arrhenius Plots for Oxygen and Nitrogen

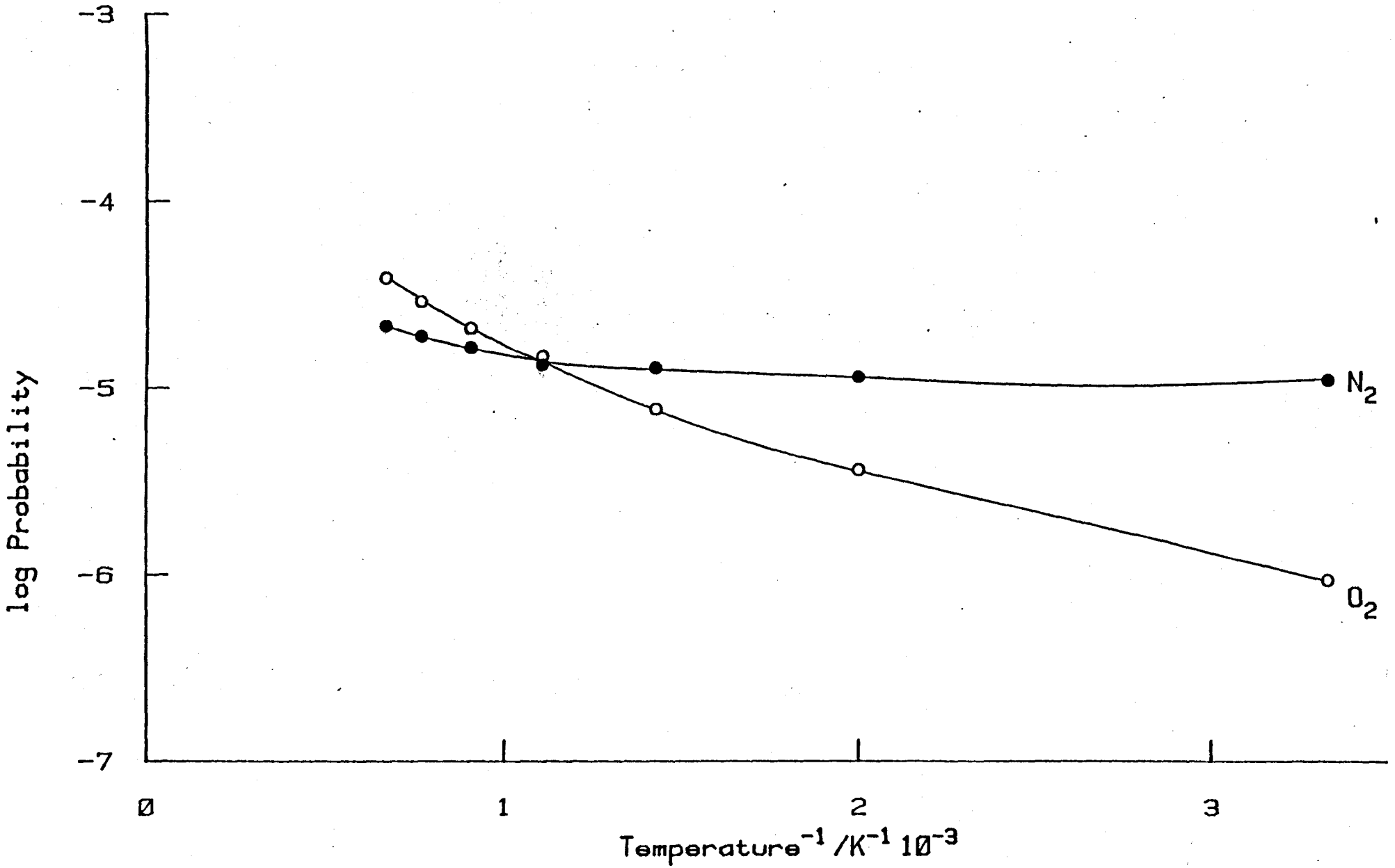

HCl of 5.0 kJ mol^{-1}. Thomas and Thrush[51] have found by infra-red emission spectroscopy that HCl(v=2) is excited in the quenching of sigma, the endothermicity of this reaction is in agreement with the measured activation energy

$$O_2(^1\Sigma_g^+) + HCl \rightarrow O_2(^1\Delta_g) + HCl(v=2) \quad \Delta H = 5.1 \text{ kJ mol}^{-1}, 427 \text{ cm}^{-1}$$

In the case of nitrogen Kohse-Hoinghaus and Stuhl found a very slow decrease in rate constant with temperature, yielding an activation energy of (-0.4 ± 1) kJ mol^{-1} (see figure 7.12). This they correlated with the nearly resonant quenching reaction

$$O_2(^1\Sigma_g^+) + N_2 \rightarrow O_2(^1\Delta_g)v=2 + N_2(v=1) \quad \Delta H = 0.4 \text{ kJ mol}^{-1}, 34 \text{ cm}^{-1}$$

However our results show that the quenching rate constant for nitrogen actually increases with temperature, though slowly. Furthermore our investigation across the wider temperature range shows that the Arrhenius plot is in fact non-linear. Figure 7.11 shows why a study up to even 700 K could give a linear Arrhenius plot with a negative activation energy; the rise is small and the curvature not apparent. Though we find a different temperature dependence the two sets of results fall well within the error limits of the experiments (see figure 6.4) and so the results seem correct. Consequently it would appear that the decrease found by Kohse-Hoinghaus and Stuhl is due to the limited temperature range available to them and the fact that the change in rate constant over that range is very small.

The effect of the small temperature range can also be seen in the results for quenching by hydrogen and deuterium. For these two molecules Kohse-Hoinghaus and Stuhl find an increase in rate constant over their temperature range by about a factor of 5. This clear

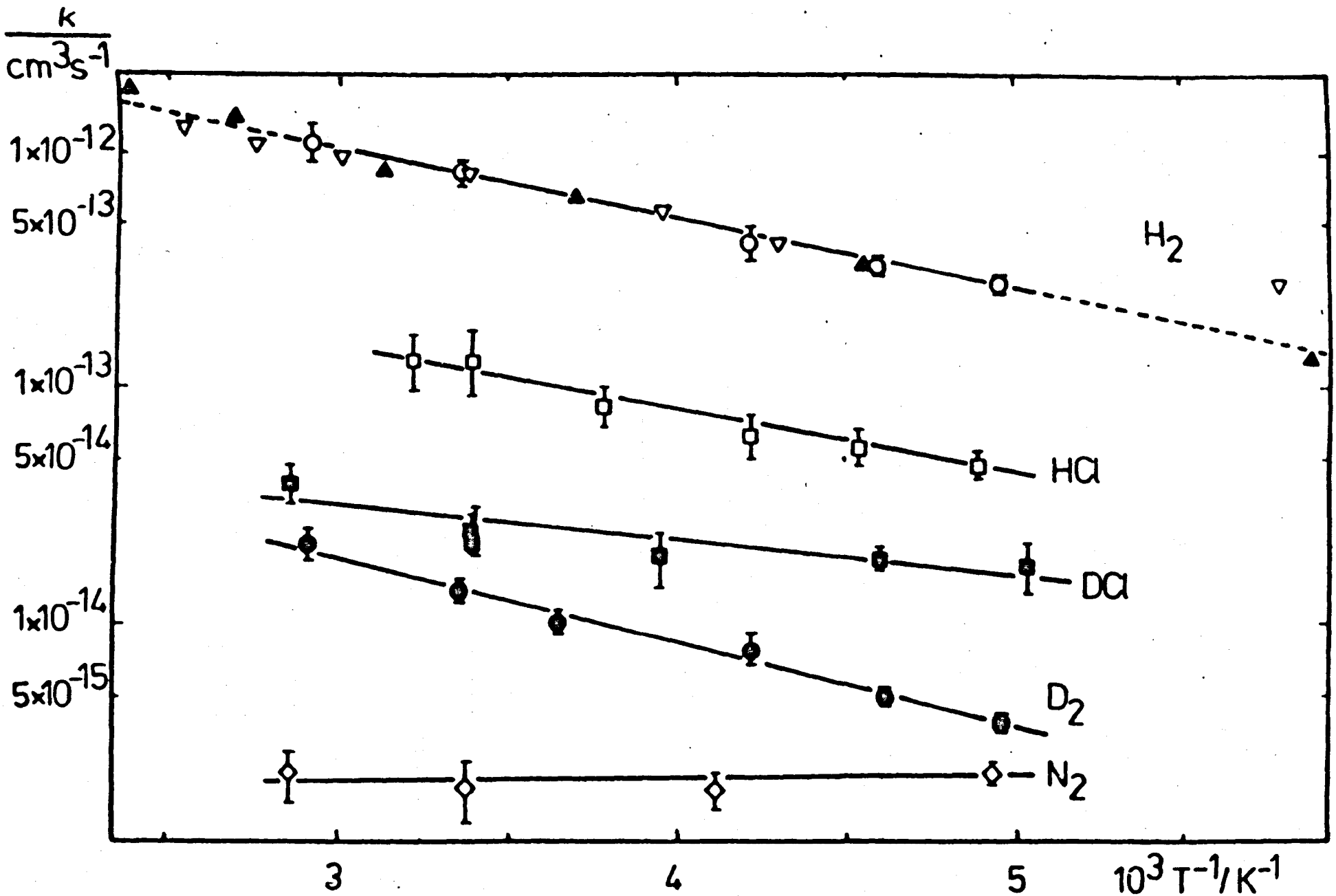

Figure 7.12 Results of Kohse-Hoinghaus and Stuhl

increase is in contrast to the case of nitrogen. (If the rate constants of Kohse-Hoinghaus and Stuhl are converted to probabilities which should be done where the temperature dependence is small the increase they find for H_2 and D_2 is still present). We find that the rate constants for quenching by carbon dioxide and nitrous oxide increase up to 700 K and hence an investigation up to this temperature might suggest the applicability of Arrhenius theory. However our results show that at higher temperatures the rate constants decrease rapidly. This indicates that while the results of Kohse-Hoinghaus and Stuhl are correct their interpretation on the basis of Arrhenius theory, which cannot account for a decrease in rate constants, may be in error. The linearity of their plots may be due to the limited temperature range available to them. To investigate this a study of a quencher that Kohse-Hoinghaus and Stuhl find shows a marked increase with temperature, e.g. HCl could be undertaken in this apparatus (see Chapter 8).

The equating of the measured activation energies with the endothermicities of the quenching reactions also leads to results which are in opposition to the observed isotope effects. Kohse-Hoinghaus and Stuhl obtained activation energies for the quenching by hydrogen and deuterium of 5.7 ± 0.6 kJ mol^{-1} and 6.7 ± 0.5 kJ mol^{-1} respectively. This lead them to assign the quenching reactions as (7.7) and (7.8), in contrast to the work of Ogryzlo et al[54] mentioned earlier

$$O_2(^1\Sigma_g^+) + H_2 \rightarrow O_2(^1\Delta_g)v=1 + H_2(v=1) \quad \Delta H = 4.8 \text{ kJ mol}^{-1}, 405 \text{ cm}^{-1} \tag{7.7}$$

$$O_2(^1\Sigma_g^+) + D_2 \rightarrow O_2(^1\Delta_g) + D_2(v=2) \quad \Delta H = 7.4 \text{ kJ mol}^{-1}, 622 \text{ cm}^{-1} \tag{7.8}$$

In this case an interpretation on the basis of oxygen Franck-Condon factors would lead one to expect the quenching by deuterium to be more rapid than that by hydrogen. The opposite is found to be the case, at 300 K $k_q(H_2) = 4.92 \times 10^8$ ℓ mol^{-1} s^{-1}, $k_q(D_2) = 8.4 \times 10^6$ ℓ mol^{-1} s^{-1}.

There is a similarity between the temperature dependence of the quenching of sigma by oxygen and nitrogen and that of the energy pooling reaction (see figures 6.4 and 6.10). A link between the quenching of singlet oxygen and the energy pooling reaction has been suggested by Thomas and Thrush.[5] They investigated the gas phase quenching of both sigma and delta with a variety of added gases, not including oxygen or nitrogen. They found a common linear surprisal plot for both species, this lead to their suggestion of a common quenching mechanism for both species. Resonant quenching paths were not generally favoured which indicated to them that quenching occurred on the repulsive part of the intermolecular potential and that vibrational excitation was the result of recoil. They found one exception to this rule, the quenching of delta by nitric oxide which predominantly populated the v=4 level of the quencher.

$$O_2(^1\Delta_g) + NO \rightarrow O_2(^3\Sigma_g^-) + NO(v=4) \quad \Delta H = 6.5 \text{ kJ mol}^{-1},\ 546 \text{ cm}^{-1}$$

The authors then suggested that this reaction could have a common mechanism with the energy pooling reaction. We have not studied the quenching of delta in this work but have obtained results for the energy pooling reaction.

Schurath[45] has also investigated the energy pooling reaction, determining the vibrational distribution of sigma by monitoring it's emission.

$$O_2(^1\Delta_g) + O_2(^1\Delta_g) \rightarrow O_2(^1\Sigma_g^+)v=n + O_2(^3\Sigma_g^-)$$

He found that the (2,1) transition was significantly stronger than would be expected from a Boltzmann distribution across the vibrational levels of sigma. He therefore concluded that in the energy pooling reaction sigma is preferentially formed in the v=2 level. This is interesting because this is the most nearly resonant reactant channel. Two molecules of delta in the v=o level yield 188.5 kJ mol^{-1} (15765 cm^{-1}) of energy to be distributed amongst the product molecules. Some possible combinations of product vibrational excitation are

$$O_2(^1\Delta_g) + O_2(^1\Delta_g) \rightarrow O_2(^1\Sigma_g^+) + O_2(^3\Sigma_g^-)v=2 \quad \Delta H = 5.3 \text{ kJ mol}^{-1}, \; 445 \text{ cm}^{-1}$$

$$O_2(^1\Delta_g) + O_2(^1\Delta_g) \rightarrow O_2(^1\Sigma_g^+)v=1 + O_2(^3\Sigma_g^-) \quad \Delta H = -14.8 \text{ kJ mol}^{-1}, \; -1239 \text{ cm}^{-1}$$

$$O_2(^1\Delta_g) + O_2(^1\Delta_g) \rightarrow O_2(^1\Sigma_g^+)v=2 + O_2(^3\Sigma_g^-) \quad \Delta H = 1.66 \text{ kJ mol}^{-1}, \; 139 \text{ cm}^{-1}$$

$$O_2(^1\Delta_g) + O_2(^1\Delta_g) \rightarrow O_2(^1\Sigma_g^+)v=3 + O_2(^3\Sigma_g^-) \quad \Delta H = 16.9 \text{ kJ mol}^{-1}, \; 1414 \text{ cm}^{-1}$$

The probability of the energy pooling reaction determined from the rate constants measured in this work is shown in figure 6.10. It can be seen to increase with temperature. This, taken with Schurath's work, indicates that the energy pooling reaction is an instance of a resonant energy transfer reaction that occurs on the repulsive part of the intermolecular potential. A temperature dependent study of the quenching of delta by nitric oxide would be useful here, on the basis of this evidence a positive temperature dependence would be expected.

In the case of the quenching of sigma by oxygen the most resonant reaction is

$$O_2(^1\Sigma_g^+) + O_2 \rightarrow O_2(^1\Delta_g) + O_2(^3\Sigma_g^-)v=3 \quad \Delta H = 7.7 \text{ kJ mol}^{-1}, \; 641 \text{ cm}^{-1}$$

As Thomas and Thrush did not investigate the quenching by oxygen or nitrogen it cannot be said whether resonant channels are favoured. However the fact that both oxygen and nitrogen show an increase in quenching probability with temperature similar to that seen for the energy pooling reaction may be indicative of a common mechanism, a resonant process on a repulsive surface. On the other hand the rise in quenching probability with temperature displayed by oxygen and nitrogen is not identical, as may be seen from figure 6.4.

In conclusion, the rate constants for the quenching of sigma by oxygen and nitrogen are found to increase with temperature. This suggests a short range quenching mechanism. The work of Thomas and Thrush indicates a link between certain quenching reactions and the energy pooling reaction. The energy pooling reaction is known to be resonant and to show a similar increase with temperature. Consequently a short range resonant mechanism for all three reactions is postulated. However a dogmatic statement cannot be made, more experiments are necessary particularly as to the quenching channel favoured in the case of oxygen and nitrogen.

The quenching probabilities for carbon dioxide and nitrous oxide are seen to fall with increasing temperature. This indicates a long range quenching mechanism. The effect of increasing temperature is to increase the average kinetic energy of the molecules and so move the turning point to smaller separations. This causes a decrease in

quenching efficiency whether quenching occurs via a curve crossing or resonant mechanism.

Parmenter and co-workers[106,107] have developed a correlation for the rate constants of state changes induced by long range forces. The relation is shown to hold for electronic quenching, collision-induced pre-dissociation and vibrational and rotational relaxation for both monatomic and polyatomic molecules. The correlation is between the cross section (or rate constant) for a reaction of an excited state A^* with a series of partners M at one temperature. The essential conditions to be met for the correlation to hold are that the reaction be induced by long range forces and that for a series of partners there must be no resonances specific to certain members.

Firstly they derive from theory the expression

$$\ln\sigma = \ln C + \varepsilon(A^*M)/kT \qquad (7.9)$$

where σ is the cross section for the reaction

C is a constant

$\varepsilon(A^*M)$ is the apparent well depth for the complex between A^* and M

This expression can be derived both assuming that the complex is in equilibrium with the separated partners or that it is simply a transient interacting pair. The well depth $\varepsilon(A^*M)$ is unknown, they assume it can be approximated by the combining rule (7.10).

$$\varepsilon(A^*M) = (\varepsilon(A^*A^*)\ \varepsilon(M\ M))^{\frac{1}{2}} \qquad (7.10)$$

where $\varepsilon(A^*A^*)$ is the well depth between excited species A^*

$\varepsilon(M\ M)$ is the well depth between partners M

(7.9) then becomes

$$\ln\sigma = \ln C + (\varepsilon(A^*A^*).\ \varepsilon(M\ M))^{\frac{1}{2}}/kT \qquad (7.11)$$

Now for a series of partners in reaction with a common species A^* (7.11) reduces to

$$\ln\sigma = \ln C + \beta(\varepsilon(MM)/k)^{\frac{1}{2}} \qquad (7.12)$$

where $\beta = (\varepsilon(A^*A^*)/kT^2)^{\frac{1}{2}}$

The ground state well depths are known for many molecules. Therefore the correlation predicts a straight line relationship between the cross section (or rate constant) for a reaction and the well depth of a series of partners (7.12), if the conditions mentioned earlier are met.

In figure 7.13 are plotted the room temperature rate constants for the quenching of sigma by a variety of molecules for which ground state well depths are available. While most of the quenchers fall on a line there are some notable exceptions; helium, oxygen, deuterium and hydrogen. The fact that oxygen does not fit the correlation is in accordance with the observation that the quenching rate constant increases with temperature and the suggestion that quenching is caused by short range interactions. The reason for the failure of hydrogen and deuterium to fit the correlation is less clear, though the results of Kohse-Hoinghaus and Stuhl show that the rate constants increase with temperature so again a short range mechanism may be occurring. Excluding these four points from the fit the correlation coefficient for a least squares analysis is 0.8. This is comparable to those obtained by Parmenter et al. Thus it might appear that the Parmenter correlation is valid for the quenching of sigma.

Figure 7.13 Parmenter Plot for Quenching of Sigma

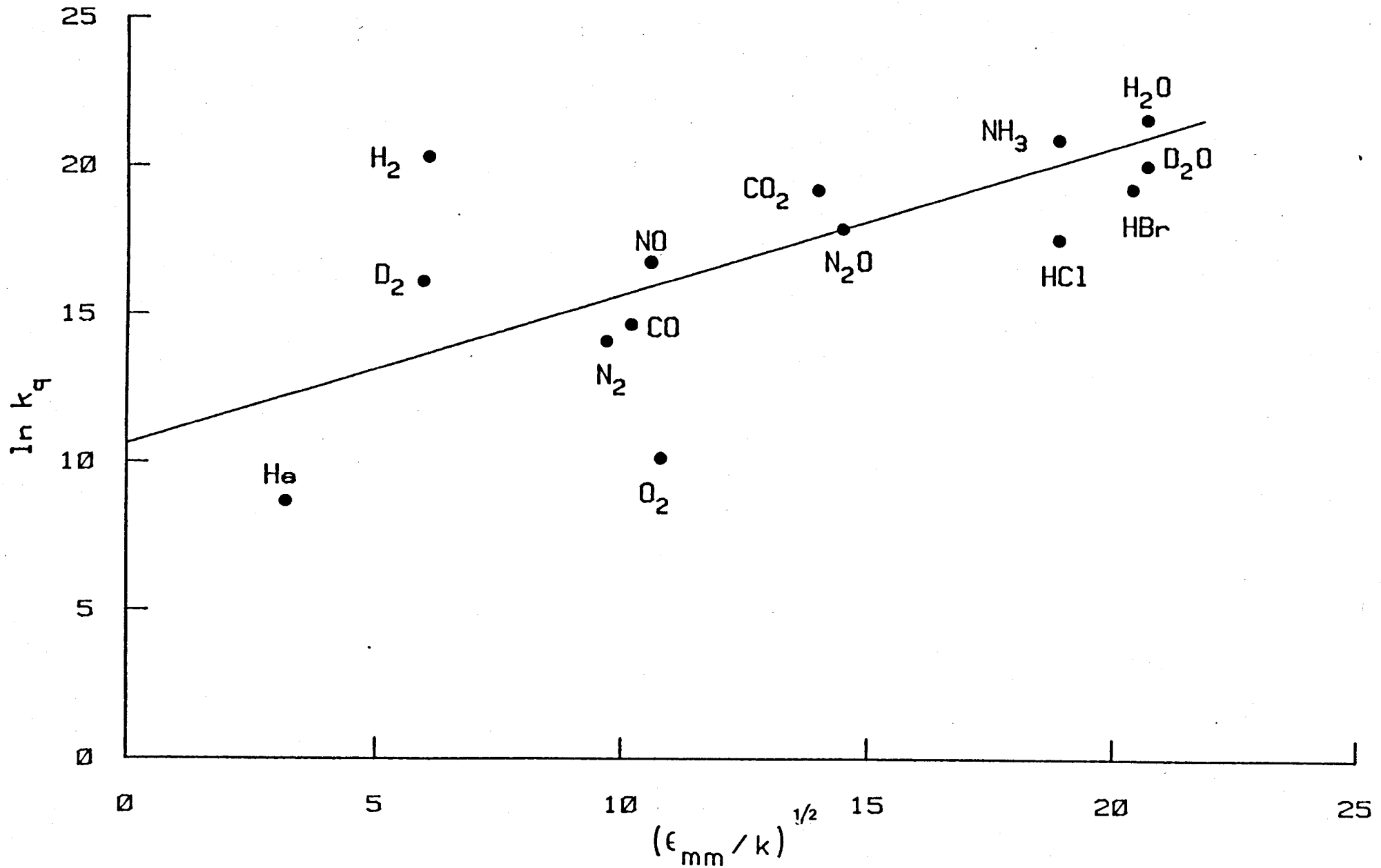

However the correlation can also be used to predict the temperature dependence of the quenching with a specific quencher. Using the combining rule (7.10) and the ground state well depths listed by Parmenter it is posible to estimate the well depth $\varepsilon(A^*M)$.

$$\varepsilon(A^*M) \approx \varepsilon(A\ M) = (\varepsilon(A\ A).\ \varepsilon(M\ M))^{\frac{1}{2}} \qquad (7.13)$$

This assumes that the well depth for the excited state A^* is not markedly different to that for the ground state A. Parmenter lists ground state well depths for oxygen and carbon dioxide. Combining (7.9) and (7.13)

$$\ln\sigma = \ln c + \varepsilon(A\ M)/kT \qquad (7.14)$$

where $\varepsilon(A\ M)/k = 151$ K

In figure 7.14 a graph of the log of the quenching probability for carbon dioxide against temperature is shown with the behaviour predicted using (7.14). Two points can be made concerning figure 7.14. Firstly, the experimental behaviour is quite different to that predicted. The well depth calculated in (7.13) causes a small decrease in probability, mostly in the range 300-500 K, at higher temperatures it is appromixately constant. Secondly the form of the curve obtained using the Parmenter relation is wrong. Even if the approximation (7.13) was invalid and the true well depth for sigma and carbon dioxide were different to that calculated the Parmenter relation could not reproduce the observed behaviour. A larger well depth would cause a sharper decrease at lower shock temperatures and the same levelling out at higher temperatures. This is in contrast to the experimentally observed behaviour where the probability falls rapidly at higher temperatures. So it appears that the correlation apparent in figure 7.13 is fortuitous and not significant.

Figure 7.14

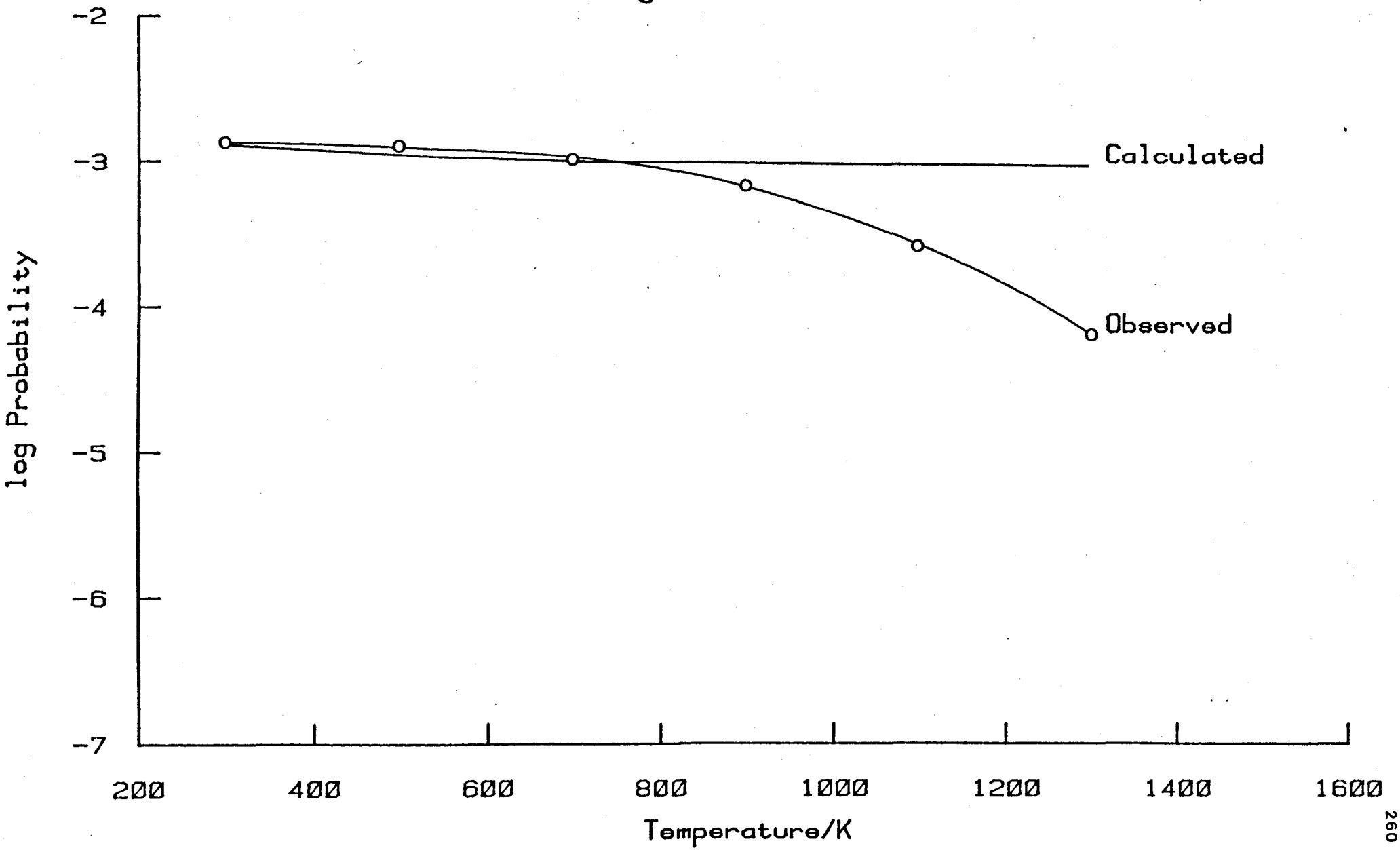
-2
-3
-4
-5
-6
-7
log Probability
200
400
600
800
1000
1200
1400
1600
Temperature/K
Calculated
Observed

This would concur with the finding that there is no relationship between the quenching rate constant and quencher properties that could influence complex formation.

Ogryzlo and Thrush[108] have investigated the infra-red emission from carbon dioxide in the quenching of sigma at room temperature. Their work firstly confirms that quenching occurs to delta and not to the ground state and secondly reveals the major quenching channels. They deduced that the quenching reactions were

$$O_2(^1\Sigma_g^+) + CO_2 \rightarrow O_2(^1\Delta_g)v=1 + CO_2(1,0,1) \quad \Delta H = 1.7 \text{ kJ mol}^{-1}, \; 146 \text{ cm}^{-1}$$

$$O_2(^1\Sigma_g^+) + CO_2 \rightarrow O_2(^1\Delta_g)v=1 + CO_2(0,2,1) \quad \Delta H = 0.47 \text{ kJ mol}^{-1}, \; 39 \text{ cm}^{-1}$$

These are also the transitions nearest resonance. Our results for the quenching by carbon dioxide show that it decreases in efficiency with temperature, thus a long range resonant mechanism is indicated. The temperature dependence of the quenching by nitrous oxide is similar to that for carbon dioxide suggesting a common mechanism. A useful experiment would therefore be to monitor the infra-red emission from nitrous oxide to find if a resonant channel was favoured (see Chapter 8).

7.5. Summary

Though the precise nature of the reactions cannot be deduced from experiments such as these they have revealed several important features. The following is a summary of the major findings.

1. The quenching of sigma by argon has been investigated. The increase with temperature is too slow to allow rate constants to be measured but an upper limit at 1500 K of 8×10^5 ℓ mol^{-1} s^{-1} has been determined.

2. The rate constant for the energy pooling reaction has been determined from 300 to 1850 K. The reaction shows no composition dependence and a positive temperature dependence. A short range resonant reaction is indicated.

3. In the temperature range 300-1500 K the probabilities for the quenching of sigma by oxygen and nitrogen are found to increase. Arrhenius plots are non-linear. Quenching by oxygen becomes more efficient than that by nitrogen above 1100 K. On the basis of the temperature dependence a short range reaction is indicated, perhaps similar to that for energy pooling reaction.

4. Rate constants for the quenching of sigma at room temperature by carbon dioxide and nitrous oxide have been determined, $kq(CO_2) = 2.18 \times 10^8$ ℓ mol^{-1} s^{-1} $k_q(N_2O) = 5.88 \times 10^7$ ℓ mol^{-1} s^{-1}. The values are found to agree well with those in the literature.

5. The quenching reactions of carbon dioxide and nitrous oxide have been investigated up to 1400 K. The molecules display similar behaviour, an approximately constant quenching probability up to 700 K followed by a rapid decrease. A long range quenching mechanism is indicated.

6. An unexpected emission was detected from nitrous oxide/oxygen mixtures at temperatures above 1200 K. The glow was found not to be dependent on the presence of singlet oxygen. The chemilumiscent reaction (6.15) is suggested

$$NO + O \rightarrow NO_2 + h\nu \qquad (6.15)$$

The effect on the emission traces at 762 nm, and hence on the kinetic measurements, is negligible.

Chapter 8

SUGGESTIONS FOR FURTHER WORK

In this chapter some possible future studies of singlet oxygen or other systems using the discharge flow/shock tube are described. Firstly further work on singlet oxygen is discussed in the light of the present results.

8.1. Further Studies of Singlet Oxygen

The rate constant for the quenching of delta by oxygen does not increase fast enough with temperature to be measurable in the present apparatus. However several interesting reactions of delta have proved more amenable to study; the energy pooling reaction, the dimol emissions and the vibrational relaxation of $O_2(^1\Delta_g)v=1$.

The first experiments reported in this thesis were concerned with an investigation of the dimol emissions of delta. While the emissions at 634 nm, 579 nm and 703 nm were assigned and relative emissivities obtained there are several features which require more study.

From the work carried out on the 634 nm emission from an oxygen/carbon dioxide mixture it was proposed that the hot band emission at 637 nm made a significant contribution. On the basis of the vibronic components of the simultaneous transitions it was suggested that the 703 nm and 582 nm hot bands would be of less importance than that at 637 nm. By a study of the 703 nm emission in mixtures of oxygen and carbon dioxide (or nitrous oxide) this could be investigated.

There are also several other dimol emissions that could be studied. Two possibilities are from the mixed dimol (8.1) and from the sigma dimol (8.2)

$$O_2(^1\Delta_g) + O_2(^1\Sigma_g^+) \rightarrow O_2(^3\Sigma_g^-) + O_2(^3\Sigma_g^-) + h\nu \ (\lambda = 476 \text{ nm}) \quad (8.1)$$

$$O_2(^1\Sigma_g^+) + O_2(^1\Sigma_g^+) \rightarrow O_2(^3\Sigma_g^-) + O_2(^3\Sigma_g^-) + h\nu \ (\lambda = 381 \text{ nm}) \quad (8.2)$$

The problem here will be experimental due to the low emission intensity caused by the low concentration of sigma. However this effect would be countered by the greater sensitivity of the 9658 B photomultiplier towards the blue end of the spectrum.

If these emissions are visible then an investigation of their associated transitions.

$$O_2(^1\Delta_g) + O_2(^1\Sigma_g^+) \rightarrow O_2(^3\Sigma_g^-)v{=}1 + O_2(^3\Sigma_g^-) + h\nu \ (\lambda = 514 \text{ nm})$$

$$O_2(^1\Delta_g)v{=}1 + O_2(^1\Sigma_g^+) \rightarrow O_2(^3\Sigma_g^-) + O_2(^3\Sigma_g^-) + h\nu \ (\lambda = 445 \text{ nm})$$

and

$$O_2(^1\Sigma_g^+) + O_2(^1\Sigma_g^+) \rightarrow O_2(^3\Sigma_g^-)v{=}1 + O_2(^3\Sigma_g^-) + h\nu \ (\lambda = 405 \text{ nm})$$

$$O_2(^1\Sigma_g^+)v{=}1 + O_2(^1\Sigma_g^+) \rightarrow O_2(^3\Sigma_g^-) + O_2(^3\Sigma_g^-) + h\nu \ (\lambda = 362 \text{ nm})$$

would provide an interesting comparison with the intensities of the (0,1) and (1,0) transitions of the delta dimol already studied.

The results of the study of the vibrational relaxation of delta suggested that V-V exchange with the ground state was important at high temperatures. Here however there is little more that can be done in the present apparatus. What is needed is a study of the relaxation of both states, this cannot be done for the ground state in the present apparatus. One technique that would allow the relaxation of either state to be followed is laser Raman excitation (see Chapter 5).

The quenching of sigma has proved to be well suited to a discharge flow/shock tube investigation. There are several reasons for this, firstly the method of formation of sigma.

Sigma is continually formed by the energy pooling reaction from the delta present at any point in the tube. As delta is deactivated only slowly by collisional quenching and quenching at the wall it is present in appreciable quantities down the length of the tube; so, via the energy pooling reaction, is sigma. This allows the concentration of sigma to be monitored using the weak 762 nm emission. The fact that a large glow is measured at the observation station allows efficient quenchers to be studied e.g. carbon dioxide.

Secondly there is the fact that sigma is quenched only slowly by oxygen itself. This means that the contribution of most additives to the overall quenching rate constant is significant and so individual rate constants may be accurately determined.

Given the constraint of rate constant in the region 10^5-5 x 10^8 $\ell\ mol^{-1}\ s^{-1}$ then several new quenchers could be studied, possibilities are HCl, HBr, CO, NO and NO_2. Hydrogen chloride and hydrogen bromide would seem worthwhile because they are highly polar, unlike any of the quenchers studied so far.

If the room temperature rate constant is sufficiently large, $>10^6$ $\ell\ mol^{-1}\ s^{-1}$, then it too may be measured. While this is desirable for all quenchers it is necessary if the use of a quencher for which there have been few previous determinations is contemplated, e.g. HBr.

A study of the temperature dependence of the quenching by HCl and HBr would allow comparison with previous work by other groups. Kohse-Hoinghaus and Stuhl[43] found linear Arrhenius plots for the quenching by HCl and HBr, a study in the present apparatus across the wider temperature range should show if this interpretation is correct. Moreover the quenching by HBr has been modelled by Ogryzlo et al[55] using a long range mechanism. Once again the wide temperature range

available in the discharge flow/shock tube will provide a severe test of the theory.

The theoretical modelling of the quenching of sigma is another area that could be developed. It has been established in the present work that the quenching by carbon dioxide and nitrous oxide show a negative temperature dependence. Calculation of quenching rate constants for these compounds by for example Landau-Zener theory and comparison with the experimental behaviour would be useful. It is here that an investigation of the quenching channel favoured would be of use. This has been done for carbon dioxide using the infra-red emission[108] and a similar study of nitrous oxide is necessary.

8.2. Studies of Other Systems

8.2.1. Studies of SO and S_2

Recently some work has been done on chemiluminescence from states isoelectronic with oxygen, SO[48,109] and S_2[110]. The excited states are produced by energy transfer from singlet oxygen formed in a discharge.

$$O_2(^1\Delta_g) + SO(^3\Sigma) \rightarrow O_2(^3\Sigma_g^-) + SO(^1\Sigma)$$

$$O_2(^1\Delta_g) + S_2(^3\Sigma_g^-) \rightarrow O_2(^3\Sigma_g^-) + S_2(^1\Delta_g)$$

$$O_2(^1\Delta_g) + S_2(^1\Delta_g) \rightarrow O_2(^3\Sigma_g^-) + S_2(^1\Sigma_g^+)$$

SO and S_2 are formed by discharging sulphur containing compounds, for example $SOCl_2$ and S_2Cl_2.

Emission from the excited states has been seen[48,109,110]

$$SO(^1\Delta) \rightarrow SO(^3\Sigma) + h\nu \ (\lambda = 1305 \text{ nm})$$

$$SO(^1\Sigma) \rightarrow SO(^3\Sigma) + h\nu \ (\lambda = 955 \text{ nm})$$

$$S_2(^1\Delta_g) \rightarrow S_2(^3\Sigma_g^-) + h\nu \ (\lambda = 1745 \text{ nm})$$

$$S_2(^1\Sigma_g^+) \rightarrow S_2(^3\Sigma_g^-) + h\nu \ (\lambda = 1256 \text{ nm})$$

The reactions of singlet oxygen and the singlet states of SO and S_2 seem to be similar, it is known[109] that $SO(^1\Delta)$ shows a similar resistance to quenching by CO_2 as does $O_2(^1\Delta_g)$. Other comparisons with the behaviour of singlet oxygen can be made, for example $SO(^1\Delta)$ and $S_2(^1\Delta_g)$ show energy pooling reactions.

$$SO(^1\Delta) + SO(^1\Delta) \rightarrow SO(^1\Sigma) + SO(^3\Sigma)$$

$$S_2(^1\Delta_g) + S_2(^1\Delta_g) \rightarrow S_2(^1\Sigma_g^+) + S_2(^3\Sigma_g^-)$$

There is however no report of dimol emissions being observed. Such

emissions would be expected on the basis of other similarities with singlet oxygen and they should be searched for.

Observations of the emissions above 900 nm will require the use of an infra-red sensitive detector. Ishiwata and Tanaka[48] have used a red sensitive photomultiplier and Barnes,Becker and Fink[109] a cooled germanium photodiode.

Altogether the SO and S_2 systems provide a useful comparison to singlet oxygen

8.2.2. Metastable Oxygen Emission Bands

Figure 1.4 shows that recombination of two $O(^3P)$ atoms can result in the population of six electronic states of molecular oxygen. This study has been of the two lowest excited states $^1\Delta_g$ and $^1\Sigma_g^+$. Transitions from the ground state to each of the five excited states have been observed in laboratory experiments.[26] In emission the transition from $^3\Sigma_u^+$ to the ground state has been seen, it is a feature of the night airglow.[111]

The night airglow on Venus presents a different picture, despite the low concentration of oxygen the most intense feature is the $^1\Sigma_u^- - ^3\Sigma_g^-$ transition.[112] The atmospheres of Venus and the earth differ in chemical composition, that of Venus being mainly CO_2 and that of the earth mainly N_2.

Laboratory investigators of the effect of CO_2 on the emission from oxygen states produced on recombination of oxygen atoms (formed in a discharge) have been undertaken by Slanger[112] and by Kenner, Ogryzlo and Turley.[113] Slanger identified the new emissions $^3\Delta_u \rightarrow {}^1\Delta_g$, $^3\Delta_u \rightarrow {}^3\Sigma_g^-$, $^1\Sigma_u^- \rightarrow {}^1\Delta_g$ (figure 8.1). He also found that the presence of CO_2 suppresses the emission from $^3\Sigma_u^+$ and $^3\Delta_u$. It thus appears that CO_2 quenches $^3\Sigma_u^+$ and $^3\Delta_u$ fast and $^1\Sigma_u^-$ slowly. This is interesting in

view of the fact that $^1\Sigma_g^+$ is quenched rapidly by CO_2

As Slanger has pointed out the explanation of the differences in the airglows must be in the quenching reactions as both atmospheres contain approximately the same amount of atomic oxygen. If the mercury bubbler and mercuric oxide film were removed the present apparatus would be a suitable instrument for such a study.

Figure 8.1 The Emission Spectrum of Oxygen[112]

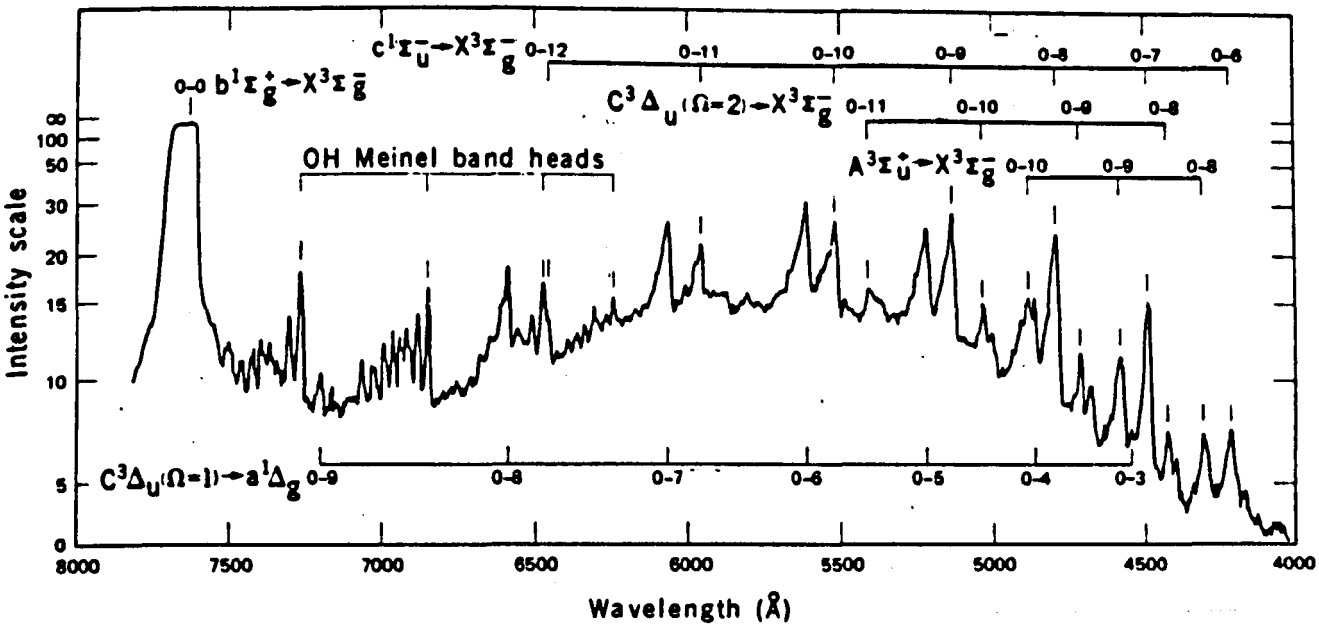

Pure Oxygen

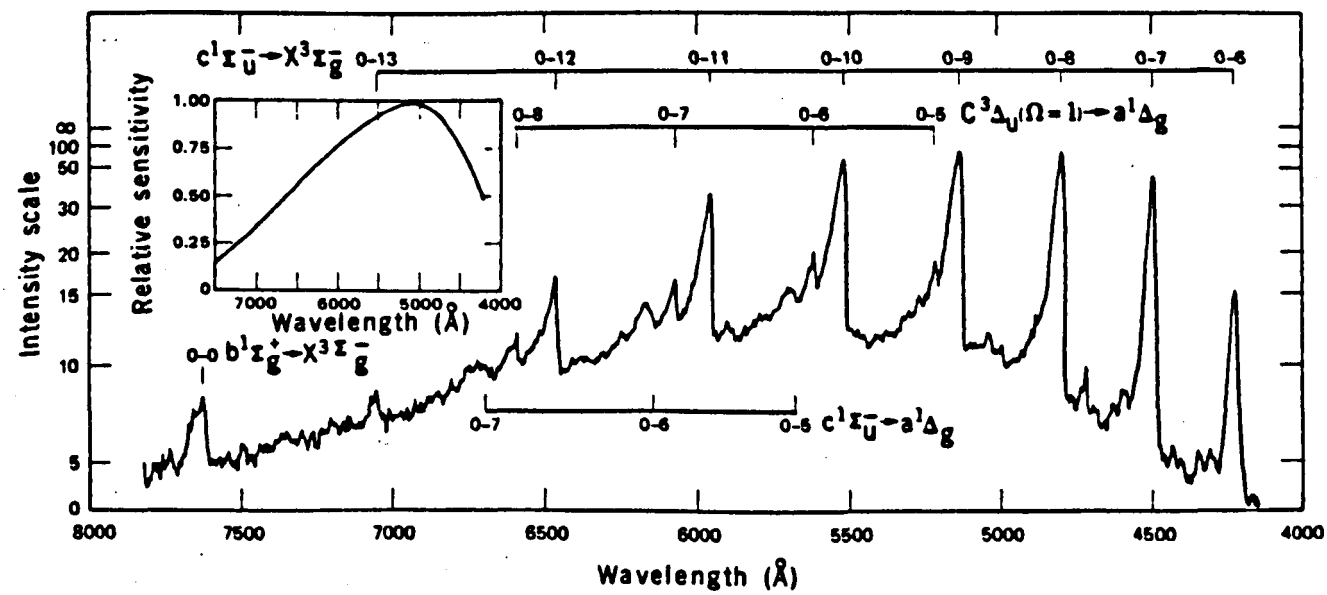

Oxygen plus Carbon Dioxide

References

1. "Singlet Oxygen" H.H. Wasserman, R.W. Murray eds., Academic Press, New York, (1979).
2. "Singlet Oxygen; reactions with organic compounds and polymers", B. Ranby, J.F. Rabek eds., Wiley, Chichester (1978).
3. J. Bland, J. Chem. Ed., 53 274 (1976).
4. J. Heicklen, "Atmospheric Chemistry", Academic Press, New York (1976).
5. R.G.O. Thomas, B.A. Thrush, Proc. Roy. Soc. Lond. A356 307 (1977).
6. M. Braithwaite, E.A. Ogryzlo, J.A. Davidson, H.I. Schiff, J. Chem. Soc. Faraday II 72 2075 (1976).
7. K. Kohse-Hoinghaus, F. Stuhl, J. Photochem. 9 102 (1978).
8. C.J. Howard, J. Phys. Chem. 83 3 (1979).
9. J.D. Lambert, "Vibrational and Rotational Relaxation in Gases", Clarendon Press, Oxford (1977).
10. A.G. Gaydon, I.R. Hurle, "The Shock Tube in High Temperature Chemical Physics", Chapman and Hall, London (1963).
11. C.T. Bowman, R.K. Hanson, J. Phys. Chem. 83 757 (1979).
12. P. Borrell, in "Transfer and Storage of Energy by Molecules", Volume 2, G.M. Barnett, A.M. North eds., Wiley, London (1969).
13. R.A. Hartunian, W.P. Thompson, E.W. Hewitt, J. Chem. Phys. 44 1765 (1966).
14. R.W.F. Gross, J. Chem. Phys. 48 1302 (1968).
15. R.W.F. Gross, N. Cohen, J. Chem. Phys. 48 2582 (1968).
16. R.W.F. Gross, N. Cohen, J. Chem. Phys. 50 3119 (1969).
17. J.E. Breen, R.B. Quy, G.P. Glass in "Recent Developments in Shock Tube Research", Stanford University Press, (1973).
18. G.P. Glass, R.B. Quy, J. Phys. Chem. 81 30 (1979).
19. P. Borrell, P.M. Borrell, A. Brittain, U.S. Clearing-house Fed. Sci. Tech. Inform. AD1969 702808.

20. R.A. Young, G. Black, J. Chem. Phys. 42 3740 (1965).

21. P.M. Borrell, P. Borrell, M.D. Pedley, Chem. Phys. Lett. 51 300 (1977).

22. P.M. Borrell, P. Borrell, M.D. Pedley, K.R. Grant, Proc. Roy. Soc. Lond. A367 395 (1979).

23. G. Herzberg, "Spectra of Diatomic Molecules", Van Nostrand, New York, (1945).

24. H. Katayama, S. Ogawa, M. Ogawa, Y. Tanaka, J. Chem. Phys. 67 2132 (1977).

25. R.M. Badger, A.C. Wright, R.F. Whitlock, J. Chem. Phys. 43 4345 (1965).

26. K.P. Huber, G. Herzberg, "Constants of Diatomic Molecules", Van Nostrand, New York (1979).

27. M. Kasha, D.E. Brabham in "Singlet Oxygen", H.H. Wasserman, R.W. Murray eds., Academic Press, New York (1979).

28. E.W. Gray, E.A. Ogryzlo, Chem. Phys. Lett. 3 658 (1969).

29. R.P. Wayne in "Recent Advances in Photochemistry" 7 J.N. Pitts, G.S. Hammond, W.A. Noyes, Wiley, New York (1969).

30. L.W. Bader, E.A. Ogryzlo, Disc. Faraday Soc. 37 46 (1964).

31. E. Castellano, H.J. Schumacher, Chem. Phys. Lett. 13 625 (1972).

32. R.W. Murray, M.L. Kaplan, J. Am. Chem. Soc. 90 4161 (1968).

33. R.W. Murray, M.L. Kaplan, J. Am. Chem. Soc. 91 5358 (1969).

34. L.J. Andrews, E.W. Abrahamson, Chem. Phys. Lett. 10 113 (1971).

35. J.A. Davidson, E.W. Abrahamson, Photochem. Photobiol. 15 403 (1972).

36. J.A. Davidson, K. Kear, E.W. Abrahamson, J. Photochem. 1 307 (1972/3).

37. T.C. Frankiewicz, R.S. Berry, J. Chem. Phys. 58 1787 (1973).

38. R.P. Steer, J.L. Sprung, J.N. Pitts, Environ. Sci. Tech. 3 946 (1969).

39. I.B.C. Matheson, J. Lee, B.S. Yamanashi, M.L. Wohlbarsht, Chem. Phys. Lett. 27 355 (1974).

40. J.G. Parker, D.N. Ritke, J. Chem. Phys. 59 3713 (1973).

41. L.R. Martin, R.B. Cohen, J.F. Schatz, Chem. Phys. Lett. 41 394 (1976).

42. S.A. Lawton, S.E. Novick, H.P. Broida, A.V. Phelps, J. Chem. Phys. 66 1381 (1977).

43. K. Kohse-Hoinghaus, F. Stuhl, J. Chem. Phys. 72 3720 (1980).

44. R.G. Derwent, B.A. Thrush, Trans. Faraday Soc. 67 2036 (1971).

45. U. Schurath, J. Photochem. 1 215 (1975).

46. A. Carrington, D.H. Levy, T.A. Miller, Trans. Faraday Soc. 62 2994 (1966).

47. R. Colin, Can. J. Phys. 46 1359 (1968).

48. T. Ishiwata, I. Tanaka, J. Phys. Chem. 84 119 (1980).

49. R.G. Derwent, B.A. Thrush, J. Chem. Soc. Faraday II 68 720 (1972).

50. K. Kear, E.W. Abrahamson, J. Photochem. 3 409 (1975).

51. R.G.O. Thomas, B.A. Thrush, Proc. Roy. Soc. Lond. A356 295 (1977).

52. E.A. Ogryzlo, C.W. Tang, J. Am. Chem. Soc. 92 5034 (1970).

53. H. Ishida, H. Tabuhashi, H. Sata, H. Tsubomura, J. Am. Chem. Soc. 92 275 (1970).

54. M. Braithwaite, J.A. Davidson, E.A. Ogryzlo, J. Chem. Phys. 65 771 (1970).

55. M. Braithwaite, E.A. Ogryzlo, J.A. Davidson, H.I. Schiff, Chem. Phys. Lett. 42 158 (1976).

56. M.D. Pedley, Ph.D. Thesis, University of Keele, (1978).

57. "Handbook of Chemistry and Physics" 45th Edition, Chemical Rubber Publ., Cleveland (1964).

58. M. Outred, C. Howard, J. Phys. E. Sci. Instrum. 11 276 (1978).

59. R.C. Millikan, General Electric Research Report 64-RL-3700C, New York (1964).

60. J.A.N.A.F. Thermochemical Tables, The Dow Chemical Company Michigan, (1965).

61. E.M.I. Photomultipliers, E.M.I. Industrial Electronics, London (1978).

62. S.H. Whitlow, F.D. Findlay, Can. J. Chem. 45 2087 (1967).

63. A. Leiss, U. Schurath, K.H. Becker, G.H. Fink, J. Photochem. 8 211 (1978).

64. J.S. Arnold, R.S. Browne, E.A. Ogryzlo, Photochem. Photobiol. 4 963 (1965).

65. P.H. Vidaud, R.P. Wayne, M. Yaron, Chem. Phys. Lett. 38 306 (1976).

66. P. Borrell, Computers in Chemistry, in press.

67. P. Moore, J. Chem. Soc. Faraday I, 68 1890 (1972).

68. P. Moore, J. Chem. Soc. Faraday I, 73 826 (1976).

69. Nottingham Algorithms Group, Fortran Manual 6, (1977).

70. A.U. Khan, M. Kasha, J. Am. Chem. Soc. 92 3293 (1970).

71. D.L. Huestis, G. Black, S.A. Edelstein, R.L. Sharpless, J. Chem. Phys. 60 4471 (1974).

72. P.W. Atkins, "Physical Chemistry", Oxford (1978).

73. H.H. Seliger, J. Chem. Phys. 40 3133 (1964).

74. P.H. Krupenie, J. Phys. and Chem. Ref. Data, 1 423 (1972).

75. J. Goodman, L.E. Brus, J. Chem. Phys. 67 4398 (1977).

76. N. Turro, "Modern Molecular Photochemistry", Benjamin-Cummings, Menlo Park (1978).

77. G.W. Robinson, J. Chem. Phys. 46 579 (1967).

78. S.J. Arnold, E.A. Ogryzlo, H. Witzke, J. Chem. Phys. 40 1769 (1964).

79. L. Elias, E.A. Ogryzlo, H.I. Schiff, Can. J. Chem. 37 1680 (1959).

80. M.A.A. Clyne, B.A. Thrush, R.D. Wayne, Nature, 199 1057 (1963).

81. R.J. Collins, D. Husain, J. Photochem. 1 481 (1973).

82. H.J. Bauer, Physical Acountics, 2 A 48 (1964).

83. H.J. Bauer,,J. Chem. Phys. 51 3261 (1969).

84. R.C. Millikan, D.R. White, J. Chem. Phys. 39 3209 (1963).

85. D.R. White, J. Chem. Phys., 49 5472 (1968).

86. R. Frey, J. Jukasik, J. Ducuing, Chem. Phys. Lett. 14 514 (1972).

87. P.M. Borrell, Ph.D. Thesis, University of Keele (1980).

88. M. Braithwaite, E.A. Ogryxlo, J. Chem. Soc., Faraday II 72 2075 (1976).

89. J.A. Davidson, E.A. Ogryzlo in "Chemiluminescence and Bioluminescence" M.J. Cormier, D.M. Hercules, J. Lee. eds., Plenum Press, New York (1973).

90. K.H. Becker, W. Groth, U. Schurath, Chem. Phys. Lett. 8 259 (1971).

91. J.F. Noxon, J. Chem. Phys. 52 1852 (1970).

92. S.V. Filseth, A. Zia, K.H. Welge, J. Chem. Phys. 52 5502 (1970).

93. F. Stuhl, K.H. Welge, Can. J. Chem. 47 1870 (1969).

94. R.G. Aviles, D.F. Muller, P.L. Houston, Private Communication.

95. F. Stuhl, M. Niki, Chem. Phys. Lett. 7 473 (1971).

96. R.G.O. Thomas, B.A. Thrush, Proc. Roy. Soc. Lond. A356 287 (1971).

97. J.P. Monat, R.K. Hanson, C.H. Kruger, Combust Sci. Technol. 16 21 (1977).

98. R.B. Cundall in "Transfer and Storage of Energy by Molecules", 1 G.M. Burnett, A.M. North eds., Wiley, London (1969).

99. A.B. Callear, J.D. Lambert in "Comprehensive Chemical Kinetics", 3, C.H. Bamford, C.F.H. Tipper eds., Elsevier, Amsterdam (1969).

100. A.B. Callear in "Gas Kinetics and Energy Transfer" 3, The Chemical Society, London,(1978).

101. S. Lemont, G.W. Flynn, Ann. Rev. Phys. Chem. 28 261 (1977).

102. J.A. Davidson, E.A. Ogryzlo, Can. J. Chem. 52 240 (1974).

103. T.H. Dunning, P.J. Hay, J. Chem. Phys. 66 3767 (1977).

104. J.S. Cohen, W.R. Wadt, P.J. Hay, J. Chem. Phys. 71 2955 (1979).

105. E. Bauer, E.R. Fisher, F.R. Gilmore, J. Chem. Phys. 51 4173 (1969).

106. H.M. Lin, M. Seaver, K.Y. Tang, A.E.W. Knight, C.S. Parmenter, J. Chem. Phys. 70 5442 (1979).

107. C.S. Parmenter, M. Seaver, J. Chem. Phys. 70 5458 (1979).

108. E.A. Ogryzlo, B. Thrush, Chem. Phys. Lett. 24 314 (1974).

109. I. Barnes, K.H. Becker, E.H. Fink, Chem. Phys. Lett. 67 310 (1979).

110. I. Barnes, K.H. Becker, E.H. Fink, Chem. Phys. Lett. 67 314 (1979).

111. H.P. Broida, A.G. Gaydon, Proc. Roy. Soc. Lond. 222 181 (1954).

112. T.G. Slanger, Science 202 751 (1978).

113. R.D. Kenner, E.A. Ogryzlo, S. Turley, J. Photochem. 10 199 (1979).

APPENDIX 1

Laboratory and Particle Time

See figures A1 and A2.

In these experiments the gas is observed as it is forced back past the observation station. Assume the shock velocity is w_1, the gas particle velocity w_2. The laboratory time is that since the shock front passed the observer, t_ℓ; the particle time is that since the particle entered the shock, t_p. From figure A.2

$$w_1 t_p = w_2 t_p - w_1 t_\ell \tag{A.1.1.}$$

$$\frac{t_p}{t_\ell} = \frac{w_1}{w_1 - w_2} \tag{A.1.2}$$

Or, in shock fixed co-ordinates (figure A.1)

$$\frac{t_p}{t_\ell} = \frac{u_1}{u_2} \tag{A.1.3}$$

For conservation of mass across the shock front

$$\rho_1 u_1 = \rho_2 u_2 \tag{A.1.4}$$

From A.1.2 and A.1.3

$$\frac{w_1}{w_1 - w_2} = \frac{u_1}{u_2} \tag{A.1.5}$$

Hence

$$w_2 = w_1 \left\{ 1 - \frac{1}{\rho_{21}} \right\} \tag{A.1.6}$$

a) Laboratory Coordinates

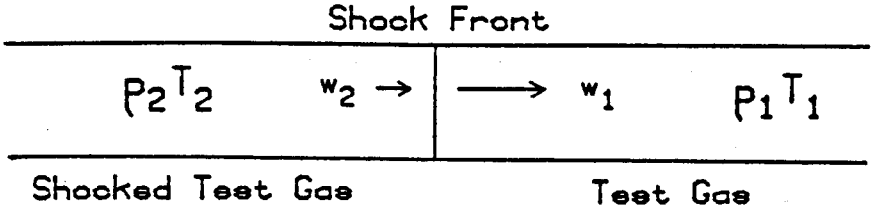

b) Shock Fixed Coordinates

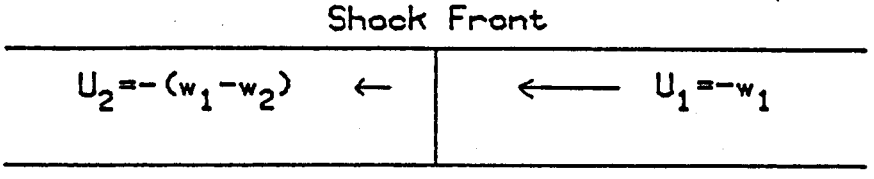

Figure A1 Coordinate Systems for Shock Equations

Figure A2 Laboratory and Particle Time

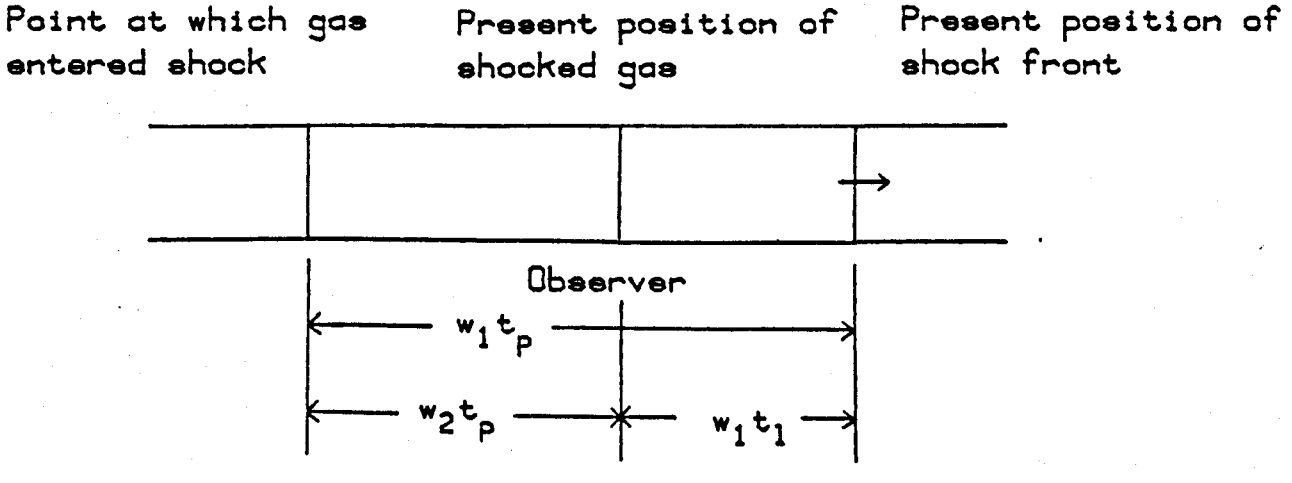

APPENDIX 2

Effect of Vibrational Relaxation on Analysis

From the results of chapter 4 it can be seen that vibrational relaxation of oxygen occurs during the shock, consequently the density and temperature change with time. The effect on the results of such changes is significant and so the graphical analysis has been modified to take them into account. However, because of the systems studied, only runs C4-10A of this work, were so analysed.

During the analysis of runs C4-10A, containing 10% nitrogen, equations A2.3 and A2.2 were used to determine the correct density and temperature.

$$\rho_{t1} = \rho_{A1} + (\rho_{B1} - \rho_{A2})(1-\exp -t/\tau_{O2}) + (\rho_{21} - \rho_{B1})(1-\exp -t/\tau_{N2}) \quad (A.2.1)$$

$$T_t = T_A + (T_B - T_A)(1-\exp -t/\tau_{O2}) + (T_2 - T_B)(1-\exp -t/\tau_{N2}) \quad (A.2.2)$$

This analysis, based on White's experiments,[85] assumes that relaxation of oxygen occurs first, to state B where nitrogen is still frozen. Subsequent relaxation of nitrogen takes the system to state 2. The timescale for the graphical analysis (then on the 4130) was changed to particle time which changed with the density ratio.

Experience has shown that the changes to the results due to the changing timescale are not significant, consequently the analysis now proceeds in laboratory time.

The vibrational relaxation times of carbon dioxide and nitrous oxide are very fast,[9] about 1 μs atm at 1000 K. Consequently, as V-V exchange is likely to be rapid in O_2/CO_2 and O_2/N_2O systems the fully relaxed temperature and density are used in the analysis.

APPENDIX 3

Effects of Non-Uniform Flow on Analysis

The formation of a boundary layer, that is a layer of cold gas behind the shock front, is one of the major causes of non-ideal behaviour in shock tubes. The boundary layers cause momentum to be transferred from the shock front to the contact surface, accelerating the latter and causing changes in density and temperature.

The work of Pedley[56] has shown that while the theoretical model of Mirels predicts considerable changes to density and temperature due to non-uniform flow, our experimental evidence suggests they are negligible. Firstly there is no evidence from the shock trace that the flow is non-ideal. Secondly experiments have shown that the hot flow time is still increasing with distance near the observation station. If a boundary layer were formed the transfer of momentum means that eventually the shock front and contact surface travel with equal velocity and so the hot flow time is constant.

On the basis of this evidence the effects of non-uniform flow are ignored during the analysis.

Appendix 4

Comparative Emission Results

All runs 100% O_2, 100W, 28ml s^{-1}

No.	λ /nm	Init. Pres. /torr	Init. Temp. /K	Pre-Shock Glow /mV	Speed /kms^{-1}	T /K	Ratio K	Decay /m^{-1}	Int. Time /us
C128	703	6.68	298	65.3	1.362	1136	0.90	1.313	130.2
C128A	634	6.68	298	22.3	1.362	1136	1.12	1.289	64.3
C129	703	6.59	298	65.5	1.354	1126	0.80	1.160	127.5
C129A	634	6.59	298	22.3	1.354	1126	1.12	1.274	95.3
C130	703	6.68	298	63.0	1.546	1372	1.00	0.967	91.8
C130A	634	6.68	298	22.1	1.546	1372	1.16	1.216	70.6
C131A	634	6.47	296	42.7	1.345	1116	1.07	1.284	79.8
C132	579A	6.51	296	7.3	1.370	1146	3.17	1.386	35.4
C132A	634A	6.51	296	44.7	1.370	1146	0.95	1.170	63.2
C133	579A	6.55	297	6.9	1.573	1408	4.25	1.091	30.0
C133A	634A	6.55	297	42.7	1.573	1408	1.18	1.254	90.7
C134	634C	6.51	298	40.2	1.359	1132	0.93	1.201	72.9
C134A	634A	6.51	298	41.4	1.359	1132	0.98	1.202	98.4
C135	703B	6.51	297	49.7	1.370	1146	0.84	1.093	77.2
C135A	634A	6.51	297	39.3	1.370	1146	1.02	1.151	87.6
C136	703B	6.55	298	49.3	1.554	1382	1.06	0.981	102.4
C136A	634A	6.55	298	38.6	1.554	1382	1.06	1.046	55.6

Appendix 5
Vibrational Relaxation Results
All runs 100% O_2, 100 W, 28 ml s^{-1}

No.	λ /nm	Init. Pres. /torr	Init. Temp. /K	Pre-Shock Glow /mV	Speed /kms^{-1}	Rel. Const. /us	Ratio K	Decay /m^{-1}	Int. Time /us
C54	579	6.72	295	6.1	1.624	72.68	5.64	1.392	35.6
C54A	634	6.72	295	34.6	1.624		1.39	1.229	126.1
C57	579	6.39	293	5.3	1.607	55.40	6.00	1.268	31.9
C57A	634	6.39	293	29.8	1.607		1.51	1.146	91.5
C58	579	6.47	294	4.5	1.589	48.81	4.68	1.039	33.4
C58A	634	6.47	294	27.9	1.589		0.71	0.968	95.4
C59	579	6.47	295	5.0	1.602	55.90	4.78	1.213	35.3
C59A	634	6.47	295	27.8	1.602		1.36	1.160	129.1
C60	579	6.55	294	6.0	1.373	162.35	3.67	1.480	33.7
C60A	634	6.55	294	30.6	1.373		1.25	1.127	117.1
C61	579	6.88	298	6.6	1.582	43.78	4.90	1.201	31.7
C61A	634	6.88	298	35.4	1.582		1.36	1.177	100.0
C62	579	6.88	298	6.1	1.565	43.79	5.23	1.345	31.5
C62A	634	6.88	298	35.0	1.565		1.27	1.253	99.2
C63	579	6.64	300	7.6	1.523	70.20	4.63	1.251	32.7
C63A	634	6.64	300	42.7	1.523		1.23	1.079	93.0
C64	579	6.72	298	7.4	1.473	59.34	4.64	1.332	31.5
C64A	634	6.72	298	41.8	1.473		1.41	1.324	66.1
C65	579	6.72	300	7.6	1.523	46.40	3.72	1.180	34.4
C65A	634	6.72	300	41.9	1.523		1.06	1.007	96.5
C67	579	6.84	300	7.4	1.506	60.68	4.06	1.272	32.5
C67A	634	6.84	300	40.5	1.506		1.13	1.070	104.5
C68	579	6.76	300	6.7	1.529	62.14	5.26	1.305	34.5
C68A	634	6.76	300	41.0	1.529		1.12	1.126	70.7
C69	579	6.40	293	6.8	1.630	25.89	5.76	1.319	33.8
C69A	634	6.40	293	39.2	1.630		1.29	0.873	75.9
C70	579	6.68	293	7.1	1.604	44.67	5.47	1.359	26.0
C70A	634	6.68	293	42.6	1.604		1.16	0.792	78.7
C71	579	6.64	293	8.0	1.630	51.43	5.51	1.361	26.2
C72	579	6.76	295	7.6	1.714	21.10	5.80	1.164	28.2
C72A	634	6.76	295	43.6	1.714		1.42	1.022	74.6
C73	579	6.59	295	7.2	1.620	39.88	5.51	1.282	26.1
C73A	634	6.59	295	42.2	1.620		1.26	0.944	68.9
C94	579	6.72	293	5.9	1.358	109.26	3.57	1.519	28.7
C94A	634	6.72	293	33.8	1.358		1.12	1.103	74.0
C95	579	6.72	294	6.8	1.376	216.91	5.03	1.372	30.4
C95A	634	6.72	294	38.7	1.376		1.23	0.894	80.6
C96	579	6.72	294	7.7	1.363	85.62	3.00	1.120	24.7
C96A	634	6.72	294	42.9	1.363		1.17	1.011	116.3

Appendix 5 continued

Vibrational Relaxation Results
All runs 100% O_2,80 W,28 ml s^{-1}

No.	λ /nm	Init. Pres. /torr	Init. Temp. /K	Pre-Shock Glow /mV	Speed /kms^{-1}	Rel. Const. /us	Ratio K	Decay /m^{-1}	Int. Time /us
C74	579	6.55	295	7.0	1.390	81.49	1.84	1.175	27.6
C74A	634	6.55	295	40.2	1.390		0.85	1.250	73.2
C75	579	6.64	296	4.3	1.378	98.18	2.82	1.091	30.4
C75A	634	6.64	296	21.3	1.378		1.37	1.239	138.9

Appendix 6

Sigma Quenching Results

All runs 100W, 28ml s^{-1}

90% O_2, 10% N_2 Runs

No.	λ /nm	Init. Pres. /torr	Init. Temp. /K	Pre-Shock Glow /mV	Speed /kms^{-1}	Rel. Const /us	Ratio K
C4	762	6.55	291	585	0.867	458.8	1.48
C4A	762	6.55	291	585	0.867	664.9	1.58
C5	762	6.40	292	554	0.855	615.1	1.37
C5A	762	6.40	292	543	0.855	776.0	1.48
C6	762	6.47	293	578	0.932	1195.0	1.62
C6A	762	6.47	293	575	0.932	432.9	1.58
C7	762	6.31	293	579	0.930	409.2	1.43
C7A	762	6.31	293	563	0.930	388.6	1.55
C8	762	6.47	294	550	0.925	392.1	1.44
C8A	762	6.47	294	550	0.925	457.7	1.52
C9	762	6.50	293	100	1.520	88.9	2.93
C9A	762	6.50	293	115	1.520	141.0	3.10
C10	762	6.55	294	133	1.610	38.3	2.97
C10A	762	6.55	294	122	1.610	56.8	3.30
			45% O_2, 45% N_2, 10% Ar Runs				
C121A	762	6.55	294	37.2	1.379	181.0	6.08
C123A	762	6.39	291	37.6	1.404	176.0	6.50
C124	762	6.51	293	66.6	1.437	134.5	6.63
C124A	762	6.51	293	106.1	1.437	126.3	6.13
C125	762	6.47	293	103.6	1.411	149.2	6.43
C125A	762	6.47	293	108.1	1.411	156.9	6.45
C126	762	6.92	293	89.6	1.380	169.7	6.03
C126A	762	6.92	293	86.1	1.380	163.9	5.94

Appendix 6 continued

Sigma Quenching Results

All runs 100W, 28ml s^{-1}

30% O_2, 30% N_2, 40% Ar Runs

No.	λ /nm	Init. Pres. /torr	Init. Temp. /K	Pre-Shock Glow /mV	Speed /kms^{-1}	Rel. Const /us	Ratio K
C138	762	6.96	296	57.0	1.393	261.3	8.73
C139	762	6.96	297	78.7	1.401	141.7	6.89
C140	762	6.47	297	80.2	1.393	197.0	8.64
C141	762	6.72	297	60.1	1.581	99.9	12.01
C142	762	6.84	298	53.8	1.608	106.1	14.95
C142A	762	6.84	298	53.4	1.608	86.7	10.36
C143	762	6.76	298	46.6	1.616	103.0	13.53
C143A	762	6.76	298	51.6	1.616	85.1	10.66
C144	762	6.64	297	50.1	1.479	134.9	8.11
C144A	762	6.64	297	47.7	1.479	138.6	7.29
C145	762	7.08	298	42.6	1.470	123.6	9.99
C145A	762	7.08	298	44.2	1.470	169.0	7.77
C146	762	6.80	297	34.3	1.200	196.1	4.55
C146A	762	6.80	297	41.5	1.200	376.0	4.16
C147	762	6.68	297	57.2	1.201	492.4	7.44
C147A	762	6.68	297	54.4	1.201	593.6	7.15
C148	762	6.76	297	53.4	1.212	432.9	6.48
C148A	762	6.76	297	53.4	1.212	359.4	4.75
C149	762	6.60	296	68.1	0.869	471.5	2.55
C149A	762	6.60	296	69.4	0.869	362.2	2.02
C150	762	6.60	297	109.2	0.881	725.6	2.08
C150A	762	6.60	297	110.4	0.881	358.9	2.06
C151	762	6.92	298	120.1	0.873	567.9	2.39
C151A	762	6.92	298	112.7	0.873	573.2	2.17

Appendix 6 continued

Sigma Quenching Results

All runs 100W,28ml s^{-1}

79% O_2,21% CO_2 Runs

No.	λ /nm	Init. Pres. /torr	Init. Temp. /K	Pre-Shock Glow /mV	Speed /kms^{-1}	Rel. Const /us	Ratio K
C152A	762	6.40	293	4.5	1.360	8.6	61.0
C153	634	6.40	292	8.4	1.320		1.47
C153A	762	6.40	292	4.8	1.320	14.0	59.9
C154	634	6.72	293	10.0	1.315		1.32
C154A	762	6.72	293	5.5	1.315	12.1	48.2
C155	634	6.80	293	9.8	1.340		1.65
C155A	762	6.80	293	5.8	1.340	5.8	45.6
C156	634	6.92	293	8.9	1.550		1.21
C156A	762	6.92	293	5.2	1.550	5.5	159.8
C157A	762	6.58	293	5.9	1.547	4.9	149.0
C158A	762	6.76	293	5.3	1.540	5.3	138.8
C159	634	6.26	295	11.2	1.365		1.39
C159A	762	6.26	295	6.7	1.365	11.1	54.9
C160A	762	6.64	293	6.1	1.208	13.4	16.6
C161	634	6.43	293	17.9	1.243		1.39
C161A	762	6.43	293	8.9	1.243	5.2	24.4
C162A	762	6.51	293	6.8	1.261	14.1	37.7
C163A	762	6.72	293	6.6	1.182	17.4	21.0

Appendix 6 continued

Sigma Quenching Results

All runs 100W,28ml s^{-1}

95% O_2,5% CO_2 Runs

No.	λ /nm	Init. Pres. /torr	Init. Temp. /K	Pre-Shock Glow /mV	Speed /kms^{-1}	Rel. Const /us	Ratio K
C178	634	6.96	293	19.6	1.342		1.41
C178A	762	6.96	293	12.6	1.342	11.2	22.6
C179	634	6.88	293	30.6	1.336		1.44
C179A	762	6.88	293	21.3	1.336	16.4	26.1
C180	762	6.76	292	20.8	1.347	17.5	32.0
C180A	634	6.76	292	19.7	1.347		1.25
C181	762	6.55	293	20.5	1.192	13.1	13.6
C181A	634	6.55	293	20.3	1.192		1.14
C182	762	6.76	293	20.3	1.209	14.3	15.5
C182A	634	6.76	293	20.2	1.209		1.07
C186	762	6.43	293	77.9	0.860	41.1	3.8
C186A	634	6.43	293	22.4	0.860		0.96
C187	762	6.51	293	80.6	0.858	11.3	3.2
C187A	634	6.51	293	23.5	0.858		0.94
C188	762	6.68	293	95.5	0.862	27.6	3.7
C188A	634	6.68	293	22.3	0.862		1.00
C189	762	6.68	293	91.0	1.093	11.3	6.8
C189A	634	6.68	293	21.7	1.093		1.13
C190	762	6.82	293	92.6	0.964	24.9	4.77
C190A	634	6.82	293	21.7	0.964		0.91
C191	762	6.72	290	98.7	0.942	18.6	4.87
C191A	634	6.72	290	21.6	0.942		1.22
C192	762	6.43	292	111.1	0.952	17.3	4.84
C192A	634	6.43	292	23.1	0.952		0.99
C193	762	6.47	293	110.4	0.992	11.3	4.87
C193A	634	6.47	293	22.7	0.992		1.00
C194	762	6.43	293	116.0	1.095	17.4	7.78
C194A	634	6.43	293	24.2	1.095		1.07
C195	762	6.43	292	105.3	1.218	17.5	14.0
C195A	634	6.43	292	21.3	1.218		1.20
C196	762	6.51	293	101.8	1.151	23.1	10.8
C196A	634	6.51	293	21.4	1.151		1.04
C197	762	6.51	293	103.4	1.114	20.0	8.88
C197A	634	6.51	293	22.1	1.114		1.22
C198	762	6.64	293	98.3	1.131	14.8	9.45
C198A	634	6.64	293	21.4	1.131		1.11
C199	762	6.54	290	5.3	1.428	12.3	40.1
C199A	634	6.54	290	21.7	1.428		1.27

Appendix 6 continued

Sigma Quenching Results

All runs 100W, 28ml s^{-1}

95% O_2, 5% CO_2 Runs

No.	λ /nm	Init. Pres. /torr	Init. Temp. /K	Pre-Shock Glow /mV	Speed /kms^{-1}	Rel. Const /us	Ratio K
C200	762	6.76	292	18.3	1.459	8.3	46.4
C200A	634	6.76	292	21.2	1.459		1.32
C201	762	6.55	293	19.4	1.329	14.9	25.1
C201A	634	6.55	293	22.1	1.329		1.33
C202	762	6.41	293	18.5	1.403	10.0	35.4
C202A	634	6.41	293	21.6	1.403		1.32
C203	762	6.64	293	17.9	1.460	10.3	46.6
C203A	634	6.64	293	21.2	1.460		1.32
			90% O_2, 10% CO_2 Runs				
C204	762	6.64	292	9.3	1.551	8.5	111.7
C204A	634	6.64	292	18.5	1.551		1.49
C205	762	6.72	292	9.2	1.552	15.1	129.7
C205A	634	6.72	292	18.7	1.552		1.71
			98.3% O_2, 1.7% CO_2 Runs				
C208	762	6.51	293	29.2	1.103	32.6	6.83
C208A	634	6.51	293	21.4	1.103		1.07
			90% O_2, 10% N_2O Runs				
C214	762	6.68	296	20.2	1.360	12.0	12.0
C215	762	6.88	296	14.6	1.328	14.3	15.1
C216	762	6.47	296	16.9	1.361	18.2	16.8
C217	762	6.76	293	14.3	1.170	18.3	8.74
C218	762	6.64	294	35.6	1.184	14.0	8.65
C219	762	6.75	295	36.0	1.181	15.8	8.46
C223	762	6.80	295	36.8	1.357	13.2	17.3
C226	762	6.64	294	22.6	1.421	10.1	22.7
C227	762	6.47	294	27.7	1.413	5.8	21.7
C228	762	6.59	295	27.0	1.455	11.0	28.1